Identification of Roquin-regulated mRNAs in T helper cells and molecular characterization of the Roquin-RNA interaction

Dissertation der Fakultät für Biologie
der Ludwig-Maximilians-Universität München
zur Erlangung des Doktorgrades der Naturwissenschaften

vorgelegt von
Gitta Anne Maren Heinz
aus Ludwigshafen (Rhein)

München, 18. November 2014

The world is a thing of utter inordinate complexity and richness
and strangeness that is absolutely awesome.

Douglas Adams

Diese Dissertation wurde angefertigt

unter der Leitung von Prof. Dr. Vigo Heissmeyer

am Institut für molekulare Immunologie, Abteilung für molekulare Immunregulation

am Helmholtz Zentrum München

Erstgutachter: Prof. Dr. Daniel Krappmann

Zweitgutachter: Prof. Dr. Elisabeth Weiß

Tag der Abgabe: 18. November 2014

Tag der mündlichen Prüfung: 13. März 2015

Erklärung

Hiermit versichere ich, Gitta Anne Maren Heinz, an Eides statt, dass meine Dissertation mit dem Titel **„Identification of Roquin-regulated mRNAs in T helper cells and molecular characterization of the Roquin-RNA interaction"** von mir selbständig und ohne unerlaubte Hilfsmittel angefertigt worden ist.

Die vorliegende Dissertation wurde weder ganz, noch teilweise bei einer anderen Prüfungskommission vorgelegt. Ich habe noch zu keinem früheren Zeitpunkt versucht eine Dissertation einzureichen oder an einer Doktorprüfung teilzunehmen.

München, den 18.11.2014

Summary

The immune system combines potent humoral and cellular mechanisms fighting invading pathogens and infections. To prevent excessive inflammation and autoimmunity, immune responses are subject to extensive regulation on different levels of gene expression. Signaling via costimulatory receptors for example sets a threshold for T cell activation. Roquin-1 is an RNA-binding protein targeting the inducible costimulator (*Icos*) mRNA in T cells for post-transcriptional repression. The importance of Roquin-1 function for immune regulation became obvious in *sanroque* mice developing severe lupus-like autoimmune disease due to a single amino acid exchange in Roquin-1. A lack of Roquin-1 in T cells is compensated by its paralog Roquin-2, suggesting that Roquin-2 similarly represses mRNAs.

In this thesis work, assays were established to identify additional mRNAs that are bound and regulated by Roquin proteins in T helper cells. Acute deletion of Roquin-encoding genes in primary $CD4^+$ T cells led to an upregulation of more than 50 mRNAs. One newly identified target was the mRNA of the costimulator Ox40, being specifically bound and post-transcriptionally regulated by Roquin proteins via its 3'UTR. To address the molecular requirements of Roquin-RNA interactions, I performed affinity-based selection experiments (SELEX) from a random RNA library and found a novel RNA sequence motif embedded in an RNA hexaloop to be preferentially bound by the Roquin-1 N-terminus. In collaboration with structural biologists we investigated the crystal structure of a protein-RNA complex that contains the RNA-binding ROQ domain and an RNA stem-loop structure from the *Tnf* 3'UTR, called constitutive decay element (CDE). The structure of this complex identified amino acids forming close RNA contacts and showed mainly non-sequence-specific protein-RNA interactions via the phosphate backbone of the RNA stem. In cell-based reporter assays using Roquin-1 mutants, I proved that the ability to bind RNA is required for Roquin-mediated post-transcriptional regulation of Icos and Ox40. Furthermore, I analyzed the *Ox40* 3'UTR and identified a CDE-like triloop and a SELEX-like hexaloop as the two functional *cis*-elements through which Roquin-1 regulates Ox40 expression.

Taken together, my studies identified potential mRNA targets of Roquin in T helper cells and shed light on the molecular picture of Roquin-RNA interactions. Thereby, I could show that Roquin accepts a number of different *cis*-regulatory RNA elements, which are rather defined by structural than sequence requirements. My work contributes to the understanding of Roquin-mediated post-transcriptional gene regulation, underlying the prevention of excessive inflammation and autoimmunity.

Zusammenfassung

Das Immunsystem vereint wirksame humorale und zelluläre Mechanismen zur Bekämpfung von Pathogenen und Infektionen. Um übermäßige Inflammation und Autoimmunität zu verhindern, unterliegen Immunantworten umfassender Regulation auf verschiedenen Ebenen der Genexpression. Signaltransduktion kostimulatorischer Rezeptoren erzeugt beispielsweise einen Schwellenwert für die T-Zell-Aktivierung. Roquin-1 ist ein RNA-bindendes Protein, das die mRNA des induzierbaren Kostimulators *Icos* auf post-transkriptioneller Ebene reprimiert. Die Bedeutung der Roquin-1 Funktion für Immunregulation zeigte sich deutlich in *sanroque* Mäusen, die aufgrund eines Aminosäureaustausches in Roquin-1 eine schwere Lupus-ähnliche Autoimmunerkrankung entwickeln. Das Fehlen von Roquin-1 in T-Zellen wird durch sein Paralog Roquin-2 kompensiert, was nahelegt, dass Roquin-2 ebenfalls mRNAs reprimiert.

In dieser Dissertation wurden Experimente etabliert, um weitere mRNAs zu identifizieren, die von Roquin-Proteinen in T-Helfer-Zellen gebunden und reguliert werden. Akute Deletion der Roquin-kodierenden Gene in primären $CD4^+$ T-Zellen führte zu einer Hochregulation von mehr als 50 mRNAs. Eines der neu identifizierten Zielmoleküle war die mRNA des Kostimulators *Ox40*, die über den 3'UTR von Roquin Proteinen spezifisch gebunden und post-transkriptionell reguliert wird. Um die molekularen Voraussetzungen der Roquin-RNA Interaktion zu adressieren, führte ich affinitätsbasierte Selektionsexperimente (SELEX) mit einer RNA Bibliothek mit zufälliger Nukleotidsequenz durch. Dabei identifizierte ich ein neuartiges, in eine Sechserschleife eingebettetes Sequenzmotiv, das vom Roquin-1 N-Terminus bevorzugt gebunden wird. In Zusammenarbeit mit Strukturbiologen untersuchten wir die Kristallstruktur eines Protein-RNA Komplexes bestehend aus der RNA-bindenden ROQ Domäne und einer RNA Haarnadelstruktur aus dem *Tnf* 3'UTR, die als „constitutive decay element" (CDE) bezeichnet wird und eine Dreierschleife ausbildet. Die Struktur dieses Komplexes zeigte Aminosäuren auf, die in engem Kontakt zur RNA stehen und es stellte sich heraus, dass hauptsächlich sequenzunabhängige Protein/RNA Interaktionen über das Phosphat-Rückgrat der doppelsträngigen RNA-Abschnitte stattfinden. In zellbasierten Reporter-Experimenten wies ich unter der Verwendung von Roquin-1 Mutanten nach, dass die Fähigkeit RNA zu binden notwendig ist für die Roquin-vermittelte post-transkriptionelle Regulation von Icos und Ox40. Darüberhinaus analysierte ich den *Ox40* 3'UTR und identifizierte eine CDE-ähnliche und eine SELEX-ähnliche Haarnadelstruktur als die zwei funktionellen *cis*-Elemente, über die Roquin-1 Ox40 reguliert.

Zusammengefasst identifizierten meine Untersuchungen potentielle Ziel-mRNAs in T-Helfer-Zellen und gaben Aufschluss über die molekulare Gestalt von Roquin-RNA Interaktionen. Dabei konnte ich zeigen, dass Roquin eine Anzahl verschiedener *cis*-regulatorischer RNA Elemente akzeptiert, die sich eher über strukturelle als sequenzabhängige Bedingungen definieren. Meine Arbeit leistet einen Beitrag zum Verständnis der Roquin-vermittelten post-transkriptionellen Genregulation, welche der Verhinderung übermäßiger Inflammation und Autoimmunität zugrunde liegt.

Directory

Erklärung 1

Summary 3

Zusammenfassung 5

Directory 7

List of figures 9

List of tables 11

Abbreviations 13

1 Introduction 17

1.1 The immune system 17
1.1.1 T cell immunity 18
1.1.2 Peripheral tolerance and autoimmunity 26
1.2 Post-transcriptional gene regulation 28
1.2.1 Processes targeted during post-transcriptional regulation 28
1.2.2 Mediators of post-transcriptional gene regulation 31
1.2.3 Post-transcriptional gene regulation in the immune system 35
1.3 The protein Roquin 36
1.3.1 Roquin in mouse models 37
1.3.2 Domain organization and function of Roquin proteins 38
1.3.3 Roquin as RNA-binding protein and post-transcriptional regulator 40

2 Aim of the project 43

3 Material and Methods 45

3.1 Material 45
3.1.1 Mice 45
3.1.2 Cell lines and cell culture 46
3.1.3 Plasmids and bacteria culture 47
3.1.4 Oligonucleotides 50
3.1.5 Antibodies and cytokines 54
3.1.6 Chemicals, enzymes and kits 56
3.1.7 Buffers 59
3.1.8 Columns and consumables 61
3.1.9 Instruments 61
3.1.10 Software and databases 63
3.2 Methods 64

3.2.1 Molecular biological methods 64
3.2.2 RNA methods 67
3.2.3 Cell biological methods 70
3.2.4 Flow cytometry and cell sorting 72
3.2.5 Structural analysis 74
3.2.6 High throughput assays 75

4 Results 79

4.1 Identification of mRNAs targeted by Roquin 79
4.1.1 Microarray analyses of Th1 cells upon acute deletion of *Rc3h1-2* 79
4.1.2 The mRNA of the costimulatory receptor Ox40 is bound and regulated by Roquin 88
4.1.3 Analysis of a combined Roquin and Ox40 knockout in mice 90
4.1.4 Roquin CLIP and PAR-CLIP assays in primary Th1 cells 99
4.2 Molecular analysis of the Roquin-RNA interaction 107
4.2.1 Selection of Roquin-bound RNAs from a random library 107
4.2.2 Crystal structures of the ROQ domain and the ROQ-RNA complex 113
4.2.3 Mutational analysis of the ROQ-RNA interaction site 117
4.2.4 Investigating the spectrum of CDE stem-loops 122
4.2.5 *Cis*-element analysis of the *Ox40* 3'UTR 127

5 Discussion 133

5.1 Roquin target identification 133
5.1.1 Microarray analyses of Th1 cells upon acute deletion of Roquin 133
5.1.2 Roquin CLIP and PAR-CLIP assays in primary Th1 cells 137
5.1.3 Conclusions on Roquin target identification 139
5.2 Molecular requirements for the Roquin-RNA interaction 142
5.2.1 Identification of high-affinity Roquin binding sites by SELEX 142
5.2.2 Structural analysis of the Roquin-RNA interaction 144
5.3 The inducible costimulator Ox40 is a target of Roquin 150
5.3.1 *Ox40* is specifically bound and regulated by Roquin 150
5.3.2 Ox40 contribution to the Roquin knockout phenotype in T cells 151
5.3.3 Roquin recognizes two distinct *cis*-elements in the *Ox40* 3'UTR 153
5.4 Conclusions and perspectives for Roquin-mediated post-transcriptional gene regulation 154

References 159

Appendices 175

Publications 181

Curriculum vitae 183

Acknowledgements 185

List of figures

Figure 1: Schematic representation of T helper cell differentiation and plasticity. ... 21
Figure 2: Overview of costimulatory receptors on T helper cells and their corresponding ligands on antigen presenting cells. ... 24
Figure 3: T helper cell signaling pathways involved in costimulation. ... 26
Figure 4: Scheme of mRNA degradation pathways. ... 30
Figure 5: Roquin-1 and Roquin-2 domain organization and amino acid (aa) sequence similarity. ... 39
Figure 6: Scheme of Roquin function as RNA-binding protein. ... 41
Figure 7: Schematic representation of genetically modified alleles used in this study. ... 45
Figure 8: Gating strategy for Tfh cells using FlowJo. ... 74
Figure 9: Schematic representation of the PAR-CLIP procedure. ... 76
Figure 10: Evaluation of the acute Roquin deletion in Th1 cells. ... 81
Figure 11: Sample preparation for mRNA expression arrays. ... 83
Figure 12: Preparation of *Icos*$^{-/-}$ samples for the second array experiment. ... 84
Figure 13: Heatmap showing relative expression of Roquin target candidates. ... 85
Figure 14: Evaluation of Roquin target candidates by qPCR. ... 87
Figure 15: Validation of *Ox40* as Roquin target mRNA. ... 89
Figure 16: Analysis of spleens from mice with a combined Roquin and Ox40 knockout in T cells. ... 90
Figure 17: CD4^{+} T cells are reduced and highly activated in triple knockout mice. ... 92
Figure 18: CD8^{+} T cells are excessively activated in triple knockout mice. ... 93
Figure 19: Double knockout and triple knockout mice have increased levels of Tfh cells and GC B cells. ... 95
Figure 20: Frequency of different lymphocyte subsets in triple knockout mice. ... 96
Figure 21: Icos and Ctla4 MFI are increased in different T cell subsets of double as well as triple knockout mice. ... 98
Figure 22: Immunoprecipitation (IP) of Roquin-1 and Roquin-2 from Th1 cell lysates. ... 100
Figure 23: Documentation of the PAR-CLIP assays (samples 1-3). ... 101
Figure 24: Mutation plots of all CLIP and PAR-CLIP samples. ... 103
Figure 25: Sequence patterns of the area next to T to C conversion sites. ... 104
Figure 26: Number of clipped sequences in the proximity of CDE stem-loops. ... 105
Figure 27: Two sequence clusters are clipped in the *Ox40* 3'UTR. ... 106
Figure 28: Documentation of the SELEX experimental procedure. ... 108
Figure 29: Sequence statistics of the Roquin-1 SELEX experiment (replicate 1). ... 109
Figure 30: SELEX patterns bind to Roquin-1 N-terminus (aa 2-440). ... 110

Figure 31: High-affinity patterns are specifically bound by the ROQ domain. 111
Figure 32: Analysis of enriched hexamers within the SELEX patterns. 112
Figure 33: Secondary structure prediction of the SELEX motif. 113
Figure 34: Definition of the minimal ROQ domain by RNA binding. 114
Figure 35: Crystal structure of the ROQ domain. 115
Figure 36: Crystal structure of the ROQ-*Tnf* CDE complex. 116
Figure 37: Mutational analysis of the ROQ RNA-binding interface. 118
Figure 38: Comparable overexpression of Roquin-1 wild-type (WT) and RNA-binding-impaired mutants. 119
Figure 39: Functional analysis of Roquin-1 ROQ domain mutants. 121
Figure 40: Mutational analysis of the *Tnf* CDE RNA. 123
Figure 41: Binding of CDE-like RNA stem-loops from *ICOS* and *Ox40* 3'UTR. .. 124
Figure 42: CDE-like stem-loops are functional *cis*-elements in Roquin-mediated regulation. 126
Figure 43: Motif and conservation analysis of the *Ox40* 3'UTR. 128
Figure 44: *Ox40* SELEX-like RNA binding analysis with ROQ domain mutants. 129
Figure 45: *Ox40* 3'UTR constructs as tested in binding and functional analyses. 130
Figure 46: Binding analysis of the *Ox40* 3'UTR in band shift assays. 131
Figure 47: Functional analysis of truncated and mutated *Ox40* 3'UTRs. 132
Figure 48: Model of Roquin-mediated post-transcriptional regulation targeting different 3'UTRs. 156
Figure 49: Model of Roquin function in T cells. 158

List of tables

Table 1: Cell culture components ... 46
Table 2: Entry vectors ... 47
Table 3: Destination vectors and their applications ... 48
Table 4: Plasmids for recombinant protein expression ... 49
Table 5: RNA oligonucleotides ... 50
Table 6: Primers for cloning and site directed mutagenesis ... 50
Table 7: Primers for SELEX ... 51
Table 8: *In vitro* transcription templates ... 52
Table 9: Primers for qPCR ... 54
Table 10: Antibodies and cytokines ... 54
Table 11: Chemicals and solutions ... 56
Table 12: Enzymes ... 58
Table 13: Kits ... 58
Table 14: Buffers for standard procedures ... 59
Table 15: Buffers for CLIP and PAR-CLIP assays ... 60
Table 16: Buffers for SELEX and Filter binding assays ... 60
Table 17: Columns and consumables ... 61
Table 18: Instruments ... 61
Table 19: Software and databases ... 63
Table 20: Potential Roquin targets with ≥1.5-fold expression in the first set of arrays and their fold change in *Icos*$^{-/-}$ validation arrays. ... 86
Table 21: Number of reads and read annotation in CLIP and PAR-CLIP samples according to standard analysis procedure of the Clipz database pipeline. ... 102
Table 22: Number of total reads and reads mapping to mRNAs after removal of linker sequences. This analysis was performed by Dr. Andreas Gruber. ... 102
Table 23: Comparison of methods for Roquin target identification and summary of the subsequent target validation procedure ... 141
Table 24 Comparison of Roquin structure investigations from Schlundt et al. and Tan et al. ... 147

Abbreviations

4SU	4-thiouridine
aa	Amino acid(s)
ANA	Anti-nuclear antibody
AP1	Activator protein 1
APC	Allophycocyanin (Fluorochrome)
APC	Antigen presenting cell
ARE	AU-rich element
AUF1	AU-binding factor 1
BSA	Bovine serum albumin
CAG	CMV early enhancer/chicken beta-actin
CAR	Coxsackievirus and adenovirus receptor
CC	Coiled-coil
CD	Cluster of differentiation
CDE	Constitutive decay element
CDS	Coding DNA sequence, coding sequence
CLIP	Cross-linking and immunoprecipitation
CSPF	Cleavage/polyadenylation specificity factor
CTL	Cytotoxic T lymphocyte
Ctla4	Cytotoxic T lymphocyte antigen 4
DMEM	Dulbecco's Modified Eagle Medium
DNA	Desoxyribonucleic acid
Dox	Doxycyclin
DTT	Dithiothreitol
EAE	Experimentally induced autoimmune encephalomyelitis
ECL	Enhanced chemoluminescence
eEF	Eukaryotic elongation factor
eIF	Eukaryotic initiation factor
EMSA	Electrophoretic mobility shift assay
eRF1	Eukaryotic release factor 1
FBA	Filter binding assay
FCS	Fetal calf serum
fl	Full-length
GC B cell	Germinal center B cell
GFP	Green fluorescent protein
HEK293T	Human embryonic kidney cell line 293T
HRP	Horseradish peroxidase
HTH	Helix-turn-helix
IB	Immunoblotting
Icos	Murine inducible T cell costimulator
ICOS	Human inducible T cell costimulator
Ifn	Interferon
IL	Interleukin
IP	Immunoprecipitation

IPEX	Immune dysregulation, polyendocrinopathy, enteropathy, X-linked
IRES	Internal ribosomal entry site
iTreg	Induced regulatory T cell
kb	kilobases
kDa	kilodalton
Klrg1	Killer cell lectin-like receptor G1
KSRP	K homology splicing regulatory protein
LM	Loop mutant
LPS	Lipopolysaccharide
LR	Lambda recombination
MAP kinase	Mitogen-activated protein kinase
MEF	Mouse embryonic fibroblast
MEK	MAPK/ERK kinase
MFI	Mean fluorescence intensity
MHC	Major histocompatibility complex
min	Minutes
miRNA	microRNA
mRNA	Messenger RNA
mTOR	Mammalian target of rapamycin
NEAA	Non-essential amino acids
NFAT	Nuclear factor of activated T cells
NMR	Nuclear magnetic resonance
nts	Nucleotides
OD	Optical density
Ox40	Murine Tnfrsf4
P bodies	Processing bodies
PABP	Poly(A)-binding protein
PAGE	Polyacrylamide gel electrophoresis
PAMP	Pathogen associated molecular pattern
PAR-CLIP	Photoactivatable ribonucleoside-enhanced CLIP
PBS	Phosphate-buffered saline
PCR	Polymerase chain reaction
PE	R-Phycoerythrin
PFA	Paraformaldehyde
PI3K	Phosphatidylinositol 3-kinase
PKCΘ	Protein kinase CΘ
PLCγ	Phospholipase Cγ
PNK	Polynucleotide kinase
PRR	Pattern recognition receptor
PRS	Proline-rich sequence
qPCR	Quantitative Realtime PCR
RAG	Recombination-activating gene
RBP	RNA-binding protein
RING	Really interesting new gene
RNA	Ribonucleic acid
RT	Room temperature
SD	Standard deviation

SDS	Sodium dodecyl sulfate
SDS PAGE	SDS polyacrylamide gel electrophoresis
sec	Seconds
SELEX	Systematic evolution of ligands by exponential enrichment
SLBP	Stem-loop binding protein
SLE	Systemic lupus erythematosus
SLECs	Short-lived effector cells
SM	Stem mutant
STAT	Signal transducer and activator of transcription
TAC	Tris-buffered ammonium chloride
TBE buffer	Tris/Borate/EDTA buffer
TBS	Tris-buffered saline
TCE	Translation control element
TCR	T cell receptor
Tfh cells	Follicular T helper cell
TGF	Transforming growth factor
Th1 cell	Type 1 T helper cell
TIA-1	T-cell-restricted intracellular antigen 1
TIAR	TIA-1-related protein
TLR	Toll-like receptor
Tnf	Tumor necrosis factor
TRAF	Tnf receptor associated factor
Treg	Regulatory T cell
tRNA	Transfer RNA
TTP	Tristetraprolin
UTR	Untranslated region
UV	Ultraviolet
WH	Winged-helix
WT	Wild-type

1 Introduction

1.1 The immune system

Throughout its lifetime every organism is in close contact with foreign structures and molecules, which may be harmless as parts of nutrition or threatening as infectious agents. The natural barriers of an organism are specialized for selective exchange with the outside world. In addition, plants and animals evolved an innate immune system mounting rapid responses (within hours) against invading pathogens based on the recognition of pathogen-associated molecular patterns (PAMPs) (Ausubel 2005). In animals this is accomplished by innate immune cells or by the complement system (Murphy et al. 2008). The complement system is constituted of preformed proteins circulating in the blood to be activated in a cascade of proteolytic cleavage resulting in pathogen opsonization, chemotaxis and cell lysis. In contrast, tissue-resident innate immune cells such as macrophages and dendritic cells carry a number of different receptors, termed pattern recognition receptors (PRRs), to identify invading pathogens by surface structures and molecules distinguishable from the organism's own repertoire (Janeway & Medzhitov 2002). Toll-like receptors (TLRs) are a group of PRRs and they recognize for example bacterial cell wall components like LPS (lipopolysaccharide) or double-stranded viral RNA (ribonucleic acid). Upon binding TLRs trigger signaling pathways that lead to the activation of innate immune cells and secretion of immune stimulatory molecules. This promotes phagocytosis of the recognized microbe by macrophages and recruitment of neutrophil granulocytes, which are also potent phagocytes.

However, pathogens have developed mechanisms to evade this first line of host defense. Therefore, a second line of defense, the adaptive immune system, evolved in jawed fish and higher vertebrates (Murphy et al. 2008). The characteristics distinguishing the adaptive from the innate immune system are the generation of specific receptors to detect the invading pathogen and the establishment of memory cells to be protected against re-infection with the same pathogen. In contrast to PRRs that are inherited via the germ-line, receptors of the adaptive immune system (namely B and T cell receptors) are encoded by various gene segments that undergo somatic rearrangement during cell maturation. This process is known as V(D)J recombination. Different variable (V), diversity (D) and joining (J) gene segments are joined together by the lymphocyte-specific RAG (recombination-activating gene) proteins (Grawunder et al. 1998). This somatic recombination occurs independently in individual lymphocytes and brings about a polyclonal receptor repertoire of 10^{13}-10^{18} mainly through combinatorial and

junctional diversity. The abundance of one receptor specific for a certain pathogen is increased by clonal expansion of the respective cell clone within 4 to 5 days (Murphy et al. 2008). Instead of PAMPs, receptors of the adaptive immune system recognize antigens, consisting of protein and polysaccharide and rarely also of lipid structures. Yet, the specifically bound epitope is only a small part of the antigen. On the one hand, this allows the discrimination between closely related antigens, resulting in very specific immune responses. On the other hand, because of the merely molecular restrictions, epitopes can be derived from harmless foreign or self-molecules, involving the danger of inappropriate immune activation.

The cell types representing the adaptive immunity are T and B lymphocytes developing from common lymphoid progenitor cells within the bone marrow. Whereas B cells undergo further maturation in the bone marrow, T cell precursors migrate to the thymus where final maturation takes place. Like the innate immune system, the adaptive immunity is composed of a cellular and a humoral arm, the latter being provided by B cells that produce antibodies, also known as immunoglobulins, after differentiation into plasma cells. Antibodies, as the secreted form of the B cell receptor, exhibit a broad range of antigen specificities allowing them to potently bind pathogens or toxins within the extracellular space. On the molecular level they possess a variable region for specific epitope binding and a constant region by which they are recognized themselves. Thus, they tackle foreign structures and at the same time recruit other innate immune cells or activate the complement system. Hence, immunoglobulins are one example for the interaction between adaptive and innate immunity. After class switch and affinity maturation, antibody binding to epitopes can achieve a remarkably high affinity (lower nanomolar to picomolar range) (Estep et al. 2013), which in part explains their potency in fighting infections and re-infections. In mammals, the importance of antibodies is further underlined by the fact that maternal immunoglobulins are transferred to the developing fetus via the placenta. These antibodies remain in the organism for several weeks after birth and thereby provide protection against infections. The cellular arm of adaptive immunity is conferred by different T cell subsets, which either induce apoptosis in infected cells or stimulate other immune cells through secretion of cytokines. Despite its importance for the integrity of higher organisms, the adaptive immunity does not act independently but depends on antigen presentation and stimulatory signals provided by cells of the innate immunity.

1.1.1 T cell immunity

T lymphocytes obtained their name from the dependency on the thymus during development (Murphy et al. 2008). The thymus is colonized by T cell precursors from the bone marrow, which undergo differentiation, proliferation and maturation steps.

Different stages of this development are defined by the presence of the rearranged T cell receptor (TCR) chains in the context of the cluster of differentiation (CD) 3 TCR complex and expression of the co-receptor molecules CD4 and CD8. Following the double-negative ($CD4^-$ $CD8^-$) state, thymocytes with a successful rearrangement of TCR α and β chains reach the double-positive ($CD4^+$ $CD8^+$) state. During the subsequent maturation steps, expression of one co-receptor is lost, finally resulting in single-positive ($CD4^+$ or $CD8^+$) αβ T cells. Only a small portion of thymocytes rearranges the TCR γ and δ chains and develops into γδ T cells (Murphy et al. 2008).

Apart from T cell maturation and differentiation, the thymus also provides space for important selection procedures. Since peripheral antigen presentation to T cells is performed within the context of MHC (Major histocompatibility complex) molecules on the surface of antigen presenting cells (APCs), these molecules have to be recognized by T cells. Therefore, TCR rearrangement is followed by positive selection of TCRs that are able to recognize self-MHC molecules. Interestingly, T cells recognizing predominantly MHC I (class 1) molecules will maintain the expression of CD8, whereas specificity for MHC II (class 2) is accompanied by CD4 expression. The second selection step is termed negative selection and is based on the expression of ubiquitous proteins of the organism by specialized thymic stromal cells and bone marrow-derived antigen presenting cells. These cells process the proteins and present them as antigen on MHC molecules to identify self-reactive T cells. Strong TCR signaling in this process causes the elimination of the respective T cell clone, whereas weak TCR signaling in response to stimulation with self-antigen leads to the development of thymic regulatory T cells (Tregs) (Josefowicz et al. 2012). Tregs are a subset of T cells that suppresses immune responses of other cells. In total, only 3% of the double-positive thymocytes pass both the positive and the negative selection procedure and are released into the periphery (Shortman et al. 1990; Murphy et al. 2008). Thus, the thymus is the important organ to shape the peripheral TCR repertoire and to establish self-tolerance. However, some autoreactive T cells recognizing tissue-specific antigens escape the process of negative selection. To prevent autoimmunity, these T cells must be kept in check by mechanisms of peripheral tolerance. Deletion, anergy or exhaustion of self-reactive T cells, the dependency on different co-occurring signals for T cell activation or suppression by Tregs are examples of how self-tolerance can be achieved in the periphery (Srinivasan & Frauwirth 2009).

According to the expression of the co-receptors CD4 and CD8, T cells exhibit different effector functions. $CD8^+$ T cells are termed cytotoxic T lymphocytes (CTLs), because they induce apoptosis in virus-infected or dysfunctional somatic cells. In contrast, $CD4^+$ T cells, also known as T helper cells, produce cytokines and thereby shape immune reactions and support other immune cells in their function. After leaving the thymus, T cells are predominantly located in secondary lymphoid organs (spleen and lymph

nodes), where they are in a naïve state. This naïve state is defined by high CD62L (L-selectin) expression and low expression of CD44. CD62L is a lymphoid tissue homing receptor, which is downregulated upon T cell activation (Camerini et al. 1989). On the other hand, CD44 is a marker for activated T cells with an effector-memory phenotype and plays a role in lymphocyte extravasation (DeGrendele, Kosfiszer, et al. 1997; DeGrendele, Estess, et al. 1997). High expression of both surface markers characterizes central-memory T cells. Naïve T cells become productively activated in secondary lymphoid organs by APCs with antigen-loaded MHC molecules stimulating the cognate TCRs. Effective T cell activation requires simultaneous costimulatory signaling and results in clonal expansion and differentiation into effector T cells.

1.1.1.1 T helper cell differentiation

The cytokine environment during T cell activation triggers the differentiation of T helper cells into different subsets that are defined by the expression of specific transcription factors and effector functions (**Figure 1**). The major T helper cell subtypes are Th1, Th2 and Th17 cells as well as induced Tregs (iTregs) (Nakayamada et al. 2012; Yamane & Paul 2013). Th1 cell differentiation is triggered by interleukin (IL)-12 and marked by expression of the transcription factor T-bet. Secreting interferon (IFN)-γ, Th1 cells are important in immune responses against intracellular bacteria and protozoa and they can be the driving force in autoimmune diseases. In contrast, Th2 cells stimulate humoral immunity against extracellular pathogens such as parasites and can cause allergy and asthma. Th2 cell differentiation is dependent on IL-4 stimulation and results in the expression of the transcription factor Gata3 and the production of IL-4, IL-5 and IL-13. Another T helper cell subset has been named Th17 due to its production of IL-17A and IL-17F and is involved in fighting extracellular bacterial and fungal infections. However, Th17 cells are also involved in the development of autoimmunity. Expression of Rorγt and the presence of transforming growth factor (TGF)-β, IL-6, IL-21 and IL-23 drive Th17 differentiation. Thymic as well as induced Tregs are defined by expression of the forkhead transcription factor FoxP3, and the differentiation of iTregs in the periphery requires TGF-β in combination with IL-2. Tregs suppress immune responses and maintain peripheral tolerance by production of inhibitory cytokines such as IL-10 and TGF-β.

In addition, follicular T helper (Tfh) cells were suggested as separate T helper cell subset due to their specific localization at the periphery of B cell follicles in secondary lymphoid organs (Crotty 2011). There, Tfh cells provide stimulatory signals to germinal center (GC) B cells by cytokine secretion and via CD40 and thereby support high-affinity antibody production. Differentiation of Tfh cells is driven by the expression of the transcription factor Bcl-6 and characterized by IL-21 secretion (Nurieva et al. 2009;

Johnston et al. 2009; Yu et al. 2009; Spolski & Leonard 2010). Interestingly, Tfh cells exhibit a substantial functional overlap with other T helper cell subsets in terms of cytokine production and transcription factor expression, and Tfh cells keep a considerable plasticity in response to different cytokine milieus (Lu Kanno 2011, Cannons 2013).

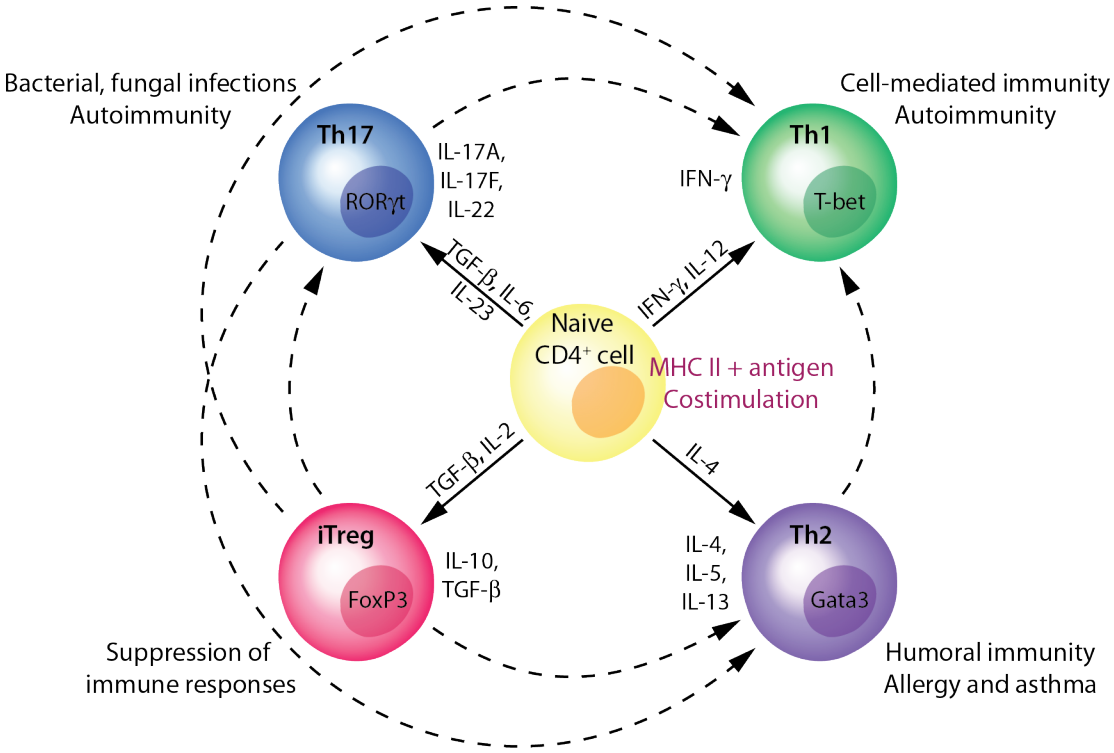

Figure 1: Schematic representation of T helper cell differentiation and plasticity. TCR stimulation via antigen-loaded MHC II together with costimulatory signaling activates naïve $CD4^+$ T cells and promotes differentiation into T helper cell subsets depending on cytokine milieu. Differentiated T helper cells express specific transcription factors (shown in the nuclei) and produce cytokines. Dashed arrows indicate possible ways of T helper cell reprogramming and plasticity. The scheme was drawn on the basis of Yamane & Paul 2013 and Nakayamada et al. 2012.

Plasticity between T helper cell subsets was also described for Th1, Th2, Th17 cells and iTregs. Fully differentiated Th2 cells were reprogrammed to exhibit a Th1 phenotype (expression of T-bet and IFN-γ) by an *in vivo* virus infection model that drives Th1-type immune responses (Hegazy et al. 2010). Similarly, in the absence of TGF-β, committed Th17 cells suppressed IL-17 production and expressed the Th1 cytokine IFN-γ and T-bet (Lee et al. 2009). Moreover, the principle of one subset-defining transcription factor was challenged by the finding that Tregs express T-bet or Gata3 in addition to FoxP3 (Koch et al. 2009; Wohlfert et al. 2011). The current concept assumes that

additional transcription factors guide Treg functions required in specific inflammatory settings.

Another factor influencing the outcome of T helper cell activation is the strength and duration of the TCR stimulus. Already in 1995 it was published that high antigen doses induced Th1 differentiation in primary cultures of TCR-transgenic $CD4^+$ T cells, while the same cells underwent Th2 differentiation in response to low doses of antigen (Constant et al. 1995; Hosken et al. 1995). Experiments measuring the interaction-time of T cells and dendritic cells now revealed that Th1 differentiation requires long-term interaction, which was achieved by higher antigen concentrations (van Panhuys et al. 2014). In contrast, lower antigen concentrations resulted in shorter interaction duration and Th2 differentiation. Furthermore, differentiation of iTregs seems to be preferentially induced by low doses of high-affinity antigenic peptides or by weak costimulatory signaling (Gottschalk et al. 2010; Josefowicz et al. 2012).

Hence, the impact of the cytokine environment, TCR signaling strength or costimulation on T helper cell differentiation and effector phenotypes has been studied intensively and revealed interesting concepts. However, due to the diversity of influencing parameters, the challenge remains to investigate and integrate single contributions in order to better understand this central process in T-cell-mediated immunity.

1.1.1.2 Costimulatory receptors on T helper cells

The importance of costimulatory signaling during T helper cell activation was acknowledged by the ‘two-signal model’, which was proposed for the first time in 1975 and further specified afterwards (Lafferty & Cunningham 1975). The two-signal model describes that T cell activation is dependent on antigen presentation within the context of MHC molecules as first signal and costimulation via CD28 as second signal. By now, a number of co-receptors providing stimulatory and inhibitory signals and regulating all phases of T cell activation has been identified (**Figure 2**) (Chen & Flies 2013).

The most prominent costimulatory receptor of T cell activation is CD28, being constitutively expressed on naïve T cells. While the TCR-CD3 complex is stimulated by MHC II bound antigen, B7-1 and B7-2 (CD80 and CD86) on the respective APC bind to CD28. This is crucial for the initiation of most T cell responses, since CD28 signaling induces transcription of IL-2 and expression of CD25, the IL-2 receptor alpha chain, thereby rendering the cells responsive to IL-2-mediated proliferative signals. CD28 is expressed from a gene cluster on the mouse chromosome 1 together with the cytotoxic T lymphocyte antigen (Ctla) 4 and the Inducible costimulator (Icos), suggesting that these genes were derived from gene duplication (Carreno & Collins 2002; Ling et al. 2001). The sequence identity on the amino acid level between CD28, Ctla4 and Icos is

around 30%. In contrast to CD28, which is present on naïve T cells, Icos expression is only induced upon T cell activation. Interestingly, Icos-induced cytokine expression is of disparate importance for different T helper cell subsets. Whereas Th2 and Th17 cytokine expression (Il-4 and IL-17 respectively) is reduced in *Icos*$^{-/-}$ CD4^{+} T cells, IFN-γ levels are increased, suggesting a bias towards Th1 differentiation (Park et al. 2005; Tafuri et al. 2001; Dong et al. 2001; McAdam et al. 2001). Moreover, Tfh cell differentiation is absent in *Icos*-deficient mice, indicating a dependency on Icos costimulatory signals (Akiba et al. 2005). Unlike CD28 and Icos, Ctla4 provides an inhibitory signal to T cells. Ctla4 is expressed on the cell surface during the late phase of T cell activation and in Tregs. By *trans*-endocytosis it removes B7 ligands from the surface of APCs and thereby antagonizes stimulation via CD28 (Qureshi et al. 2011). In addition, the competition of Ctla4 and CD28 for B7 ligands reduces CD28 signaling. Other closely related co-receptors providing inhibitory signals to activated T cells are programmed cell death (PD)-1 and B and T lymphocyte attenuator (Btla). Like Icos, PD-1 and Btla are highly expressed on Tfh cells (Crotty 2011), and PD-1 together with CXCR5 serves as surface marker to identify Tfh cells among CD4^{+} T cells.

The tumor necrosis factor receptor super family (Tnfrsf) is another group of receptors on T cells that provide costimulatory signals (**Figure 2 upper half**). The most prominent member of this family in terms of T helper cell costimulation is Tnfrsf4, also known as Ox40. Like Icos, Ox40 is not expressed on naïve T cells, but it is induced within 24 hours upon T cell activation with a peak after 48 hours and subsequent decline between 72 and 96 hours (Gramaglia et al. 1998). Mice with transgenic overexpression of Ox40 ligand (Ox40L) on dendritic cells exhibit accumulation of CD4^{+} T cells in B cell follicles (Brocker et al. 1999). In line with this, high Ox40 levels were observed on Tfh cells, indicating an impact of Ox40 signaling on Tfh differentiation and function even though it is not required for germinal center formation (Crotty 2011; Kopf et al. 1999). Ox40 stimulation results in increased cytokine production as well as survival due to an upregulation of anti-apoptotic factors. Moreover, Ox40 stimulates proliferation of T cells, particularly during memory formation. This is underlined by the finding that antigen-specific memory T cells are strongly reduced in *Ox40*$^{-/-}$ mice (Gramaglia et al. 2000). Studies, in which interrupting the Ox40-Ox40L interaction ameliorated autoimmunity or inflammatory responses, emphasize the pathogenic potential of Ox40 costimulation (Watts 2005).

Other members of the Tnfrsf promoting T helper cell survival and cytokine production are CD30 (Tnfrsf8), 4-1BB (Tnfrsf9), CD27 (Tnfrsf7), GITR (Tnfrsf18), DR3 (Tnfrsf25) and Hvem (Tnfrsf14) (Watts 2005; Chen & Flies 2013). CD30, 4-1BB and DR3 exhibit similar expression kinetics like Ox40, whereas CD27 and GITR are expressed on naïve cells and further induced upon T cell activation. However, CD27 is downregulated on effector T cells and Hvem levels are reduced in response to T cell

activation. Furthermore, activated T cells upregulate CD40L (Tnfsf5), the ligand of CD40 (Tnfrsf5), which is mainly expressed on B cells, dendritic cells and macrophages. Thereby, T cells provide costimulatory signals to APCs and further increase the level of immune activation.

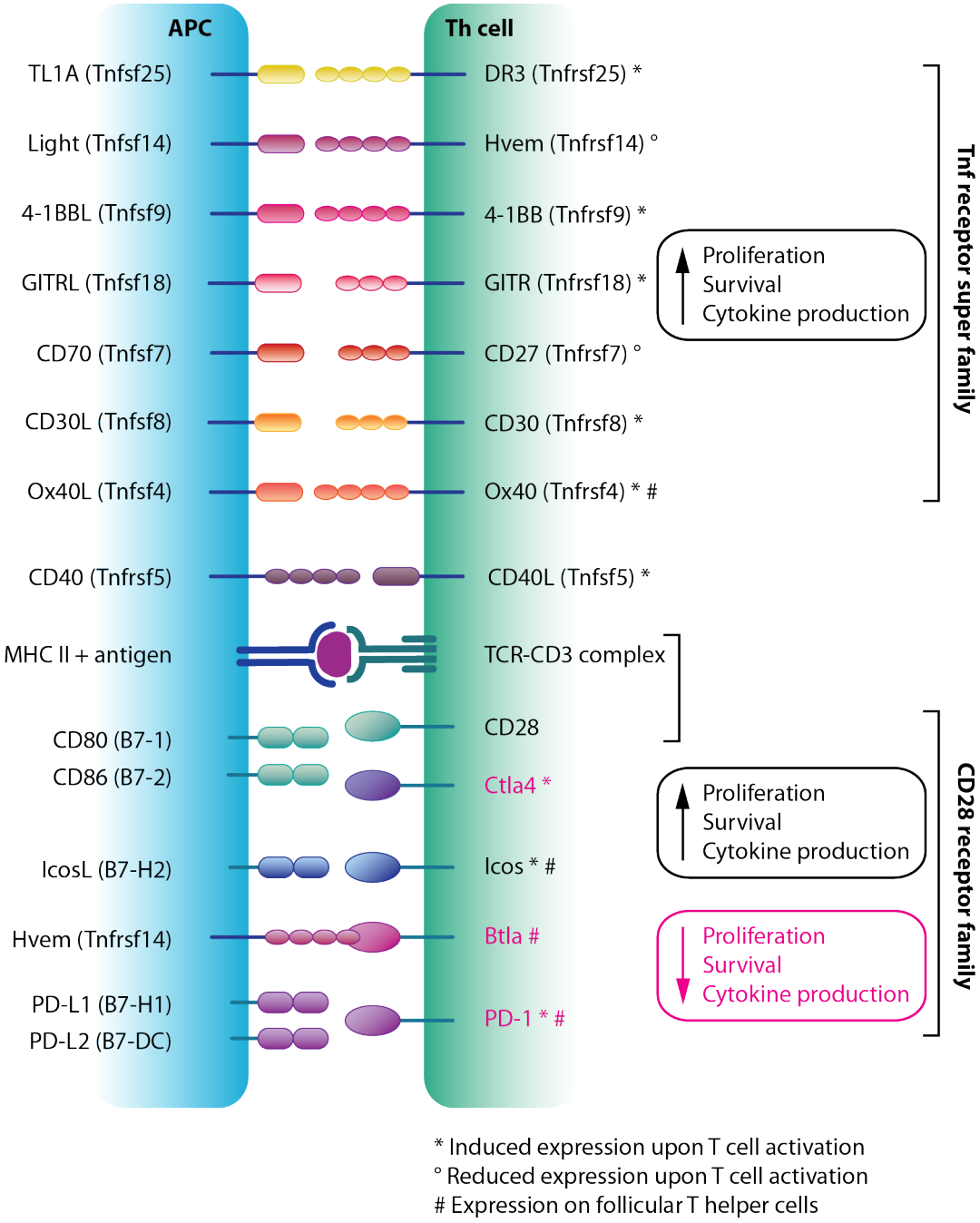

Figure 2: Overview of costimulatory receptors on T helper cells and their corresponding ligands on antigen presenting cells. The upper half shows receptors of the Tnf receptor super family, whereas the lower half shows receptors of the CD28 type. Pink color indicates inhibitory and black color stimulatory signals. The Figure was developed based on Chen & Flies 2013 and Watts 2005.

Signaling of Tnfrsf members involves trimerization of ligand and receptor and interaction with different Tnf receptor associated factor (TRAF) adaptor proteins (**Figure 3**) (Chen & Flies 2013; Watts 2005). Ox40 and CD27 recruit TRAF2, 3 and 5, 4-1BB was found to be associated with TRAF1, 2 and 3 and CD30 signaling uses TRAF1, 2, 3 and 5, yet the precise connection between these adapter proteins and downstream effectors is largely unknown. A common feature of most Tnfrsf members is the activation of both the canonical and the non-canonical NF-κB pathway, resulting in enhanced T cell survival and reduced apoptosis due to increased anti-apoptotic factors (Bcl-2, Bcl-XL and Bcl2a1). In addition, the mitogen-activated protein (MAP) kinases JNK (c-Jun N-terminal kinases), p38 and ERK (extracellular signal-regulated kinases) are targeted by Tnfrsf signaling. Via the phosphatidylinositol 3-kinase (PI3K) AKT pathway, activation of further downstream effectors, namely activator protein 1 (AP1), mammalian target of rapamycin (mTOR) and nuclear factor of activated T cells (NFAT), is achieved. These factors are also activated by TCR signaling, which suggests a synergistic effect resulting in increased cytokine production and cell cycle progression of activated T cells. Moreover, Tnfrsf interactions with the respective ligands also induce APCs to proliferate and express cytokines, which amplifies the immune response. Thus, costimulation via members of the Tnfrsf on the one hand controls the size of the effector T helper cell population through proliferation and survival signals and on the other hand controls the effector functions of these T helper cells by supporting cytokine production.

Interestingly, CD28 and Icos partially trigger the same pathways as the Tnfrsf (**Figure 3**). Stimulation of PI3K will activate AKT and its numerous downstream effectors such as NFAT, mTOR, AP1/2 and NF-κB. Thereby, CD28 and Icos likewise promote proliferation and survival of T helper cells. The inhibitory members of the CD28 family of co-receptors, Ctla4 and PD-1, are supposed to target the same key players, however the extent of their signaling potential remains elusive. The complex interplay of these numerous costimulatory receptors within separate and convergent signaling pathways supposedly allows precise T helper cell activation and differentiation and prevents inappropriate or prolonged T helper cell immune responses.

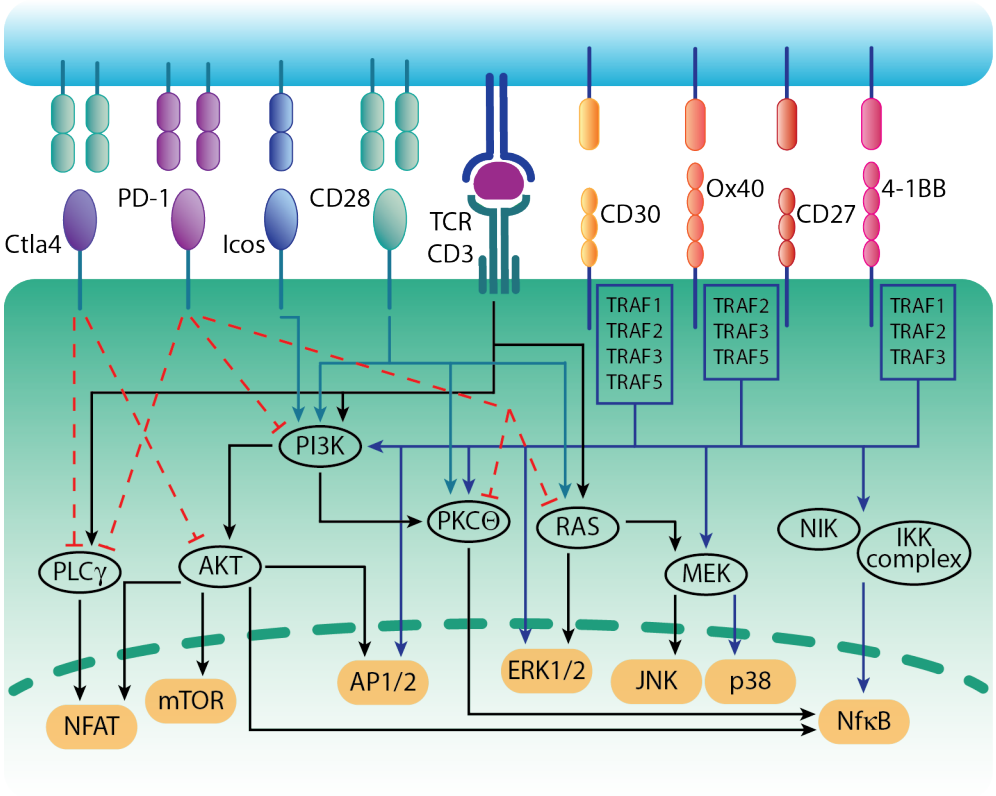

Figure 3: T helper cell signaling pathways involved in costimulation. CD28 type receptors and Tnf receptor super family members use different and convergent pathways to provide costimulatory signals, resulting in activation of the same set of downstream factors in the nucleus (shown in yellow). Dashed red lines indicate inhibitory signals. The scheme was developed based on Chen & Flies, 2013.

1.1.2 Peripheral tolerance and autoimmunity

At the beginning of the twentieth century, the immunologist Paul Ehrlich coined the term 'horror autotoxicus' (Chang 2014). This described a concept according to which autoreactive immune responses are not possible due to the fatal consequences they would have on an individual. Later on, Paul Ehrlich modified his point of view by admitting that self-reactive immunity is possible but suppressed immediately by protective mechanisms of the immune system. Today, some of the mechanisms preventing immune reactions against self-antigens and their failure, leading to diverse manifestations of autoimmunity, are examined in detail.

In the periphery, autoreactive T cell clones encountering their cognate antigen presented by MHC molecules are often not properly activated due to a lack of costimulation in a non-inflammatory environment. Furthermore, self-antigens usually cannot be removed by cells of the innate immune system, which leads to chronic TCR stimulation. Both situations bring about T cell anergy, the temporary unresponsiveness of a T cell to signals promoting proliferation, differentiation and cytokine production. The

importance of the TCR signaling strength in preventing autoimmunity was demonstrated in a study with autoreactive TCR-transgenic mice (Olasz et al. 2012). Only a particular TCR signal strength induced T-cell-dependent, antibody-mediated autoimmune arthritis, whereas stronger TCR signaling resulted in increased apoptosis of self-reactive T cells. The suppressive capacity of Treg cells is another mechanism counteracting self-reactive immune responses. This is impressively displayed in mice and humans lacking Tregs due to mutations of the transcription factor FoxP3 (Bennett et al. 2001; Brunkow et al. 2001). The *scurfy* mouse and the IPEX (immune dysregulation, polyendocrinopathy, enteropathy, X-linked) syndrome in humans are characterized by severe immune dysregulation and systemic autoimmunity attacking all endocrine organs. Interestingly, genomic deletion of the costimulatory molecules Ox40 and CD30 in combination with FoxP3 deficiency completely abrogated this systemic autoimmune disease in mice (Gaspal et al. 2011). Therefore, it is assumed that excessive costimulation of T cells, resulting in increased proliferation, cytokine expression, inflammation, B cell help and thus antibody production, can promote autoimmunity.

In line with this, blocking Ox40 signaling ameliorated different autoimmune diseases in mice such as collagen-induced arthritis (Yoshioka et al. 2000), chronic colitis (Higgins et al. 1999; Totsuka et al. 2003) and autoimmune diabetes (Martin-Orozco et al. 2003). Moreover, experimentally induced autoimmune encephalomyelitis (EAE), resembling the human autoimmune disease multiple sclerosis, was dependent on Ox40 signaling and preventing the Ox40-Ox40L interaction reduced disease parameters (Weinberg et al. 1999; Ndhlovu et al. 2001; Nohara et al. 2001). Conversely, mice expressing an Ox40L transgene causing constitutive Ox40 signaling developed autoimmunity marked by inflammatory bowel disease and anti-DNA antibodies (Murata et al. 2002). Other members of the Tnfrsf with costimulatory properties were equally investigated in models for autoimmune diseases. For example, *DR3*$^{-/-}$ mice or injection of a neutralizing antibody targeting its receptor TL1A showed strongly reduced disease symptoms of EAE, colitis and arthritis (Bull et al. 2008; Meylan et al. 2008; Takedatsu et al. 2008).

Systemic autoimmunity accompanied by excessive T cell activation and anti-nuclear autoantibodies was also observed in the so-called *sanroque* mice (Vinuesa et al. 2005). These mice express a mutated form of the Roquin-1 protein, which will be introduced in detail in 1.3, resulting in an upregulation of the costimulatory receptor Icos (Yu et al. 2007). Accordingly, Icos levels were reduced introducing a heterozygous *Icos*$^{+/-}$ background, but this only ameliorated the phenotype of the *sanroque* mice. Nevertheless, this finding suggested substantial contribution of excessive Icos signaling to the development of autoimmunity.

Despite potent tools to regulate adaptive immune responses, T cell activation and peripheral tolerance to self-antigens, these mechanisms can fail leading to inappropriate immune reactions against tissues of the own body. The etiology of autoimmune diseases

is not clear, however environmental factors and a genetic predisposition, mainly based on certain MHC molecules, are among the known risk factors. Treatment is generally performed by immunosuppressive medication and only few drugs directly target mediators of inflammation. One example are neutralizing monoclonal anti-TNF antibodies used in the therapy of rheumatoid arthritis and colitis (Lippert et al. 2014; Patel & Moreland 2010; Lapadula et al. 2014). Clearly, a deeper understanding of immune regulation in health and disease is required and desired to establish targeted therapeutic approaches.

1.2 Post-transcriptional gene regulation

For the last decades, gene regulation on the level of transcription through activators, repressors and epigenetic modifications has been studied intensively to examine regulatory networks. The increasing awareness of the abundance and variety of RNA molecules raised the interest in regulatory processes on the messenger RNA (mRNA) level. Upon gene transcription, pre-mRNAs are processed by addition of a 7-methylguanosine structure as 5' cap and by 3' polyadenylation both increasing the stability of the mRNA molecule. Furthermore, splicing events remove intronic sequences and thereby define the final mRNA sequence. A mature mRNA usually contains a 5' untranslated region (UTR), the coding sequence (CDS) determining the amino acid sequence of the encoded protein, a 3'UTR and the poly(A)-tail. After the processing steps, mRNAs are exported from the nucleus to the cytoplasm, where they are exposed to a comprehensive network of regulatory mechanisms targeting mRNA translation and stability.

1.2.1 Processes targeted during post-transcriptional regulation

Without changing the number of mRNA molecules, factors that target translation have a strong impact on the abundance of the encoded protein. Thereby, different steps of translation are found under the control of post-transcriptional regulators, namely the initiation, the elongation of the polypeptide chain and the termination.

To start translation, eukaryotic initiation factors (eIFs) bind to the 5'cap and 5'UTR of mRNAs and recruit the ribosomal subunits. Concurrently, the cap-binding eIF4F complex protects the mRNA from decapping and interacts with the poly(A)-binding protein (PABP) resulting in a circularization of the mRNA (**Figure 4**). During translation, eukaryotic elongation factors (eEFs) mediate transfer RNA (tRNA) positioning and catalyze the translocation of the tRNA and mRNA within the ribosome,

thereby promoting the synthesis of the polypeptide chain. Ribosomal pausing describes a queuing or stacking of ribosomes that interrupts translation progression and therefore has an influence on the overall translation rate of a certain protein. Finally, the termination of translation involves the eukaryotic release factor 1 (eRF1), which recognizes stop codons and promotes the release of the nascent protein.

Different methods can be applied to globally investigate translation in cells. Polysome profiling uses sucrose gradient centrifugation to separate the monosomal fractions of a cell lysate from the polysomal fractions. Accordingly, mRNAs contained in these fractions were strongly (polysomes) or weakly (monosomes) translated within the cell. The advances of high-throughput sequencing gave rise to a new approach termed ribosome profiling. Here, the ribosome occupancy of mRNAs is determined by sequencing RNA fragments, which were protected against nuclease degradation through the binding of ribosomes (Ingolia et al. 2009). Reduced numbers of ribosome-protected fragments or the accumulation of ribosomes at certain positions of the mRNA thereby indicate ongoing translational control.

Apart from translational control, a major impact on the expression of proteins is given by mRNA turnover. Stability of mRNAs is influenced by binding of stabilizing or destabilizing proteins to the 3'UTR that recruit or reject factors of the mRNA decay pathways. In general, removal of the poly(A)-tail initiates the degradation of mRNAs and is followed by two distinct pathways (**Figure 4**), one targeting the 5'cap followed by 5' to 3' degradation and the other marked by 3' to 5' nuclease activity (Garneau et al. 2007). Inhibition of either one of these degradation processes did not result in prominent changes of the transcriptome, indicating a certain redundancy between both pathways (He et al. 2003; Houalla et al. 2006). Initial shortening of the mRNA poly(A)-tail is performed by the PABP-dependent PAN2-PAN3 nuclease, resulting in PABP removal and thus in the disruption of the stabilizing eIF4F-PABP interaction. Complete deadenylation is subsequently promoted by the Ccr4-Not protein complex, with Ccr4 and Caf1 exhibiting exonuclease activity (Temme et al. 2004). 3' to 5' decay of deadenylated mRNAs is performed by the exosome, another protein complex with core subunits functioning as RNases. The final step of 3' to 5' degradation is the removal of the 5'cap by the scavenger decapping enzyme DcpS. On the other hand, the deadenylated 3' end of an mRNA can be bound by the heptameric complex of Sm-like proteins (Lsm) 1 to 7 (Tharun et al. 2000). The Lsm1-7 complex together with other factors, such as enhancers of decapping (Edc proteins) and the RNA helicase Rck, is required to efficiently promote decapping of the mRNA. Thereby, the dimeric decapping enzyme Dcp1 Dcp2 is recruited to the 5' end of the mRNA and removes the 7-methylguanosine structure. Subsequently, 5' to 3' degradation is performed by the exoribonuclease Xrn1. While the majority of mRNAs is degraded via the described pathways, there are also examples of decapping initiated through deadenylation-

independent mechanisms (Garneau et al. 2007). Furthermore, mRNAs can be targeted by endonucleolytic cleavage, which is followed by rapid 5' to 3' and 3' to 5' degradation starting from the cleavage site.

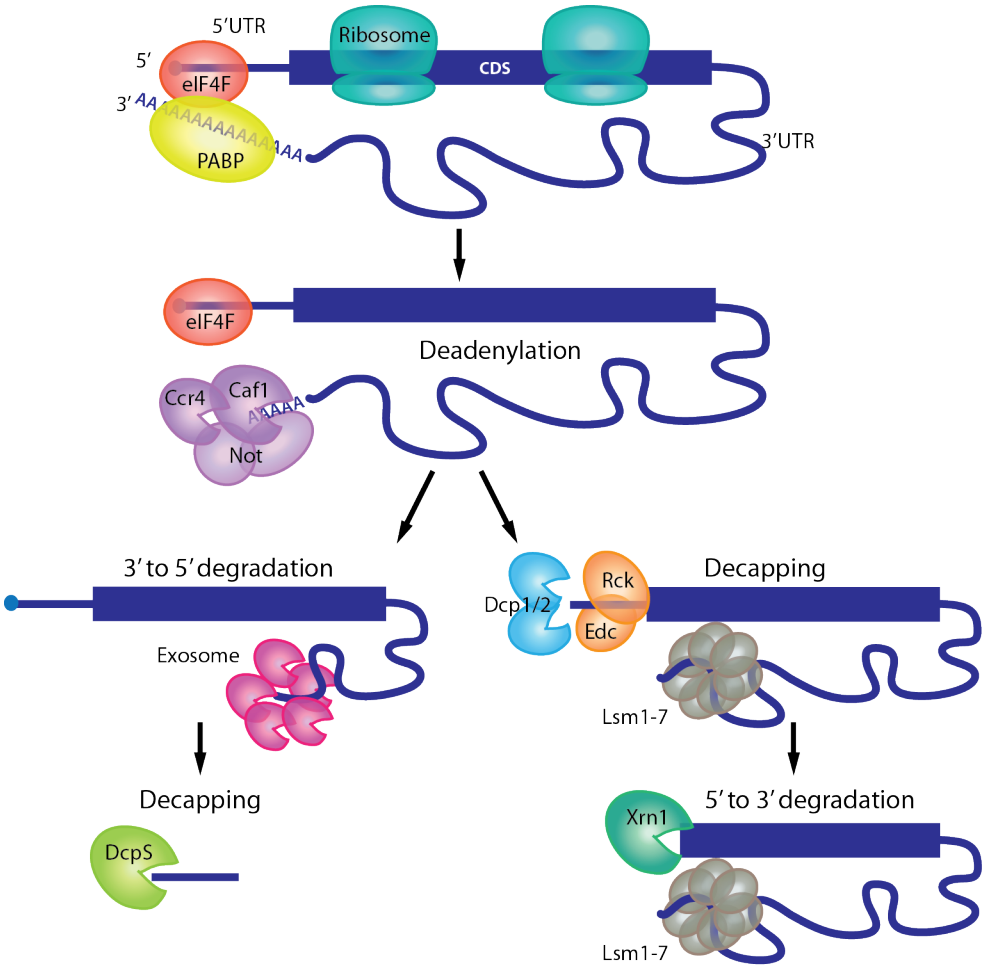

Figure 4: Scheme of mRNA degradation pathways. During translation, the mRNA 5'cap is bound by initiation factors (e.g. eIF4F) contacting the poly(A)-binding protein (PABP) at the 3' end for circularization. Deadenylation of the mRNA removes the PABP and is performed by the Ccr4-Not complex with Ccr4 and Caf1 as enzymatically active subunits. Deadenylation can be followed by exosomal 3' to 5' degradation and subsequent DcpS decapping (left side). Deadenylated mRNA can also be bound by Lsm1-7, the RNA helicase Rck and enhancers of decapping (Edc) to promote Dcp1/2 decapping and subsequent Xrn1-mediated 5' to 3' degradation.

Within the cytoplasm, mRNA storage and turnover takes place in distinct granular structures, called processing (P) bodies, which were identified due to the accumulation of proteins and enzymes involved in 3'UTR binding, mRNA decay and miRNA-induced mRNA silencing (Eulalio et al. 2007). P bodies are no pre-defined structures, but their formation depends on the amount of RNA to be degraded and on the presence of early decay factors. Upon cellular stress, a similar kind of foci, called stress granules,

can be induced. In contrast to P bodies, stress granules are mainly involved in mRNA storage during cellular stress, presumably to protect mRNA from toxic or highly reactive agents in the cytoplasm. Aggregation of the 3'UTR-binding protein TIA-1 (T cell-restricted intracellular antigen 1) is used as marker for stress granule formation (Kedersha et al. 1999; Kedersha et al. 2000). Proteins that colocalize at sites of stress granules or P bodies are assumed to be likewise involved in 3'UTR binding or mRNA decay. RNAs within P bodies and stress granules can be released and redirected to the translational machinery underlining the dynamic storage function of these structures (Brengues et al. 2005; Kedersha et al. 2000).

1.2.2 Mediators of post-transcriptional gene regulation

The concept of *trans*-acting factors and *cis*-regulatory elements introduced for transcriptional regulation has also been implemented in post-transcriptional gene regulation. Thereby, a *cis*-regulatory element is a certain sequence or structure of an mRNA that mediates regulatory processes targeting the same mRNA molecule (*cis*-acting). Accordingly, a *trans*-acting factor is a molecule promoting regulation of a target molecule. In terms of post-transcriptional regulation *trans*-acting factors can be RNA-binding proteins (RBPs), or microRNAs (miRNAs) and other non-coding RNAs that influence mRNA translation or stability in *trans*.

1.2.2.1 *Cis*-regulatory RNA elements

Target elements of post-transcriptional gene regulation are predominantly located in the UTRs of mRNAs. Whereas translation factors often bind to the 5'UTR, the great majority of miRNA binding sites and *cis*-elements for RBPs can be found in the 3'UTR (Matoulkova et al. 2012). miRNA binding sites are a class of *cis*-elements that has been intensively investigated in the context of computational miRNA target site prediction. This study focuses on RBPs and *cis*-regulatory elements involving sequence and structure requirements. Therefore, miRNA binding sites, which are clearly dependent on the sequence of the *trans*-acting miRNA, will not be discussed in detail.

The most prominent target sequences of post-transcriptional regulation in mammalian cells are AU-rich elements (AREs). This heterogeneous group of sequences is characterized by a high uridylate content interspersed with adenine residues and the presence of the AUUUA pentamer sequence, occurring in variable numbers of repeats (Matoulkova et al. 2012). The function of AREs was first described for the short-lived mRNAs of cytokines (such as *Tnf* and *Il6*) and proto-oncogenes (such as *Myc* and *Fos*) and involves the direct binding of proteins that mostly recruit mRNA decay factors

(Chen & Shyu 1995). Thereby, protein expression is kept at low levels but can be upregulated quickly by interrupting ARE-mediated mRNA decay. In line with this, removal of an ARE from the *Tnf* 3'UTR abrogated mRNA decay and increased mRNA and protein levels (Kontoyiannis et al. 1999). By computational approaches, the ARE database (ARED) identified ARE sites within human and murine transcripts, suggesting about 10% of human and at least 5% of murine genes to harbor AREs within their 3'UTR (Halees et al. 2008). A variant of AREs are GU-rich elements, sharing the presence of a pentamer core sequence (GUUUG) and the functional involvement in mRNA destabilization (Matoulkova et al. 2012).

Other RNA elements are rather defined by a certain secondary structure than a nucleotide sequence. One example is a hairpin structure at the 3' end of histone mRNAs that serves as stabilizing element instead of a poly(A)-tail and plays a role for translation efficiency (Williams & Marzluff 1995). Distinct sequence and structural properties of some *cis*-regulatory elements were investigated in detail. In *Drosophila* embryogenesis anterior-posterior patterning involves tight spatial control of Nanos protein expression, which is achieved by translational regulation of the *nanos* mRNA (Dahanukar & Wharton 1996). The *nanos* 3'UTR translation control element (TCE) was reported to contain two distinct stem-loop structures, and its function depended on sequence as well as structural properties (Crucs et al. 2000). A number of different RNA stem-loops was suggested to be recognized by the regulatory RNase Regnase-1 (also known as MCPIP1 or Zc3h12a), a post-transcriptional regulator of cytokine mRNAs (Li et al. 2012; Paschoud et al. 2006; Uehata et al. 2013). These stem-loops have diverse loop sizes and stem lengths, and specific binding of Regnase-1 to these putative *cis*-regulatory elements has not been addressed experimentally.

Several groups used global approaches to identify RNA motifs specifically bound by a certain RBP. In affinity-based selection experiments from random RNA libraries potential *cis*-elements for a number of proteins, among them MEX-3, Pum2 and QKI-5, were identified (White et al. 2001; Pagano et al. 2009; Galarneau & Richard 2005). Even though the given examples focus on linear sequence motifs, recent studies on high-throughput sequencing data analysis expose an increasing awareness of RNA secondary structures (Hoinka et al. 2012).

Taken together, *cis*-regulatory RNA elements cover a broad spectrum from distinct RNA sequence motifs and AREs to RNA stretches with certain secondary structures, being recognized by their shape rather than by the nucleotide sequence. For most of these RNA elements, little is known about how *trans*-acting factors recognize a particular *cis*-element. Even though bioinformatics tools and high-throughput methods provide some predictive power, the precise modes and requirements of these interactions still have to be addressed in small experimental steps.

1.2.2.2 *Trans*-acting factors and mechanisms of post-transcriptional regulation

The *cis*-regulatory RNA elements described in the previous paragraph can be targeted by different kinds of molecules, including miRNAs and other non-coding RNAs. However, this paragraph will only discuss RBPs, their modes of RNA recognition and downstream effects. A global approach identifying RBPs in HeLa cells by cross-linking of protein-RNA interactions with ultraviolet (UV) light and subsequent pull-down revealed that there are as many as 860 proteins qualifying as RBPs in the given setting (Castello et al. 2012). This underlines the potential lying within post-transcriptional processes and the demand for further investigations of this level of gene regulation.

The most intensively studied group of RBPs are ARE-binding proteins, among them tristetraprolin (TTP), AU-binding factor 1 (AUF1), K homology splicing regulatory protein (KSRP), TIA-1, TIA-1-related protein (TIAR) and ELAV proteins. With a tandem CCCH-type zinc finger TTP binds to AREs within the 3'UTR of *Tnf*, *Il10* and other target mRNAs and promotes degradation by recruiting deadenylation factors to the bound mRNA (Lai et al. 1999; Lai et al. 2000; Stoecklin et al. 2008). Upon activation of the p38 MAP kinase, TTP function is repressed by phosphorylation leading to an upregulation of its target mRNAs (Marchese et al. 2010; Clement et al. 2011). Another factor mediating ARE-dependent mRNA decay is KSRP, which promotes deadenylation and 3' to 5' degradation by the exosome. KSRP contacts the RNA via four nucleic-acid-binding KH domains, whose flexible organization allows recognition of diverse targets. Like TTP, KSRP is inactivated by phosphorylation. In contrast, AUF1 activity as RNA destabilizing protein is controlled by its preferred nuclear localization. Upon shuttling to the cytoplasm, it can bind to AREs and recruit the exosome for mRNA degradation (Loflin et al. 1999). However, there are also reports showing stabilization and increased translation of mRNAs upon AUF1 binding (Liao et al. 2007). In the cited study, Myc is post-transcriptionally regulated by competitive binding of AUF1 and TIA-1 to an ARE within its 3'UTR. Thereby, AUF1 antagonizes TIA-1-mediated translational silencing. Both, TIA-1 and TIAR, interfere with translation through the formation of a pre-initiation complex with eIF1 and eIF3, which blocks translation initiation (Piecyk et al. 2000; Matoulkova et al. 2012). RNA binding by TIA-1 and TIAR is performed via three RNA recognition motif (RRM) domains, which bind to U-rich RNA stretches with high affinity (Dember et al. 1996). HuR, as representative of ELAV proteins, is an mRNA stabilizing factor and binds to RNA via three RRM domains. HuR interferes with destabilizing factors mainly by competing for AREs but also by relocating RNAs from P bodies to polysomes (Matoulkova et al. 2012; Bhattacharyya et al. 2006). Interestingly, all described ARE-binding proteins share a modular composition with several RNA-binding domains,

which was proposed to increase the affinity and the specificity of RNA recognition (Lunde et al. 2007).

To investigate the quantity and quality of mRNAs targeted by a specific RBP within cells, a method based on UV cross-linking and immunoprecipitation (CLIP) was established by Jernej Ule and colleagues (Ule et al. 2005). Cells are treated with UV light of 254 nm wavelength inducing covalent bonding between proteins and RNAs. Afterwards, a cell lysate is prepared and treated with an RNase to achieve RNA fragmentation, which is followed by immunoprecipitation (IP) of the RBP of interest. Thus, RNA fragments bound by the RBP can be purified and identified by reverse transcription and sequencing. In the following years, high-throughput sequencing was used and allowed a global view on specifically bound RNAs (Licatalosi et al. 2008). Also, the cross-linking procedure was further developed by incorporation of 4-thiouridine (4SU) within cellular RNAs and the use of 365 nm UV light, termed photoactivatable ribonucleoside-enhanced CLIP (PAR-CLIP) (Hafner et al. 2010). This procedure resulted in specific T to C exchanges at positions of close protein-RNA interaction and thereby enabled the identification of preferentially bound RNA motifs.

The protein Smaug was identified as *trans*-acting factor on the *nanos* TCE, where it recognizes one of the two proposed stem-loop structures (Smibert et al. 1996; Smibert et al. 1999; Dahanukar et al. 1999). The mechanism by which Smaug regulates *nanos* mRNA involves translational inhibition but also recruitment of the Ccr4-Not complex for deadenylation and subsequent mRNA degradation (Zaessinger et al. 2006). A protein named Oskar counteracts Smaug-mediated mRNA decay to allow Nanos protein expression at the posterior pole of the *Drosophila* embryo. Binding of Smaug to the *nanos* mRNA is achieved by a sterile-α-motif (SAM) domain, whose RNA-binding interface and consensus RNA *cis*-element were determined by mutational analyses (Aviv et al. 2003).

The 3’ stem-loop of histone mRNAs is bound by the stem-loop binding protein (SLBP) and the 3’ to 5’ exonuclease Eri1, which degrades the stem-loop structure and thereby destabilizes histone mRNAs (Battle & Doudna 2001; Dominski et al. 2003; Hoefig et al. 2013). Analyzing the crystal structure of the ternary complex (SLBP, Eri1 and stem-loop RNA) revealed only few base-specific contacts, since both proteins recognize the shape of the RNA stem-loop rather than its nucleotide sequence (Tan et al. 2013). This study demonstrates the requirement for structural analyses of protein-RNA complexes to understand the molecular and steric characteristics of protein-RNA interactions.

1.2.3 Post-transcriptional gene regulation in the immune system

Cellular processes that require fast and precise regulation of gene expression are under the control of extensive regulatory networks targeting the post-transcriptional level. In addition to embryonic development and differentiation, the immune system was shown to be largely dependent on regulation of mRNA decay and translation. In fact, 50% of the differentially expressed mRNAs during T cell activation were attributed to changes in mRNA stability instead of transcription (Cheadle et al. 2005). Also, mechanisms promoting T cell anergy involve post-transcriptional regulation and translational silencing, since cytokine mRNA expression is not reduced to the same degree as cytokine production in T cells upon stimulation with self-antigen (Villarino et al. 2011).

As AREs were identified in many cytokine mRNAs, ARE-binding proteins play a major role in post-transcriptional regulation of immune responses and cytokine production. TTP destabilizes *Tnf*, *Il1b* and *Il2* mRNAs in a negative feedback loop during inflammation but also in the absence of pathogens. This was shown with TTP-deficient mice, which spontaneously develop severe autoimmunity due to excessive Tnf expression by macrophages (Taylor et al. 1996). Similarly, AUF1-deficient mice exhibit symptoms of endotoxic shock due to excessive Tnf and IL-1β production (Lu et al. 2006). Even though KSRP destabilizes *Tnf* and *Il8* mRNAs, mice lacking this ARE binding protein do not exhibit a prominent phenotype (Lin et al. 2011). It is evident that RBPs in this context do not only target several mRNAs, but one mRNA is also targeted by different RBPs that compete or collaborate with each other (Ivanov & Anderson 2013). This is also true for the *Tnf* mRNA being targeted by TTP, AUF1, KSRP as well as HuR, which stabilizes the mRNA but at the same time inhibits translation by cooperation with TIA-1 (Katsanou et al. 2005). Furthermore, an ARE-independent constitutive decay element (CDE) mediating mRNA degradation was identified within the *Tnf* 3'UTR (Stoecklin et al. 2003). Thus, a combination of different stabilizing and destabilizing effects on one mRNA is decisive for the resulting protein expression level.

The *Il6* mRNA has a short half-life due to AREs within its 3'UTR. However, in a study investigating the contribution of different 3'UTR segments to mRNA decay, a conserved *cis*-element forming a stem-loop structure was identified (Paschoud et al. 2006). Whereas ARE-mediated mRNA decay could be inhibited by overexpression of AUF1 proteins, the mechanism of stem-loop-mediated mRNA decay was not deciphered. In an independent approach the same conserved region within the *Il6* 3'UTR was identified as *cis*-element for the regulatory RNase Regnase-1 (Matsushita et al. 2009). Other proposed target elements of Regnase-1 are located within the *Il2*, *cRel* and *Zc3h12a* (*Regnase1*) 3'UTRs and are likewise predicted to fold into stem-loop structures (Iwasaki et al. 2011; Li et al. 2012; Uehata et al. 2013). Degradation of target mRNAs was proposed to be induced by the endonuclease activity of Regnase-1, but

proof of the direct interaction of Regnase-1 and RNA stem-loop structures is still missing. Nevertheless, Regnase-1-deficient mice exhibit prominent immune dysregulation marked by infiltration of lymphocytes into the lung and other organs, disruption of the splenic architecture, anti-DNA autoantibody production and increased serum levels of inflammatory cytokines (Miao et al. 2013; Matsushita et al. 2009; Uehata et al. 2013). This illustrates the power of post-transcriptional gene regulation in the immune system and emphasizes the need for molecular studies to understand protein-RNA interactions and their regulatory potential.

1.3 The protein Roquin

In an ENU (N-ethyl-N-nitrosourea) mutagenesis screen for anti-nuclear antibodies (ANAs), a point mutation of a single gene resulting in an amino acid exchange was found to cause severe autoimmunity in mice resembling the human disease systemic lupus erythematosus (SLE) (Vinuesa et al. 2005). The gene affected by this mutation was *Rc3h1*, and the corresponding protein was called Roquin-1. The M199R mutation of Roquin-1 is one rare case of a monogenic cause for autoimmunity in mice. In addition to ANAs, the so-called *sanroque* mice also exhibited massive T cell activation, high levels of Icos on T cells, spontaneous germinal center formation and plasmacytoid infiltrations in lung, kidney and liver. Subsequently, homozygosity for *Roquin-1*^{san} was also found to promote or enhance other autoimmune diseases. Mice prone to developing autoimmune diabetes showed more severe disease parameters and progression when they carried *Rc3h1*$^{san/san}$ alleles (Silva et al. 2011). Also, antibody-induced arthritis was aggravated in *sanroque* mice (Pratama et al. 2013). The underlying cause was proposed to be increased T cell activation and Tfh cell expansion resulting from high levels of the costimulator Icos on T cells (Yu et al. 2007; Lintermanet al. 2009a; Linterman et al. 2009b). In an adoptive transfer experiment of *Rc3h1*$^{san/san}$ T cells into wild-type recipient mice, this was shown to be a T cell-intrinsic process. Since Tfh cells efficiently support and stimulate B cells during the germinal center reaction, their increased abundance presumably drives the generation of high-affinity ANAs in *sanroque* mice. Heterozygosity of *Roquin-1*^{san} led to a slight increase in Icos expression on T cells and late-onset autoimmunity (Ellyard et al. 2012). Yet, about 50% of these mice developed angioimmunoblastic T cell lymphomas possibly caused by Tfh accumulation. Little is known about the regulation of Roquin protein levels in T cells. However, one group investigated transcription factors targeting the *Rc3h1* locus and their involvement in *Roquin-1* transcription regulation (Schaefer et al. 2014). *Roquin-1* mRNA levels were increased by IL-10 stimulation of a murine T cell line (EL4) through the induction of signal transducer and activator of transcription (STAT) 1, STAT3,

GATA2 and c-Rel. These transcription factors were shown to bind to the *Rc3h1* promoter region, indicating that they enhance *Roquin-1* transcription. The same group identified 26 miRNAs, which might act as negative regulators of Roquin-1 expression, suggesting intensive post-transcriptional regulation of the *Roquin-1* mRNA (Schaefer et al. 2011).

1.3.1 Roquin in mouse models

Due to the prominent phenotype caused by a single amino acid exchange within the Roquin-1 protein, mice deficient for Roquin-1 were expected to similarly show the described autoimmune symptoms. Deletion of the *Rc3h1* exons 4-6 resulted in a complete loss of Roquin-1 protein and caused perinatal lethality probably due to impaired lung function (Bertossi et al. 2011). Therefore, a conditional knockout in T cells was established, crossing mice with floxed *Rc3h1* alleles to *CD4 Cre* mice. Surprisingly, these mice did not develop autoimmunity, even though Icos levels were elevated on *Rc3h1*$^{-/-}$ T cells and the frequencies and numbers of activated CD8^{+} T cells were significantly increased. Assuming that the *sanroque* phenotype was not caused entirely by T cell intrinsic mechanisms, Bertossi et al. investigated the effect of Roquin-1 deletion in all hematopoietic cells by crossing *Rc3h1*$^{fl/fl}$ mice to *Vav Cre* mice. These mice exhibited accumulation of CD8^{+} and CD4^{+} effector T cells with high Icos levels, spontaneous germinal center formation and increased levels of IgG2. However, ANAs or signs of autoimmunity were not detected.

The described study suggested that deregulation of Icos levels on T cells may not be the exclusive disease-causing mechanism of *sanroque* mice but rather one sign of vast alterations in T cell homeostasis. This was further supported by *Roquin*$^{san/san}$*; Icos*$^{-/-}$ mice exhibiting unaltered spleen cellularity and percentage of effector memory CD4^{+} T cells compared to *sanroque* mice (Lee et al. 2012). Moreover, the lack of Icos in *sanroque* mice did not abrogate the production of ANAs. The analysis of *Rc3h1*$^{-/-}$ mice also indicated that the presence of the mammalian paralog of Roquin-1, Roquin-2, also known as membrane-associated nucleic acid binding protein (Mnab) (Siess et al. 2000), might prevent disease progression in Roquin-1 knockout mice. Roquin-2 is encoded by the *Rc3h2* gene, and Roquin-1 and Roquin-2 are highly conserved in the N-terminus, whereas lower amino acid similarity was found in the C-terminus (**Figure 5**). Roquin-1 and Roquin-2 expression was detected by immunoblotting in different tissues, including spleen, lymph nodes, brain and lung, indicating that Roquin proteins also play a role outside of the immune system (Vogel et al. 2013).

Deletion of the *Rc3h2* exon 4 resulted in a postnatally lethal loss of Roquin-2 protein, and therefore a T-cell-specific knockout (*Rc3h2*$^{fl/fl}$*; CD4 Cre*) of Roquin-2 was

investigated in detail (Vogel et al. 2013). However, T cells lacking Roquin-2 exhibited normal development and homeostasis without increased activation or Tfh differentiation. In line with this, Icos levels were not elevated on *Rc3h2*$^{-/-}$ T cells. Therefore, mice with a combined deletion of Roquin-1 and Roquin-2 in T cells were analyzed showing excessive CD4^{+} and CD8^{+} T cell activation with an accumulation of CD62^{lo}CD44^{hi} cells (Vogel et al. 2013). Moreover, Icos levels on Roquin-1/2-deficient T cells were even higher than on *sanroque* T cells, suggesting residual function of Roquin-1^{san} or compensatory effects of Roquin-2 in *sanroque* mice. Surprisingly, *Rc3h1-2*$^{fl/fl}$*; CD4 Cre* mice did not produce ANAs despite strongly increased numbers of Tfh and GC B cells. This was attributed to a vastly destroyed spleen architecture lacking intact follicle structures. A different targeting strategy deleting exon 2 of Roquin-1 and Roquin-2 resulted in alternative transcripts encoding RING-less Roquin-1 and Roquin-2 proteins (Pratama et al. 2013). Mice with a T-cell-specific expression of RING-less Roquin-1/2 only exhibited a mild phenotype with slightly elevated Icos levels on activated T cells and increased frequencies of Tfh and GC B cells upon immunization.

Furthermore, transgenic mice overexpressing Roquin-1 in a T cell-restricted manner were generated (Kim et al. 2012). Upon anti-CD3 and anti-CD28 activation, CD4^{+} T cells from these mice showed increased expression of CD28, IL-2 and Tnf, and expectedly lower Icos levels than wild-type mice. However, the underlying molecular mechanism remains entirely elusive.

1.3.2 Domain organization and function of Roquin proteins

The domain organization of the newly identified Roquin-1 protein was described based on conservation and homology studies of the *Rc3h1* gene and the amino acid sequence (Vinuesa et al. 2005). The N-terminus of Roquin-1 contains a RING (really interesting new gene)-type E3 ubiquitin ligase domain, a novel ROQ domain and a CCCH-type zinc finger. In contrast, the C-terminus appears to be rather unstructured with a proline-rich sequence and a coiled-coil domain at the C-terminal end. The Roquin-2 protein shows the same domain organization and high sequence homology in its N-terminus, whereas the C-terminus is largely different from the Roquin-1 protein with only about 50% amino acids sequence identity (**Figure 5**) (Pratama et al. 2013).

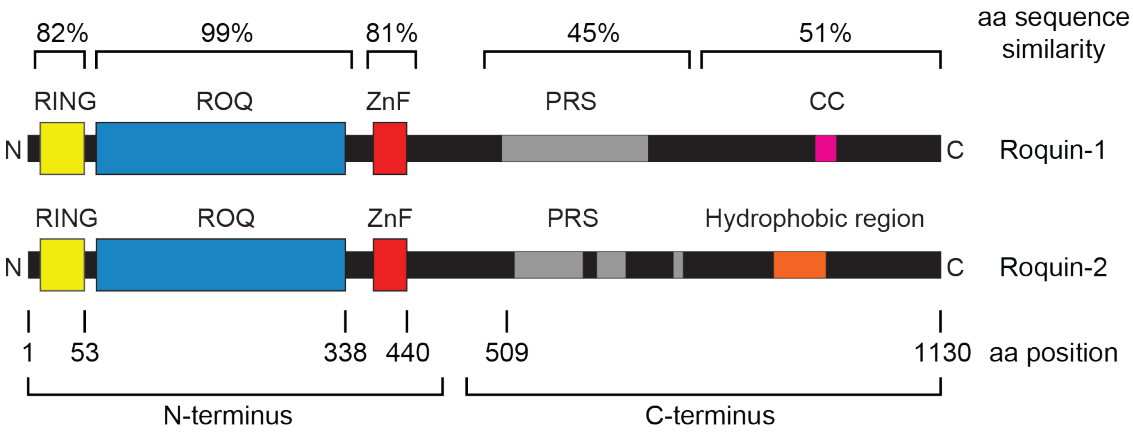

Figure 5: Roquin-1 and Roquin-2 domain organization and amino acid (aa) sequence similarity. The scheme shows the RING-type E3 ubiquitin ligase domain (RING, yellow), the ROQ domain (blue), the CCCH zinc finger (ZnF, red) in the N terminus of Roquin-1/2. The C-teminus contains proline-rich sequences (PRS, grey) and a coiled coil region (in Roquin-1, magenta) or a hydrophobic region (in Roquin-2, orange). The scheme is based on Pratama et al. 2013 and Vinuesa et al. 2005.

It is not known whether the RING domain of Roquin-1 is a functional E3 ubiquitin ligase. However, for Roquin-2 it has been shown that it acts as ubiquitin ligase of Ask1 and thereby prevents apoptosis in response to reactive oxygen species-induced cell death (Maruyama et al. 2014). Mice expressing RING-less Roquin-1 and Roquin-2 variants exhibit mild immune dysregulation, suggesting the presence of the RING domain to be favorable for Roquin function (Pratama et al. 2013). Yet, it is unclear whether this is due to a function as E3 ubiquitin ligase or because the RING domain is required for protein integrity and stability.

The ROQ domain was first defined by sequence homology and conservation between different species, and it was described to be involved in mouse and human *ICOS* mRNA binding and post-transcriptional regulation as well as stress granule localization (Athanasopoulos et al. 2010; Glasmacher et al. 2010). This was shown in functional studies with truncated Roquin-1 variants or Roquin-1 lacking the ROQ domain (here: amino acids (aa) 138-337) and will be discussed in more detail in 1.3.3.

Zinc finger structural motifs are involved in nucleic acid binding in various proteins including the post-transcriptional regulator TTP, which uses a tandem CCCH zinc finger to bind to AREs on target mRNAs (Hall 2005). In electrophoretic mobility shift assays (EMSAs) the Roquin CCCH zinc finger alone (aa 407-484) exhibited RNA-binding activity, however with lower affinity than the ROQ domain (Athanasopoulos et al. 2010). Furthermore, it was shown that mutating the third coordinating cysteine residue of the zinc finger in a construct containing RING domain, ROQ domain and CCCH zinc finger (aa 1-484) reduced binding to an RNA fragment from the *Icos*

3'UTR. This suggests a minor role of the Roquin zinc finger in RNA binding compared to the ROQ domain.

1.3.3 Roquin as RNA-binding protein and post-transcriptional regulator

It was found that Roquin-1 regulates the expression level of Icos protein by directly binding to its mRNA (Athanasopoulos et al. 2010; Glasmacher et al. 2010). High-affinity binding required the Roquin-1 N-terminus (RING-ROQ-ZnF, aa 2-440) and the *Icos* 3'UTR. In different experimental approaches two RNA fragments of this about two kilobases (kb) long 3'UTR were identified as binding partners. Shortening the human *ICOS* 3'UTR yielded a fragment at the 5' end of the 3'UTR (Glasmacher et al. 2010), whereas Athanasopoulos et al. successfully used a fragment from the 3' end for *in vitro* binding assays (Athanasopoulos et al. 2010). Yet, a general RNA motif recognized by Roquin proteins was not identified in these experiments.

The direct interaction of Roquin with the *ICOS* 3'UTR results in reduced ICOS protein levels as shown in cell-based functional assays. Thereby, ICOS surface expression from a construct harboring the 3'UTR was reduced by increased Roquin-1 levels, whereas ICOS expression from a CDS construct did not respond. In contrast to assays measuring *ICOS* mRNA half-life, which neglect effects of translational control, reporter assays integrate all possible effects of post-transcriptional regulation by measuring protein amounts. Using a truncated form of Roquin-1, these assays also revealed a requirement of the Roquin-1 C-terminus for mRNA repression, even though the N-terminus was sufficient for binding (**see Figure 5**).

In addition, Roquin-1 localization to stress granules and P bodies indicated an involvement in mechanisms of post-transcriptional regulation (Athanasopoulos et al. 2010; Glasmacher et al. 2010). In co-immunoprecipitations from T helper cell extracts Roquin-1 was associated with factors of the mRNA decapping pathway, namely Edc4 and Rck, which promote 5' to 3' mRNA degradation (Glasmacher et al. 2010). This suggests that Roquin-1 is an RBP recruiting mRNA decay factors to promote *Icos* mRNA degradation and thereby regulating Icos expression on the post-transcriptional level.

In the course of this thesis work, Leppek et al. described an RNA *cis*-element for Roquin-mediated mRNA regulation (Leppek et al. 2013). Using the mRNA decay-mediating CDE from the *Tnf* 3'UTR they found that Roquin-1 specifically binds to this RNA fragment. It was shown that the CDE folds into a hairpin structure with a triloop and a stem of six Watson and Crick base pairs. The same kind of stem-loop was found in other mRNAs potentially targeted by Roquin. Furthermore, Roquin-1 and Roquin-2 were found to be associated with Caf1 and Not1, subunits of the Ccr4-Not1

deadenylation complex, suggesting that Roquin-mediated post-transcriptional regulation also involves deadenylation of target mRNAs (**Figure 6**).

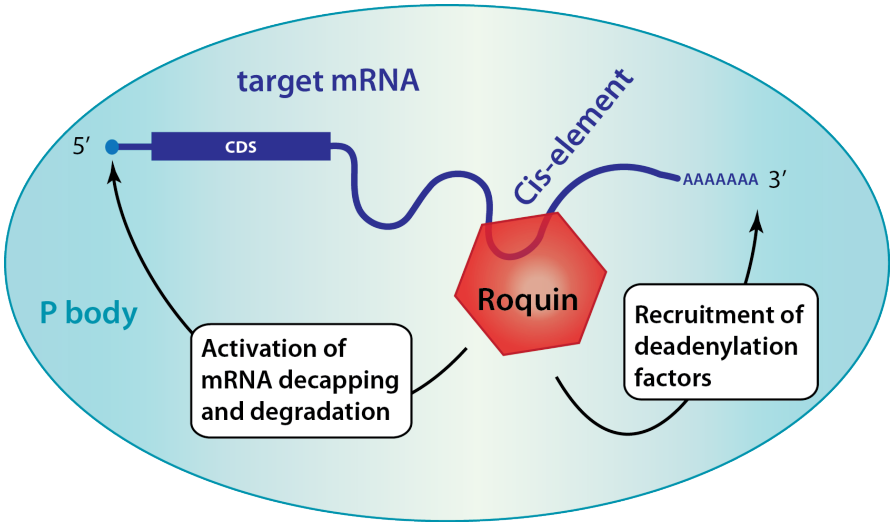

Figure 6: Scheme of Roquin function as RNA-binding protein. Roquin proteins directly bind to their target mRNA via a *cis*-regulatory element within the 3'UTR. This interaction takes place in P bodies and promotes mRNA degradation by recruiting factors of the different mRNA decay pathways.

2 Aim of the project

The analyses of mice with a point mutation in Roquin-1 and mice lacking Roquin-1 and Roquin-2 in T cells revealed a major impact of Roquin function on T cell activation and differentiation that had T cell-intrinsic causes. Appropriate function of these proteins was required to prevent excessive immune responses and autoimmunity. The first investigated target of Roquin was the inducible costimulator Icos. As an RNA-binding protein, Roquin promotes mRNA degradation and thereby reduces Icos protein levels. However, mice with a T-cell-specific Roquin-1 knockout did not develop autoimmune disease despite increased Icos levels on T cells. Furthermore, *Icos*-deficient *sanroque* mice still exhibited immune dysregulation and autoimmunity. From this, we concluded that *Icos* most likely is not the only mRNA targeted by Roquin-mediated post-transcriptional regulation, but that additional mRNAs are deregulated in *sanroque* mice to bring about the severe autoimmune phenotype.

Therefore, the first aim of this study was to establish assays to identify Roquin target mRNAs. These experiments were confined to T helper cells due to their pivotal role in shaping immune responses. Deletion of Roquin-encoding genes in primary T helper cells leads to a deregulation of putative Roquin target mRNAs compared to wild-type T helper cells. Those differentially expressed mRNAs can be identified with high sensitivity using mRNA expression arrays. CLIP and PAR-CLIP assays directly target the protein-RNA interaction by combining UV cross-linking and immunoprecipitation with high-throughput sequencing. Here, the identity of mRNAs bound by Roquin proteins as well as the contact site of the protein on the mRNAs can be identified. Since both methods cover different levels of Roquin-mediated regulation, they are supposed to complement each other in this study. Yet, there is a certain rate of false positive target candidates. Therefore, a validation strategy to prove post-transcriptional regulation by direct binding of Roquin proteins had to be established.

On the molecular level, this study aimed at investigating the Roquin-mRNA interaction in detail to identify and define *cis*-regulatory RNA elements targeted by Roquin proteins. An affinity-based selection procedure with recombinant Roquin-1 protein from a random RNA library was chosen to find preferentially bound RNA motifs. Furthermore, in close collaboration with structural biologists we aimed to characterize the ROQ domain and its RNA-binding interface. Crystallization of the ROQ domain and of a ROQ-RNA complex as well as nuclear magnetic resonance (NMR) approaches provided the basis to identify critical amino acid residues in mutational analyses. This led to functional studies dissecting the molecular requirements of Roquin-mediated post-transcriptional gene regulation.

3 Material and Methods

3.1 Material

3.1.1 Mice

CAG-CAR$^{stop\text{-}fl}$ transgenic mice (Vogel et al. 2013) express a truncated version of the human coxsackievirus and adenovirus receptor (CAR) lacking the intracellular signaling domain (CARΔ1) under the control of the synthetic CMV early enhancer/chicken beta-actin (CAG) promoter (**Figure 7**). CAR expression is only achieved when the preceding loxP-flanked STOP cassette (bovine growth hormone polyadenylation site) is excised by the Cre recombinase.

Rc3h1-2$^{fl/fl}$ mice are transgenic for Rc3h1 with loxP-flanked exons 4 to 6 (Bertossi et al. 2011) and Rc3h2 with loxP-flanked exon 4 (Vogel et al. 2013) respectively (**Figure 7**).

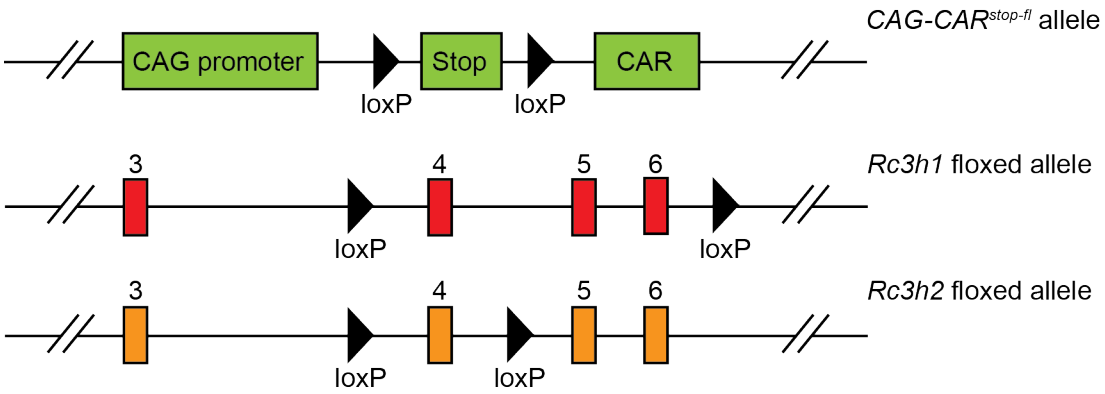

Figure 7: Schematic representation of genetically modified alleles used in this study.

CD4 Cre mice (Lee et al. 2001) were used for T-cell-specific loxP site recombination of the *Rc3h1-2*$^{fl/fl}$ alleles or as control group in combination with *Rc3h1-2*$^{+/+}$ alleles. Icos$^{-/-}$ mice (McAdam et al. 2001) were obtained from Prof. Dr. Richard Kroczek (Robert-Koch-Institut, Berlin). Ox40$^{-/-}$ mice (B6.129S4-*Tnfrsf4*^{tm1Nik}/J) were purchased from the Jackson Laboratories. The *Gt(ROSA)26Sor*$^{tm2(cre/ERT2)Brn}$ mouse line was provided by Prof. Dr. Anton Berns (Hameyer et al. 2007) and expresses a Cre recombinase estrogen receptor fusion protein. All animals were bred on a C57BL/6 genetic background and housed in a special pathogen-free barrier facility in accordance with the Helmholtz Zentrum München institutional, state and federal guidelines.

Primary T helper cells used for CLIP and PAR-CLIP assays at the Biozentrum in Basel were isolated from C57BL/6J mice. These mice were offspring from mice obtained from JANVIER LABS and were kept in a special pathogen-free barrier facility and according to the Swiss law.

3.1.2 Cell lines and cell culture

Human embryonic kidney cells (HEK293T) were purchased at ATCC.

Mouse embryonic fibroblasts (MEFs) were generated from embryos with the respective genotypes (*Rc3h1-2*$^{-/-}$ and *Rc3h1-2*$^{fl/fl}$*; Cre ERT2; CAG-CAR*$^{stop\text{-}fl}$) according to a standard protocol (Ansel et al. 2008).

To generate a Roquin-1 inducible cell line, *Rc3h1-2*$^{-/-}$ MEFs were lentivirally transduced with a CMVtight-Roquin-1-p2A-mCherry expression vector and a vector encoding the rtTA3 transactivator. This led to stable integration and allowed induced expression of Roquin-1 and the fluorescent protein mCherry in response to doxycycline treatment of the cells.

MEFs were cultured at 37°C, 10% CO_2 in DMEM complemented with 10% FCS, 100 U/ml penicillin/streptomycin and 10 mM HEPES. Primary T helper cell cultures were performed at 37°C, 5% CO_2 in RPMI complemented with 10% FCS, 1% HEPES, penicillin/streptomycin, non-essential amino acids (NEAA), sodium pyruvate, vitamin solution and β-mercaptoethanol-L-glutamine respectively (**Table 1**).

Table 1: Cell culture components

Name	Company
Dulbecco's Modified Eagle Medium (DMEM)	Gibco, life technologies
Fetal calf serum (FCS)	PAN BIOTECH GmbH
GIBCO™ L-Glutamine 200 mM (100x), solution	Gibco, life technologies
GIBCO™ MEM Vitamin Solution (100x), solution	Gibco, life technologies
HEPES, pH 7.4 (1M)	Gibco, life technologies
Non-essential amino acids (NEAA) (100x)	BioWhittaker, Lonza
Penicillin/Streptomycin (10,000 U/ml)	Gibco, life technologies
RPMI 1640, without L-glutamine	BioWhittaker, Lonza
Sodium pyruvate (100mM)	BioWhittaker, Lonza
β-mercaptoethanol	Sigma-Aldrich

3.1.3 Plasmids and bacteria culture

Table 2: Entry vectors

Entry vector	Insert
pCR8-GW	Ox40 CDS
pCR8-GW	Ox40 full-length
pCR8-GW	Ox40 3'UTR 1 to 40
pCR8-GW	Ox40 3'UTR 1 to 80
pCR8-GW	Ox40 3'UTR 1 to 120 (Ox40 ΔCDE-like)
pCR8-GW	Ox40 SELEX-like mut
pCR8-GW	Ox40 CDE-like mut
pCR8-GW	Ox40 SELEX/CDE-like mut
pCR8-GW	ICOS full-length
pCR8-GW	ICOS CDS
pCR8-GW	ICOS CDE_{260}
pCR8-GW	ICOS 1-2438 (ICOS ΔCDE)
pCR8-GW	Roquin-1
pCR8-GW	Roquin-1 K220A
pCR8-GW	Roquin-1 K239A
pCR8-GW	Roquin-1 R260A
pCR8-GW	Roquin-1 K239A R260A

After being cloned into pCR8-GW entry vectors using the TOPO®TA cloning kit (life technologies), inserts were transferred by lambda recombination (LR) into destination vectors for different applications (**Table 3**). The pDEST17 vector contains a T7 transcription start site making it suitable as template for *in vitro* transcription reactions. The retroviral expression vectors pKMV-IRES-GFP and pMSCV-IRES-Thy1.1 were used for subsequent virus production in combination with ecotropic or amphotropic packaging vectors (Eco-pac or gag-pol and ampho-env). Plasmids were amplified and cloned in chemically competent Dh5α *Escherichia coli* (*E. coli*).

Table 3: Destination vectors and their applications

Destination vector	Insert	Application
pDest17	Ox40 CDS	*In vitro* transcription
pKMV-IRES-GFP	Ox40 CDS	Retroviral expression
pDest17	Ox40 full-length	*In vitro* transcription
pKMV-IRES-GFP	Ox40 full-length	Retroviral expression
pKMV-IRES-GFP	Ox40 3'UTR 1-40	Retroviral expression
pKMV-IRES-GFP	Ox40 3'UTR 1-80	Retroviral expression
pKMV-IRES-GFP	Ox40 3'UTR 1-120 (Ox40 ΔCDE-like)	Retroviral expression
pKMV-IRES-GFP	Ox40 SELEX-like mut	Retroviral expression
pKMV-IRES-GFP	Ox40 CDE-like mut	Retroviral expression
pKMV-IRES-GFP	Ox40 SELEX/CDE-like mut	Retroviral expression
pKMV-IRES-GFP	ICOS full-length	Retroviral expression
pKMV-IRES-GFP	ICOS CDS	Retroviral expression
pKMV-IRES-GFP	ICOS CDE_{260}	Retroviral expression
pKMV-IRES-GFP	ICOS 1-2438 (ICOS ΔCDE)	Retroviral expression
pMSCV-IRES-Thy1.1	Cre recombinase	Retroviral expression
pMSCV-IRES-Thy1.1	Roquin-1 WT	Retroviral expression
pMSCV-IRES-Thy1.1	Roquin-1 K220A	Retroviral expression
pMSCV-IRES-Thy1.1	Roquin-1 K239A	Retroviral expression
pMSCV-IRES-Thy1.1	Roquin-1 R260A	Retroviral expression
pMSCV-IRES-Thy1.1	Roquin-1 K239A R260A	Retroviral expression

Table 4: Plasmids for recombinant protein expression

Plasmid	Insert
petM11	Roquin-1
petM11	Roquin-1 (2-440)
petM11	Roquin-1 M199R (2-440)
petM11	Roquin-2 (2-438)
pETTrx1a	Roquin-1 (171-326)
pETTrx1a	Roquin-1 (146-326)
pETTrx1a	Roquin-1 (146-326) R188A
pETTrx1a	Roquin-1 (146-326) R219A
pETTrx1a	Roquin-1 (146-326) K220A
pETTrx1a	Roquin-1 (146-326) R229A
pETTrx1a	Roquin-1 (146-326) R233A
pETTrx1a	Roquin-1 (146-326) S238A
pETTrx1a	Roquin-1 (146-326) K239A
pETTrx1a	Roquin-1 (146-326) Y250A
pETTrx1a	Roquin-1 (146-326) R251A
pETTrx1a	Roquin-1 (146-326) S253A
pETTrx1a	Roquin-1 (146-326) K259A
pETTrx1a	Roquin-1 (146-326) S264A
pETTrx1a	Roquin-1 (146-326) S265Y
pETTrx1a	Roquin-1 (146-326) E293A
pETTrx1a	Roquin-1 (146-326) K314A
pETTrx1a	Roquin-1 (146-326) K239A R260A

Expression of recombinant proteins was performed in the Rosetta (DE3) pLysS (petM11 constructs) or the BL21 (DE3) *E. coli* strain (pETTrx1a constructs).

3.1.4 Oligonucleotides

3.1.4.1 RNA Oligonucleotides

RNA oligonucleotides used for EMSA experiments were synthesized and PAGE-purified by IBA GmbH (Göttingen, Germany).

Table 5: RNA oligonucleotides

Name	Sequence (5' to 3')
Tnf CDE	ACA UGU UUU CUG UGA AAA CGG AG
Tnf CDE Ext	GG UGU UUU CUG UGA AAA CGG CC
Tnf CDE LM1	ACA UGU UUU CUC UGA AAA CGG AG
Tnf CDE LM2	ACA UGU UUU CUG GGA AAA CGG AG
Tnf CDE LM3	ACA UGU UUU CAC AGA AAA CGG AG
Tnf CDE SM1	ACA UGU UUU UUG UAA AAA CGG AG
Tnf CDE SM1	ACA UGU UUU GUG UCA AAA CGG AG
Tnf CDE SM1	ACA UGU UCC CUG UGG GAA CGG AG
ICOS CDE-like	AGA AUG ACU GUA UCA GUC AAU GG
Ox40 CDE-like	CUA UGU AUG CUA UGC AUA CUA CC
Ox40 SELEX-like	UCC ACA CCG UUC UAG GUG CTG GG

3.1.4.2 DNA Oligonucleotides

DNA Oligonucleotides were purchased from Metabion (Planegg, Germany).

Table 6: Primers for cloning and site directed mutagenesis

Name	Sequence (5' to 3')	Purpose
Ox40 CDS for	GAGGTCGACCATGTATGTGTGGGTTCAGC	Cloning Ox40
Ox40 CDS rev	CTCGCGGCCGCTCAGATCTTGGCCAGAG	Cloning Ox40
Ox40 3'UTR rev	CTCGCGGCCGCTAGCATGTTTATTAGGAG	Cloning Ox40
Ox40 3'UTR 1-40 rev	CTCGCGGCCGCGGTTGTCCGTGCCCCAT	Shorten Ox40
Ox40 3'UTR 1-80 rev	CTCGCGGCCGCCTAGAACGGTGTGGAG	Shorten Ox40

Name	Sequence (5’ to 3’)	Purpose
Ox40 3’UTR 1-120 rev	CTCGCGGCCGCTGCATAGCATACATAG	Shorten Ox40
ICOS CDS for	GAGGTCGACCATGAAGTCAGGCCTCTGG	Cloning ICOS
ICOS CDS rev	GAGACTCGAGGGTTATAGGGTCACATCTGTGAG	Cloning ICOS
ICOS 3’UTR rev	CTCGCGGCCGCTACTACTGTTAAAATCTC	Cloning ICOS
ICOS 2438 rev	GAGACTCGAGTGGGGATGAGGATGTGTC	Shorten ICOS
Tnf CDE_{260} for	CTCGAGGGAAGGCCGGGGTGTCC	Cloning CDE_{260}
Tnf CDE_{260} rev	CTCGAGCTCTCAATGACCCGTAGGG	Cloning CDE_{260}
Ox40 QC SELEX for	ACCCTCCACACCGTTCTACCAGCTGGGCTGGCT	Mutagenesis
Ox40 QC SELEX rev	AGCCAGCCCAGCTGGTAGAACGGTGTGGAGGGT	Mutagenesis
Ox40 QC CDE for	GGCTTTCCTATGTATGCTATCGTTACTACCTGCC TGGTGGTG	Mutagenesis
Ox40 QC CDE rev	CACCACCAGGCAGGTAGTAACGATAGCATACAT AGGAAAGCC	Mutagenesis
Roquin-1 QC K220A for	GGTTCTGCATTGTCTCGGGCAGTGTTGGTTCTCT TCGTGG	Mutagenesis
Roquin-1 QC K220A rev	CCACGAAGAGAACCAACACTGCCCGAGACAATG CAGAACC	Mutagenesis
Roquin-1 QC K239A for	CCTCAAGCCTCTGCTACCAGCATTGGGC	Mutagenesis
Roquin-1 QC K239A rev	GCCCAATGCTGGTAGCAGAGGCTTGAGG	Mutagenesis
Roquin-1 QC R260A for	GCTTCAAGGTCACCAAAGCTGATGAAGACTCTT C	Mutagenesis
Roquin-1 QC R260A rev	GAAGAGTCTTCATCAGCTTTGGTGACCTTGAAG C	Mutagenesis

Table 7: Primers for SELEX

Name	Forward primer (5’ to 3’)	Reverse primer (5’ to 3’)
N47Nε-TK	AATTCTAATACGACTCACTATAGG-GAGGAGGAGAGATGTGAACTT	GTCCTGTGGCATCCACGAAA
N47Nε-Index1	ATCACGAGGAGAGATGTGAACTT	ATCACGTGTGGCATCCACGAAA
N47Nε-Index2	CGATGTAGGAGAGATGTGAACTT	CGATGTTGTGGCATCCACGAAA
N47Nε-Index3	TTAGGCAGGAGAGATGTGAACTT	TTAGGCTGTGGCATCCACGAAA
N47Nε-Index4	TGACCAAGGAGAGATGTGAACTT	TGACCATGTGGCATCCACGAAA
N47Nε-Index5	ACAGTGAGGAGAGATGTGAACTT	ACAGTGTGTGGCATCCACGAAA

The basis for the random RNA library used in the SELEX assay was a single stranded DNA library synthesized by Metabion with 47 nucleotides (nts) random sequence flanked by primer sequences (5'- GGG AGG AGG AGA GAT GTG AAC TT- N47 - TTT CGT GGA TGC CAC AGG AC -3').

Table 8: *In vitro* transcription templates

Name	Sequence (5' to 3')
P1_A1_Seq_104	GGAGAGATGTGAACTTGGACCGTAAGGTATGCAAAGTATGTACATGGAACTGCG TTTTAGGAGTTTCGTGGATGCCAC
P2_A1_Seq_89	GGAGAGATGTGAACTTCGTTTTAGAAGGCTTGTCCATATCAATGAGTGTCATCAC GCGTTCTAGTTTCGTGGATGCCAC
P3_A1_Seq_85	GGAGAGATGTGAACTTCTGGGAAGGAAAGAAATAAGCATGCAGAGCCGTTACGT TTTAGGAACAGTTTCGTGGATGCCAC
P4_A1_Seq_82	GGAGAGATGTGAACTTACCGTGTAAGTCTCAATCAGTCGGCAAGCAAGGGGCTG CGTTGTAGTAGTTTCGTGGATGCCAC
P5_A1_Seq_81	GGAGAGATGTGAACTTGCTACAGGTACAAAAGGGCATCGCAACGTGAGGAACTG CGTTTTAGGAGTTTCGTGGATGCCAC
P6_A1_Seq_79	GGAGAGATGTGAACTTTCCAAATAGAGGCGCGCATGAGAATGCACACGGGGCTG CGTTTTAGGAGTTTCGTGGATGCCAC
P7_A1_Seq_74	GGAGAGATGTGAACTTGGATAGCTTGAAAGTTGAATGATGGTAAAATGGAATTA CGTTTTAGGAGTTTCGTGGATGCCAC
P8_A1_Seq_74	GGAGAGATGTGAACTTACCGTGTATCATGGTGGATTTTGCAGTGGTATTTGCGAG GCGTTGTAGTTTCGTGGATGCCAC
P9_A1_Seq_74	GGAGAGATGTGAACTTACGGTCTCTGTAGATGGTTGTAGGCACGACGAGCACTG CGTTTTAGGAGTTTCGTGGATGCCAC
P10_A1_Seq_73	GGAGAGATGTGAACTTAGGTTGCGTTATAGCAATCGCGCGAGGCTGGCGAGACG ATACGTTGTAGTTTCGTGGATGCCAC
P11_A1_Seq_73	GGAGAGATGTGAACTTTAGGAATTGCGTATAAAGACTTGCAGAAACGAACACTG CGTTTTAGGAGTTTCGTGGATGCCAC
P12_A1_Seq_73	GGAGAGATGTGAACTTCCTGGAGCATCATAAGAATTTGCGAACGTGACTGCGTTT TAGGAGTTAGTTTCGTGGATGCCAC
P13_A1_Seq_72	GGAGAGATGTGAACTTCCGTTATAGGAAGCAGTCAAGATCATCGATGAGTATCC GCGCGTTGTAGTTTCGTGGATGCCAC
P14_A1_Seq_71	GGAGAGATGTGAACTTAGACATGACATCAGAAATCGTGTAGGTGGACGAGGCTG CGTTTTAGGAGTTTCGTGGATGCCAC
P15_A1_Seq_70	GGAGAGATGTGAACTTCGTTTTAGCAGTGCATTCGAGCTCTGTGTACGGGATCTG CGCGTTTTAGTTTCGTGGATGCCAC
P16_A1_Seq_68	GGAGAGATGTGAACTTGCATTATTTCAAGTTAGTAGTTGTGAATTCATGGATTGC GTTGTAGGAGTTTCGTGGATGCCAC

Name	Sequence (5’ to 3’)
P17_A1_Seq_66	GGAGAGATGTGAACTTGGGCGGCTTCATAACTAGTGATAGGACAATCGGAACTG CGTTTTAGGAGTTTCGTGGATGCCAC
P18_A1_Seq_64	GGAGAGATGTGAACTTGTAACAAGTTTAGGGAGAGGTGGTATACATACAAACTA CGTTTTAGGAGTTTCGTGGATGCCAC
P19_A1_Seq_64	GGAGAGATGTGAACTTCCAGGATTAGATAAGAACATAAGAGTATATAGCATTTG GGCCCGCGTAGTTTCGTGGATGCCAC
P20_A1_Seq_64	GGAGAGATGTGAACTTCAAGAATAAGGAACAGAGTCCCAGGGCACGTGAAATTG CGTTTTAGGAGTTTCGTGGATGCCAC
P34_A1_Seq_56	GGAGAGATGTGAACTTGCGTGTATCATGCAAAAAAGCTATAGGCAGATCGACGG ATGCGTTTTAGTTTCGTGGATGCCAC
P43_A1_Seq_51	GGAGAGATGTGAACTTAGCTACCGTGTAGCCATGCCTAGTGGAGCCGGAACTAC TTTATGCGCAGTTTCGTGGATGCCAC
P44_A1_Seq_51	GGAGAGATGTGAACTTACGGAGATTGCTTGTATCAAGTAATGCGGAGGCTGGCG AAACGTTGTAGTTTCGTGGATGCCAC
ICOS_600-700	GGAGAGATGTGAACTTTATGGAACTCTGGCACCCAGGCATGAAGCACGTTGGCC AGTTTTCCTCAACTTGAAGTGCAAGATTCTCTTATTTCCGGGACCACGGAGAGTC TGACTTATTTCGTGGATGCCAC
ICOS_700-800	GGAGAGATGTGAACTTACTACATACATCTTCTGCTGGTGTTTTGTTCAATCTGGA AGAATGACTGTATCAGTCAATGGGGATTTTAACAGACTGCCTTGGTACTGCCGAG TCCTCTTTTCGTGGATGCCAC
mOX-40_UTR	GGAGAGATGTGAACTTGCATTACTACAGGAGTGGATTTTATGGGGCACGGA CAACCCATATCCTGATGCCTGCCAGTACCCTCCACACCGTTCTAGGTGCTGG GCTGGCTCTGGGCTTTCCTATGTATGCTATGCATACTACCTGCCTGGTGGTGC TCCTTTTCGTGGATGCCAC
mOX-40_UTR SELEX_mut	GGAGAGATGTGAACTTGCATTACTACAGGAGTGGATTTTATGGGGCACGGA CAACCCATATCCTGATGCCTGCCAGTACCCTCCACACCGTTCTA**CCA**GCTGG GCTGGCTCTGGGCTTTCCTATGTATGCTATGCATACTACCTGCCTGGTGGTGC TCCTTTTCGTGGATGCCAC
mOX-40_UTR CDE_mut	GGAGAGATGTGAACTTGCATTACTACAGGAGTGGATTTTATGGGGCACGGA CAACCCATATCCTGATGCCTGCCAGTACCCTCCACACCGTTCTAGGTGCTGG GCTGGCTCTGGGCTTTCCTATGTATGCTAT**CGT**TACTACCTGCCTGGTGGTGC TCCTTTTCGTGGATGCCAC
mOX-40_UTR SELEX_CDE_mut	GGAGAGATGTGAACTTGCATTACTACAGGAGTGGATTTTATGGGGCACGGA CAACCCATATCCTGATGCCTGCCAGTACCCTCCACACCGTTCTA**CCA**GCTGG GCTGGCTCTGGGCTTTCCTATGTATGCTAT**CGT**TACTACCTGCCTGGTGGTG CTCCTTTTCGTGGATGCCAC

Table 9: Primers for qPCR

Gene	Forward primer (5' to 3')	Reverse primer (5' to 3')	Probe
Bcl2l1	TGACCACCTAGAGCCTTGGA	GCTGCATTGTTCCCGTAGA	# 2
Bcl3	GAACAACAGCCTGAACATGG	TCTGAGCGTTCACGTTGG	# 18
Ctla4	TCACTGCTGTTTCTTTGAGCA	GGCTGAAATTGCTTTTCACAT	# 21
Ebi3	GCTCCCCTGGTTACACTGAA	ACGGGATACCGAGAAGCAT	# 26
Fbxo33	GCATCTACTTGGAGCTGGTGT	TCCAAAAAGACTAAACTTCTGGAGAT	# 89
Icos	CGGCAGTCAACACAAACAA	TCAGGGGAACTAGTCCATGC	# 6
Irf4	AGCACCTTATGGCTCTCTGC	TGACTGGTCAGGGGCATAAT	# 3
Lfng	GCGCCACAAGGAGATGAC	CCGAGGAGCAGTTGGTGA	# 100
Nfkbid	TTTCTACCCTCCGTCAGACC	TACAGCCGGGTATCCAGAGA	# 9
Pim2	GAGGCCGAATACCGACTTG	GATTACTTTGATGGCCACCTG	# 79
Ppan	GAACCTGTTCCCGTCCATC	CTCTTGGGAGTCAGGGTTGT	# 16
Tm2d3	GCCCTCTGTTACCTGTGTCG	AAACCTGCAAGTCATGTTGATG	# 6
Tnfrsf4 (Ox40)	GCTTGGAGTTGACTGTGTTCC	GGGTCTGCTTTCCAGATAAGG	# 79
Ywhaz	CGCTAATAATGCAGTTACTGAGAGA	TGGAAGGCCGGTTAATTTT	# 2
Zc3h12a	GAAGCAATGTGGCCATGAG	CCTCGCTCCAGAAACCAG	# 76

3.1.5 Antibodies and cytokines

Antibodies were used for different applications including immunoblotting (IB), immunoprecipitation (IP), flow cytometry and T helper cell cultures. Some monoclonal antibodies were obtained as hybridoma supernatants from an in-house antibody facility as indicated in **Table 10**. If not stated differently the antibodies are directed against mouse antigens.

Table 10: Antibodies and cytokines

Name	Company	Dilution	Application
Anti-Ago2 (2D4)	Wako	0.1 µg/µl	IP
Anti-B220 (RA3-6B2)	eBioscience	1:200	Flow cytometry
Anti-CAR (E1-1)	BD Biosciences	1:20	Flow cytometry

Name	Company	Dilution	Application
Anti-CD134 (Ox40, clone OX-86)	eBioscience	1:200	Flow cytometry
Anti-CD278 (human ICOS, ISA-3)	eBioscience	1:1000	Flow cytometry
Anti-CD278 (Icos, 7E.17G9)	eBioscience	1:200	Flow cytometry
Anti-CD279 (PD-1, clone J43)	eBioscience	1:200	Flow cytometry
Anti-CD28 (37N)	In-house production	1.0 µg/ml	Th1 cell culture
Anti-CD3 (145-2C11)	In-house production	0.1 µg/ml	Th1 cell culture
Anti-CD3 (145-2C11)	eBioscience	1:200	Flow cytometry
Anti-CD4 (RM4-5)	eBioscience	1:200	Flow cytometry
Anti-CD44 (IM7)	eBioscience	1:200	Flow cytometry
Anti-CD62L (MEL-14)	eBioscience	1:200	Flow cytometry
Anti-CD8 (53-6.7)	eBioscience	1:200	Flow cytometry
Anti-CD90.1 (Thy1.1, OX-7)	eBioscience	1:200	Flow cytometry
Anti-CD95 (Jo2)	eBioscience	1:200	Flow cytometry
Anti-Ctla4 (UC10-4B9)	eBioscience	1:100	Flow cytometry
Anti-CXCR5 (2G8)	In-house production	1:10	Flow cytometry
Anti-FoxP3 (FJK-16s)	eBioscience	1:100	Flow cytometry
Anti-GL-7	BD Pharming	1:800	Flow cytometry
Anti-hamster IgG	MP Biochemicals	0.1 mg/ml	Th1 cell culture
Anti-IFN-γ (XMG1.2)	eBioscience	1:200	Flow cytometry
Anti-IL-4 (11B11)	In-house production	10 µg/ml	Th1 cell culture
Anti-IL-4 PE (11B11)	eBioscience	1:200	Flow cytometry
Anti-KLRG1 (2F1)	eBioscience	1:200	Flow cytometry
Anti-mouse IgG (HRP coupled)	Cell signaling	1:3000	IB
Anti-NK1.1 (PK136)	eBioscience	1:200	Flow cytometry
Anti-rat IgG (biotinylated)	Jackson ImmunoResearch	1:200	Flow cytometry
Anti-rat IgG (HRP coupled)	Cell signaling	1:3000	IB
Anti-Roquin (18F8)	In-house production	2 mg/ml	IP
Anti-Roquin (3F12)	In-house production	2 mg/ml	IP
		1:10	IB
Anti-TCRβ (H57-597)	eBioscience	1:200	Flow cytometry
Anti-tubulin (B-5-1-2)	Santa Cruz	1:2000	IB
Fc-block (CD16/31; 2.4G2)	In-house production	10 µg/ml	Flow cytometry

Name	Company	Dilution	Application
PBS57-loaded CD1d Tetramer	National Institutes of Health	1:100	Flow cytometry
Recombinant human IL-2 (ProleukinS)	Novartis	20 U/ml	Th1 cell culture
Recombinant mouse IL-12	BD Biosciences	10 ng/ml	Th1 cell culture
Streptavidin	eBioscience	1:200	Flow cytometry

3.1.6 Chemicals, enzymes and kits

Table 11: Chemicals and solutions

Chemicals and solutions	Company
2-Propanol	Merck
2log DNA ladder	New England Biolabs
Acrylamide 4K solution	Applichem
Albumin fraction V (Bovine serum albumin, BSA)	Roth
Amersham ECL Prime	GE Healthcare
Ammonium persulfate (APS)	Serva
Ampicillin	Roche
ATP [γ-^{32}P]	Hartmann Analytic
Baker's yeast tRNA	Sigma
Bio-Rad Protein assay (Bradford solution)	Bio-Rad
Biozym LE Agarose	Biozym
Boric acid	Calbiochem
Brefeldin A	eBioscience
Calcium chloride	Merck
Chloroform	Sigma
Chloroquin	Sigma
Coomassie brilliant blue R-250	Roth
DETACHaBEAD® Mouse CD4 (L3T34)	Invitrogen
Dithiothreitol (DTT)	Applichem
dNTP set	Thermo Scientific
Doxycyclin	Applichem
Dynabeads® M-280 Streptavidin	Invitrogen

Chemicals and solutions	Company
Dynabeads® Mouse CD4	Invitrogen
Dynabeads® MyOneTosylactivated	Invitrogen
Dynabeads® Protein G for Immunoprecipitation	Invitrogen
EDTA, pH 8.0, 0.5 M	Roth
Epsilon aminocaproic acid	Applichem
Ethanol	Merck
EZ-link PEG4-NHS-Biotin	Pierce
Formaldehyde solution 36.5-38%	Sigma
GlycoBlue	Ambion
H_2O_2	Applichem
Isopropyl β-D-1-thiogalactopyranoside (IPTG)	Sigma-Aldrich
Kanamycin	Roth
Methanol	Merck
Nonfat dry milk powder	Applichem
Nonidet P-40	Sigma-Aldrich
NOVEX loading buffer	Invitrogen
NTP set	Thermo Scientific
Paraformaldehyde (PFA) solution, 8%	Merck
Polybrene	Sigma-Aldrich
Protease inhibitor tablets, cOmplete Mini EDTA-free	Roche Diagnostics
Rotiphorese Gel 30 (polyacrylamide for EMSAs)	Roth
Saponin	GPR Rectapur
Sodium acetate 3M, pH 5.2	Ambion
Sodium dodecyl sulfate (SDS) pellets	Serva
Spectinomycin	Applichem
Tamoxifen	Sigma-Aldrich
TEMED	Applichem
TRI reagent solution	Ambion
Trypsin-EDTA	Gibco, life technologies
Tween 20	Applichem
UTP [α-^{32}P]	Hartmann Analytic

Table 12: Enzymes

Enzyme	Company
FastAP (Alkaline phosphatase)	Fermentas
Gateway® LR Clonase® II Enzyme Mix	life technologies
PNK (Polynucleotide kinase)	Fermentas
Proteinase K	Roche
RNase T1	Thermo scientific
RNasin®	Promega
SuperScript® III Reverse Transcriptase	Invitrogen
T4 Polynucleotide Kinase	Thermo scientific
T4 RNA ligase	Fermentas
T7 RNA Polymerase	Agilent technologies
Taq Polymerase	Invitrogen
Turbo-DNase	Ambion

Table 13: Kits

Kit	Company
Foxp3 staining buffer set	eBioscience
GeneChip WT Terminal Labeling and Controls Kit	Affymetrix
LIVE/DEAD® Fixable Blue Dead Cell Stain Kit	Invitrogen
LR Clonase enzyme mix	Invitrogen
mMESSAGE mMACHINE® T7 Transcription Kit	Ambion
Nucleobond®Xtra Maxi	Machery-Nagel
One-Step RT-PCR Kit	Qiagen
pCR™8/GW/TOPO® TA Cloning® Kit	life technologies
PureYield™ Plasmid Miniprep System	Promega
QIA®quick Gel extraction Kit	Qiagen
QIA®quick Nucleotide removal Kit	Qiagen
QuantiTect Reverse Transcription Kit	Qiagen
QuikChange XL Site-Directed Mutagenesis Kit	Agilent Technologies
RNeasy® Mini Kit	Qiagen

Kit	Company
Universal Probe Library LightCycler® 480 Probes Master	Roche Diagnostics
WT Expression Kit	Ambion

3.1.7 Buffers

Table 14: Buffers for standard procedures

Name	Composition
Blotting buffer	25 mM Tris 192 mM glycine 20% methanol
Coomassie destaining solution	50% methanol 40% H_2O 10% acetic acid
Coomassie staining solution	50% methanol 40% H_2O 10% acetic acid 0.25 g/l Coomassie brilliant blue R-250
FACS buffer	PBS with 2 % FCS
HBS (2x)	274 mM NaCl 10 mM KCl 1.4 mM Na_2HPO_4, pH 7.0
Lysis buffer	20 mM Tris-HCl pH 7.5 150 mM NaCl 0.25 % NP-40 1.5 mM $MgCl_2$
PBS	137 mM NaCl 10 mM Na_2HPO_4, pH 7.4 2.7 mM KCl
Saponin buffer	PBS with 0.5% saponin and 1% BSA
SDS PAGE buffer	25 mM Tris 200 mM glycine 0.1% SDS
SDS sample buffer (4x)	200 mM Tris-HCl, pH 6.8 8% SDS 4% glycerol 0.1% bromophenol blue 10% β-mercaptoethanol
TAC lysis buffer	13 mM Tris 140 mM NH_4Cl, pH 7.2
TBE (1x)	89 mM Tris-borate 2 mM EDTA, pH 8.0
TBS	50 mM Tris-HCl pH 8.0 150 mM NaCl
TBS-T	TBS with 0.05 % Tween-20

Table 15: Buffers for CLIP and PAR-CLIP assays

Name	Composition
5x PNDS buffer (High salt wash)	5x PBS 0.5% NP-40 0.25% Deoxychelate 0.1% SDS 1 mM DTT
EGTA wash buffer	20 mM Tris-HCl pH 7.5 20 mM EGTA 0.2% Tween-20
Mg wash buffer	20 mM Tris pH 7.5 10 mM $MgCl_2$ 0.2% Tween-20 1mM DTT
PN8	0.1 M Na-Phosphate pH 8.0 0.01% NP-40
PNDS lysis buffer	1x PBS 0.5% NP-40 0.25% Deoxychelate 0.05% SDS
Proteinase K (PK) digestion buffer	100 mM Tris-HCl pH 7.5 50 mM NaCl 10 mM EDTA
RNA elution buffer	1 M sodium acetate, pH 5.5 1 mM EDTA

Table 16: Buffers for SELEX and Filter binding assays

Name	Composition
Filter activation buffer	40 mM aminocaproic acid 20% Methanol
PAA-loading buffer	9 M Urea 50 mM EDTA, pH 8.0
Selection buffer	20 mM HEPES, pH 7.4 150 mM NaCl 1 mM $MgCl_2$ 1 mM DTT 1µg/µl BSA
Washing buffer	20 mM HEPES, pH 7.4 150 mM NaCl 1 mM $MgCl_2$ 1 mM DTT

3.1.8 Columns and consumables

Table 17: Columns and consumables

Name	Company
Centrifugal filter units, Amicon Ultra, 30K	Millipore
Costar Spin-X centrifuge tube filter	Sigma-Aldrich
Disposable PD-10 Desalting Columns	GE Healthcare
Filter paper, 1 mm and 2 mm	Whatman
GeneChip Mouse Gene 1.0 ST Arrays	Affymetrix
His-Trap HP	GE Healthcare
Immobilon® PVDF Membrane	Millipore
Mesh, fine (41 µm) and rough (150 µm)	Reichelt Chemietechnik
MicroSpin Columns P30	Bio-Rad
Nitrocellulose membrane (Protran®)	Whatman
Surgical disposable scalpels	Braun

3.1.9 Instruments

Table 18: Instruments

Instrument	Company
96-well dotblotter	SRC 96 D Minifold I (Schleicher und Schüller)
Accuracy weighing machine	KERN ABJ-220-4M (Kern und Söhne GmbH)
	KERN EW 220-3NM (Kern und Söhne GmbH)
Agarose gel chambers	Peqlab Biotechnologie GmbH
Bacterial incubator	Brutschrank BINDER BF 53 (Binder Labortechnik)
	Innova 4400 incubator shaker (New Brunswick Scientific GmbH)
BD FACS AriaIII Cell Sorter	BD Biosciences
BD LSR Fortessa Cell Analyzer	BD Biosciences
Bead separation magnet	DynaMag^{TM}-5 Magnet (Invitrogen)
Cell counting chamber	Neubauer counting chamber (Marienfeld Superior)

Instrument	Company
Centrifuges and rotors	Beckman Coulter Avanti-J-26XP (Beckman Coulter); JA-10 Rotor, Fixed Angle (Beckman Coulter)
	Allegra®X-12R Centrifuge (Beckman Coulter); Rotor SX 4750 (Beckman Coulter)
	Eppendorf Centrifuge 5810R (Eppendorf); Rotor A-4-62 and F-34-6-38
CO_2 incubator	Forma Direct Heat CO_2 Incubator HEPA Class 100 (Thermo Electron Corporation)
Coasting mixer	Tube Roller-Mixers, SRT1 (Stuart) (ScienceLab)
Gel documentation	Quantum ST4 (Vilber)
Gel drying system	SLAB Gel dryer Model GD2000 (Hoefer)
Ice machine	Scotsman AF 200 (Scotsman Ice system)
Magnet stirrer	RCT basic safety control (IKA)
Magnetic phosphoimager screen	Imaging plate BAS-IP MS 2025 (Fujifilm)
Microscope	Axiovert 40C (Zeiss)
Microwave	Bosch
Mixing wheel	Dynabeads® MX 12-tube Mixing Wheel (Applied biosystems)
pH meter	pH-Meter inoLab® pH 720 (WTW GmbH)
Phospho-image reader	FLA 5100 Image analysis system (Fujifilm)
Power supply	Stromgeber EC105 (Thermo Electron Corporation)
	Bio-Rad energy supplier (Bio-Rad)
Sonification device	Digital sonifier Model 250 D (Branson)
Spectrophotometer	Eppendorf Bio Photometers (Eppendorf)
	NanoDrop TM 1000 Spectrophotometer (Thermo Scientific)
Sterile-working bench	BDK, Luft und Reinraumtechnik
Table centrifuges	Centrifuge 5415D (Eppendorf)
	Centrifuge 5417R (Eppendorf)
Tank blotting chamber	Trans-blot Cell, Bio-Rad
Thermo cycler	DNA Engine 48/48 Dual Alpha Unit (Bio-Rad)
	Light Cycler 480II (Roche)
Thermo mixer	Thermomixer comfort (Eppendorf)
UV crosslinker	Stratagene
UV transilluminator	TS-40 (Ultra-Violet Products Ltd.)

Instrument	Company
Vacuum pump	Diaphragm Vacuum Pump MZ 2C (Vacuubrand)
Vertical Electrophoresis apparatus	Vertical Electrophoresis apparatus (Bio-Rad)
Vortexer	Vortex Genius 3 (IKA)

3.1.10 Software and databases

Table 19: Software and databases

Name	Application	Company/URL
Adobe Creative suite 5	Illustrator (Figures, Schemes) Photoshop (Image processing)	Adobe
AIDA Image Analyzer	Quantification of ^{32}P signals	Raytest
ClipZ	Analysis of PAR-CLIP data	http://www.clipz.unibas.ch/
Clustalw	Multiple alignments	http://www.ebi.ac.uk/Tools/msa/clustalw2/
FlowJo version 9.4.10	FACS data analysis	FlowJo
Graphpad Prism®	Statistics and graphs	Graphpad
LightCycler software	qPCR data analysis	Roche Diagnostics
MEME	Sequence motif search	http://meme.nbcr.net/meme/cgi-bin/meme.cgi
Mfold	RNA folding	http://mfold.rna.albany.edu/?q=mfold
Microsoft Office 2011	Data analysis (Excel) Writing (Word)	Microsoft
NCBI Nucleotide	cDNA sequences	http://www.ncbi.nlm.nih.gov/nucleotide/
ProbeFinder version 2.49 (Mouse)	qPCR primer design	Roche Diagnostics
QuickChange primer design	Primer design for mutagenesis	http://www.genomics.agilent.com/primerDesignProgram.jsp
RNAalifold	RNA structure analysis	http://rna.tbi.univie.ac.at/cgi-bin/RNAalifold.cgi

3.2 Methods

3.2.1 Molecular biological methods

3.2.1.1 Polymerase chain reaction (PCR)

Using heat-stable Taq DNA Polymerases and cycling temperature profiles, PCR allows exponential amplification of specific DNA fragments that are flanked by the respective primer sequences. In addition to PCR reactions for library preparations (3.2.5), the method was used to amplify *Ox40* (NM_011659) full-length (fl) and CDS from murine T cell cDNA. Using the Taq Polymerase (Invitrogen) resulted in deoxyadenosine (A) overhangs, which were required in the subsequent TA cloning procedure. The reaction mix contained about 100 ng cDNA as template, 5 µl 10x reaction buffer, 1 µl dNTP Mix (10 mM each), 1 µl $MgCl_2$ (50 mM), 2 µl forward and reverse primer (10 mM each) and 1 µl Taq Polymerase. Deionized water was added to reach the final volume of 50 µl. The PCR was performed for 30 cycles with denaturation at 95°C for 30 sec, annealing at 52°C for 30 sec and elongation at 72°C for 45 sec. The reaction products were visualized and size separated by electrophoresis on a 1.5% (w/v) agarose gel in 1x TBE buffer. The band with the correct size was cut, and DNA was purified using the QIA®quick gel extraction Kit according to the given instructions.

3.2.1.2 Cloning and bacterial culture

Purified PCR products were transferred into the topoisomerase-I-activated entry vector pCR8-GW via TOPO®TA-cloning following the manual of the kit (life technologies). Amplification and cloning of the obtained plasmids was performed in bacterial cultures of the Dh5α *E. coli* strain. The bacteria were grown in LB medium or on LB agar plates supplemented with ampicillin (100 µg/ml), spectinomycin (100 µg/ml) or kanamycin (50 µg/ml) to select for bacteria with the respective plasmids. Plasmid DNA was purified using the PureYield™ Plasmid Miniprep System (Promega) kit for small-scale and the Nucleobond®Xtra Maxi (Machery-Nagel) kit for large-scale bacterial cultures.

Cloned DNA sequences can be transferred into different destination vectors using the Gateway® technology that promotes lambda recombination (LR) via recombination sites within the entry vector (AttL1 and 2) and destination vector (AttR1 and 2) backbones. The LR reaction using the LR Clonase® II Enzyme Mix (life technologies) was performed for one hour at room temperature (RT) followed by Proteinase K treatment and heat-shock transformation of Dh5α *E. coli*. Correct recombination removes the toxin-encoding *ccdB* gene from the destination vector that also carries an antibiotic resistance gene different from the entry vector. Both features ensure that only bacteria transformed with the correct destination plasmid form colonies.

For site directed mutagenesis of plasmid DNA the QuickChange XL Mutagenesis Kit (Agilent) was used according to the manufacturer's suggestions. Using specifically mismatching primers in a PCR that amplifies the whole plasmid causes nucleotide deletions, insertions or nucleotide exchanges that can result in amino acid exchanges in the encoded protein. A DpnI digest of the template plasmid ensures high mutation rates in the clones resulting from bacterial transformation. Primers for this method were designed using the manufacturer's online tool (QuickChange primer design, **Table 19**).

3.2.1.3 Recombinant protein expression and purification

Expression of Roquin N-terminal proteins (Roquin-1 aa 2-440, Roquin-1 M199R aa 2-440, Roquin-2 aa 2-438) from the respective pETM11 constructs was induced in transformed Rosetta (DE3) pLysS *E. coli* cultures. Having an optical density (OD) of 0.6-0.8 the cultures were complemented with 1 mM IPTG and incubated over night, shaking at 12°C. Harvested bacteria pellets were resuspended in PBS complemented with protease inhibitors (Roche) and 1 mM DTT for sonification on ice (amplitude 30%). The disrupted cells were further lysed by addition of 1% Triton-X100 and 30 min incubation on ice, and cell debris was removed by centrifugation. Recombinant Roquin proteins were then purified from the bacterial lysate using a HisTrap column (GE Healthcare) according to the instructions of the manufacturer. The eluted fractions containing the protein were combined and desalted via a PD10 gel filtration column (GE Healthcare). The proteins were kept in storage buffer (100 mM NaCl, 20 mM NaH_2PO_4, pH 7.5) and snap frozen in liquid nitrogen for storage at -80°C.

Full-length Roquin-1 was expressed from a construct containing an N-terminal His_6-tag and a C-terminal Strep-tag II in the *E. coli* strain Rosetta2 (DE3). The protein was purified using two consecutive affinity chromatography steps on a HiTrap chelating column (GE Healthcare) and a StrepTrap column (GE Healthcare). The purification buffer was 50 mM Tris-HCl pH 8.0, 300 mM NaCl and 0.01% (v/v) 1-thioglycerol. Full-length Roquin-1 protein was provided by Dr. Arie Geerlof, Helmholtz Zentrum München.

The minimal ROQ domain (Roquin-1 aa 147-326) was defined and purified as described (Schlundt et al. 2014). Protein samples for EMSA experiments were obtained from Dr. Andreas Schlundt, Helmholtz Zentrum München.

3.2.1.4 Monoclonal antibody production and coupling to magnetic beads

A new monoclonal antibody for immunoprecipitations (IPs) of Roquin-1 and Roquin-2 was produced in collaboration with Dr. Elisabeth Kremmer's group, Helmholtz

Zentrum München. To do so, a rat was immunized with N-terminal Roquin-1 and Roquin-2 proteins (aa 2-440 and aa 2-438 respectively), and hybridoma cells lines were generated from B cells of the spleen. By testing the antibody containing hybridoma supernatants first in ELISA (Enzyme-linked immunosorbent assay) and then in an IP screening procedure the antibody clone 18F8 was found to be highly efficient and specific in Roquin-1 and Roquin-2 IPs.

In-house produced monoclonal antibodies were purified from cell culture supernatants and coupled to tosyl-activated magnetic beads (Invitrogen) to achieve highly efficient IPs of endogenous Roquin proteins. For one coupling reaction, 4 mg of antibody were spin-concentrated (Centrifugal filter units) to a concentration of 2 mg/ml and combined with 50 mg magnetic beads in coating buffer according to the protocol provided with the beads. After completing the coupling protocol, the beads were stored in PBS (complemented with 0.1% BSA, 0.05% Tween-20, 0.02% sodium azide) at 4°C.

3.2.1.5 Immunoprecipitation, SDS-PAGE and immunoblotting

For protein analyses, MEFs and Th1 cells were harvested, washed once in PBS and lysed in lysis buffer (1 mM DTT and protease inhibitors added freshly), using three times the volume of the cell pellet. After 10 min incubation on ice and repeated mixing, the cell debris was removed by centrifugation (10,000 g, 10 min, 4°C), and the protein concentration of the lysate was determined using the Bio-Rad protein assay according to the manufacturer's instructions. For SDS-PAGE (SDS polyacrylamide gel electrophoresis), the lysate was complemented with 4x SDS sample buffer and boiled for 5 min at 95°C. Depending on the expression level of the protein of interest 30-80 µg of protein were loaded onto an SDS polyacrylamide gel (8% to 10% depending on the size of the protein of interest) and separated by electrophoresis at 120V for about 1 hour.

Immunoprecipitations were performed using cell lysates (2-5 mg of protein) and 50 µl of antibody-coupled tosyl-activated beads. After 4 hours of incubation on a mixing wheel at 4°C, the lysate was removed from the beads using a magnetic separator. The beads were washed 5x with lysis buffer and finally resuspended in a small volume of 1x SDS sample buffer for elution at 95°C. The samples were separated by SDS PAGE as described above.

For immunoblotting samples were transferred from the SDS polyacrylamide gel onto a PVDF membrane by tank blotting over night at 40 V and 4°C. Subsequently, the membrane was blocked using 5% nonfat dry milk in TBS for 1 hour at RT, followed by incubation in a dilution of the primary antibody to detect the protein of interest (2 hours RT for anti-tubulin or 2 hours 4°C and 1 hour RT for anti-Roquin 3F12). After three

10 min washing steps with 1% nonfat dry milk in TBS-T, the membrane was incubated in the corresponding HRP-coupled anti-IgG antibody solution for 1 hour at RT. Subsequently, the membrane was again washed three times (10 min each time), and protein bands were detected on an X-ray film using ECL substrate for the HRP to promote light emission.

3.2.2 RNA methods

3.2.2.1 *In vitro* transcription

For *in vitro* transcription of large (>500 nts) RNAs to be used in Electrophoretic mobility shift assays (EMSAs), the mMessage mMachine kit was used according to the protocol provided by the manufacturer. To do so, pDest17 plasmids containing *Ox40* fl or *Ox40* CDS (NM_011659) as inserts were linearized in a NotI restriction digest and purified by ethanol precipitation. The obtained DNA was used as template in the T7 RNA polymerase transcription reaction.

Short RNAs (20-180 nts) for EMSAs or filter binding assays (FBAs) were *in vitro* transcribed from DNA templates that had been generated in a PCR adding a T7 transcription start site to purchased DNA oligonucleotides. For the reaction, equimolar amounts of DNA template, NTPs (1.25 mM each), 10x reaction buffer, 17 mM $MgCl_2$ and an enzyme mix (2:1) of T7 RNA polymerase (Agilent technologies) and RNasin (Promega) were combined and incubated at 37°C for 4 hours. Radioactive labeling was achieved by adding α-^{32}P-UTP to the transcription reaction.

3.2.2.2 RNA purification and radioactive labeling

To purify total RNA from Th1 cell samples, cell pellets were resuspended in 1 ml TRI reagent solution (Ambion). Upon addition of 200 µl of chloroform, the aquaeous phase was separated by centrifugation (12,000 g, 15 min, 4°C) and collected in a fresh tube. After isopropanol precipitation in the presence of 1 µl glycogen, the RNA pellet was washed in 75% ethanol and finally resuspended in RNase-free water. RNA yield and purity were determined by spectrophotometer measurements using the NanoDrop device.

Radioactive labeling of purchased RNA oligonucleotides was performed using γ-^{32}P-ATP and the T4 Polynucleotide Kinase (PNK) in a forward reaction (30 min, 37°C). The mix contained 50 pmol RNA, 2 µl 10x reaction buffer (PNK buffer A), 20 pmol γ-^{32}P-ATP, 1 µl T4 PNK and RNase-free water to a final volume of 20 µl. To terminate

the reaction, 1 µl 0.5 M EDTA (pH 8.0) was added and the sample was incubated another 10 min at 70°C.

After the labeling reaction, RNAs were purified using the QIAquick nucleotide removal kit according to the instructions of the manufacturer. Assuming that no RNA was lost during the reaction and purification process, 50 µl of RNase-free water were used for elution to obtain a 1 µM RNA solution. The same purification procedure was applied to short RNAs from *in vitro* transcription reactions. For the purification of large RNAs after *in vitro* transcription (mMessage mMachine kit) the RNeasy® mini kit (Qiagen) was used according to the manufacturer's protocol. RNA yield and purity were measured with the NanoDrop device.

3.2.2.3 Reverse transcription and quantitative real-time PCR (qPCR)

Reverse transcription of total RNA to obtain cDNA for qPCR measurements was performed using the QuantiTect Reverse Transcription Kit (Qiagen) according to the provided protocol. Primer sequences and the respective probes used for the assays are given in **Table 9**.

For qPCR reactions, the Universal probe library was used together with the LightCycler 480 probes Master (both Roche Diagnostics) according the instructions of the manufacturer. The assays were run on a Light Cycler 480II equipped with the Light Cycler 480 SW 1.5 software. The qPCR primer design was performed with the help of the assay design software (ProbeFinder version 2.49 for Mouse) provided by Roche. All reactions were run in duplicates to control for technical errors, *Ywhaz* served as reference gene in Th1 cell samples, and the relative expression was calculated with the equation: *fold change=2^-(C_t(GOI)- C_t(RG))* (Ct: threshold cycle, GOI: Gene of interest, RG: reference gene). The C_t values were obtained from the Light Cycler 480 SW 1.5 software.

3.2.2.4 Filter binding assay (FBA)

To probe many different RNAs at the same time for protein binding, FBAs were performed as described (Vogel et al. 2013). In short, radioactively labeled RNA was employed in a binding reaction with recombinant Roquin-1 and Roquin-2 N-terminal protein for 30 min at 37°C in 20 mM HEPES, pH 7.4, 150 mM NaCl, 1 mM $MgCl_2$, 1 mM DTT and 1 µg/µl BSA. After the binding, the samples were applied onto nitrocellulose filters in a dot blot device, and after five washing steps, protein-bound RNA could be detected on the membrane using a phosphoimager screen. To calculate the relative retention, the same amount of labeled RNA as in a binding reaction was

spotted onto the membrane, and radioactive signals were quantified using the AIDA Image analyzer software.

FBAs with competitor RNA were performed as described above, yet with the addition of the respective amount of unlabeled competitor RNA (*ICOS* nts 600-700 or nts 700-800, NM_012092.3) to the binding reaction.

3.2.2.5 Electrophoretic mobility shift assays (EMSAs)

Depending on the size of the RNA being probed in an EMSA experiment, different approaches were used. Short RNAs (20-180 nts) were labeled with ^{32}P and gel shifts were investigated in acrylamide gels. Binding of Roquin to long RNAs (>500 nts) was visualized in agarose gels using ethidiumbromide.

Shift assays in agarose gels were conducted as published (Glasmacher et al. 2010) with slight modifications. The binding buffer contained 150 mM NaCl, 20 mM HEPES (pH 7.4), 1 mM $MgCl_2$ and 1 mM DTT. After binding of recombinant Roquin-1 and Roquin-2 N-terminal protein and RNA for 30 min on ice, glycerol was added to the sample to achieve a final concentration of 16%. The electrophoresis was performed in a 0.75% agarose gel in TBE buffer at 120 V for 1.5 hours. Subsequently, the gel was stained in an ethidiumbromide bath for 30 min, and the RNA bands were visualized on a UV transilluminator.

EMSAs with short ^{32}P-labeled RNAs were established on the basis of Leppek et al. and performed as published (Schlundt et al. 2014). The binding reaction containing 2.5 µg/µl tRNA from baker's yeast (Sigma), 1 pmol ^{32}P-labeled RNA, 20 mM HEPES (pH 7.4), 50 mM NaCl, 1 mM $MgCl_2$, 1 mM DTT, 1 µg/µl BSA and the indicated amount of recombinant protein was performed in a volume of 20 µl for 10 min at RT or for 20 min on ice. Subsequently, 4 µl 30% glycerol were added to load the samples onto a 6% polyacrylamide gel (5% glycerol, in 0.5x TBE) for PAGE (120 V, 40 min, RT) of the protein-RNA complexes. The gels were placed in fixing solution (20% methanol, 20% acetic acid) for 30 min before drying and exposing them to a phosphorimager screen.

The detected signals of the RNA were quantified using the AIDA Image Analyzer software. For calculation of the dissociation constant (K_d value), the bound fraction was normalized to the unbound fraction for each lane and plotted against the respective protein concentration. Using the Graphpad Prism software, a non-linear regression curve was fitted to the data points with the equation: $y=Bmax*x^h/(K_d^h+x^h)$ (*Bmax*: maximum specific binding, K_d: dissociation constant, *h*: Hill coefficient).

3.2.3 Cell biological methods

3.2.3.1 Calcium phosphate transfection and retrovirus production

The calcium phosphate transfection method was used to introduce retroviral expression plasmids (pMSCV-IRES-Thy1.1 or pKMV-IRES-GFP) and packaging plasmids into HEK293T cells for retrovirus production. In detail, production of ecotropic retroviruses required 50 µg expression plasmid DNA and 5 µg eco-pac packaging plasmid to transfect a 15 cm cell culture dish of HEK293T cells (60-80% confluent). For amphotropic retroviruses, 16 µg expression plasmid DNA, 4 µg gag-pol and 2 µg ampho-env packaging plasmids were used per 15 cm dish. To increase the transfection efficiency, HEK293T cells were treated with 100 µM chloroquine in DMEM (10% FCS, 100 U/ml penicillin/streptomycin and 10 mM HEPES) for 1 hour before adding the transfection mix containing plasmid DNA, $CaCl_2$ (125 mM) and HBS. 6-8 hours after transfection, the cells were provided with fresh DMEM (10% FCS, 100 U/ml penicillin/streptomycin and 10 mM HEPES). After 48 hours, the cell culture supernatant containing retrovirus particles was harvested, filtered through 0.45 µm-filter units and stored at -80°C.

3.2.3.2 Retrovirus infection of MEFs and primary T helper cells

Retroviral transduction of MEFs or primary $CD4^+$ T cells was achieved by spin infection protocols. The retrovirus containing supernatants were used either pure or in dilution and complemented with polybrene (MEFs: 5 µg/ml; T cells: 9 µg/ml) before applying them to the cells.

Best infection levels in MEFs were achieved with 30% confluent cells and spinning for 1 hour at 300 g and 32°C. After centrifugation, the virus remained on the cells for 6-8 hours and was then exchanged for fresh DMEM (10% FCS, 100 U/ml penicillin/streptomycin and 10 mM HEPES).

Infection of primary T helper cell cultures was performed 40 h after plate-bound anti-CD3/anti-CD28 activation of naïve $CD4^+$ T cells by adding the prepared undiluted retrovirus-containing supernatants to the attached cells. Spinning was performed for 1 hour at 820 g and 18°C, and the cells were rinsed from the plate and transferred to fresh T cell medium 6-8 hours after infection.

Expression levels of virus-encoded genes were determined 2-3 days after infection by immunoblotting or flow cytometry.

3.2.3.3 $CD4^+$ T cell isolation and Th1 cell culture

For primary Th1 cell cultures, $CD4^+$ T cells were isolated from spleen and lymph nodes of mice. To this end, the organs were collected and mashed through a 150 µm mesh to obtain a single-cell suspension. Upon erythrocyte lysis in TAC buffer (5 min on ice) and subsequent washing, the remaining leukocytes were filtered (fine mesh, 41 µm) and transferred to CD4 Dynabeads (Invitrogen) for selection of $CD4^+$ cells (30 min, 4°C) according to the protocol provided by the manufacturer. Specific elution of $CD4^+$ cells that were bound to the beads was achieved by incubating the beads in CD4 DETACHaBEAD solution (Invitrogen) for 1 hour at RT. To set up a Th1 cell culture, $CD4^+$ cells were seeded in T cell medium containing 0.1 µg/ml anti-CD3 and 1.0 µg/ml anti-CD28, 10 µg/ml anti-IL-4 and 10 ng/ml IL-12. For the first 48 hours, 5-6 million $CD4^+$ cells/ml were cultured on anti-hamster IgG coated 6-well plates. The anti-hamster IgG binds the anti-CD3 and anti-CD28 antibodies and thereby renders T cell activation more efficient. Subsequently, the activated Th1 cells were removed from the 6-well plate and further expanded in T cell medium with 20 U/ml IL-2 for 3-4 days at a concentration of 1 million cells/ml.

3.2.3.4 Cellular assay to monitor Ox40 regulation in response to Roquin-1 overexpression

To investigate the regulation of different *Ox40* expression constructs by Roquin-1, a *Rc3h1-2*$^{-/-}$ MEF cell line was stably transduced with a doxycyclin (Dox)-inducible Roquin-1-p2A-mCherry construct. These cells were retrovirally infected with *Ox40* constructs of different 3'UTR length or mutation, which led to the expression of Ox40 on the cell surface. 48 hours after infection, the cells were split, and one half of the cells was treated with doxycyclin (1 µg/ml) to induce expression of Roquin-1 and mCherry, connected via the self-cleaving peptide p2A. Thus, Roquin-expressing cells were marked by mCherry expression. 16-20 hours after induction, the cells were harvested, stained with APC-conjugated anti-Ox40 and analyzed by flow cytometry. To compare the Ox40 expression levels achieved by different constructs, the relative Ox40 mean fluorescence intensity (MFI) was determined by dividing the MFI of treated ($mCherry^+$) cells by the MFI of untreated ($mCherry^-$) cells.

3.2.3.5 Cellular assay to monitor target regulation in response to acute Rc3h1-2 deletion

To assess the post-transcriptional regulation of different target constructs mediated by endogenous Roquin-1 and Roquin-2 levels, an acute deletion assay was established in *Cre ERT2; Rc3h1-2*$^{fl/fl}$*; CAG-CAR*$^{stop\text{-}fl}$ MEFs. This transgenic cell line expresses a Cre

recombinase-ERT2 fusion protein that is translocated to the nucleus upon tamoxifentreatment. Thus, genomic deletion of *Rc3h1-2* alleles and of the STOP cassette proceeding *CAR* is achieved, which induces CAR surface expression. The cells were transduced with ecotropic retroviruses expressing *Ox40* and *ICOS* constructs and split 24 hours after infection to treat one half of the cells with tamoxifen (0.3 µM). After 2-4 days of tamoxifen treatment, the cells were stained and analyzed by flow cytometry. Thereby, the reporter expression of untreated (CAR^-) cells was compared to the reporter expression of treated (CAR^+) cells.

3.2.3.6 Cellular assays to monitor Roquin function

The function of the Roquin-1 and different Roquin-1 mutants (obtained by QuickChange mutagenesis) was studied in *Rc3h1-2*$^{-/-}$ MEFs as published (Schlundt et al. 2014). *ICOS* fl, *Ox40* fl or *ICOS* CDE_{260} expressing amphotropic retroviruses were used as reporters for Roquin-1 function. After primary infection with the reporter constructs, the cells were split and again spin-infected with different Roquin-1-expressing viruses or an empty virus as control. For the secondary infection, the viruses were titrated to achieve infection levels of 50-70%. Expression levels of the different Roquin-1 variants were checked by immunoblotting, using the 3F12 monoclonal antibody against Roquin-1 and Roquin-2 compared to anti-tubulin as loading control. 60 hours after the secondary infection, the expression of the infection markers GFP (primary infection) and Thy1.1 (secondary infection) as well as the expression level of the reporter ICOS or Ox40 was determined. To this end, the cells were stained with anti-mouse Thy1.1, anti-human ICOS or anti-mouse Ox40 antibodies and analyzed by flow cytometry. To compare different Roquin-1 variants, the relative MFI of $Thy1.1^+/Thy1.1^-$ cells was calculated.

3.2.4 Flow cytometry and cell sorting

3.2.4.1 Cell surface staining

MEFs were trypsinized prior to cell surface staining using antibodies diluted according to **Table 10** in FACS buffer (PBS, 2% FCS). After 20 min incubation at 4°C, the cells were washed and fixed in 2% formaldehyde in PBS for 15 min at RT. The cells were washed again and analyzed using the LSR Fortessa flow cytometer (BD Bioscience).

Splenocyte suspensions were prepared by mashing mouse spleens through a 150 µm mesh and performing TAC lysis (5 min on ice) followed by a washing step. Before staining, the cells were incubated with 10 µg/ml Fc-block in FACS buffer for 10 min on ice. The commercially available antibodies were diluted in FACS buffer (**Table 10**),

and cells were stained for 20 min on ice. Staining with the in-house produced anti-CXCR5 antibody (1:10 dilution in FACS buffer) was performed for 1 hour at RT and followed by stainings with anti-rat IgG-biotin and strepatividin-APC. The PBS57-loaded CD1d Tetramer to detect NKT cells was provided by the National Institute of Health and used in a 1:100 dilution. Shortly before analysis using the LSR Fortessa device, 10 µl of DAPI solution (5 mg/ml) were added to the sample for live/dead staining of the cells.

3.2.4.2 Intracellular stainings

Cell samples for intracellular staining were pre-incubated with fixable LIVE/DEAD® dye (Invitrogen, diluted 1:1000 in PBS) for 30 min on ice.

After Fc-block treatment and surface staining, the cells were fixed using 4% paraformaldehyde in PBS for 10 min at RT and permeabilized by washing with Saponin buffer. Thus, the cells were prepared for intracellular staining of Ctla4 using the respective antibody diluted 1:100 in FACS buffer (20 min, on ice).

Intracellular FoxP3 staining to identify peripheral Tregs required a specific fixing and permeabilization procedure using the Foxp3 Fixation/Permeabilization Concentrate and Diluent solutions (eBioscience). The solutions were used according to protocol provided by the supplier. In short, fixation (45 min, 4°C) and permeabilization (20 min, 4°C) were followed by FoxP3 staining (30 min 4°C, antibody diluted in permeabilization buffer). After washing, the cells were analyzed by flow cytometry.

3.2.4.3 Flow cytometry data analysis

Flow cytometry data was exported from the FACS Diva software and analyzed using FlowJo. The analysis of splenocytes from control mice (*CD4 Cre* or *Rc3h1-2*$^{fl/fl}$), Ox40 knockout mice (*Ox40*$^{-/-}$*; Rc3h1-2*$^{fl/fl}$), Roquin-1 and Roquin-2 double knockout mice (*Rc3h1-2*$^{fl/fl}$*; CD4 Cre*) and Roquin and Ox40 triple knockout mice (*Ox40*$^{-/-}$*; Rc3h1-2*$^{fl/fl}$*; CD4 Cre*) followed a standardized gating strategy (Vogel et al. 2013). As an example, gating for Tfh cells is given in **Figure 8**. For statistical analysis, cell frequencies were obtained from FlowJo and further evaluated using GraphPad prism.

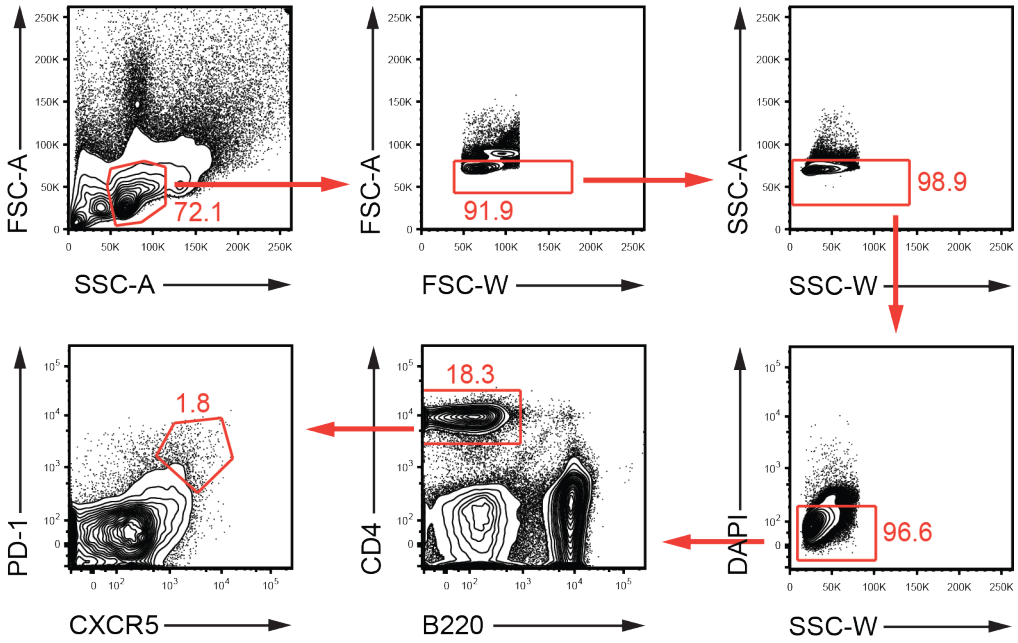

Figure 8: Gating strategy for Tfh cells using FlowJo. After choosing lymphocytes (FSC-A, SSC-A) for further analysis, doublet discrimination was accomplished and dead cells ($DAPI^{+}$) were excluded. Tfh cells were identified as PD-1^{hi} $CXCR5^{hi}$ subpopulation of $CD4^{+}$ T cells.

3.2.4.4 Cell sorting

For cell sorting, primary Th1 cells were harvested, and cell surface staining was performed as described (3.2.4.1). Using the FACS Aria III Cell Sorter (BD Bioscience), $Thy1.1^{+}$ CAR^{+} or $Thy1.1^{hi}$ cells were sorted for microarray experiments. The purity of the cell populations was checked by subsequent flow cytometric analysis.

3.2.5 Structural analysis

Methods concerning the crystal structure of the ROQ domain and the ROQ-*Tnf* CDE complex and NMR spectroscopy were performed by our collaborators Dr. Robert Janowski, PD Dr. Dierk Niessing's group and Dr. Andreas Schlundt, Prof. Dr. Michael Sattler's group (both Helmholtz Zentrum München). The work was published (Schlundt et al. 2014).

3.2.6 High throughput assays

3.2.6.1 Microarray analyses

For microarray analyses, primary Th1 cell cultures were set up from three *Rc3h1-2*$^{fl/fl}$*; CAG-CAR*$^{stop\text{-}fl}$ and three *Rc3h1-2*$^{+/+}$*; CAG-CAR*$^{stop\text{-}fl}$ mice as described in 3.2.3.3. 40 hours after T cell activation, the cells were transduced with Cre recombinase-expressing retrovirus to achieve acute deletion of *Rc3h1-2* accompanied by CAR upregulation. After expansion of the Th1 cell culture in T cell medium with IL-2, the cells were harvested, stained and sorted to purify Thy1.1^{+} CAR^{+} cells. For each sample 3 million sorted cells were obtained and resuspended in 1 ml TRI reagent for subsequent RNA purification. For a repeat of the experiment in animals lacking Icos, three *Icos*$^{-/-}$*; Rc3h1-2*$^{fl/fl}$ and three *Icos*$^{-/-}$*; Rc3h1-2*$^{+/+}$ mice were used. Due to the lack of the *CAG-CAR*$^{stop\text{-}fl}$ allele in these mice, Thy1.1^{hi} cells (highest 25%) were sorted from the Th1 cultures upon Cre-mediated deletion of *Rc3h1-2*.

RNA purification, quality check and processing of microarrays (GeneChip Mouse Gene 1.0 ST Arrays, Affymetrix) using the respective reagents (WT Expression Kit, Ambion and GeneChip WT Terminal Labeling and Controls Kit, Affymetrix) was performed by Andrea Klanner from Dr. Helmut Blum's group (Genzentrum, München).

The bioinformatics data analysis was kindly performed by Dr. Dirk Repsilber (University of Örebro) based on Storey & Tibshirani, 2003. In short, he selected genes that show significant (q<0.05; the q-value is the false discovery rate analogue of the p-value) differential expression in WT (*Rc3h1-2*$^{+/+}$) compared to Roquin knockout (*Rc3h1-2*$^{fl/fl}$) samples. Among these, genes with a fold change ≥1.5 were considered to be potential Roquin targets. To present the data in a heatmap he normalized the values according to Smyth & Speed 2003.

3.2.6.2 CLIP and PAR-CLIP assays

For cross-linking and immunoprecipitation (CLIP) and photoactivatable ribonucleoside-enhanced CLIP (PAR-CLIP) assays (Ule et al. 2003; Hafner et al. 2010) (**Figure 9**), primary Th1 cell cultures from C57BL/6J mice were prepared according to 3.2.3.3 at the Biozentrum, Basel. 4 days after T cell activation, the cells were harvested, washed in PBS and irradiated with UV light. Half of the Th1 cells were treated with 100 µM 4-thiouridine (4SU) 24 hours prior to UV cross-linking with 2x 0.15 J/cm^2 and 365 nm (PAR-CLIP samples). The other half of the cells was irradiated with 254 nm UV light and 3x 0.1 J/cm^2 (CLIP samples).

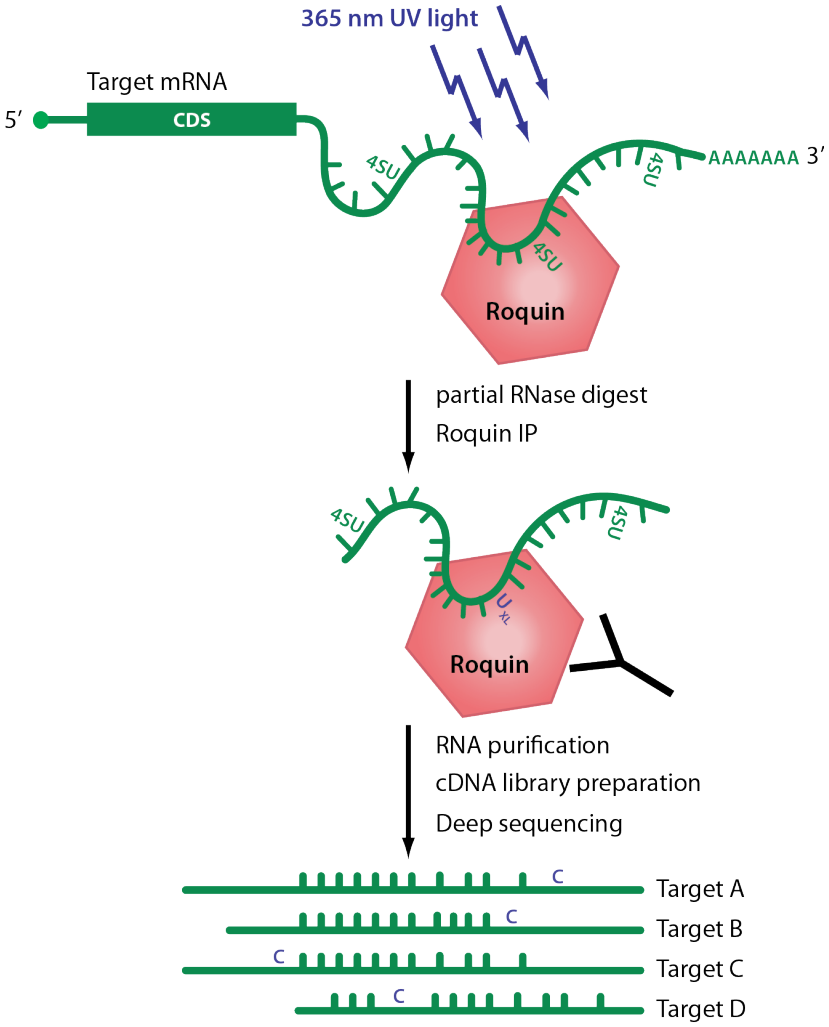

Figure 9: Schematic representation of the PAR-CLIP procedure. After incorporation of 4-thiouridine (4SU), the protein-RNA interactions were cross-linked by UV irradiation of the cells. Following cell lysis and partial RNase digest, protein-RNA complexes were immunoprecipitated and RNA fragments were purified for Illumina Solexa sequencing.

The assays were performed together with Georges Martin, Prof. Dr. Mihaela Zavolan's group (Biozentrum, Basel). 3F12 and 18F8 monoclonal antibodies coupled to tosyl-activated magnetic beads (3.2.1.4) were used for Roquin-specific assays. A commercial anti-Ago2 antibody (Wako) bound in PN8 buffer to magnetic beads via protein G (20 µg antibody per 10 µl magnetic beads) served as control. Th1 cell lysates were prepared using PNDS lysis buffer complemented with protease inhibitors, Turbo-DNase (1:500), RNasin (10 µl/ml), DTT (1mM) and 1 µl RNase T1 (1:20 dilution). The cleared lysate was combined with magnetic antibody beads for IP (3 hours, 4°C, rotating). Subsequently, the beads were washed once with high salt buffer (5x PNDS buffer) and twice with PNDS buffer. RNase T1 was diluted 1:1000 in PNDS buffer for on-beads RNA digestion (15 min, 22°C), followed immediately by high salt and Mg washing steps. Next, the RNA in the complexes was dephosphorylated (20 min, 37°C, FastAP,

Fermentas), washed (Mg wash and EGTA wash), and 3' adapter (5'-P-uggaauucucgggugccaagg-block) ligation was performed at 16°C over night using the T4 RNA ligase (Fermentas). On the next day, the beads were washed (5x PNDS, 3x Mg wash), the bound RNA was labeled with ^{32}P, and after elution into NOVEX loading buffer the samples were separated by SDS PAGE.

After blotting the protein-RNA complexes onto a nitrocellulose membrane, they were visualized using a phosphorimager. Bands corresponding to the size of the investigated proteins and up to 30 kDa higher were excised from the membrane and RNA fragments were eluted by Proteinase K digestion (4 mg/ml in 200 µl PK digestion buffer, 30 min, 37°C). Upon addition of 200 µl 7 M urea, incubation (30 min, 55°C) and addition of 50 µl 3 M sodium acetate, phenol-chloroform extraction was performed twice. By ethanol precipitation (30 min, -20°C), the RNA was purified and ligation of the PAGE-purified 5' adapter (5'-OH-guucagaguucuacaguccgacgauc-OH) was performed (over night, 4°C). The obtained RNA fragments were separated on a 10% TBE/Urea gel, and the gel pieces corresponding to 70-100 nts were excised. To extract the RNA from the gel pieces, they were incubated in 350 µl RNA elution buffer for 1 hour at 37°C. After that, the supernatant was mixed with ethanol for RNA precipitation and purification.

Finally, the RNA was reverse transcribed (Superscript III reverse transcriptase, 45 min, 42°C) into cDNA, which served as template for barcoding PCRs and thus preparation of the cDNA library. To reduce adapter-adapter sequences, the samples were size fractionated on an agarose gel. DNA fragments between 130 and 170 nts of length were purified and applied to IlluminaSolexa sequencing analysis. The sequencing data was first processed automatically via the Clipz database (Khorshid et al. 2011). Dr. Andreas Gruber from Prof. Mihaela Zavonlan's group (Biozentrum, Basel) performed further analyses.

3.2.6.3 SELEX

Selection of Roquin-bound RNAs from a random RNA library was performed in collaboration with Dr. Raymund Buhmann's group (Clinical Cooperative Group, Helmholtz Zentrum München). Dr. Michael Blank provided the protocol and suggested to perform three rounds of selection with extending washing procedures (3x 100 µl, 4x 100 µl and 5x 100 µl washing steps) and decreasing protein concentration (250 nM, 150 nM and 50 nM) to increase stringency.

Prior to selection, 100 µg recombinant Roquin-1 and Roquin-1 M199R N-terminal protein (N-term) (aa 2-440) were incubated for 30 min on ice with 10x molar excess of EZ-link PEG4-NHS-Biotin (Pierce) resolved in PBS (0.1 mg/ml). Subsequently, the biotinylated protein was purified via gel filtration (MicroSpin column P6, BioRad).

Since precipitation was observed, the loss of protein during the biotinylation procedure was estimated on an SDS gel by Coomassie staining. To prove the efficiency of the biotinylation reaction, three concentrations of biotinylated and non-biotinylated protein were spotted onto a nitrocellulose membrane. After blocking the membrane with 1% BSA in PBS, it was incubated in streptavidin-PE (R-Phycoerythrin) diluted 1:1000 in PBS for 30 min at RT. Subsequently, the membrane was washed 3x with PBS and fluorescence intensity of PE bound to biotinylated protein was determined by fluoroimaging (Raytest, FLA5000, 473 nm, Y510 filter).

The RNA startpool with a 47 nts random sequence was *in vitro* transcribed from double-stranded random DNA according to Chang et al. (Chang et al. 2010) using common NTPs. Following the transcription reaction, the samples were mixed with PAA-loading buffer and fractionated via denaturing PAGE (8%). RNA containing gel pieces were excised and RNA was purified.

Every round of selection started by combining the RNA pool (400 pmol) with biotinylated protein and incubating the mix for 30 min at 37°C. Subsequently, binding buffer-equilibrated streptavidin-magnetic beads were added, incubated (10 min, 37°C) to bind the protein-RNA complexes and washed. By boiling the beads in 0.2 mM EDTA in H_2O for 3 min, protein and RNA molecules were released. After removal of the beads, the solution served as template for reverse transcription (One-Step RT-PCR Kit, Qia-gen), and from the obtained cDNA the RNA pool for the next round of selection was transcribed.

The cDNAs from every selection round (startpool, round 1, round 2, round 3) were finally used for Index-PCRs to analyze the pool composition at every stage during selection. Comparable amounts of the PCR products were combined to one cDNA library and analyzed by Solexa Illumina sequencing. Dr. Michael Blank and Dr. Carsten Gröber (both AptaIT) performed the processing of the raw data, tested sequence statistics and identified enriched sequences in the third round of selection. Further analyses concerning motif search within enriched sequence patterns (hexamers) and structural implications were provided by Dr. Andreas Gruber, Prof. Dr. Mihaela Zavolan's group (Biozentrum, Basel).

4 Results

4.1 Identification of mRNAs targeted by Roquin

Roquin binding to target mRNAs results in a decreased protein expression of the target as well as in a reduction of the mRNA levels. Although Roquin presumably targets a number of mRNAs, only few have been identified or characterized in detail to date. In this study, different methods that approach the protein-RNA interaction and its effect on different levels were used to identify new target mRNAs. Since Roquin function in T cells has been described in detail and the M199R mutant of Roquin-1 had a strong impact on T helper cells (Vinuesa et al. 2005), all assays were performed in primary murine T helper cells to identify T-cell-specific target candidates.

The use of mRNA expression arrays allows the detection of mRNAs that show a high dynamic range in response to varying Roquin activity. Target candidates identified with this method are therefore supposed to also show a strong response to Roquin regulation on the protein level. However, there is no prove that Roquin directly binds these mRNAs and that their regulation is not due to secondary effects. This disadvantage can be overcome with immunoprecipitation (IP)-based methods. CLIP and PAR-CLIP assays are useful to identify mRNAs that are directly bound by Roquin within the T helper cells, but they do not give any information about the downstream effects of this binding. Combining both approaches was expected to yield the most comprehensive list of mRNA candidates targeted by Roquin in T helper cells.

4.1.1 Microarray analyses of Th1 cells upon acute deletion of *Rc3h1-2*

The strongest upregulation of the known Roquin target Icos and its mRNA was observed in T cells that completely lack Roquin-1 and Roquin-2 proteins (Vogel et al. 2013). $CD4^+$ T cells isolated from *Rc3h1-2*$^{fl/fl}$*; CD4 Cre* mice were strongly activated (Vogel et al. 2013) and therefore not comparable to the mainly naïve $CD4^+$ T cells from control mice. Thus, an *in vitro* deletion system using a Cre recombinase expressing retrovirus was established. The *CAG-CAR*$^{stop\text{-}fl}$ allele was introduced into *Rc3h1-2*$^{fl/fl}$ mice to monitor the deletion efficiency. This was indicated by upregulation of the coxsackievirus and adenovirus receptor (CAR) as a result of Cre-mediated deletion of the stop cassette. RNA from Th1 cells upon acute deletion of Roquin was compared to control Th1 cells in mRNA expression array analyses.

4.1.1.1 Evaluation of the acute Roquin deletion in Th1 cells

To identify the best time point for cell harvesting and RNA isolation, a time course experiment was performed (**Figure 10**). Purified $CD4^+$ T cells from *Rc3h1-2$^{fl/fl}$; CAG-CAR$^{stop\text{-}fl}$* mice and *Rc3h1-2$^{+/+}$; CAG-CAR$^{stop\text{-}fl}$* control mice were activated by CD3 and CD28 stimulation in Th1 polarizing T cell medium. 40 hours after activation, the cells were spin infected with a Cre recombinase-expressing retrovirus that also encoded Thy1.1 as infection marker. Eight hours after infection (48 hours after activation), the cells began to express Thy1.1 on their cell surface showing a transduction efficiency of 70% (**Figure 10A**). An additional expression of CAR, demonstrating the ongoing Cre-mediated deletion, was observed 72 hours after activation and further increased until 144 hours after activation (**Figure 10A**). In parallel to observing deletion through CAR upregulation, cells were harvested at every time point and Roquin levels were investigated by immunoblotting (**Figure 10B**). Roquin levels were comparable for *Rc3h1-2$^{+/+}$*and *Rc3h1-2$^{fl/fl}$* cells during the first 72 hours after activation. Subsequently, a reduction of Roquin-1 and Roquin-2 proteins in the *Rc3h1-2$^{fl/fl}$* cells was observed. Since only 50-60% of the cells used for immunoblotting were CAR^+, it was assumed that the $Thy1.1^+$ CAR^+ population would show an even more prominent loss of Roquin. In addition to the virus infection and the Roquin levels, the abundance of Icos as representative target was monitored. Icos surface staining and flow cytometry gave an insight into the protein expression (**Figure 10C**), whereas the results of qPCR measurements reflected the changes on the mRNA level (**Figure 10D**). The mean fluorescence intensity (MFI) of Icos on the cell surface of $Thy1.1^+$ CAR^+ *Rc3h1-2$^{fl/fl}$* cells continuously increased compared to *Rc3h1-2$^{+/+}$* cells and reached an eightfold higher expression (**Figure 10C**). On the mRNA level the differences only became obvious after 120 hours, when *Icos* expression was almost fourfold higher in *Rc3h1-2$^{fl/fl}$* versus *Rc3h1-2$^{+/+}$* cells (**Figure 10D**). Taken together, the time course experiment suggested to use Th1 cells 120 hours after activation for the array experiment, since that was the earliest time point to observe differential expression of an mRNA targeted by Roquin.

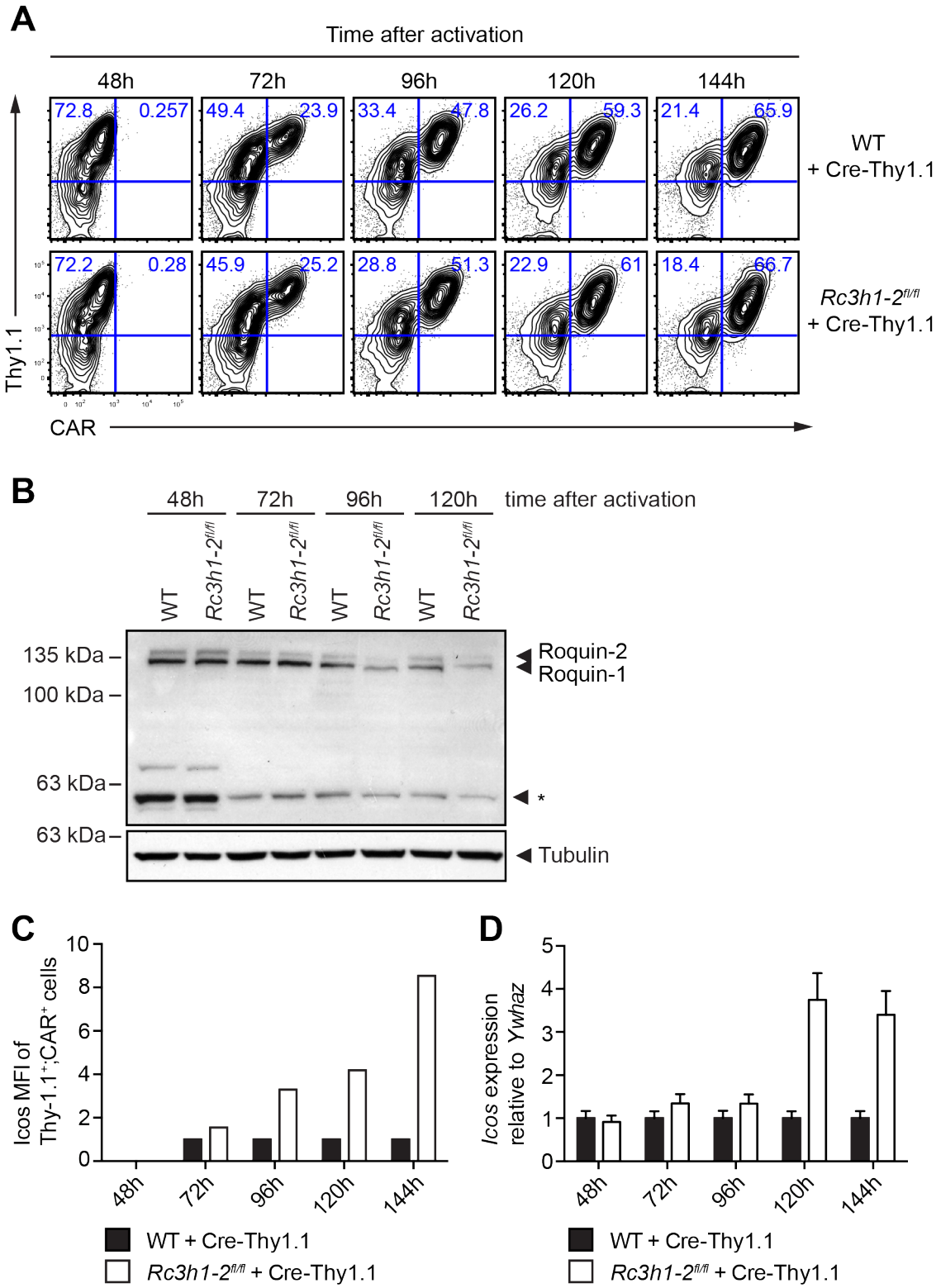

Figure 10: Evaluation of the acute Roquin deletion in Th1 cells. After activation, Th1 differentiation and infection with a Cre recombinase expressing retrovirus (40 hours after activation), $CD4^+$ T cells were analyzed in a time course experiment (h: hours). **A** Thy1.1 and CAR were gradually upregulated after retrovirus infection as assessed by flow cytometry. **B** Deletion of *Rc3h1-2* resulted in reduced Roquin protein expression 96 hours after T cell activation as shown by immunoblotting. The band marked with an asterisk was derived from a Roquin degradation product. Tubulin detection served as loading control. **C** and **D** Upon Roquin deletion, Icos was increased on the protein level as assessed by flow cytometry (**C**) and on the mRNA level as determined by qPCR (**D**).

4.1.1.2 Sample preparation for mRNA expression arrays

Thy1.1^{+} CAR^{+} cells were purified by cell sorting for the final experiment to reduce background signals from inefficiently infected cells. The affymetrix mRNA expression arrays were run in triplicates using one mouse per array. The three samples showed very similar infection rates (**Figure 11A**), deletion efficiency (**Figure 11A and B**), and the upregulation of Icos on the surface of Thy1.1^{+} CAR^{+} *Rc3h1-2$^{fl/fl}$* cells was also highly comparable (**Figure 11C**). Cell sorting resulted in 97% purity of Thy1.1^{+} CAR^{+} cells that were subsequently collected in TRI reagent solution for RNA preparation (**Figure 11D**).

To exclude candidates that were only regulated in response to the strong Icos upregulation upon Roquin deletion, the array experiment was repeated on an *Icos$^{-/-}$* genetic background. Since *Icos$^{-/-}$* and *Icos$^{-/-}$; Rc3h1-2$^{fl/fl}$* mice did not carry the *CAG-CAR$^{stop\text{-}fl}$* allele, cell sorting had to be performed on the 25% percent cells with the highest Thy1.1 levels (**Figure 12**). Those cells are supposed to have high deletion efficiencies, since there were no CAR^{-} Thy1.1^{high} cells present in the first set of samples (**Figure 11A**).

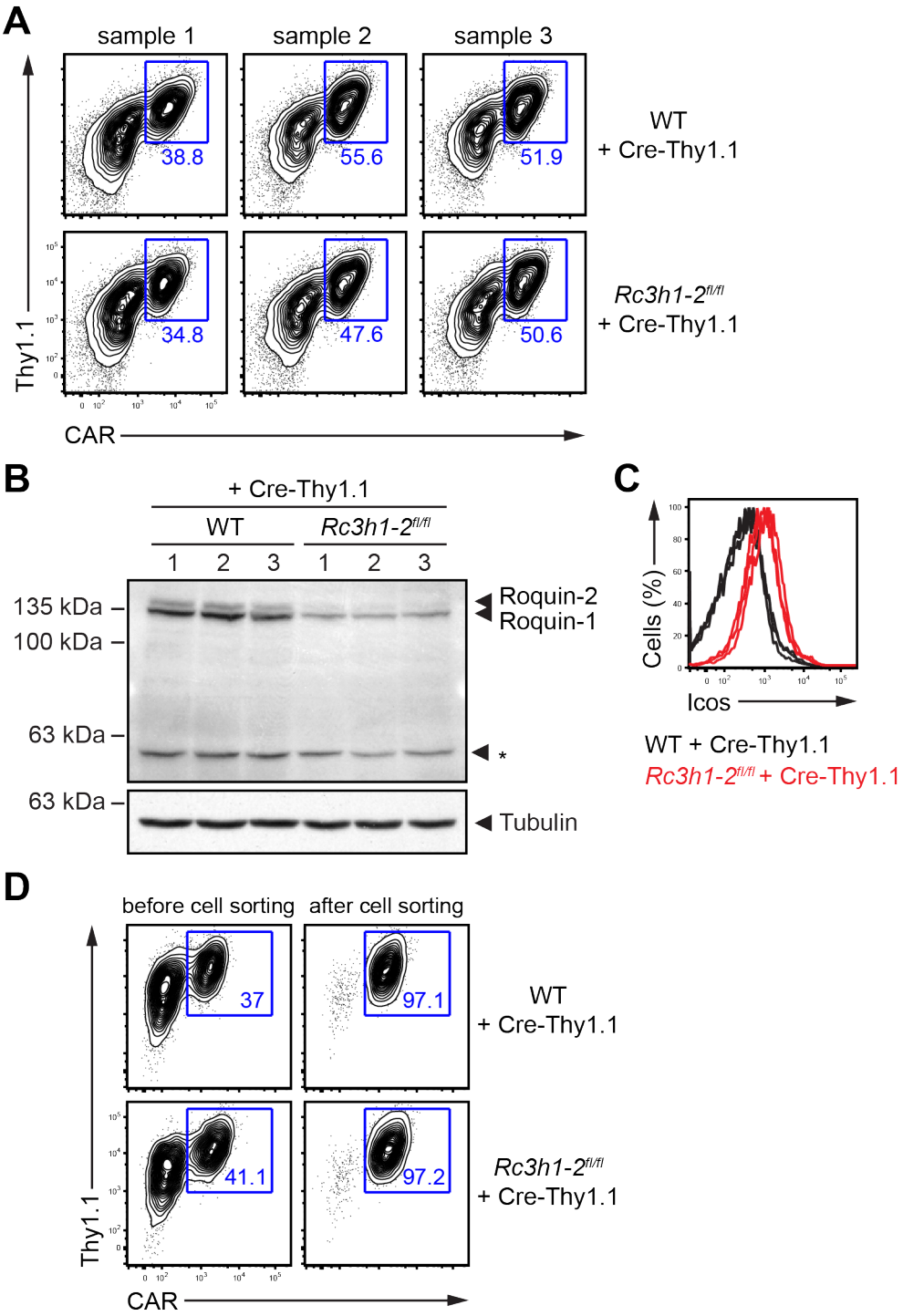

Figure 11: Sample preparation for mRNA expression arrays. $CD4^+$ T cells from three mice for each condition were cultured under Th1 conditions and infected with Cre recombinase-expressing retrovirus. **A** 120 hours after activation, all samples showed comparable Thy1.1 and CAR expression levels in flow cytometry measurement. **B** Immunoblotting analysis of Roquin expression in the treated cells 120 hours after activation. Tubulin detection served as loading control. **C** Flow cytometric measurement of Icos surface expression on $Thy1.1^+$ CAR^+ cells. **D** Representative dot plots of cell samples before and after cell sorting.

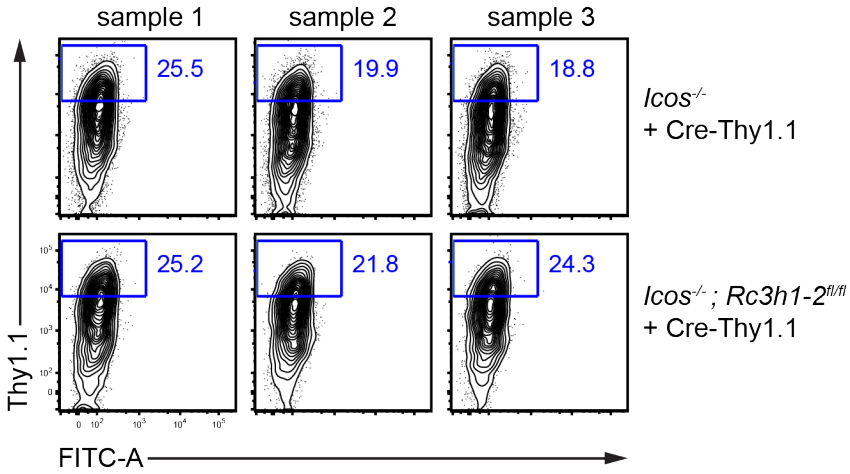

Figure 12: Preparation of *Icos*$^{-/-}$ samples for the second array experiment. CD4^{+} T cells from three mice of each genotype (*Icos*$^{-/-}$ and *Icos*$^{-/-}$*; Rc3h1-2*$^{fl/fl}$) were cultured under Th1 conditions and transduced with Cre-Thy1.1 retrovirus. After 120 hours of cell culture, Thy1.1 levels were analyzed by flow cytometry. The blue gates indicate the proportion of cells purified by cell sorting.

4.1.1.3 Microarray hybridization and data analysis

Next, the samples obtained by cell sorting of Th1 cell cultures (**Figure 11 and Figure 12**) were handed over to the microarray hybridization facility of the Gene Center Munich. Andrea Klanner, Dr. Helmut Blum's group, conducted the RNA preparation and the microarray procedure, and the overall quality of the array performance was irreproachable. The raw data was transferred to Dr. Dirk Repsilber (University of Örebro) who performed the bioinformatics data analysis. In short, he selected for mRNAs that were at least 1.5-fold up- or down-regulated in *Rc3h1-2*$^{fl/fl}$ versus *Rc3h1-2*$^{+/+}$ samples. In the first set of arrays, 84 mRNAs were at least 1.5-fold, 17 mRNAs at least 2.0-fold and 5 mRNAs at least 3.0-fold upregulated. 45 of these mRNAs were also found to be upregulated 1.5-fold or more in the *Icos*$^{-/-}$ arrays upon Roquin deletion (**Table 20**). The heatmap in **Figure 13** gives an overview of the obtained data. The dendrogram on top of the graph is the result of a clustering analysis showing that the triplicates are indeed most similar in their expression patterns for all samples. Also, the diagram shows that in cells with Roquin deletion (*Rc3h1-2*$^{fl/fl}$ and *Icos*$^{-/-}$*; Rc3h1-2*$^{fl/fl}$) the majority of differentially expressed mRNAs is upregulated (blue), whereas only few mRNAs are downregulated (yellow). Thus, derepression of mRNAs was the main effect of Roquin deletion. This is also underlined by the fact that upregulation of mRNAs is much more reproducible than downregulation in the *Icos*$^{-/-}$ samples.

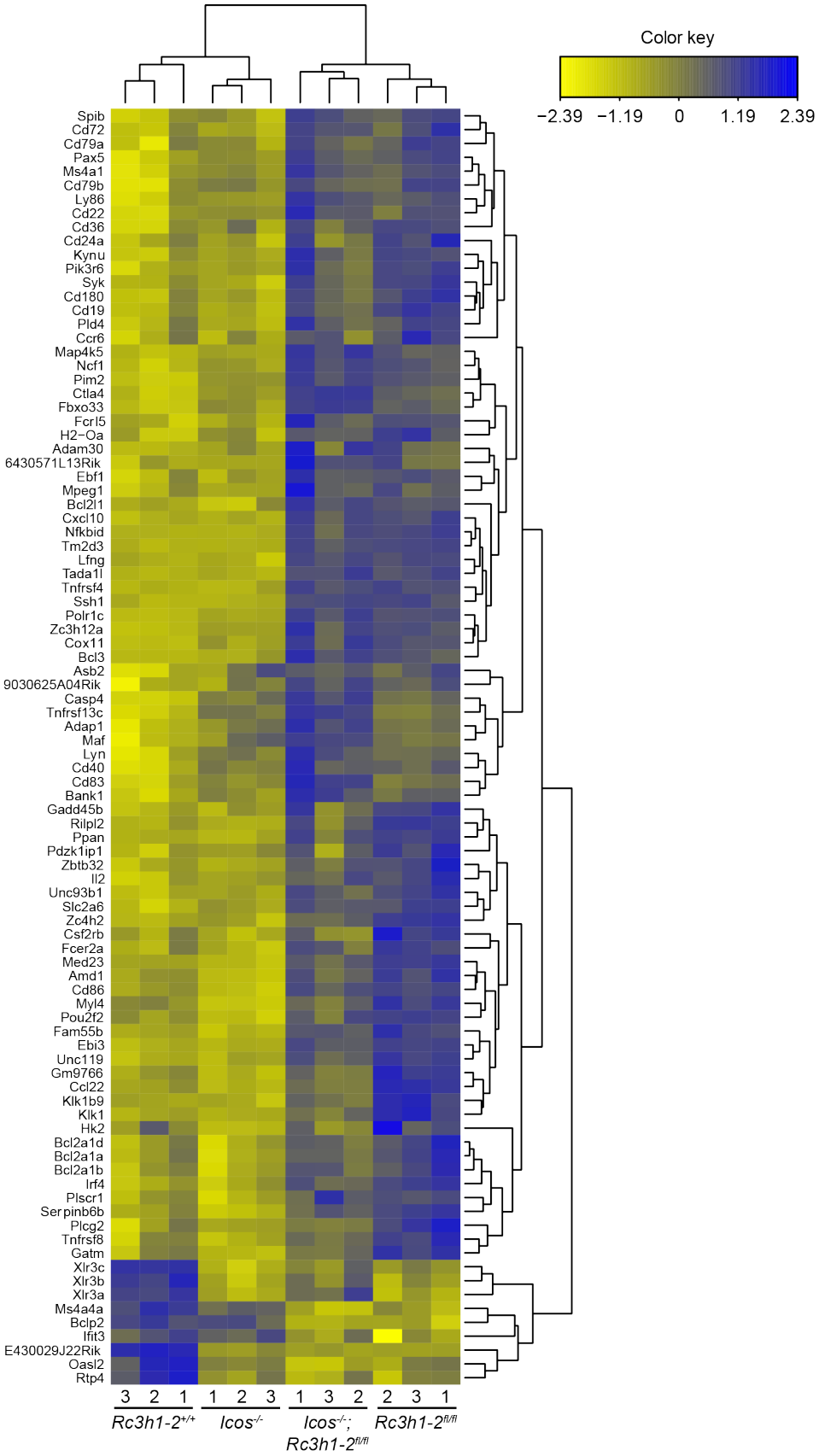

Figure 13: Heatmap showing relative expression of Roquin target candidates. Listed are genes with a significant (q≤0.05) fold change of ±1.5 or more normalized to their mean expression. Blue indicates relative upregulation and yellow downregulation of gene expression. The dendrograms are derived from a hierarchical cluster analyses. This analysis was provided by Dr. Dirk Repsilber.

Table 20: Potential Roquin targets with ≥1.5-fold expression in the first set of arrays and their fold change in *Icos*$^{-/-}$ validation arrays. Dark turquoise: fold change ≥ 3, turquoise: fold change ≥ 2, light turquoise: fold change ≥ 1.5. The known target *Icos* is highlighted in red.

Gene	fold change	*Icos*$^{-/-}$ array
Ccl22	5.0	2.3
Ebi3	4.2	3.0
Pim2	3.1	2.3
Cxcl10	3.1	2.6
Il2	3.0	1.7
Tnfrsf8 (CD30)	2.9	2.0
Nfkbid	2.8	2.4
Zbtb32	2.6	1.7
Cd86	2.5	3.0
Ppan	2.5	2.0
Cd19	2.4	1.8
Zc3h12a	2.3	1.8
Tm2d3	2.3	2.0
Polr1c	2.2	2.1
Cd180	2.1	1.6
Kynu	2.1	1.6
Ms4a1	2.1	1.5
Tnfrsf4 (Ox40)	2.1	2.3
Ly86	2.1	1.8
Ctla4	2.1	2.3
Icos	2.0	
Cd24a	2.0	1.4
Ncf1	1.9	1.7
Unc119	1.9	1.5
Maf	1.9	1.4
Hk2	1.8	1.6
Spib	1.8	1.6
Cd79b	1.8	1.2

Gene	fold change	*Icos*$^{-/-}$ array
Fcer2a	1.8	1.6
Pax5	1.8	1.3
Cd36	1.8	
Asb2	1.8	
Pou2f2	1.8	1.9
Syk	1.8	1.5
Bcl3	1.8	1.9
Gadd45b	1.7	1.3
Gatm	1.7	1.5
Rilpl2	1.7	1.4
Cd72	1.7	1.7
Myl4	1.7	1.8
Gm9766	1.7	1.4
Lyn	1.7	1.3
Cd79a	1.7	1.3
Fbxo33	1.7	1.6
Casp4	1.7	1.3
9030625A04Rik	1.6	1.3
6430571L13Rik	1.6	1.9
Ebf1	1.6	1.5
Map4k5	1.6	1.6
Cd22	1.6	1.4
Med23	1.6	1.5
Bcl2a1a	1.6	1.5
Plcg2	1.6	1.2
Tada1l	1.6	1.6
Csf2rb	1.6	1.2
Bcl2l1	1.6	1.8

Gene	fold change	*Icos*$^{-/-}$ array
Tnfrsf13c (Baffr)	1.6	1.4
Bcl2a1d	1.6	1.5
Zc4h2	1.6	1.3
Mpeg1	1.6	1.6
Slc2a6	1.6	1.3
Serpinb6b	1.6	1.6
Irf4	1.6	1.4
Ccr6	1.6	1.3
Lfng	1.6	1.8
Plscr1	1.6	1.7
Cd83	1.6	1.6
Cox11	1.6	1.4
Adap1	1.5	1.4
Cd40	1.5	1.2
Bank1	1.5	1.4
Fcrl5	1.5	1.4
H2-Oa	1.5	1.2
Unc93b1	1.5	1.3
Klk1b9	1.5	1.3
Ssh1	1.5	1.5
Pik3r6	1.5	1.3
Pld4	1.5	1.5
Bcl2a1b	1.5	1.5
Adam30	1.5	1.4
Amd1	1.5	1.5
Pdzk1ip1	1.5	
Klk1	1.5	1.4
Fam55b	1.5	1.4

Taking a more detailed look at the mRNAs that were significantly upregulated in Th1 cells after Roquin deletion revealed that several groups of genes are represented. Interestingly, among the potential target mRNAs there are three activation-induced co-stimulatory receptors. Ox40 (Tnfrsf4) and CD30 (Tnfrsf8), members of the Tnf receptor super family, are stimulatory co-receptors that support cytokine production and

expansion of T cells (Watts 2005). In contrast, Ctla4 is an inhibitory co-receptor upregulated in the late stage of T cell activation. Another group of genes possibly targeted by Roquin are members of the Bcl-2 protein family (*Bcl2a1a*, *Bcl2a1b*, *Bcl2a1d* and *Bcl2l1*), known to be negative regulators of apoptosis in the mitochondrial pathway. Furthermore, a number of cytokines and chemokines (for example *Ccl22*, *Ebi3*, *Cxcl10* and *Il2*) and T cell activation associated genes (for example *Nfkbid*, *Cd24a*, *Bcl3* and *Tnfrsf13c*) were upregulated upon Roquin deletion in T cells. Unexpectedly, also the expression of several B cell specific genes, such as *Cd86*, *Cd19* and *Cd40*, was increased in this setting.

The array data was evaluated by qPCR measurements of selected target candidates in the RNA samples (**Figure 14**). All tested candidates were confirmed yielding a higher fold change than measured in the arrays. Also, the qPCR data showed that most of the candidates are upregulated in an Icos-independent manner. Only *Ctla4* exhibited a weaker deregulation upon Roquin deletion in the *Icos*$^{-/-}$ sample indicating that high Icos levels contribute to the deregulation of *Ctla4* (**Figure 14**). In summary, the microarray analyses identified an interesting set of putative target mRNAs that can be further validated to decipher their role in Roquin-mediated regulation. However, due to time constraints and previous experiments with this candidate, further investigations in this study were focused on the costimulatory receptor Ox40.

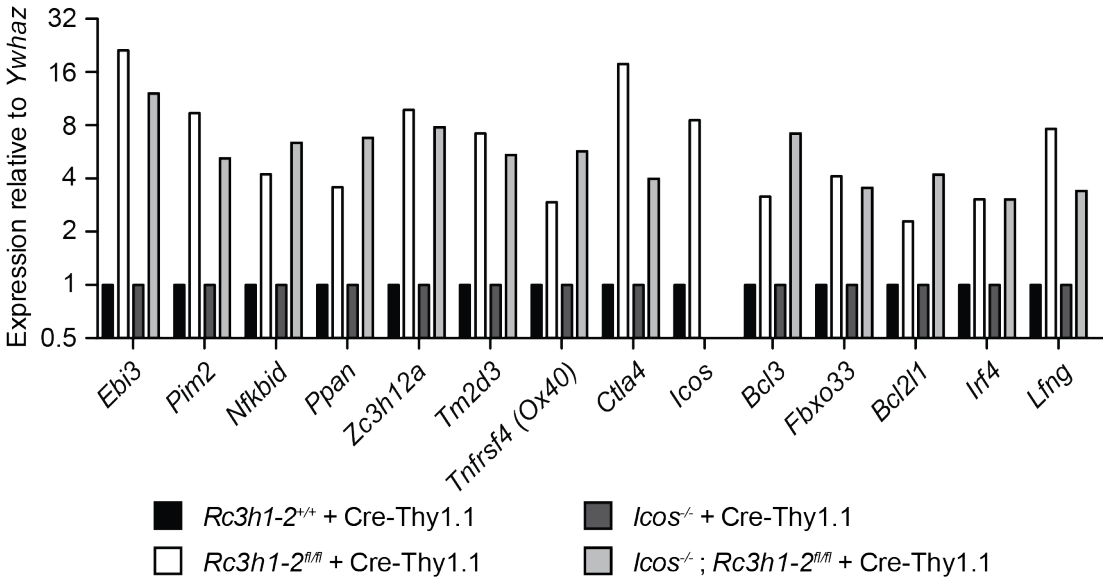

Figure 14: Evaluation of Roquin target candidates by qPCR. The expression of potential Roquin target mRNAs relative to *Ywhaz* is shown normalized to the respective control sample. Black and white bars represent samples from the first set of arrays and the grey bars are derived from measurements of *Icos*$^{-/-}$ samples.

4.1.2 The mRNA of the costimulatory receptor Ox40 is bound and regulated by Roquin

Due to its functional overlap with Icos, Ox40 is a particularly interesting target candidate of Roquin. Therefore, it was investigated whether *Ox40* mRNA is directly bound by Roquin and if this interaction results in a regulation of Ox40 expression.

Analyzing $CD4^+$ T cells from *Rc3h1-2$^{fl/fl}$; CD4 Cre* mice compared to control animals revealed that the lack of Roquin indeed resulted in increased Ox40 expression (**Figure 15A**). Even though this costimulatory receptor is only induced upon T cell activation (Mallett et al. 1990; al-Shamkhani et al. 1996), low expression was observed on naïve ($CD62L^{hi}$ $CD44^{lo}$) $CD4^+$ T cells of *Rc3h1-2$^{fl/fl}$; CD4 Cre* mice. In effector-like ($CD62L^{lo}$ $CD44^{hi}$) $CD4^+$ T cells lacking Roquin, the upregulation of Ox40 was even more prominent. To exclude that high Ox40 levels resulted from the excessive T cell activation in Roquin knockout mice, a cell culture assay was established to monitor Roquin function. To this end, a Roquin-1-p2A-mCherry-inducible *Rc3h1-2$^{-/-}$* MEF cell line was transduced with ecotropic retroviruses expressing *Ox40* fl or *Ox40* CDS. Subsequently, the Ox40 surface expression in response to doxycyclin (Dox)-induced Roquin-1 overexpression was determined by flow cytometry (**Figure 15B**). Whereas expression from the *Ox40* CDS barely changed after doxycyclin treatment, Ox40 expression from the full-length construct was strongly reduced in Roquin-1-p2A-mCherry-expressing cells. This indicated that Ox40 is post-transcriptionally regulated by Roquin-1 via its 3'UTR.

Next, the specificity of the Roquin-*Ox40* 3'UTR interaction was investigated on the molecular level. In a filter binding assay (FBA), recombinant Roquin N-terminal proteins (Roquin-1 aa 2-440 and Roquin-2 aa 2-438) were used for binding reactions with ^{32}P-labeled *Ox40* 3'UTR and unlabeled competitor RNAs comprising 100 nts of the *ICOS* 3'UTR (**Figure 15C and D**). The specific competitor (*ICOS*, nts 700-800) clearly reduced *Ox40* 3'UTR binding with increasing molar excess, whereas an unspecific competitor RNA (*ICOS*, nts 600-700) only had minor effects. Roquin-2 (aa 2-438) seemed to bind the *Ox40* 3'UTR with higher affinity than Roquin-1 (aa 2-440), since the same amount of competitor RNA did not reduce binding of Roquin-2 to the same extent as binding of Roquin-1. The combination of methods to analyze Roquin-mediated post-transcriptional regulation on different levels, such as measuring target protein expression in response to Roquin-1 overexpression and *in vitro* binding assays to detect the direct interaction of protein and RNA, proved that *Ox40* is a direct mRNA target of Roquin-1 and Roquin-2.

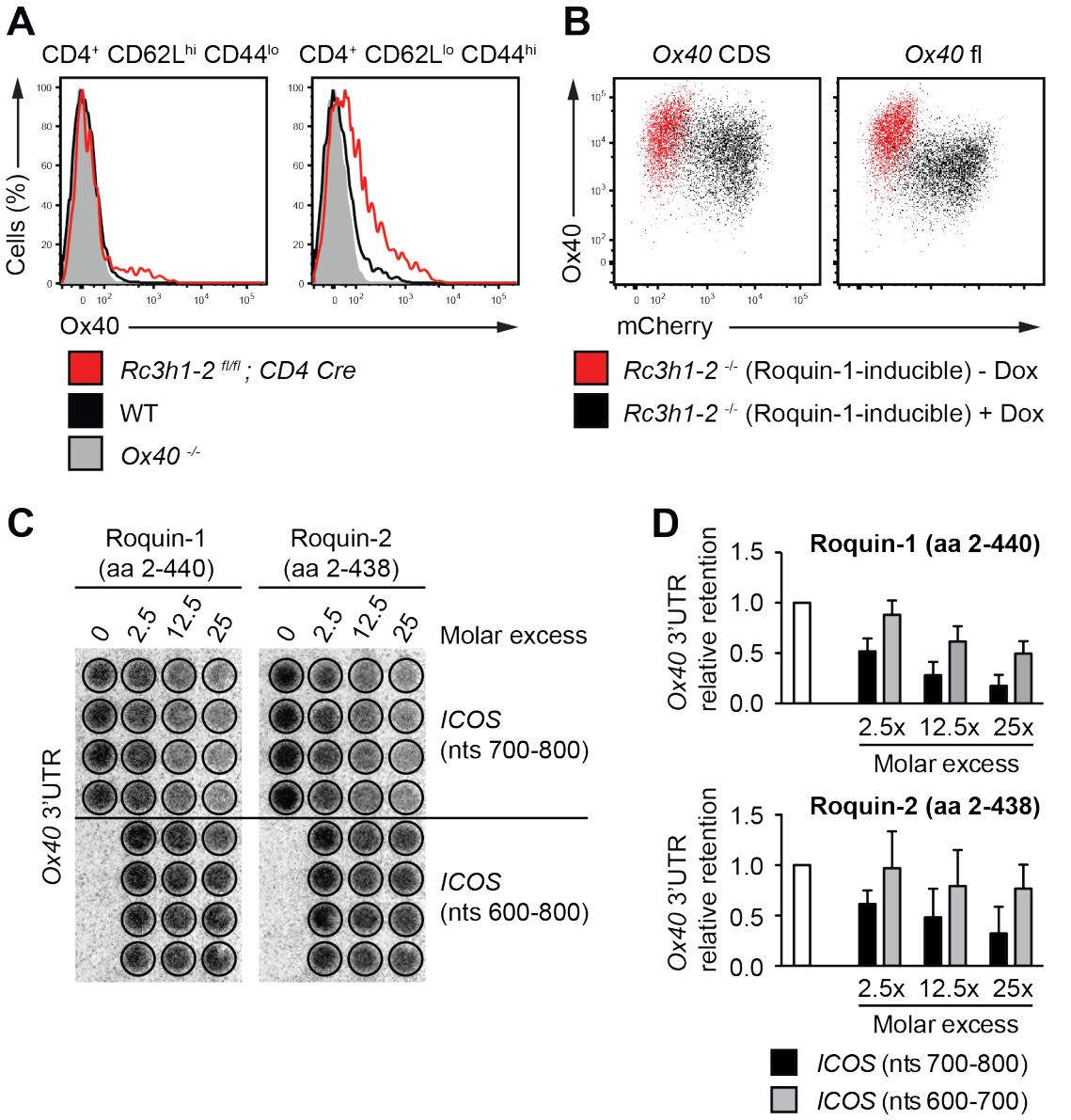

Figure 15: Validation of *Ox40* as Roquin target mRNA. A Ox40 expression on naïve (CD62L^{hi} CD44^{lo}) and effector-like (CD62L^{lo} CD44^{hi}) CD4^{+} T cells as determined by flow cytometry. **B** Ox40 expression on *Rc3h1-2*$^{-/-}$ MEFs with and without Dox-induced expression of Roquin-1-p2A-mCherry. **C** Competitive FBA with Roquin-1 and Roquin-2, the ^{32}P-labeled *Ox40* 3'UTR and unlabeled specific (*ICOS* 700-800) and unspecific (*ICOS* 600-700) competitor RNA. 4 technical replicates are shown for each condition. **D** Quantification of **C**, error bars show standard deviation (SD) of 3 (Roquin-2) or 4 (Roquin-1) independent experiments.

4.1.3 Analysis of a combined Roquin and Ox40 knockout in mice

The next aim was to investigate how Ox40 upregulation on $CD4^+$ T cells in *Rc3h1-2$^{fl/fl}$; CD4 Cre* mice contributes to the phenotype of these mice. Therefore, *Ox40$^{-/-}$; Rc3h1-2$^{fl/fl}$; CD4 Cre* mice were bred and analyzed comparing them to the conditional Roquin-1 and Roquin-2 knockout mice and *Ox40$^{-/-}$* mice as well as control animals. The age of the analyzed mice was in the range between 7 and 18 weeks, with the majority of animals at the age of 9 to 12 weeks.

The most prominent phenotype of the *Rc3h1-2$^{fl/fl}$; CD4 Cre* mice (termed double knockout) was the splenomegaly, which was quantified by spleen weight. The combined Ox40 and conditional Roquin-1 and Roquin-2 knockout (termed triple knockout) resembles this phenotype, however to a significantly lesser extent (**Figure 16A right side**). As opposed to the double knockout, the splenomegaly could not be explained by higher numbers of splenocytes in the triple knockout, since those numbers were not increased compared to the control animals (**Figure 16B**). In contrast, there was a mild reduction of splenocytes in the *Ox40$^{-/-}$* control samples, which could possibly manifest in the triple knockout.

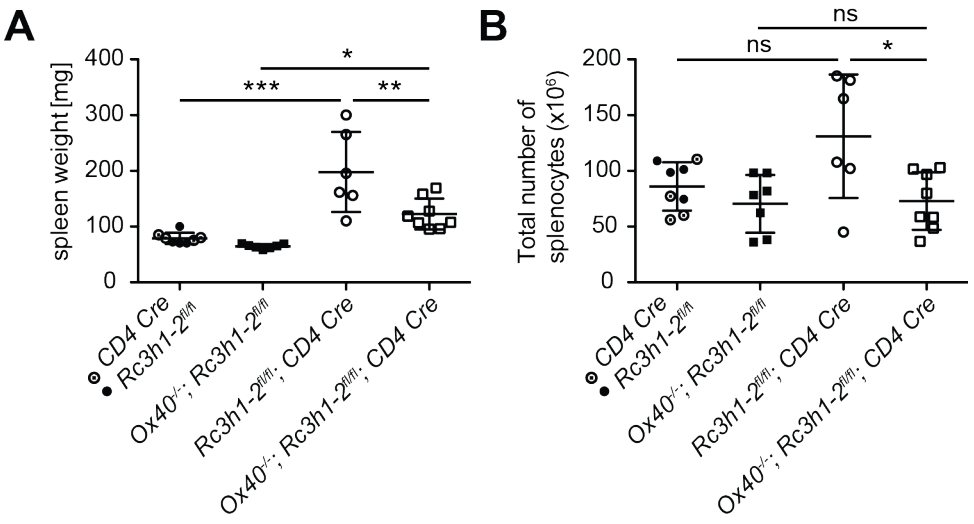

Figure 16: Analysis of spleens from mice with a combined Roquin and Ox40 knockout in T cells. Spleen weight (**A**) and number of splenocytes (**B**) of 8 control mice (4 *CD4 Cre* and 4 *Rc3h1-2$^{fl/fl}$* as indicated), 7 *Ox40$^{-/-}$; Rc3h1-2$^{fl/fl}$* mice, 6 *Rc3h1-2$^{fl/fl}$; CD4 Cre* mice and 8 *Ox40$^{-/-}$; Rc3h1-2$^{fl/fl}$; CD4 Cre* mice. Error bars show SD and statistical analysis was performed by one-way ANOVA and subsequent Tukey's multiple comparison test (ns: not significant, *p<0.05, **p<0.01, ***p<0.005).

4.1.3.1 Analysis of $CD4^+$ and $CD8^+$ T cells from triple knockout mice

Using the conditional *CD4-Cre* allele causes a deletion of *Rc3h1-2* in T cells during the $CD4^+$ $CD8^+$ double positive stage of thymic development. Therefore, $CD4^+$ and $CD8^+$ T cells as well as other T cell subsets were investigated in more detail. Like the double knockout mice, the triple knockout animals showed a significant reduction of $CD4^+$ T cells in percentage as well as in total cell numbers (**Figure 17A**). The activation status of these T cells revealed that the reduced number of total $CD4^+$ T cells was mainly due to significantly lower numbers of naïve ($CD62L^{hi}$ $CD44^{lo}$) T helper cells, which in turn resulted in a relative increase in activated $CD62L^{lo}$ $CD44^{hi}$ $CD4^+$ T cells (**Figure 17B and C**). A slightly but not significantly increased frequency of central memory-like cells ($CD62L^{hi}$ $CD44^{hi}$) was observed in the triple knockout (**Figure 17C**). The increase of $CD8^+$ T cells in double knockout animals was ameliorated in the triple knockout, particularly on the level of total cell numbers (**Figure 18A**). Excessive T cell activation ($CD62L^{lo}$ $CD44^{hi}$) and loss of naïve T cells ($CD62L^{hi}$ $CD44^{lo}$) was apparent in $CD8^+$ double knockout cells and did not change upon additional lack of Ox40 (**Figure 18B and C**). The only difference between double and triple knockout cells was observed in the total numbers of $CD8^+$ central memory-like T cells, which was slightly lower in the triple knockout than in the double knockout or the control samples (**Figure 18C**).

Taken together, the excessive activation of $CD4^+$ and $CD8^+$ T cells observed in double knockout mice was not prevented in triple knockout mice despite the abrogation of Ox40 expression.

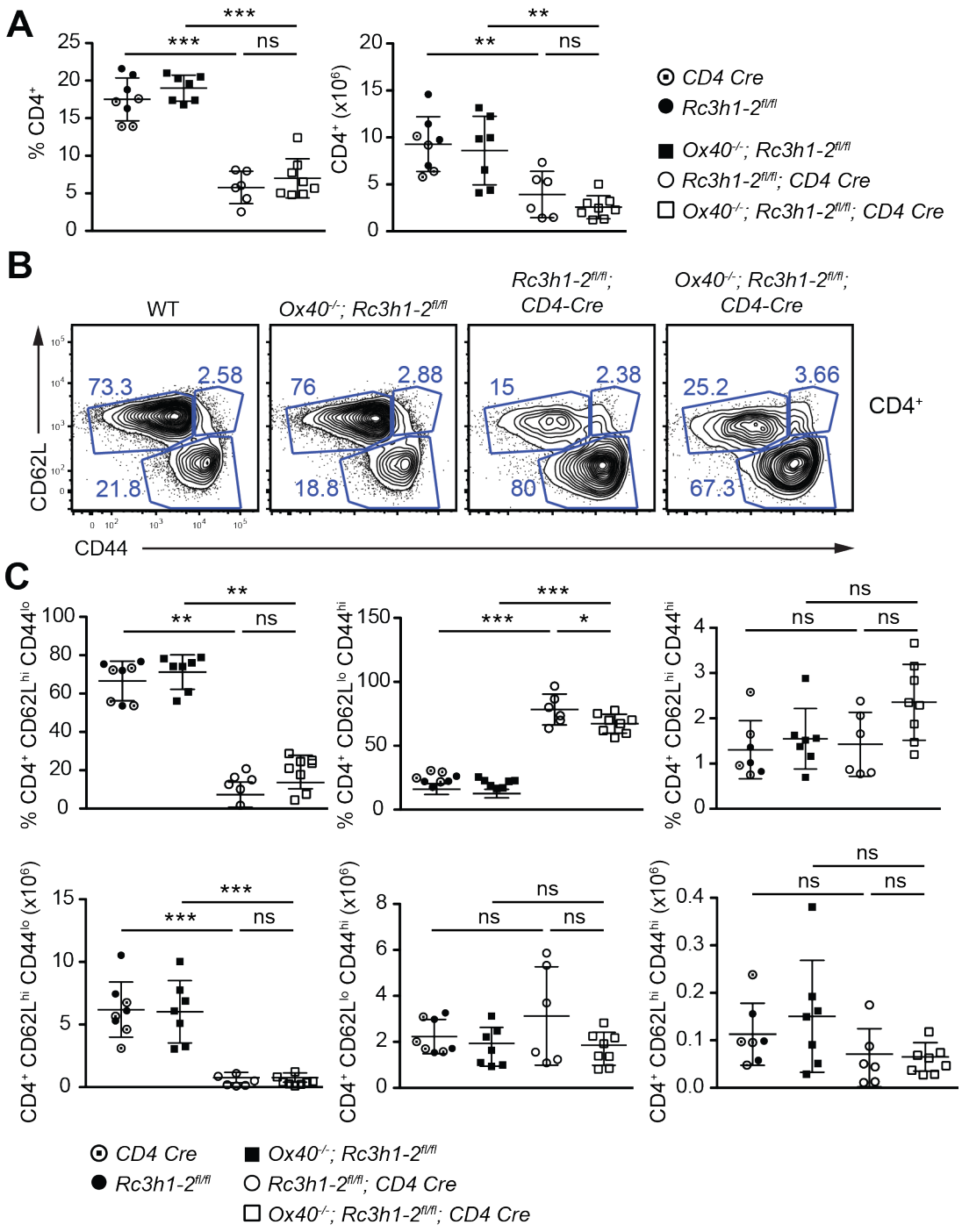

Figure 17: CD4$^+$ T cells are reduced and highly activated in triple knockout mice. A Relative (left) and absolute (right) numbers of CD4$^+$ T cells. **B** Representative contour plots of CD62L and CD44 stainings, gated on CD4$^+$ cells. **C** Relative (upper panel) and total (lower panel) numbers of naïve (CD62L^{hi} CD44^{lo}), effector memory-like (CD62L^{lo} CD44^{hi}) and central memory-like (CD62L^{hi} CD44^{hi}) T helper cells in all analyzed mice. Error bars show SD and statistical analysis was performed by one-way ANOVA and Tukey's multiple comparison test or one-way ANOVA Kruskal-Wallis Test followed by Dunn's multiple comparison test (ns: not significant, *p<0.05, **p<0.01, ***p<0.005).

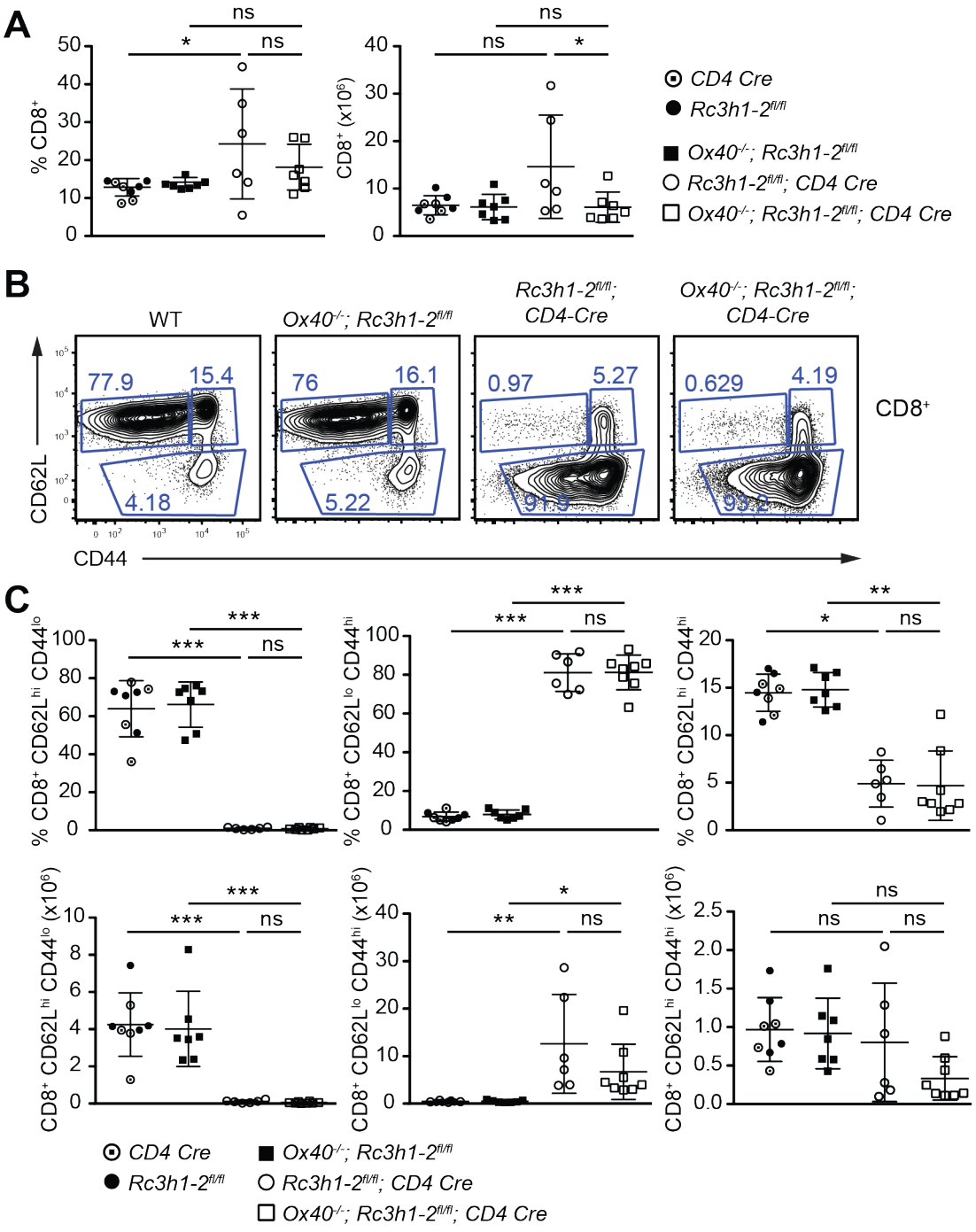

Figure 18: CD8$^+$ T cells are excessively activated in triple knockout mice. A Relative (left) and absolute (right) numbers of CD8$^+$ T cells. **B** Representative contour plots of CD62L and CD44 stainings, gated on CD8$^+$ cells. **C** Relative (upper panel) and total (lower panel) numbers of naïve (CD62L^{hi} CD44^{lo}), effector memory-like (CD62L^{lo} CD44^{hi}) and central memory-like (CD62L^{hi} CD44^{hi}) CD8$^+$ T cells in all analyzed mice. Error bars show SD and statistical analysis was performed by one-way ANOVA and Tukey's multiple comparison test or one-way ANOVA Kruskal-Wallis Test followed by Dunn's multiple comparison test (ns: not significant, *p<0.05, **p<0.01, ***p<0.005).

4.1.3.2 Analysis of autoimmunity-associated lymphocyte subsets

Next, other lymphocyte subsets having been connected to the development of autoimmunity were analyzed in conditional double and triple knockout mice.

Follicular T helper cells (Tfh cells) are a subset of $CD4^+$ T cells that is involved in the germinal center reaction and thus might promote high-affinity autoantibody production. Tfh cells were increased in double knockout mice, and this phenotype was not rescued but rather enhanced in mice that additionally lack Ox40 (**Figure 19A and B**). Since Tfh cells support germinal center B cell (GC B cell) formation, an increase in Tfh cells might result in increased levels of GC B cells. This was found in conditional double knockout and triple knockout mice, the latter having slightly higher total numbers of GC B cells (**Figure 19A and B**).

Regulatory T cells (Tregs) are a T helper cell subset that plays a role in preventing autoimmunity and is marked by the expression of the transcription factor Foxp3. Whereas control, *Ox40*$^{-/-}$ and double knockout samples had similar levels of peripheral Tregs in the spleen, this cell subset was significantly increased in triple knockout mice compared to the Ox40 single knockout (**Figure 20A and B**). A tendency to higher Treg levels was also apparent in double knockout mice, however there are strong variances between the four animals. This suggests that double knockout T helper cells might have an intrinsic preference for Treg differentiation that is suppressed by the high expression levels of Ox40 in those cells.

Short-lived effector cells (SLECs) are a subset of activated $CD8^+$ T cells characterized by the killer cell lectin-like receptor G1 (KLRG1) expression and their inability to become memory cells. Increased numbers of SLEC-like T cells have been associated with the development of autoimmune diseases (Chang et al. 2012). The percentage of SLECs was significantly increased in spleens from double knockout as well as from triple knockout mice, indicating that Ox40 signals are not required for the excessive formation of SLECs in double knockout mice (**Figure 20C**).

Finally, natural killer cells (NK cells) and natural killer T cells (NKT cells), that were both reduced in the double knockout mice, were investigated in the triple knockout samples (**Figure 20D**). Although it was shown that NK cells as well as NKT cells express Ox40 (Croft 2010), the loss of this costimulatory receptor did not alter their frequency compared to control or double knockout mice (**Figure 20E**).

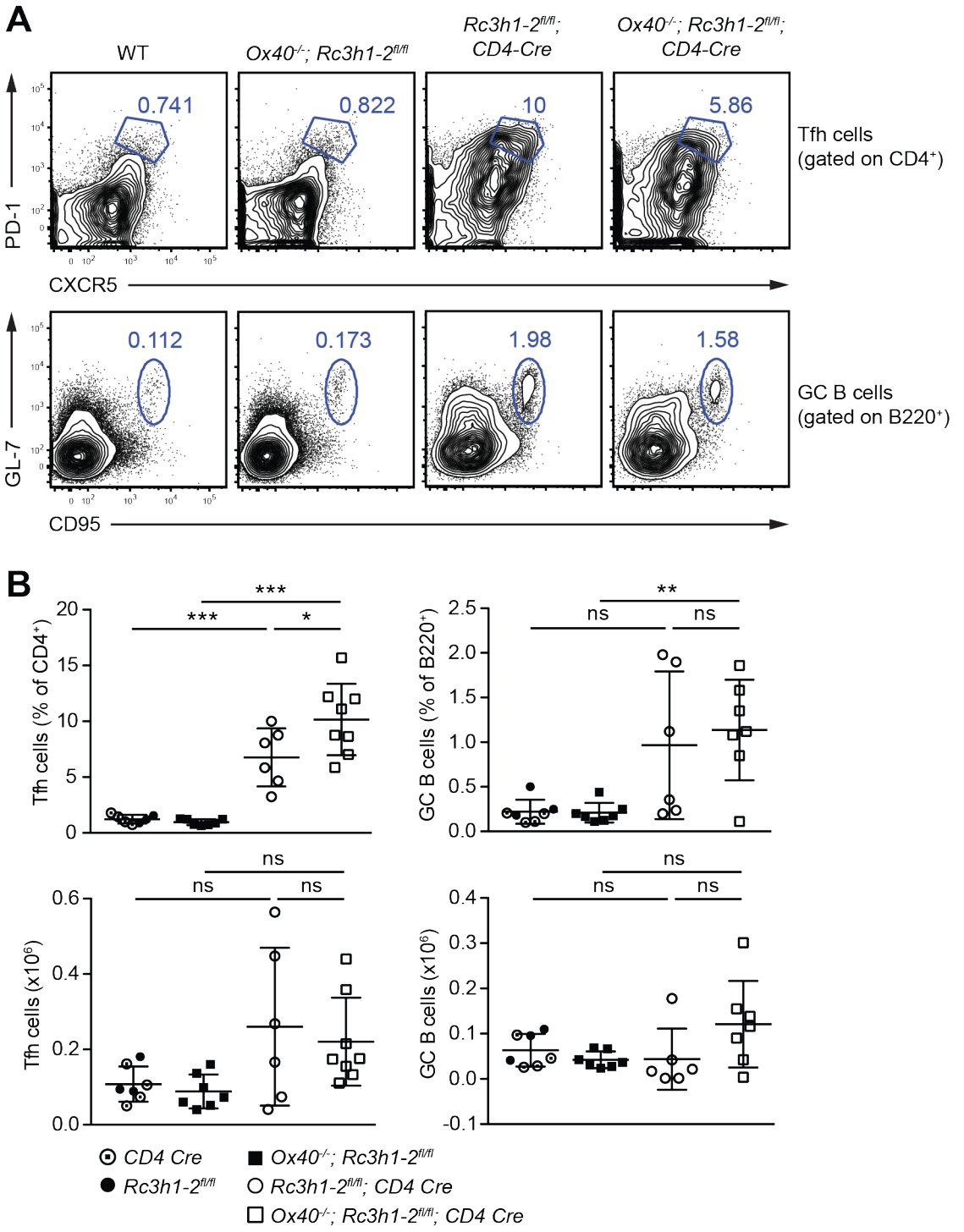

Figure 19: Double knockout and triple knockout mice have increased levels of Tfh cells and GC B cells. A Representative contour plots of Tfh stainings (upper panel) and GC B cell stainings (lower panel). **B** Relative (upper part) and total (lower part) numbers of Tfh cell and GC B cells in spleens of the respective mice. Error bars show SD and statistical analysis was performed by one-way ANOVA and Tukey's multiple comparison test and one-way ANOVA Kruskal-Wallis Test followed by Dunn's multiple comparison test for total number of GC B cells (ns: not significant, *p<0.05, **p<0.01, ***p<0.005).

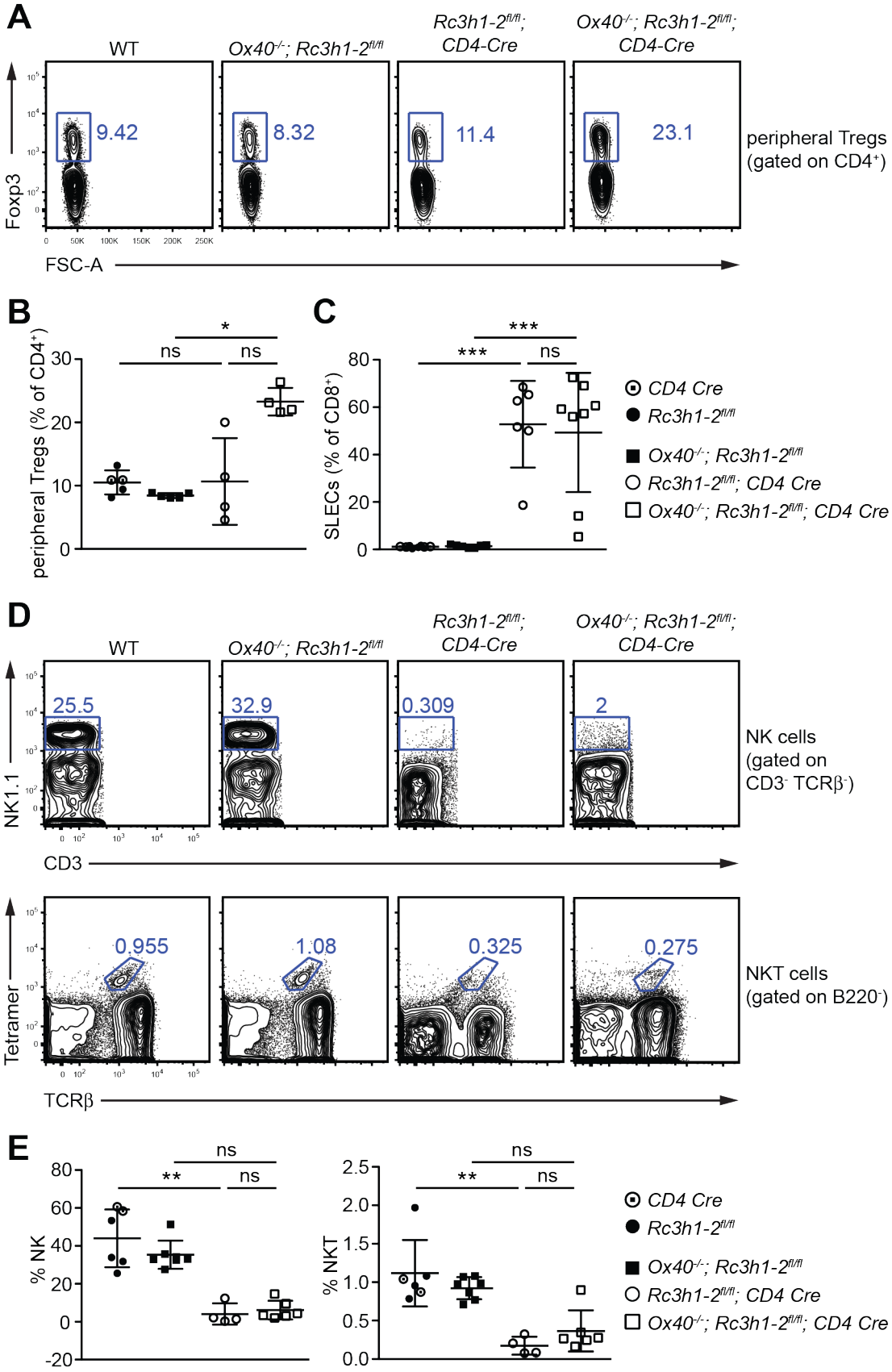

Figure 20: Frequency of different lymphocyte subsets in triple knockout mice. A Representative contour plots of FoxP3$^+$ peripheral regulatory T cells. **B** Overview of Treg percentages among CD4$^+$ T cells. **C** Relative numbers of SLECs among CD8$^+$ T cells. **D** Representative contour plots of NK1.1$^+$ NK cells (upper panel) and of PBS57-loaded CD1d tetramer$^+$ NKT cells (lower panel). **E** Frequency of NK

and NKT cells. Error bars show SD and statistical analysis was performed by one-way ANOVA and Tukey's multiple comparison test for SLECs and one-way ANOVA Kruskal-Wallis Test followed by Dunn's multiple comparison test for all other subsets (ns: not significant, *p<0.05, **p<0.01, ***p<0.005).

4.1.3.3 Expression of Roquin targets in triple knockout T cells

To find out whether the known Roquin targets Ox40 and Icos influence each other's expression in addition to the post-transcriptional regulation by Roquin, the Icos MFI was quantified on different $CD4^+$ and $CD8^+$ T cells. In all $CD4^+$ subsets, the relative Icos level was equally high in double knockout and triple knockout samples and increased compared to *Ox40*$^{-/-}$ or control animals (**Figure 21A upper panel**). A similar tendency was observed in $CD8^+$ cells with the most prominent effects in the effector-like population (**Figure 21A lower panel**). Interestingly, the costimulatory receptor Ctla4, suggested to be a Roquin target in the microarray analyses, showed a similar expression pattern in $CD4^+$ T cells from the different mice (**Figure 21B**), indicating that it is regulated by Roquin-1 and Roquin-2.

In summary, the analysis of *Ox40*$^{-/-}$*; Rc3h1-2*$^{fl/fl}$*; CD4 Cre* in comparison to *Rc3h1-2*$^{fl/fl}$*; CD4 Cre* animals did not reveal a certain phenotypical feature to be rescued by the loss of Ox40 on double knockout T cells. Most probably, the double knockout phenotype results from derepression of multiple Roquin target mRNAs acting together in T cell activation and differentiation.

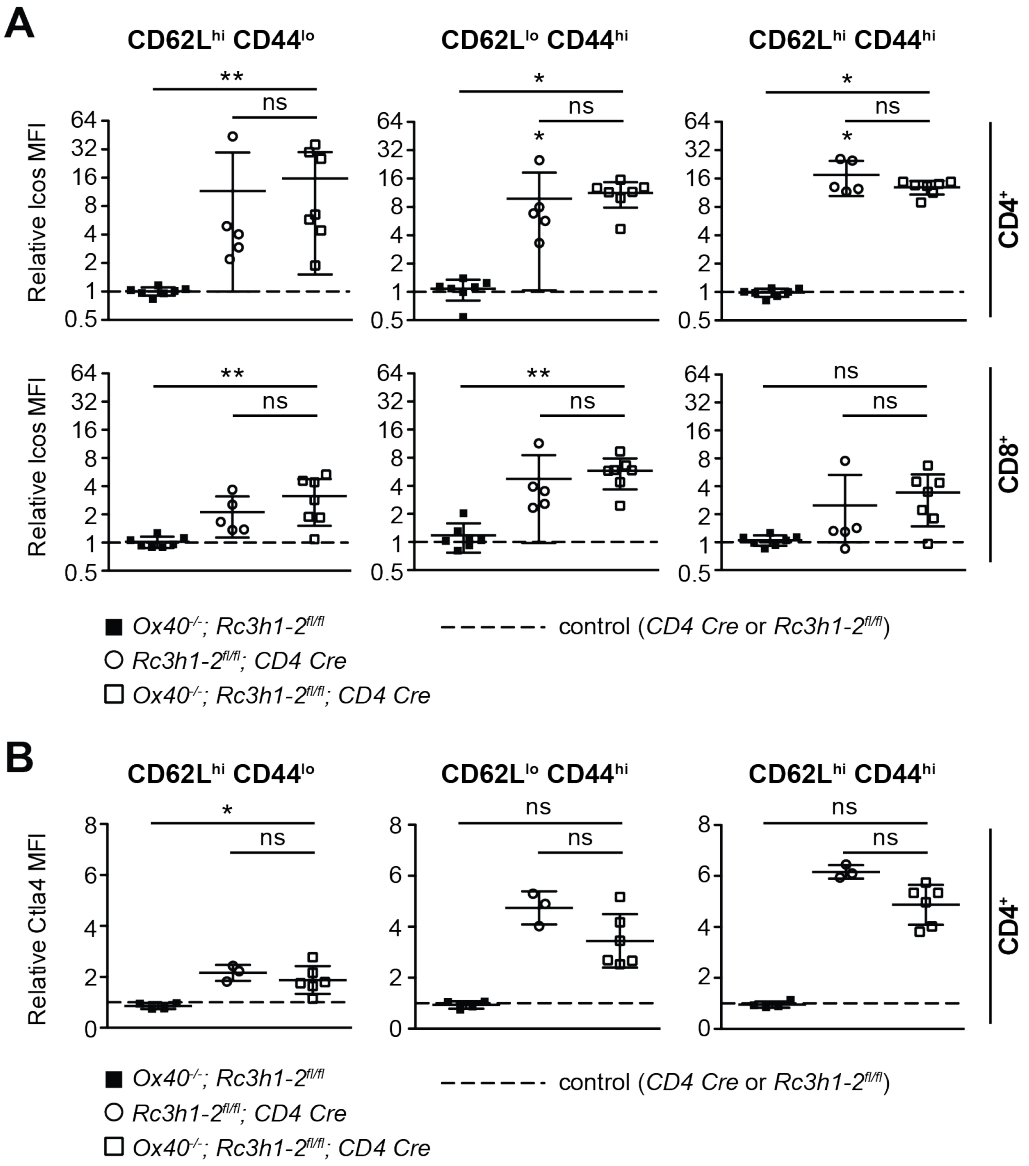

Figure 21: Icos and Ctla4 MFI are increased in different T cell subsets of double as well as triple knockout mice. A Relative Icos expression levels (normalized to control animals) on naïve (right), effector-like (middle) and memory-like (left) $CD4^+$ (upper panel) and $CD8^+$ (lower panel) T cells. **B** Relative expression of Ctla4 (normalized to control animals) in the same $CD4^+$ T cell subsets as in **A**. Error bars show SD and statistical analysis was performed by one-way ANOVA Kruskal-Wallis Test followed by Dunn's multiple comparison test (ns: not significant, *p<0.05, **p<0.01). An asterisk above one group indicates statistically significant difference to the control group (dashed line).

4.1.4 Roquin CLIP and PAR-CLIP assays in primary Th1 cells

As a second approach to identify Roquin-targeted mRNAs, CLIP and PAR-CLIP assays were performed in collaboration with the Group of Prof. Dr. Mihaela Zavolan (Biozentrum Basel). To be able to identify T-cell-specific targets and to use *Icos*, which is only expressed in T cells, as a positive control, PAR-CLIP and CLIP analyses were to be done in primary T helper cells. Moreover, previous experiments had shown that high Roquin concentrations exhibit an unspecific RNA affinity *in vitro* (Glasmacher et al. 2010) and cells did not tolerate Roquin overexpression for more than a few days (unpublished observation). Therefore, the assay was performed in primary T helper cells on the endogenous Roquin-1 and Roquin-2 proteins, which limited the availability of cells and the amount of Roquin protein in the starting lysate.

4.1.4.1 CLIP and PAR-CLIP assay procedure

The first step towards PAR-CLIP and CLIP assays was to test different antibodies in Roquin immunoprecipitations (IPs) from primary Th1 cell lysates to achieve a high pull-down efficiency. Specificity of the antibodies was confirmed comparing IPs from wild-type and *Rc3h1*$^{-/-}$ Th1 cell lysates. Two different antibodies were tested in this experiment, namely clone 3F12 that recognizes Roquin-1 and Roquin-2 (Vogel et al. 2013) and a newly generated monoclonal antibody, clone 18F8, which also recognizes both Roquin paralogs. The antibodies were purified from hybridoma cell culture supernatants and coupled to tosyl-activated magnetic beads. IPs using these beads exhibited a strong enrichment of Roquin proteins compared to the input control (**Figure 22**). Surprisingly, Roquin proteins in IP samples seemed to be slightly different in size, which might be due to dissimilar salt concentrations in the IP samples, or due to varying affinity of the two antibodies for certain post-translationally modified Roquin variants. The control IPs from Roquin-1 knockout Th1 cells showed that the upper prominent band represents Roquin-2, whereas the lower prominent band in the wild-type IPs is derived from Roquin-1. Since the clones 3F12 and 18F8 achieved similar enrichment of Roquin-1 and Roquin-2, they were both used in CLIP and PAR-CLIP experiments. The anti-Ago2 antibody 2D4 was bound to magnetic protein G beads and used for a reference IP.

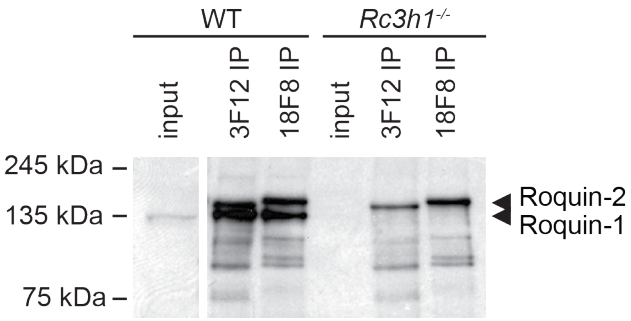

Figure 22: Immunoprecipitation (IP) of Roquin-1 and Roquin-2 from Th1 cell lysates. Immunoblot of IPs performed with different anti-Roquin-1/2 antibodies. The 3F12 antibody, which recognizes both Roquin paralogs, was used for detection.

With the help of Georges Martin, Prof. Dr. Mihaela Zavolan's group, three CLIP assays (samples 4-6) using 254 nm UV light for irradiation were performed together with three PAR-CLIP assays (samples 1-3) using 4SU treatment of the Th1 cells and irradiation with 365 nm UV light. After cell lysate preparation and IP, the ^{32}P-labeled samples were separated in SDS PAGE (**Figure 23A right**) and then blotted to a nitrocellulose membrane (**Figure 23A left**). Whereas there were almost no bands visible within the SDS gel, clear signals were observed after blotting to the nitrocellulose membrane for the Roquin 3F12 and the Ago2 samples, most probably because the procedure reduced background signals. Unexpectedly, the 18F8 antibody seemed to have performed much worse, even though it was comparable to the 3F12 antibody in Roquin IPs (**Figure 22**). However, since the autoradiographic signals on the membrane do not provide information about the quality of the bound RNA, all samples were further processed. The parts of the membrane corresponding to the protein size (about 135 kDa for Roquin and about 100 kDa for Ago2) and up to 30 kDa above were cut and RNA fragments on those membrane pieces were purified. After linker ligation and size selection of the RNA fragments (**Figure 23B**), a cDNA library was prepared by reverse transcription (**Figure 23C**). At this step, all samples showed comparable PCR product amounts, which is in contrast to the picture observed after SDS PAGE and blotting. The cDNA library was analyzed using the Illumina Solexa sequencing technology.

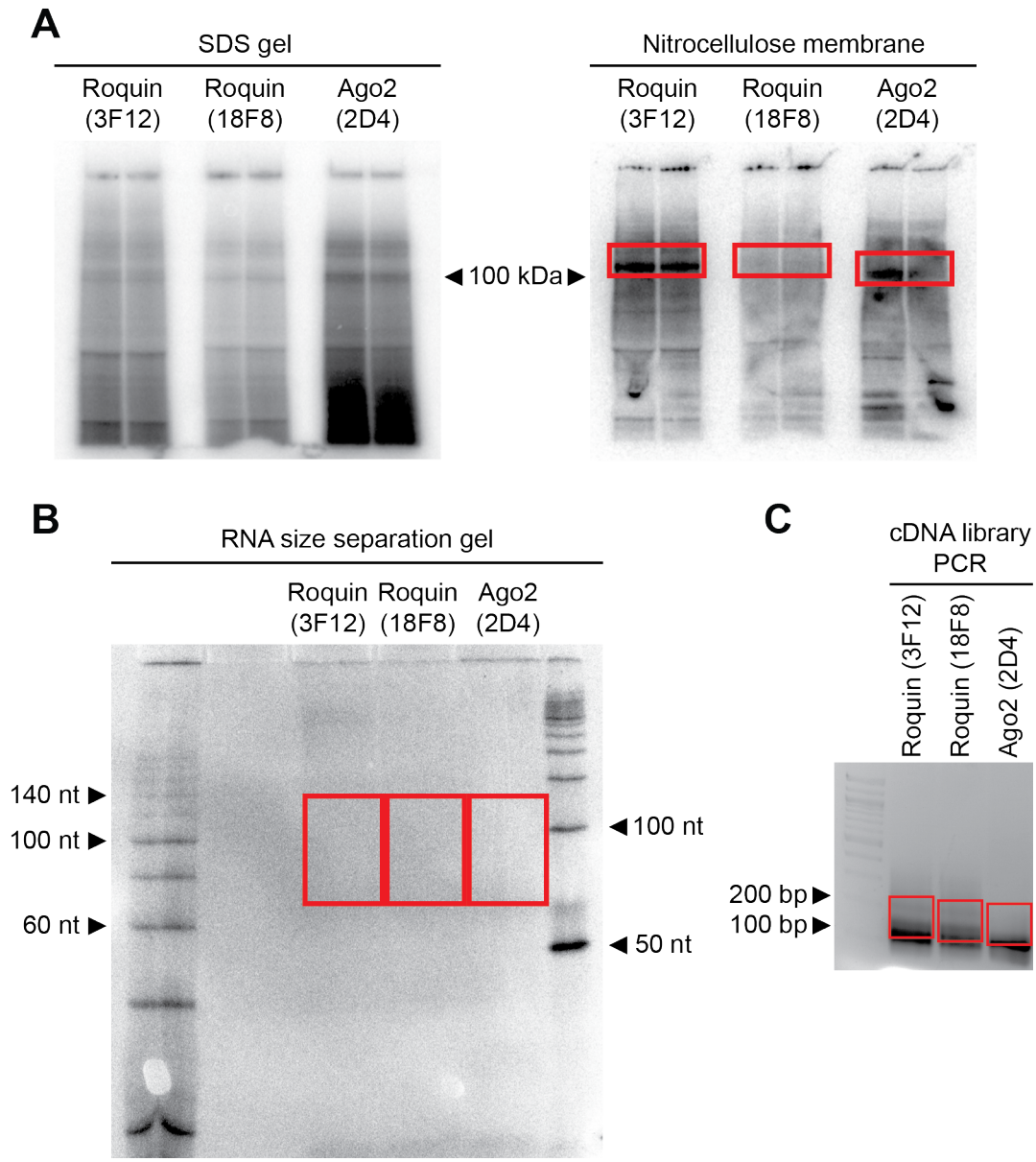

Figure 23: Documentation of the PAR-CLIP assays (samples 1-3). A Left: autoradiography of SDS gel after PAGE of ^{32}P-labeled IP samples. Right: as on the left side after blotting the content of the gel onto a nitrocellulose membrane. Parts of the membrane that were cut for sample purification are indicated in red. **B** Autoradiography of a denaturing RNA gel, run for size separation of the RNA fragments after linker ligation. The gel was cut to purify fragments between 70 and 140 nts as indicated by the red boxes. **C** Agarose gel visualizing PCR products. For cDNA library preparation DNA was purified from gel pieces covering 130-170 basepairs (bp) length as indicated in red. CLIP assays were performed and documented in the same way (data not shown).

4.1.4.2 CLIP and PAR-CLIP sequencing data analysis

An overview of the sequencing results obtained from the Clipz database (Khorshid et al. 2011) is presented in **Table 21**. The number of reads ranged between 24 and 50 million per sample, and only the Ago2 PAR-CLIP sample had less than 10 million reads. However, only about 5% of these reads mapped to mRNAs, whereas half of the reads were based on an excessive number of degraded 5' adapter sequences (defined as vector in the Clipz database). Therefore, the overall quality of the libraries was rather poor, and those adapter sequences had to be excluded for further data evaluation. Customized bioinformatics analyses of the CLIP and PAR-CLIP data sets were performed by Dr. Andreas Gruber, Prof. Dr. Mihaela Zavolan's group.

Table 21: Number of reads and read annotation in CLIP and PAR-CLIP samples according to standard analysis procedure of the Clipz database pipeline.

	Antibody	Assay	Number of reads	% reads mapping to mRNAs	% reads mapping to vector
1	Roquin 3F12	PAR-CLIP	24,959,528	5.18	51.56
2	Roquin 18F8	PAR-CLIP	49,801,557	4.66	46.82
3	Ago2 2D4	PAR-CLIP	8,714,767	4.24	44.64
4	Roquin 3F12	CLIP	27,044,116	4.76	48.78
5	Roquin 18F8	CLIP	25,062,000	5.08	46.29
6	Ago2 2D4	CLIP	31,164,857	4.07	49.07

Table 22: Number of total reads and reads mapping to mRNAs after removal of linker sequences. This analysis was performed by Dr. Andreas Gruber.

	Antibody	Assay	Number of unique mappers	Reads mapping to mRNAs	% reads mapping to mRNAs
1	Roquin 3F12	PAR-CLIP	2,844,920	231,055	8.12
2	Roquin 18F8	PAR-CLIP	5,518,583	328,781	5.96
3	Ago2 2D4	PAR-CLIP	828,595	105,596	12.74
4	Roquin 3F12	CLIP	2,908,436	244,933	8.42
5	Roquin 18F8	CLIP	2,528,968	379,627	15.01
6	Ago2 2D4	CLIP	3,413,487	212,334	6.22

Upon removal of adapter sequences, reads mapping uniquely to the genome were defined as the total number of reads. Thus, the frequency of reads mapping to mRNAs was increased up to 15% (**Table 22**). The results of mutation analyses revealed that PAR-CLIP samples had the expected high T to C conversion rates (**Figure 24, 1-3**), whereas CLIP samples exhibited increased rates of T deletion and insertion and A to C conversion (**Figure 24, 4-6**). Subsequently, sequence preferences next to the 200 most abundant T positions that show T to C conversions in mRNAs were investigated for the PAR_CLIP samples 1 and 2 (**Figure 25**). Surprisingly, no position 25 nts upstream or downstream of the T to C conversion showed a bias for a certain base, suggesting that Roquin binding to these RNAs might be non-sequence-specific.

1) Roquin 3F12_PAR-CLIP

	A	C	G	N	T
A	0	4.59	1.75	0.07	2.22
C	2.33	0	1.07	0.04	1.99
G	1.78	1.38	0	0.05	2.28
N	0	0	0	0	0
T	2.48	**52.05**	1.87	0.05	0
Ins	1.31	2.79	2.19	0.06	6.87
Del	1.81	0.82	0.81	0	7.33

4) Roquin 3F12_CLIP

	A	C	G	N	T
A	0	**9.38**	4.18	0.14	5.66
C	4.21	0	1.97	0.08	5.64
G	3.30	2.74	0	0.08	5.07
N	0	0	0	0	0
T	3.42	5.99	3.87	0.09	0
Ins	2.34	5.78	3.41	0.09	**11.20**
Del	5.00	2.89	2.68	0	**10.78**

2) Roquin 18F8_PAR-CLIP

	A	C	G	N	T
A	0	4.65	1.79	0.07	2.26
C	2.16	0	1.08	0.04	1.86
G	1.62	1.57	0	0.04	2.40
N	0	0	0	0	0
T	2.68	**43.26**	2.05	0.05	0
Ins	1.75	4.14	2.81	0.09	9.24
Del	2.49	1.18	1.17	0	9.56

5) Roquin 18F8_CLIP

	A	C	G	N	T
A	0	**11.81**	4.69	0.14	5.22
C	4.66	0	2.24	0.08	5.74
G	3.56	3.07	0	0.08	5.21
N	0	0	0	0	0
T	4.52	**7.18**	4.88	0.14	0
Ins	1.56	6.10	2.30	0.04	5.13
Del	5.84	3.14	2.31	0	**10.37**

3) Ago2 2D4_PAR-CLIP

	A	C	G	N	T
A	0	10.48	4.12	0.09	2.12
C	1.86	0	1.67	0.09	3.97
G	4.74	2.08	0	0.05	2.39
N	0	0	0	0	0
T	2.50	**48.91**	1.65	0.08	0
Ins	0.83	2.70	1.23	0.03	2.69
Del	0.92	0.78	0.55	0	3.47

6) Ago2 2D4_CLIP

	A	C	G	N	T
A	0	**18.36**	3.80	0.13	3.75
C	2.73	0	2.19	0.15	5.42
G	3.27	2.56	0	0.09	5.08
N	0	0	0	0	0
T	3.30	5.23	3.48	0.14	0
Ins	2.28	5.69	4.10	0.16	**9.78**
Del	3.85	3.21	2.57	0	**8.69**

Figure 24: Mutation plots of all CLIP and PAR-CLIP samples. T to C conversions are highlighted in PAR-CLIP samples (1-3) and other frequent mutations are highlighted in CLIP samples (4-6). The data was provided by Dr. Andreas Gruber.

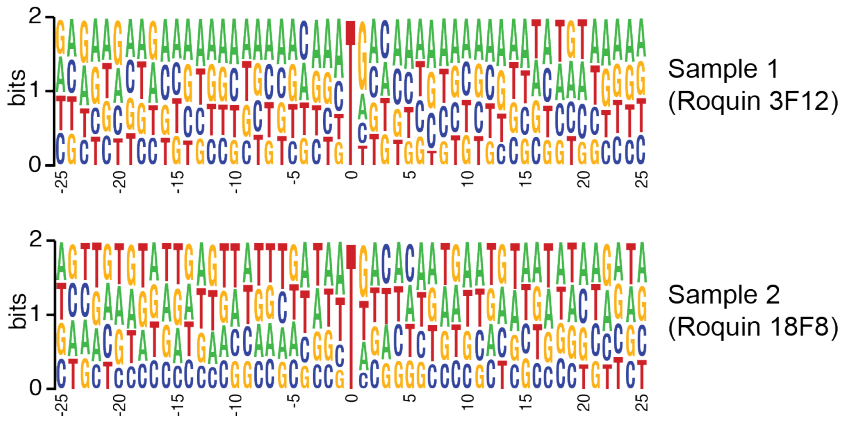

Figure 25: Sequence patterns of the area next to T to C conversion sites. The size of the letters at every nucleotide position reflects the frequency within the analyzed sequences. The analysis was performed by Dr. Andreas Gruber.

An RNA stem-loop structure, named constitutive decay element (CDE), was proposed to be specifically recognized by Roquin-1 (Leppek et al. 2013). Therefore, the number of sequence reads in the proximity of such putative CDE stem-loops was determined for all Roquin samples. **Figure 26** shows sequence profiles 100 nts upstream and downstream of three example CDE sites located in the mRNAs of *Tnf*, *Nfkbid* and *Ier3*. Interestingly, samples 2 and 5 had higher numbers of clipped sequences in all analyzed areas, indicating that the antibody clone 18F8 was more efficient in IPs of specific Roquin-RNA complexes. *Tnf*, harboring the prototypic CDE stem-loop, represented a mixed picture of clipped sites (**Figure 26A**). Only sample 2 showed a cluster of clipped sequences at the position of the CDE. Apart from that, clipped sequences were present throughout the 200 nts stretch in all samples with an accumulation about 60 to 70 nts upstream of the stem-loop structure. *Nfkbid*, a target candidate from the previously described array analyses (**Table 20**), supposedly has two CDE stem-loops in a tandem conformation with 13 nts as spacer sequence (Leppek et al. 2013). The histograms in **Figure 26B** were centered on the more downstream CDE and they revealed a preference for clipped sequences 50 nts upstream and downstream of this stem-loop. The third example, *Ier3*, is a Roquin-1 target suggested by Leppek et al. due to a CDE in its 3'UTR. For this candidate the CLIP and PAR-CLIP samples exhibited the highest read numbers and also a very uniform picture (**Figure 26C**). Clipped *Ier3* sequences are exclusively located at the position of the stem-loop with a less stringent endpoint on the upstream side of the sequence cluster. Comparing the given examples for clipped sequences in the area of CDE stem-loops showed high variability and did not reveal a clear bias to upstream or downstream regions.

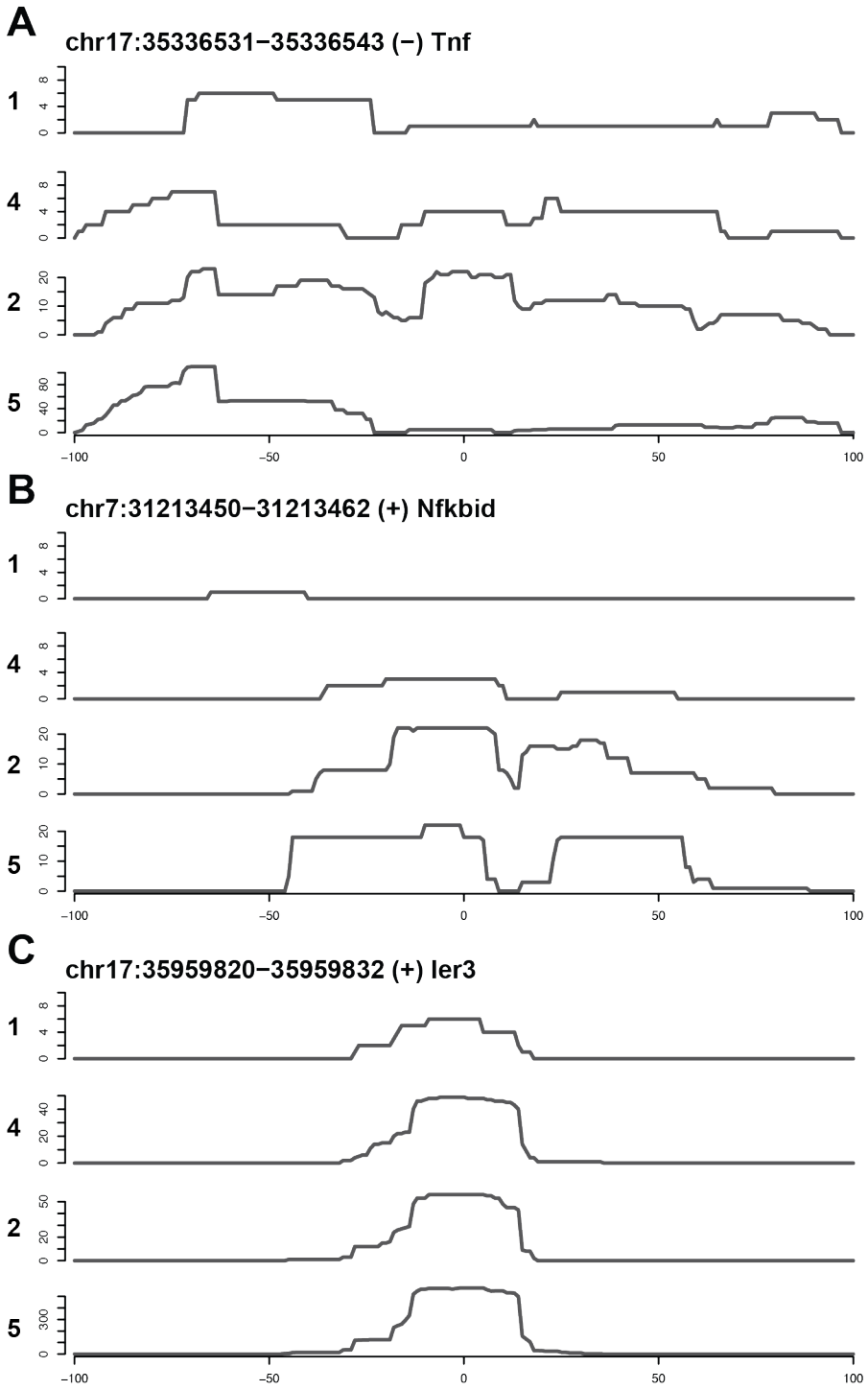

Figure 26: Number of clipped sequences in the proximity of CDE stem-loops. A Clipped sequences in samples 1,4 (Roquin 3F12) and 2,5 (Roquin 18F8) in the area 100 nts upstream and downstream of the *Tnf* CDE. **B** As in **A** for sequences flanking the more downstream CDE in the *Nfkbid* 3'UTR. **C** As **A** and **B** for a CDE within the *Ier3* 3'UTR. The analysis was performed by Dr. Andreas Gruber.

The newly identified Roquin target *Ox40* does not have a consensus CDE in its 3'UTR and was therefore analyzed separately. Clipped sequences covering the *Ox40* mRNA from all four Roquin samples were extracted from the Clipz database and aligned.

Unexpectedly, the largest sequence cluster was located at the 3' end of the *Ox40* CDS (data not shown), whereas two smaller clusters of clipped sequences were identified in the *Ox40* 3'UTR (**Figure 27A**). To get an idea of the structural composition of the 157 nts spanning *Ox40* 3'UTR, mfold structure prediction was performed. The thermodynamically most stable structure (initial ΔG = -55.00) suggests the formation of two hairpin structures, one with a hexaloop and one with a triloop, which is reminiscent of the CDE stem-loop structure (**Figure 27B**). Those putative stem-loop structures are in close proximity to the described sequence clusters.

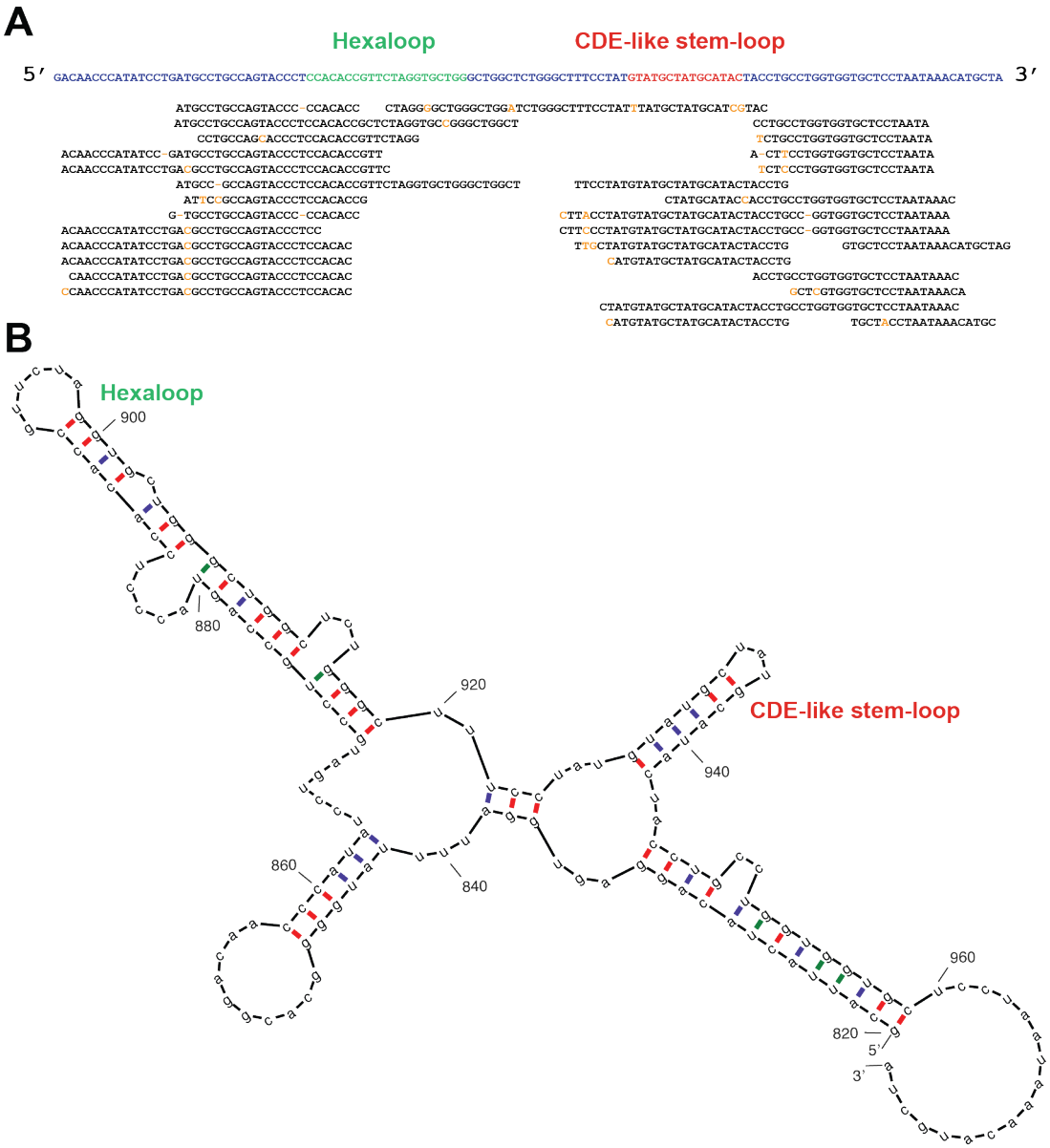

Figure 27: Two sequence clusters are clipped in the *Ox40* 3'UTR. A Alignment of all clipped sequences in the *Ox40* 3'UTR (violet). Two putative structural features are shown in green (hexaloop) and red (CDE-like stem-loop). Mutated positions in the clipped sequences are marked in orange. **B** Secondary structure prediction of the *Ox40* 3'UTR as obtained from the mfold Web Server. Numbers indicate position relative to the first nucleotide of the CDS.

4.2 Molecular analysis of the Roquin-RNA interaction

4.2.1 Selection of Roquin-bound RNAs from a random library

SELEX (Systematic evolution of ligands by exponential enrichment) is a method to select for single stranded nucleic acids that bind with high affinity to the ligand used during the selection procedure. By employing a random RNA library in combination with an RNA-binding protein such as Roquin, it is an unbiased approach to identify RNA sequences that are preferentially bound by the protein. Ideally, SELEX helps to identify high-affinity *cis*-elements for the respective *trans*-acting factor.

4.2.1.1 Selection experiments

For the SELEX experiment, recombinant Roquin-1 N-terminus (aa 2-440) was biotinylated and used to perform three rounds of selection from an RNA library with a random sequence of 47 nts. With every round of selection the protein concentration was reduced and the washing procedure was intensified to increase the stringency of the selection. The output of the biotinylation step was estimated on a coomassie gel and showed a slight loss of material during the procedure (**Figure 28A left**). The efficiency of the reaction was then analyzed in a filter spot assay using PE-coupled streptavidin to detect biotinylated protein by fluoroimaging. Increasing signal strength correlated with higher protein amounts, and the negative control did not show any signal (**Figure 28A right**).

After transcription of the random RNA library, the first round of selection was performed, the selected RNAs were reverse transcribed and the cDNA served as template for the first RNA pool (**Figure 28B**). In total, three rounds of selection were successfully performed, and the cDNAs of every round were used as template in the Index PCR reactions. The experiment was repeated using Roquin-1 M199R (aa 2-440) in addition to Roquin-1 (aa 2-440). The obtained PCR products were analyzed by Illumina Solexa sequencing to identify sequences that were enriched during the three rounds of selection.

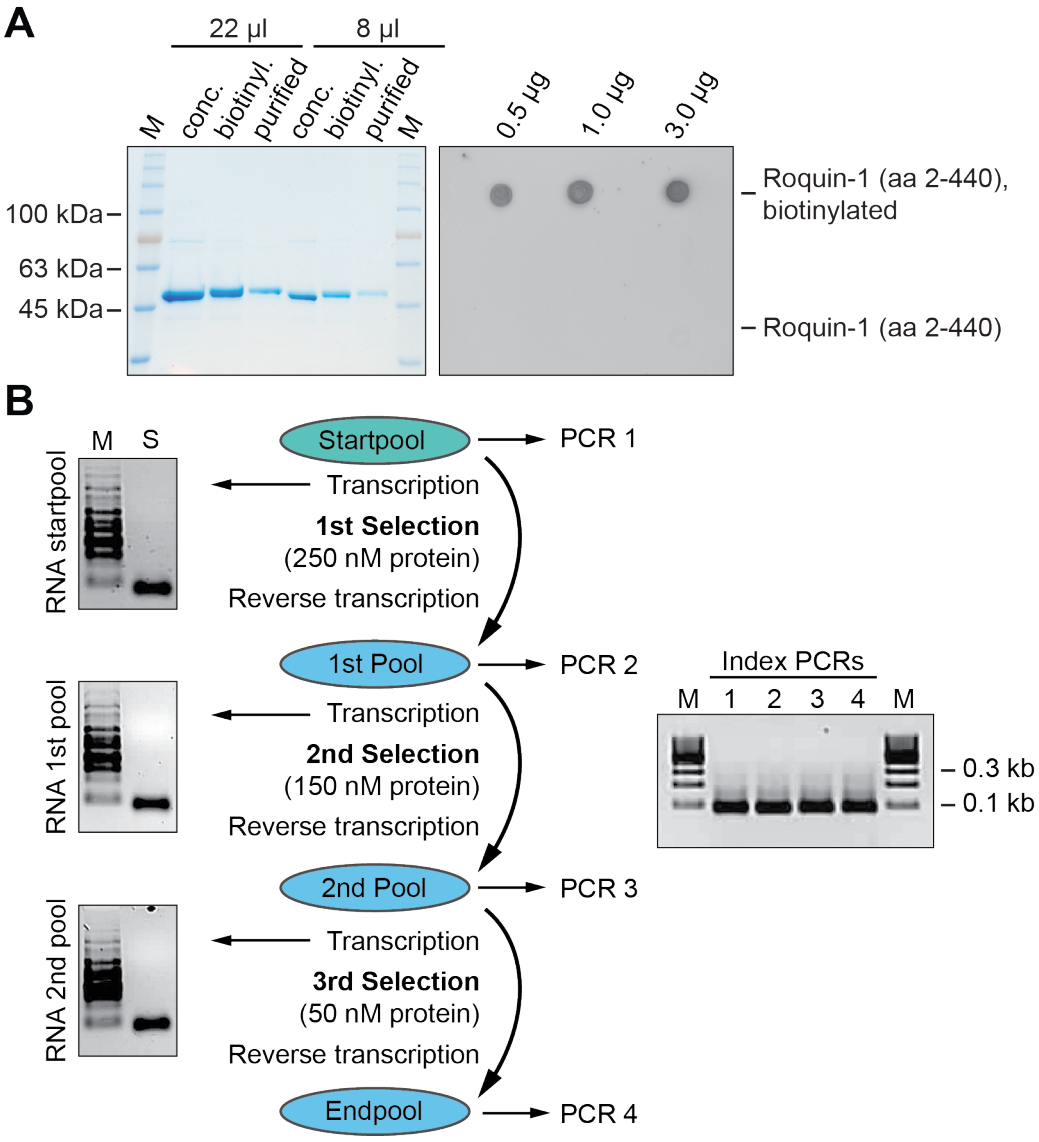

Figure 28: Documentation of the SELEX experimental procedure. A Left: Coomassie gel showing Roquin-1 (aa 2-440, 50 kDa) after spin concentration (conc.), after the biotinylation reaction (biotinyl.) and after purification of the biotinylated protein (purified). Right: Fluorography of biotinylated protein detected and visualized using streptavidin-PE. **B** Schematic representation of the selection procedure. Left side: Agarose gels showing the RNA pools resulting from *in vitro* transcription reactions (S: sample, M: marker). Right side: Final PCR products for the Illmina Solexa sequencing on agarose gel (M: marker).

4.2.1.2 SELEX data analysis

A first data analysis was performed by Dr. Michael Blank and Dr. Carsten Gröber (both AptaIT) and revealed that the RNA startpool consisted to almost hundred percent of unique sequence reads (**Figure 29A**). This changed after three rounds of selection with about eighty percent of unique reads, indicating that certain sequences had been enriched during the selection process. Unexpectedly, the first round of selection was covered by twice as many reads, although similar amounts of the Index PCR products

were to be combined for the final library. The random sequence stretch of the startpool showed an almost equal distribution of bases at every position (**Figure 29B**), being clearly different from the RNA pool after three rounds of selection (**Figure 29C**). Most prominently, the 3' end of the sequences showed a bias to thymine and guanine after the selection, and cytosine was less prevalent in the middle part of the sequence. Based on the co-occurrence of two frequent motifs of defined length, enriched sequences were identified and grouped in so-called patterns with highly homologous sequences. In total, 5559 enriched sequence patterns were identified in the first experiment.

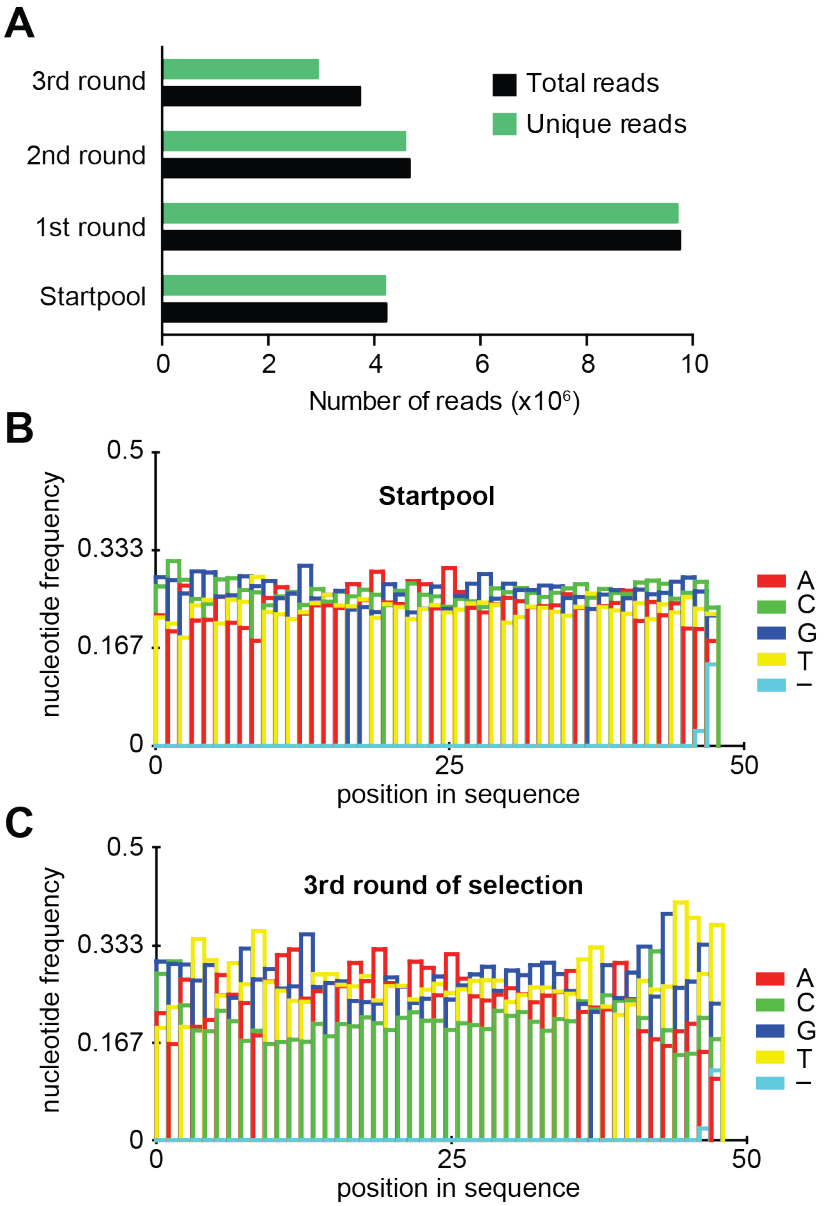

Figure 29: Sequence statistics of the Roquin-1 SELEX experiment (replicate 1). A Number of total and unique reads for every selection round. **B** Distribution of nucleotides for every position of the random sequence as found in the startpool. **C** Frequency of nucleotides at every position of the random sequence after three rounds of selection with Roquin-1 (aa 2-440). The analysis was performed by AptaIT.

To validate those patterns, the most frequent sequences were tested in a filter binding assay (FBA) using increasing amounts of recombinant Roquin-1 N-terminus (aa 2-440) to retain the ^{32}P-labeled RNA on a nitrocellulose filter (**Figure 30**). Without Roquin-1 there was no binding of RNA to the membrane, and patterns clearly exhibited Roquin-1-specific binding, since they did not bind to 250 nM and 500 nM streptavidin (data not shown). However, the patterns differed in their affinity to Roquin-1, with P1, P9, P12 and P15 being the strongest binders, and P19 showing a result similar to the random RNA pool, which served as negative control.

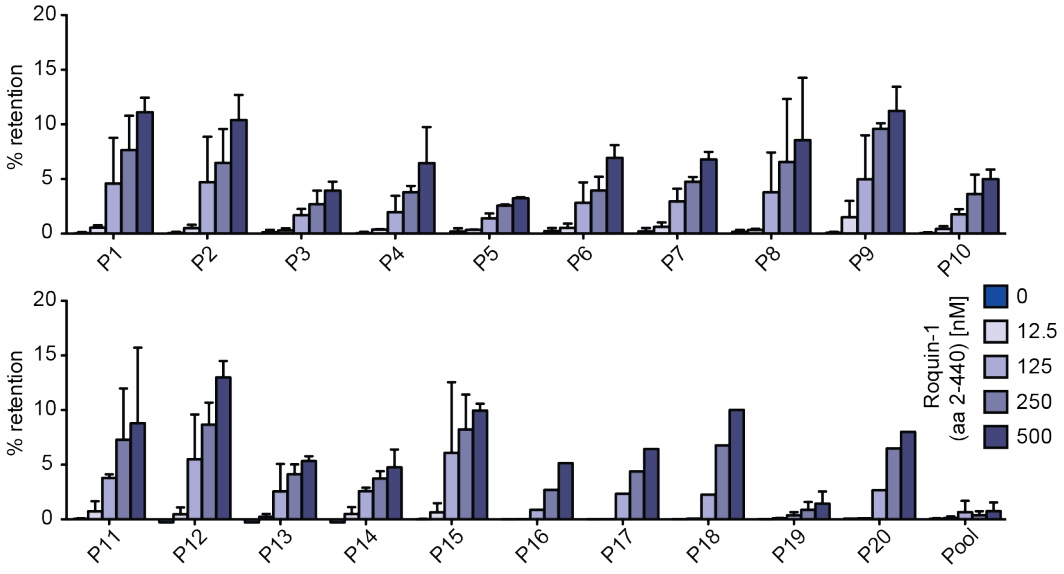

Figure 30: SELEX patterns bind to Roquin-1 N-terminus (aa 2-440). FBA analysis of enriched sequences with increasing protein concentrations as indicated. Startpool (Pool) RNA served as negative control. Error bars represent SD of 2 or 3 independent experiments.

In a second binding experiment, P9 and P12 were investigated more closely concerning their specific affinity to Roquin-1 (**Figure 31**). Here, the minimal ROQ domain (aa 147-326) was used in EMSA experiments and exhibited half maximal binding to those patterns in the lower nanomolar range. In addition, the same shift assays using an RNA-binding-deficient mutant of the ROQ domain (K239A R260A) showed no binding. This supports the hypothesis that the SELEX-enriched RNAs use the same protein interface like the *Tnf* CDE stem-loop for binding to Roquin-1. The definition of the minimal ROQ domain and the screening for binding-deficient mutants is described in paragraphs 4.2.2 and 4.2.3 respectively.

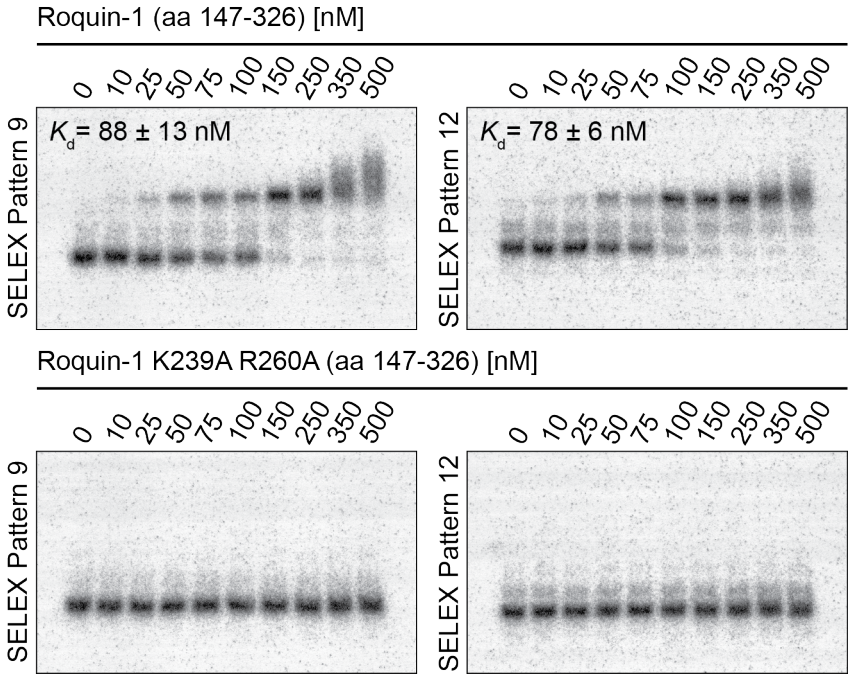

Figure 31: High-affinity patterns are specifically bound by the ROQ domain. EMSA experiment with pattern 9 and 12 and the minimal ROQ domain (aa 147-326; upper panel) or an RNA-binding-deficient mutant (aa 147-326, K239A R260A; lower panel). K_d values are obtained from curve fitting to the relative bound fraction per lane (not shown).

Dr. Andreas Gruber, Prof. Dr. Mihaela Zavolan's group, performed additional bioinformatics analyses to elucidate similarities between the enriched sequences. Searching for hexamer enrichment, he identified sequences that were strongly enriched in the first experiment (Roquin-1, replicate 1) and exhibited a similar tendency for Roquin-1 and Roquin-1 M199R in the second set of experiments (**Figure 32A**). Comparing the two replicates of Roquin-1 concerning their z-scores for all possible hexamers revealed a correlation of 0.56 and identified four candidates with the strongest enrichment in both data sets (**Figure 32B**). Sequence logos embedding the enriched hexamers clearly demonstrated that the common motif was rather a 12-mer (5'-TGCGTTTTAGGA-3') with reduced strictness at position two (G), seven (T) and eleven (G) (**Figure 32A**). The distribution of the enriched hexamers within the random sequence stretch was surprisingly homogenous with a strong bias to the 3' end (**Appendix I**), which raised the question whether those areas are prone to form secondary structures. Indeed, the sequence motif most probably folds into a hexaloop that is closed via a C-G base pair followed by a double-stranded stem structure (**Figure 33**). Interestingly, the *Ox40* 3'UTR contains a sequence stretch closely resembling the SELEX sequence motif and structure. Binding and functional analyses of this *Ox40* SELEX-like stem-loop are shown in 4.2.5.

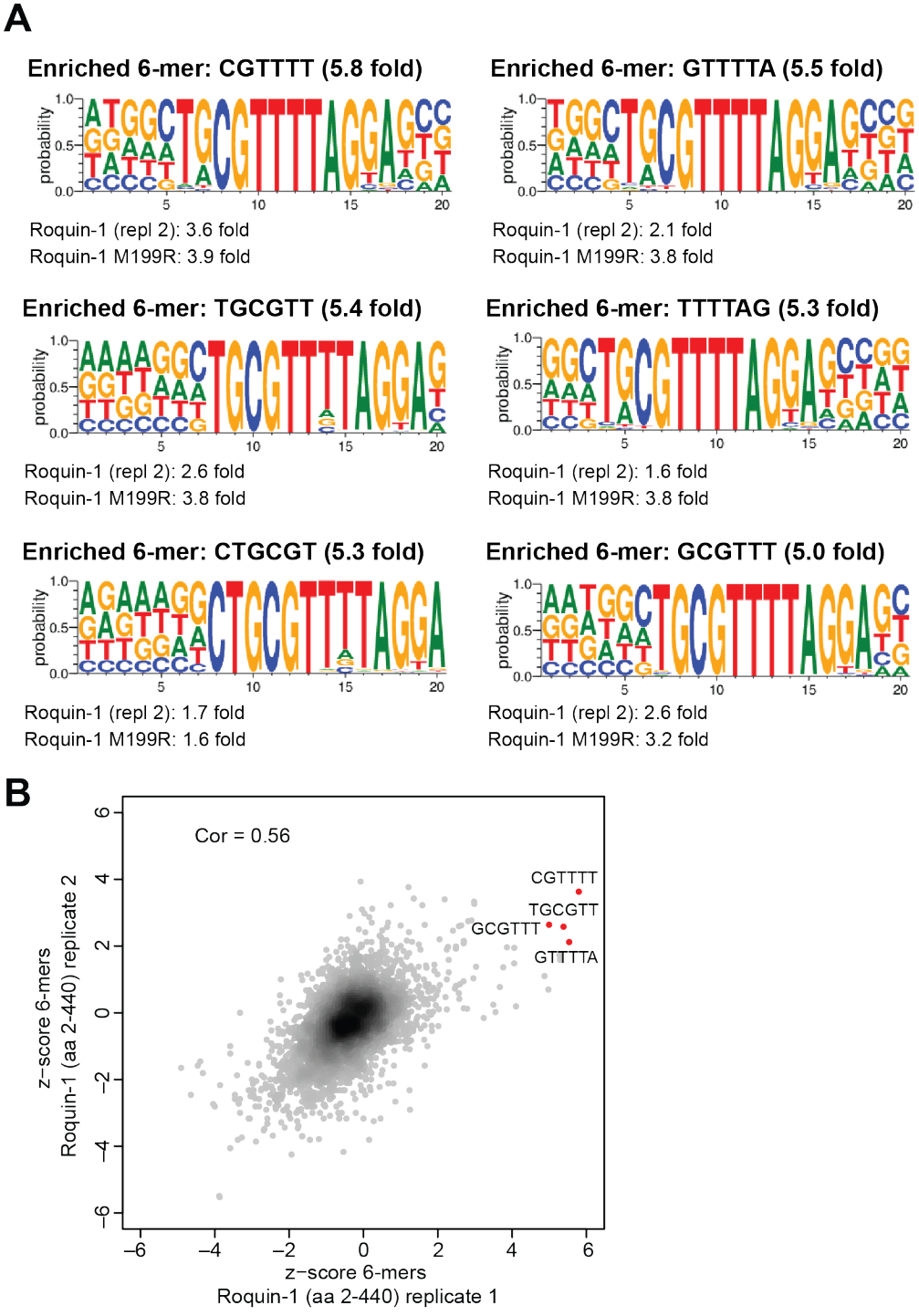

Figure 32: Analysis of enriched hexamers within the SELEX patterns. A Enrichment of hexamers in Roquin-1, replicate 1 (bold headline) and in the second set of samples (fold changes given below). The sequence logo shows the nucleotide distribution around the enriched hexamers. **B** Correlation analysis of hexamer enrichment in Roquin-1 replicate 1 and replicate 2. The most frequent hexamers in both samples are highlighted in red. This analysis was performed by Dr. Andreas Gruber.

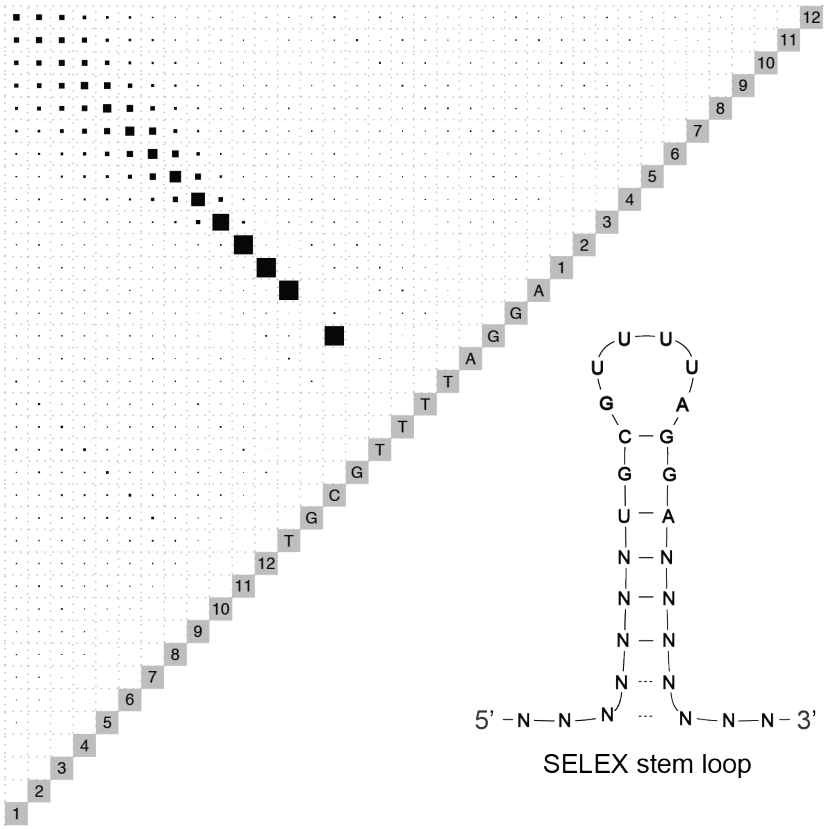

Figure 33: Secondary structure prediction of the SELEX motif. Left side: Boxplot analysis showing base paring probabilities as the size of black boxes for each nucleotide combination. Right side: Schematic representation of the putative RNA structure of the SELEX sequence motif. The boxplot was provided by Dr. Andreas Gruber.

4.2.2 Crystal structures of the ROQ domain and the ROQ-RNA complex

An accurate picture of Roquin interactions with its target mRNAs on a molecular level can be obtained by solving the protein structure and the structure of the protein-RNA complex. This was successfully done in collaboration with Prof. Dr. Michael Sattler's group and Prof. Dr. Dierk Niessing's group (both Helmholtz Zentrum München) and enabled a mutational analysis of amino acids located within the binding interface as well as a validation of the *Tnf* CDE RNA. The results of this project (paragraphs 4.2.2 to 4.2.4) are published in Schlundt et al., 2014.

The first step in this analysis aimed at the re-definition of the ROQ domain, which was so far only defined by sequence homology and domain prediction (Vinuesa et al. 2005). Using limited proteolysis, Dr. Andreas Schlundt, Prof. Dr. Michael Sattler's group, identified a stable minimal domain spanning Roquin-1 aa 147-326, a region completely conserved in the human homolog. To make sure this minimal ROQ domain is fully capable of binding the *Tnf* CDE, the best-characterized Roquin-bound RNA element, dissociation constants (K_d values) for Roquin-1 full-length (fl), N-terminus (aa 2-440)

and ROQ (aa 147-326) recombinant proteins were determined in EMSA experiments (**Figure 34**). All three proteins yielded comparable K_d values (120-240 nM), with the full-length protein being remarkably comparable to the minimal domain, indicating that the ROQ domain is sufficient for *Tnf* CDE binding. Dr. Andreas Schlundt confirmed the stem-loop structure of the *Tnf* CDE (**Figure 34B**) in a 2D imino proton NOESY, visualizing the present hydrogen bonds and thus the base pairing of the RNA stem (data not shown).

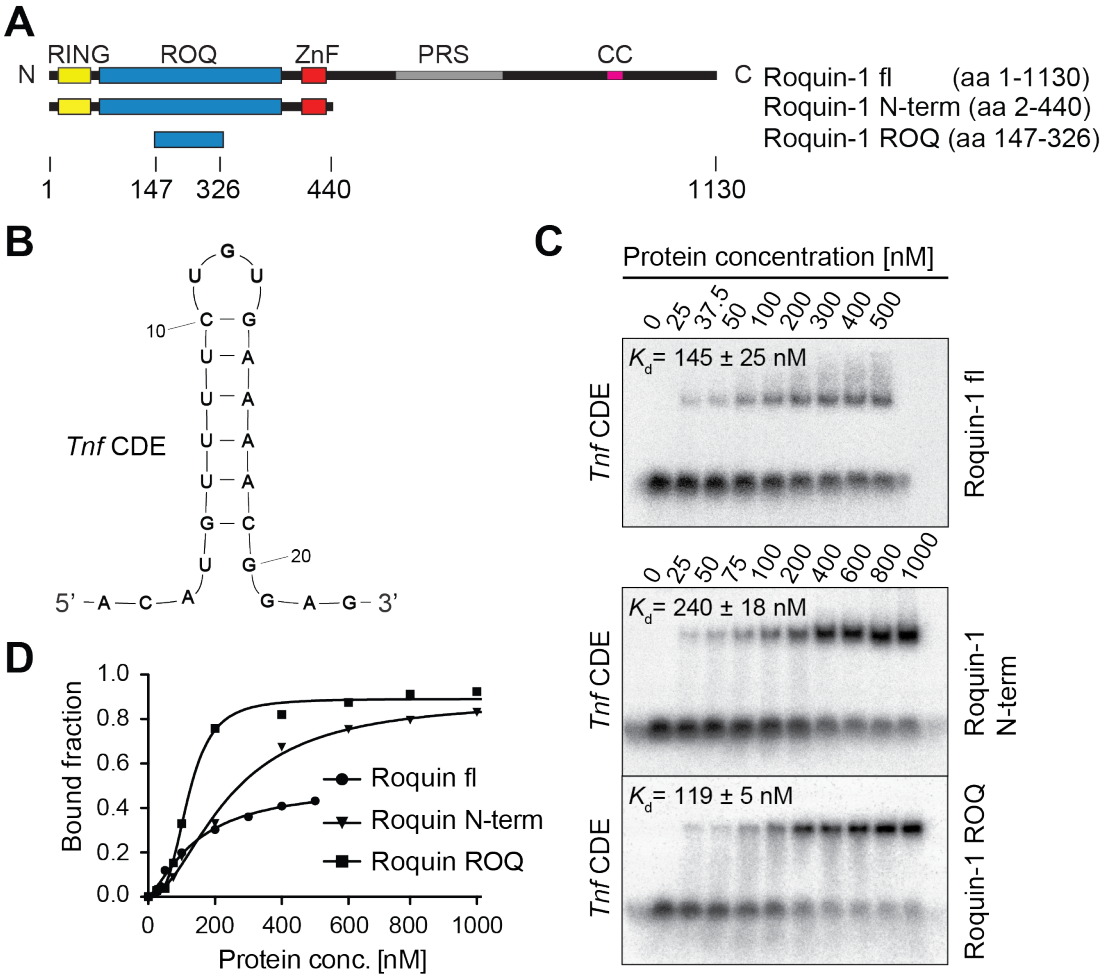

Figure 34: Definition of the minimal ROQ domain by RNA binding. A Three length variations of the Roquin-1 protein, namely Roquin-1 full-length (fl, showing the domain organization of the protein; ZnF: zinc finger, PRS: proline-rich sequence, CC: coiled coil region), N-terminus (N-term), and ROQ, as used for RNA binding analysis. **B** *Tnf* CDE stem-loop as used in EMSA and crystallization experiments. **C** Band shift assays with different Roquin-1 proteins and the *Tnf* CDE RNA. **D** Quantification of **C** and curve fitting to determine dissociation constants, K_d±s.e. (standard error) (given in **C**).

Determining the atomic structure of the ROQ domain (aa 147-326) was achieved by successful protein crystallization experiments. Dr. Robert Janowski, Prof. Dr. Dierk Niessing's group, subsequently solved the crystal structure to a resolution of 1.9 Å. The

domain adopted a canonical Winged Helix (WH) fold involving α-helices 2, 3, 4 and β-strands 2, 3, 4 (**Figure 35**). The regions N- and C-terminal to the WH domain contain α-helices that contact each other and form a second domain-like fold.

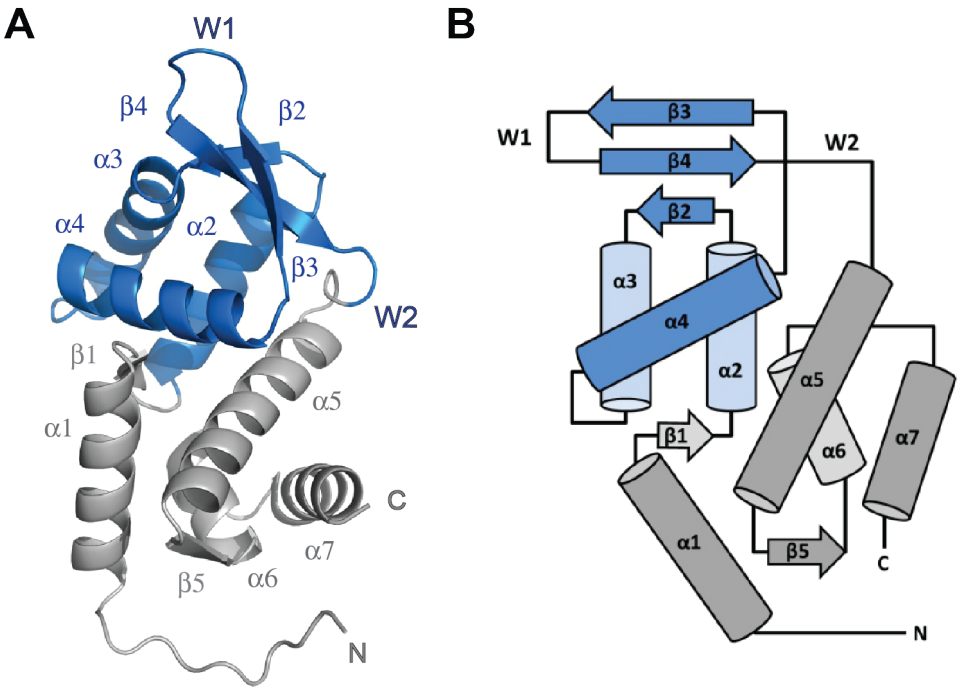

Figure 35: Crystal structure of the ROQ domain. A Cartoon presentation of the ROQ protein structure. α-helices, β-sheets and loops (W) are numbered according to their sequential order from N- to C-terminus. Blue color highlights the winged helix (WH) domain. **B** Schematic domain topology of the crystal structure shown in **A**. The figures were obtained from Dr. Andreas Schlundt.

Next, the ROQ-*Tnf* CDE complex was crystallized and again Dr. Robert Janowski solved the structure (**Figure 36A**). The conformation of the ROQ domain within the complex was very similar to the structure of the protein alone, yet with a more compact folding of the W1 region located between β3 and β4. The *Tnf* CDE RNA showed a triloop structure with six Watson and Crick base pairs forming the stem (**Figure 36A**). Interestingly, the interaction between the WH fold of the ROQ domain and the *Tnf* CDE was mainly non-sequence-specific via electrostatic contacts to the phosphate backbone of the RNA stem (**Figure 36B and C**). ROQ binding did not involve the 3' half of the *Tnf* CDE stem. The W1 region recognized the loop of the RNA structure and showed base specific interactions for all nucleotides forming the triloop. U11 and U13 were flipped out and thus more exposed to the protein interface, and G12 was found in a tight coordination with the surrounding amino acids (R219 and Q247) (**Figure 36D**). Another base-specific contact was observed for U4, which was flipped out of the stem and interacts with the amino acids W184, R188 and F194 (**Figure 36D**).

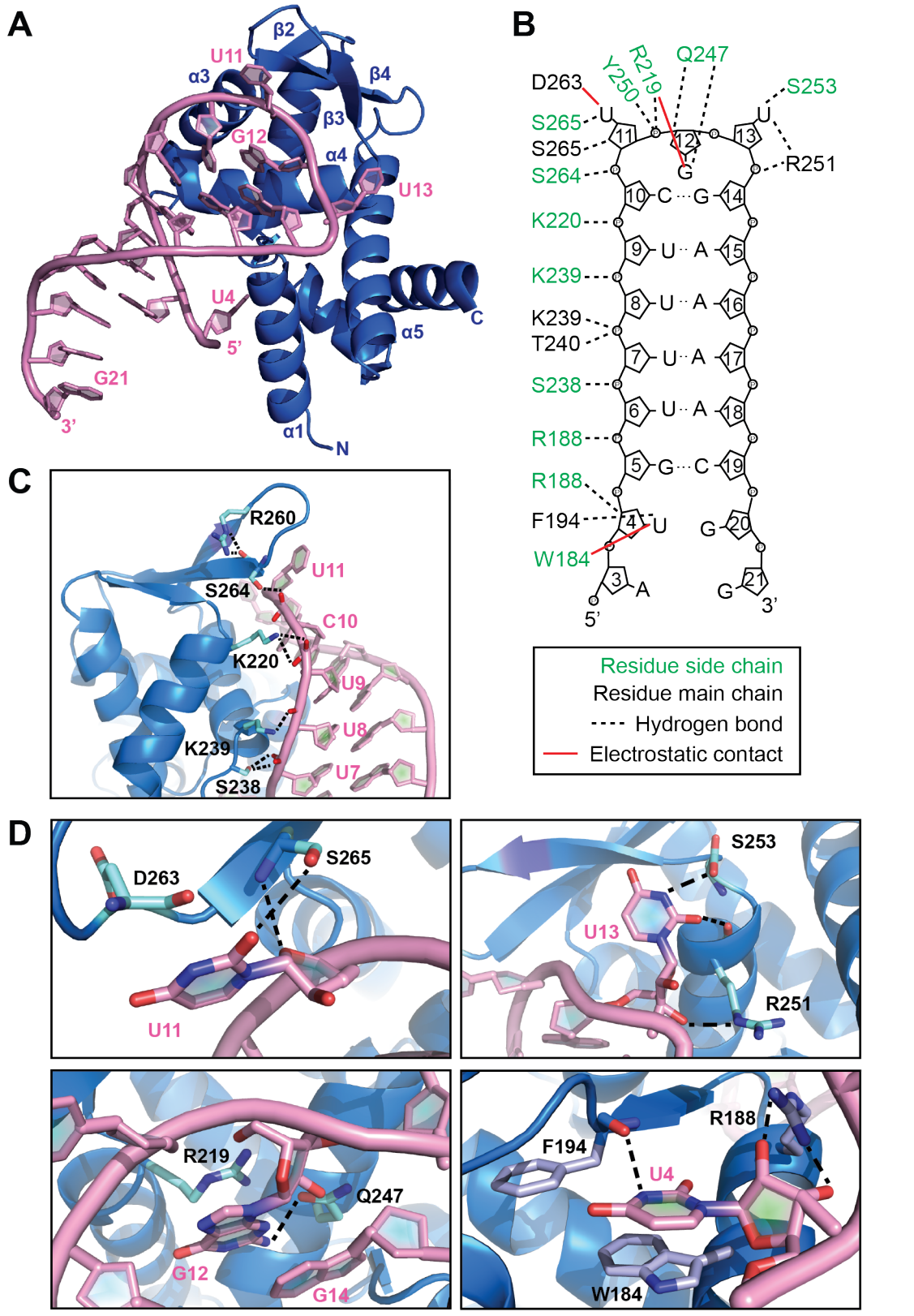

Figure 36: Crystal structure of the ROQ-*Tnf* CDE complex. A Cartoon presentation of the ROQ domain (aa 174-325, blue) and the bound *Tnf* CDE RNA stem-loop (magenta). **B** Scheme of the RNA stem- loop and the contacting amino acids in the ROQ-*Tnf* CDE complex. Different types of interactions are indicated. **C** Close-up of the 5' arm of the stem within the complex structure. **D** Close-ups of base-specific protein-RNA contacts. Figures provided by Dr. Robert Janowski and Dr. Andreas Schlundt.

4.2.3 Mutational analysis of the ROQ-RNA interaction site

4.2.3.1 Binding assays

The impact of specific protein-RNA contacts for the binding was studied in a mutational analysis using EMSA experiments to monitor the complex formation. Based on the crystal structure and on NMR (Nuclear magnetic resonance) data from Dr. Andreas Schlundt, amino acids were chosen for mutagenesis. Key residues being directly or indirectly influenced by *Tnf* CDE interactions were identified through strong chemical shift perturbations upon RNA binding and plotted on the crystal structure of the complex (**Figure 37A**). In total, fifteen amino acids of the ROQ domain, most of them positively charged, were mutated into alanine, whereas one was mutated into tyrosine, and the recombinant proteins were then applied to binding reactions with the *Tnf* CDE (**Figure 37B, Appendix II and III**). Most mutations had minor effects on the complex formation, yet mutations of certain lysine residues (K220A, K239A and K259A) resulted in a strong reduction of affinities. Binding was also considerably impaired by the R260A mutation that affected the W1 region of the WH fold. Combining K239A and R260A within one protein further reduced binding to almost undetectable levels in the probed concentration range (**Figure 37B and C**), which underlines that the interaction of the ROQ domain with the *Tnf* CDE depends on several contacts at the same time. Interestingly, mutations of amino acids forming base-specific contacts to the *Tnf* CDE RNA (R219, R251, S253, S265) had minor or no effects on RNA binding (**Appendix II and III**).

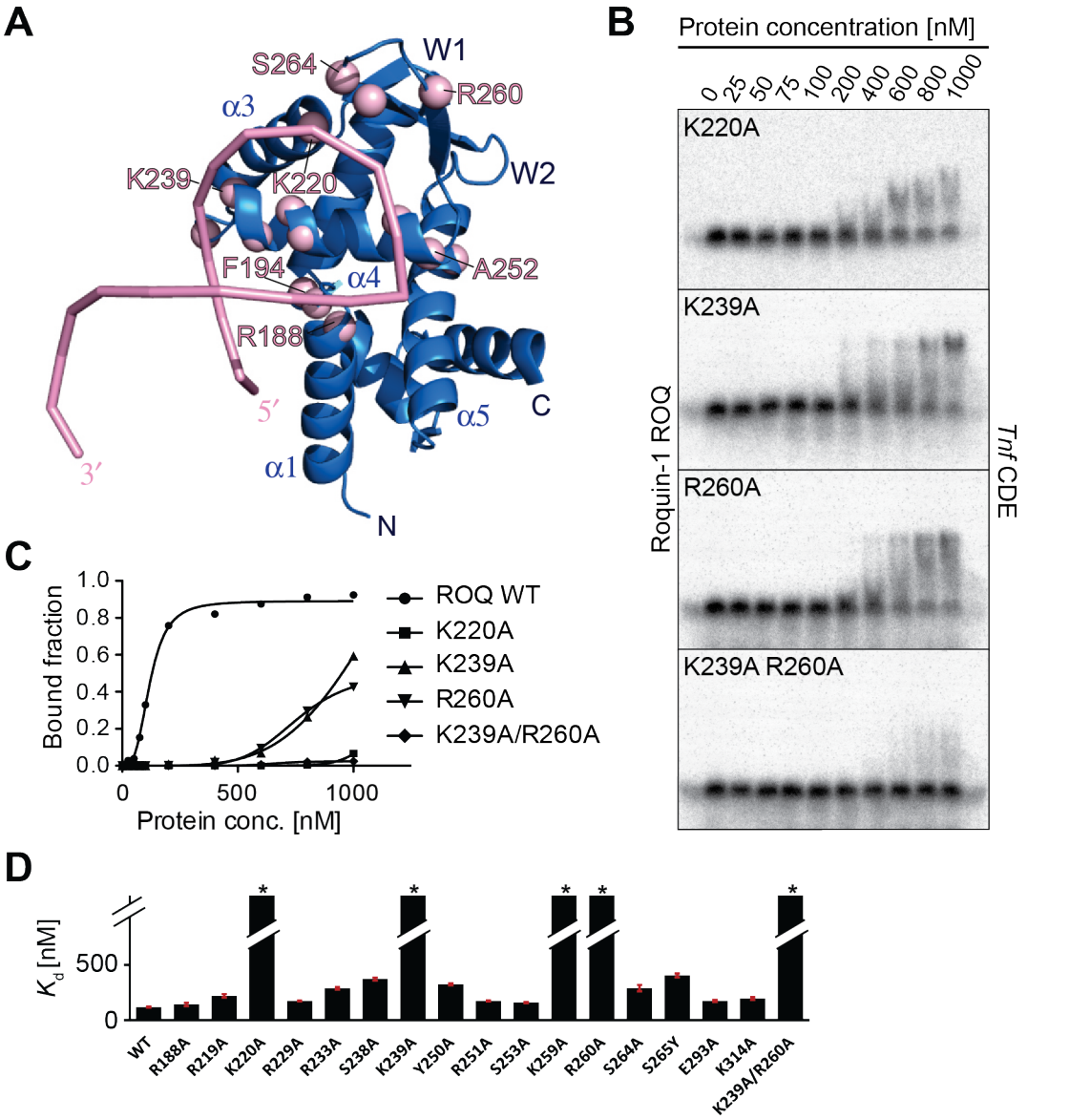

Figure 37: Mutational analysis of the ROQ RNA-binding interface. A Amino acids with large chemical shift perturbations as determined by NMR analysis of ROQ and ROQ-*Tnf* CDE were plotted on the crystal structure of the complex. The scheme was provided by Dr. Andreas Schlundt. **B** Autoradiographies of EMSA experiments using ROQ mutants with a strong impact on *Tnf* CDE binding. **C** Binding curves of ROQ mutants (**B**) compared to ROQ wild-type (WT). Overview of dissociation constants of ROQ WT and all protein mutants tested in *Tnf* CDE binding assays. The plotted values are K_d±s.e. (see also **Appendix II and III**). Asterisks indicate extrapolated K_d values >1000 when calculation was not possible from the EMSA quantification.

4.2.3.2 Cell-based functional assays

To assess whether impaired RNA binding results in compromised post-transcriptional regulation of Roquin-1 targets, a functional cell culture assay was established. Thereby, *Rc3h1-2*$^{-/-}$ MEFs were transduced to express different reporter genes, namely *ICOS* fl or *Ox40* fl. Furthermore, *ICOS* CDE_{260} was used, which is a chimeric construct consisting of the *ICOS* CDS and an artificial 3'UTR of 260 nts from the *Tnf* 3'UTR. The CDE_{260} contains the CDE but lacks AU-rich elements (AREs). The expression levels of those reporter genes were determined by cell surface staining of ICOS or Ox40 and flow cytometric analysis. In a second retroviral infection, Roquin-1 wild-type (WT) or the RNA-binding-impaired mutants were overexpressed from retroviral expression constructs containing the Thy1.1 marker gene to monitor infection rates. Comparable Roquin-1 expression levels were achieved by carefully titrating the virus supernatants to infection rates between 30% and 70% in a preliminary experiment (**Figure 38 and Appendix IV**). Half-maximal infection also made it possible to investigate infected ($Thy1.1^+$) and non-infected cells ($Thy1.1^-$) within one sample and to calculate the relative MFI of the reporter. Thus, the results from different combinations of reporters and protein mutants could be compared.

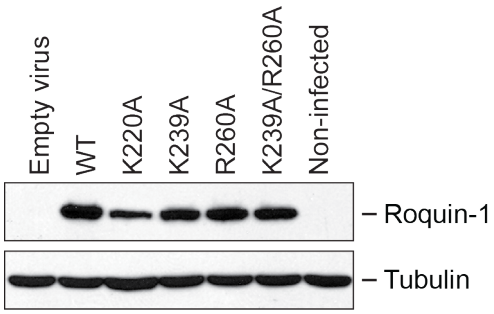

Figure 38: Comparable overexpression of Roquin-1 wild-type (WT) and RNA-binding-impaired mutants. Roquin-1 proteins (WT, K220A, K239A, R260A and K239A R260A as indicated) were expressed in *Rc3h1-2*$^{-/-}$ MEFs by retroviral transduction and detected in the cell lysates by immunoblotting with the 3F12 monoclonal antibody that recognizes Roquin-1 and Roquin-2. Detection of tubulin served as loading control.

Functional assays using the *ICOS* fl reporter are shown as contour plots in **Figure 39A**, **top**, and a quantification of all experiments is presented in **Figure 39B**, **left**. As expected, overexpression of Roquin-1 WT induced a strong reduction of ICOS on the cell surface. Roquin-1 mutants harboring one amino acid exchange (K220A, K239A and R260A) exposed impaired regulation but were still able to reduce ICOS levels by 30-60%. Furthermore, the K239A R260A double mutant no longer reduced ICOS expression. This is in line with the prominent deficiency of the double mutants in RNA

binding being observed in EMSA experiments (**Figure 37**). When *Ox40* fl was used as reporter gene, Roquin-mediated regulation followed a similar pattern (**Figure 39A, middle**). While Roquin-1 WT overexpression reduced Ox40 to 30% relative to uninfected cells, the single mutants of Roquin-1 had an intermediate regulatory capacity. However, the K239A R260A double mutant did not repress Ox40 protein expression.

Finally, Roquin-1 function on a *Tnf* CDE-containing 3'UTR was analyzed using the *ICOS* CDE_{260} reporter construct (**Figure 39A, bottom**). Compared to *ICOS* fl and *Ox40* fl, the *ICOS* CDE_{260} was even more effectively repressed by Roquin-1 WT, suggesting that the CDE_{260} 3'UTR is highly responsive to Roquin-1 regulation. Accordingly, the single mutants (K220A, K239A and R260A) that were strongly compromised in *Tnf* CDE binding *in vitro* still repressed ICOS expression. The Roquin-1 K239A R260A mutant showed functional impairment but still reduced ICOS levels by 40%. Taken together, these experiments show that Roquin-1-mediated post-transcriptional regulation directly correlates with its RNA binding affinity.

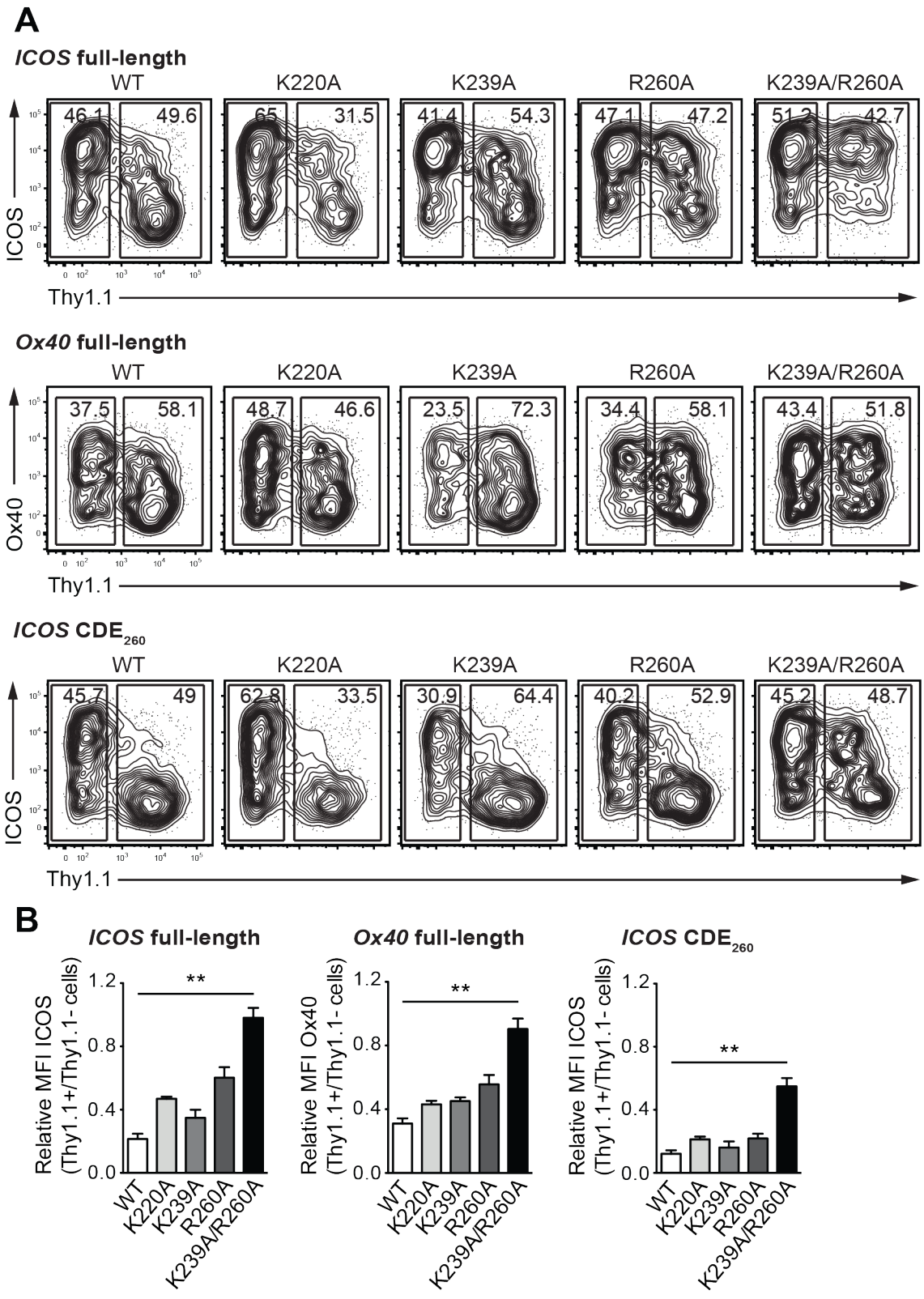

Figure 39: Functional analysis of Roquin-1 ROQ domain mutants. A Flow cytometry analysis of ICOS or Ox40 reporter expression in *Rc3h1-2*$^{-/-}$ MEFs upon overexpression of Roquin-1 variants. Thy1.1 serves as marker for transduction with Roquin-1-expressing retroviruses (WT or mutants as indicated). *ICOS* fl (top), *Ox40* fl (middle) and *ICOS* CDS with a truncated *Tnf* 3'UTR (260 nts) containing the *Tnf* CDE (bottom). **B** Relative reporter MFI (Thy1.1+/Thy1.1-) of **A**. Error bars indicate range of two measured values (K220A) or SD of four independent experiments. Statistical significance was determined by one-way ANOVA Kruskal-Wallis test and Dunn's multiple comparison test (**p<0.01).

4.2.4 Investigating the spectrum of CDE stem-loops

From the crystal structure of the ROQ-*Tnf* CDE complex it was deduced that the protein-RNA contacts are mainly non-sequence specific. Hence, different *Tnf* CDE mutants were generated to test which parts of the stem-loop structure allow for deviation from the CDE consensus sequence in EMSA experiments. In addition, more distantly related triloops were proposed and tested as functional Roquin *cis*-elements.

4.2.4.1 Mutational analysis of the *Tnf* CDE

Inverting the purine (Pu) and pyrimidine (Py) order of the triloop from Py-Pu-Py to Pu-Py-Pu (loop mutant 3: LM3) had the strongest impact and completely abolished binding of the ROQ domain (**Figure 40B and E**). However, inverting single positions as in G12C (LM1) or U13G (LM2) was well tolerated. LM1 exhibited the same affinity as the WT *Tnf* CDE and LM2 binding was only mildly affected. Next, different stem mutants (SM) were probed in ROQ binding assays (**Figure 40C and E**). The closing base pair of the loop structure was mutated from C-G to U-A (SM1), which increased the dissociation constant three-fold. Compared to that, SM2 with an inversion of C10 and G14 was less affected, implying that a C-G base pair is preferred at this position. Exchanging the upper two U-A base pairs for C-G (SM3) resulted in a slightly attenuated complex formation. Extending the stem of the *Tnf* CDE by two possible G-C pairs also decreases ROQ binding (**Figure 40D**). The mutational analysis of the *Tnf* CDE RNA revealed that a number of different variants have reduced affinities for the ROQ domain but are nevertheless tolerated in binding. This finding indicates that the ROQ domain might be able to recognize a broader spectrum of RNA stem-loop structures than anticipated by Leppek et al., 2013.

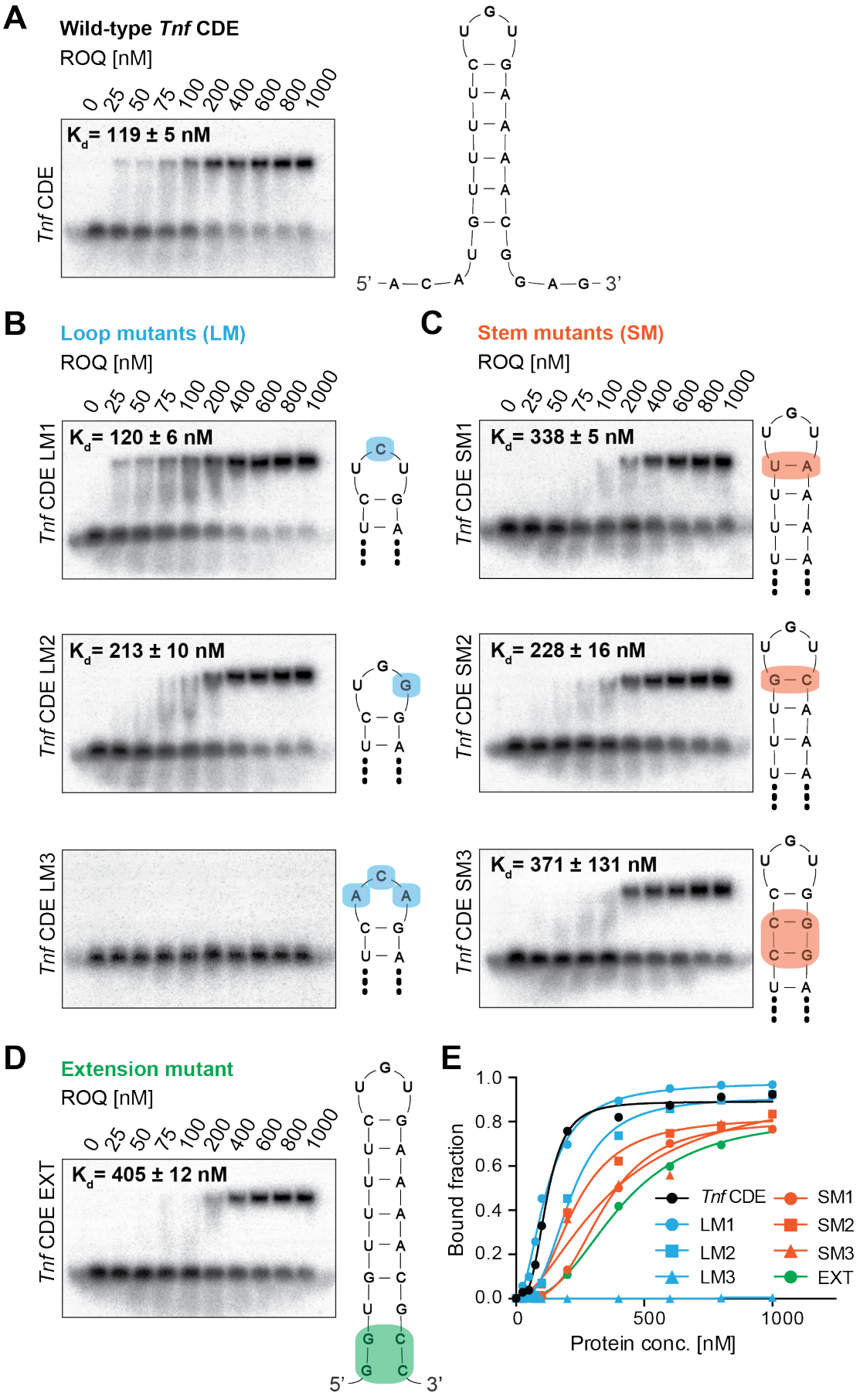

Figure 40: Mutational analysis of the *Tnf* CDE RNA. A EMSA showing binding of ROQ domain to the *Tnf* CDE (scheme on the right). **B** ROQ binding analysis of three loop mutants (LM). Nucleotides

different from *Tnf* CDE are highlighted in blue. **C** Stem mutants (SM) probed for ROQ binding. Differences from *Tnf* CDE are marked in orange. **D** EMSA experiment with extension mutant (EXT). **E** Binding curves of the *Tnf* CDE RNA and indicated mutants. K_d±s.e. values are calculated from the respective curve fitting to the relative bound fraction per lane.

4.2.4.2 CDE-like stem-loops

In the 3'UTRs of *ICOS* and *Ox40* there are triloops predicted that differ from the *Tnf* CDE in several positions. Those CDE-like stem-loops were probed in EMSAs and exhibited binding to the ROQ domain, yet with clearly reduced affinities (**Figure 41**).

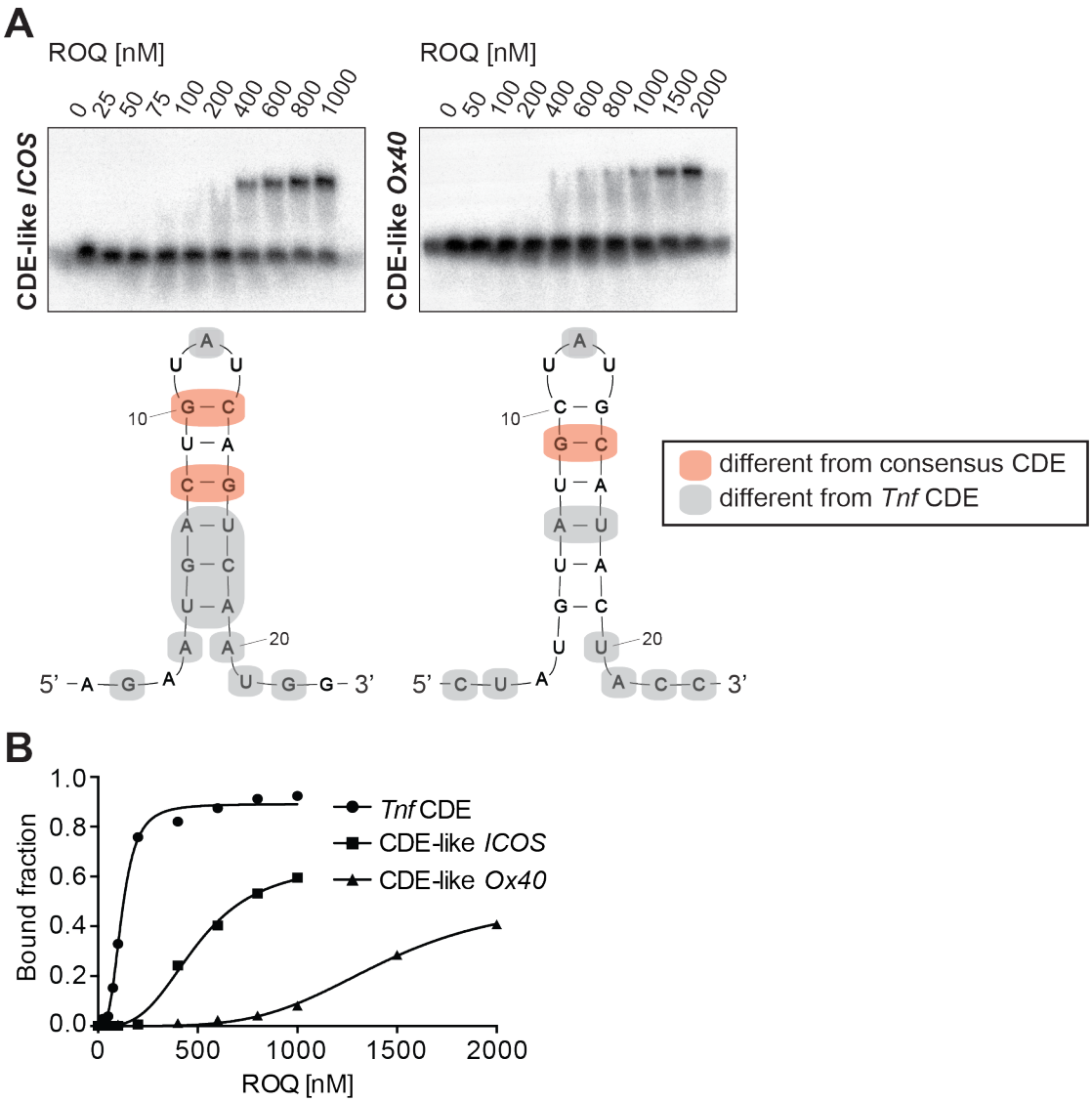

Figure 41: Binding of CDE-like RNA stem-loops from *ICOS* and *Ox40* 3'UTR. A Autoradiographies of EMSAs using *ICOS* CDE-like (nts 740-762) (left) and *Ox40* CDE-like (nts 924-946) (right) RNA and the ROQ domain. Nucleotide positions different from the *Tnf* CDE or the CDE consensus sequence are marked in grey or orange respectively. **B** Binding curves of CDE-like stem-loops compared to *Tnf* CDE.

To test whether those low-affinity stem-loops can be functional *cis*-elements, a cell-based assay was established by Dr. Stephanie Edelmann, Prof. Dr. Vigo Heissmeyer's group, to monitor target expression upon acute deletion of Roquin-1 and Roquin-2. To this end, *Cre-ERT2; Rc3h1-2*$^{fl/fl}$*; CAG-CAR*$^{stop\text{-}fl}$ MEFs were treated with tamoxifen, and CAR surface expression served as marker for efficient genomic deletion in flow cytometry analyses (**Figure 42A right**). By immunoblotting it was confirmed that Roquin-1 and Roquin-2 proteins are almost completely eliminated after four days of tamoxifen treatment (**Figure 42A left**). To decipher the role of CDE-like stem-loops in post-transcriptional gene regulation, different *ICOS* and *Ox40* reporter constructs were tested (**Figure 42B and C**). Overexpression of *ICOS* and *Ox40* full-length constructs and subsequent tamoxifen treatment resulted in an upregulation of ICOS and Ox40 on the surface of CAR$^+$ cells. This derepression upon *Rc3h1-2* deletion was not observed for constructs containing only the CDS of *ICOS* and *Ox40*. The *ICOS* 3'UTR contains one consensus CDE stem- loop at its 3' end and one CDE-like stem-loop located at the 5' end. Truncation of the 3'UTR to remove the CDE stem-loop did not reduce the responsiveness of the *ICOS* ΔCDE construct compared to the *ICOS* full-length construct. This suggests that the presence of a consensus CDE stem-loop is not required for Roquin-mediated *ICOS* regulation. On the other hand, the *Ox40* 3'UTR only contains a CDE-like stem-loop. When this was removed by shortening the 3'UTR, Ox40 upregulation due to Roquin deletion was drastically reduced, indicating that Roquin-mediated *Ox40* regulation requires the presence of a CDE-like stem-loop structure.

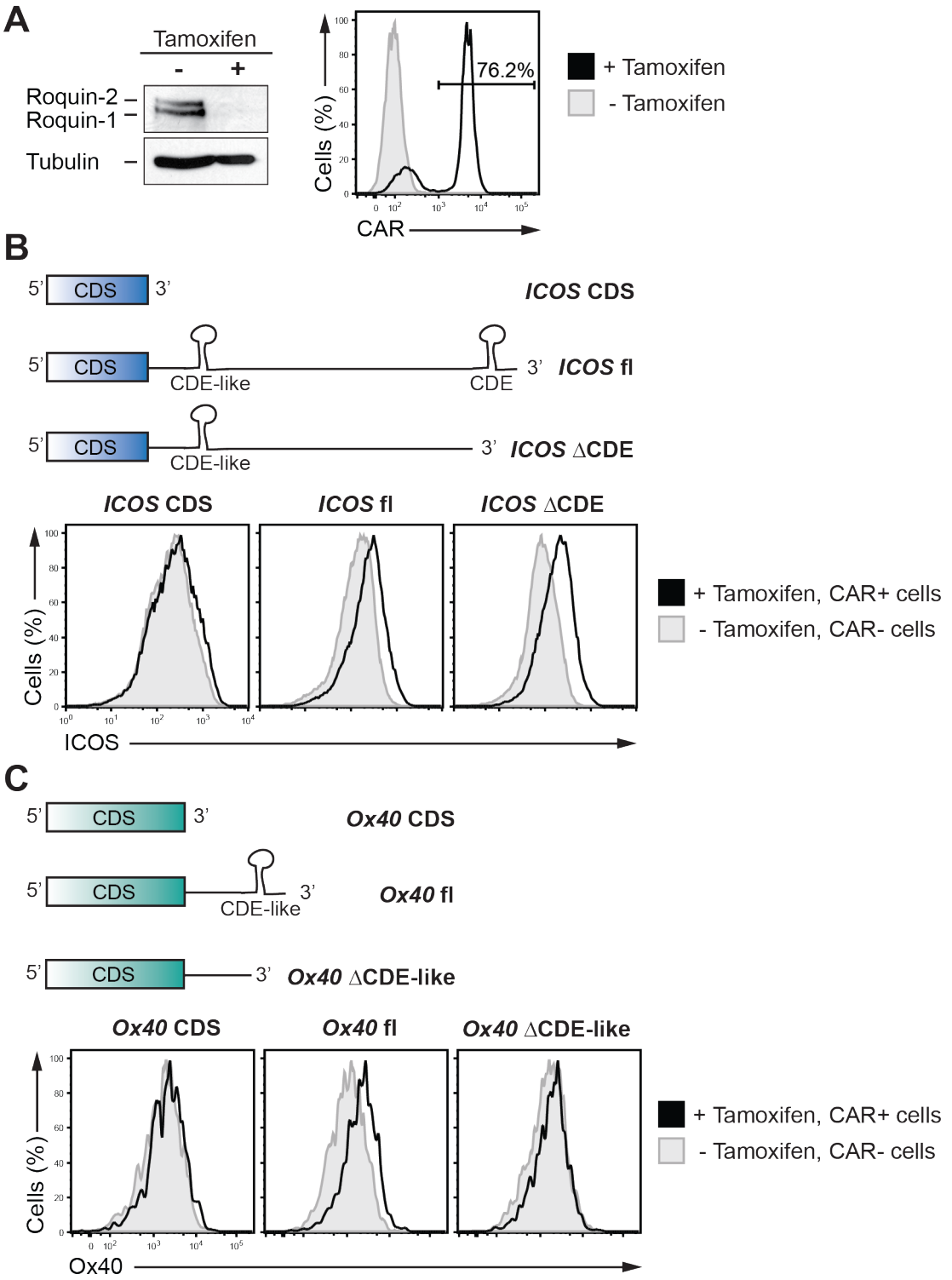

Figure 42: CDE-like stem-loops are functional *cis*-elements in Roquin-mediated regulation. **A** Tamoxifen induced deletion of Roquin-1 and Roquin-2 in *Cre-ERT2;Rc3h1-2*$^{fl/fl}$*; CAG-CAR*$^{stop\text{-}fl}$ MEFs was monitored by immunoblotting (left) and by upregulation of CAR on the cell surface as assessed by flow cytometry (right). **B** Schematic representation of *ICOS* constructs with different 3'UTR lengths (top) and expression levels of ICOS in response to tamoxifen treatment measured by flow cytometry. **C** As in **B** with different *Ox40* constructs. The ICOS data (**B**) was provided by Dr. Stephanie Edelmann.

4.2.5 *Cis*-element analysis of the *Ox40* 3'UTR

Combining the findings of the different analyses creates a comprehensive picture of Roquin-mediated Ox40 regulation. Roquin-1 and Roquin-2 specifically bound to the 3'UTR (**Figure 15C and D**) and substantial regulation of Ox40 protein expression required the presence of the 3'UTR (**Figure 15B and Figure 42C**).

Secondary structure prediction of the *Ox40* 3'UTR sequence suggested the presence of a triloop (**Figure 27B**) that was shown to be a functionally active CDE-like *cis*-element (**Figure 42C**). Interestingly, also a hexaloop was proposed, which closely resembles the RNA stem-loop that was independently identified in SELEX experiments (**Figure 33**). Those structures do not only have the same shape but also share the SELEX sequence motif within the hexaloop (**Figure 43A and B**). By multiple sequence alignment (Clustalw) and subsequent structural analysis (RNAalifold) of *Ox40* 3'UTRs from different species, conservation of the SELEX-like stem-loop was investigated (**Figure 43C**). Whereas the overall sequence conservation of the *Ox40* 3'UTR is rather poor, the region of the SELEX-like stem-loop (position 128-137 of the 3'UTR) shows high conservation. Interestingly, only the position being less well-defined in the sequence motif of the SELEX patterns shows some variation. The structural analysis shows that this region is most likely forming a hexaloop with two C-G pairs at the top of the stem. Another highly conserved part is located at position 171-185 of the 3'UTR. This part forms the previously described CDE-like stem-loop (**Figure 41A**). Again, the twelve nucleotides forming the stem are fully conserved, whereas the three nucleotides in the loop allow some variation.

To prove that the SELEX-like stem-loop is bound by Roquin-1 comparable to other known *cis*-elements, EMSA experiments were performed using the ROQ domain and some of the mutants described in section 4.2.3.1. The *Ox40* SELEX-like stem-loop was recognized and bound by Roquin-1 ROQ with a slightly higher K_d value (~370 nM) than the *Tnf* CDE (~120 nM), and mutations that reduced binding to the *Tnf* CDE also impaired the *Ox40* SELEX-like stem-loop binding (**Figure 44**). However, some differences became evident. ROQ K220A seemed to be less impaired compared to the *Tnf* CDE experiment, but Y250A and S265Y clearly decreased *Ox40* SELEX-like binding to a larger extent. Meanwhile, crystallization of the ROQ *Ox40* SELEX-like RNA complex was successful, and Dr. Robert Janowski was able to solve the crystal structure. Together with NMR data from Dr. Andreas Schlundt it proves that the ROQ domain uses the same interface to contact the SELEX-like hexaloop from the *Ox40* 3'UTR and the *Tnf* CDE (data not shown).

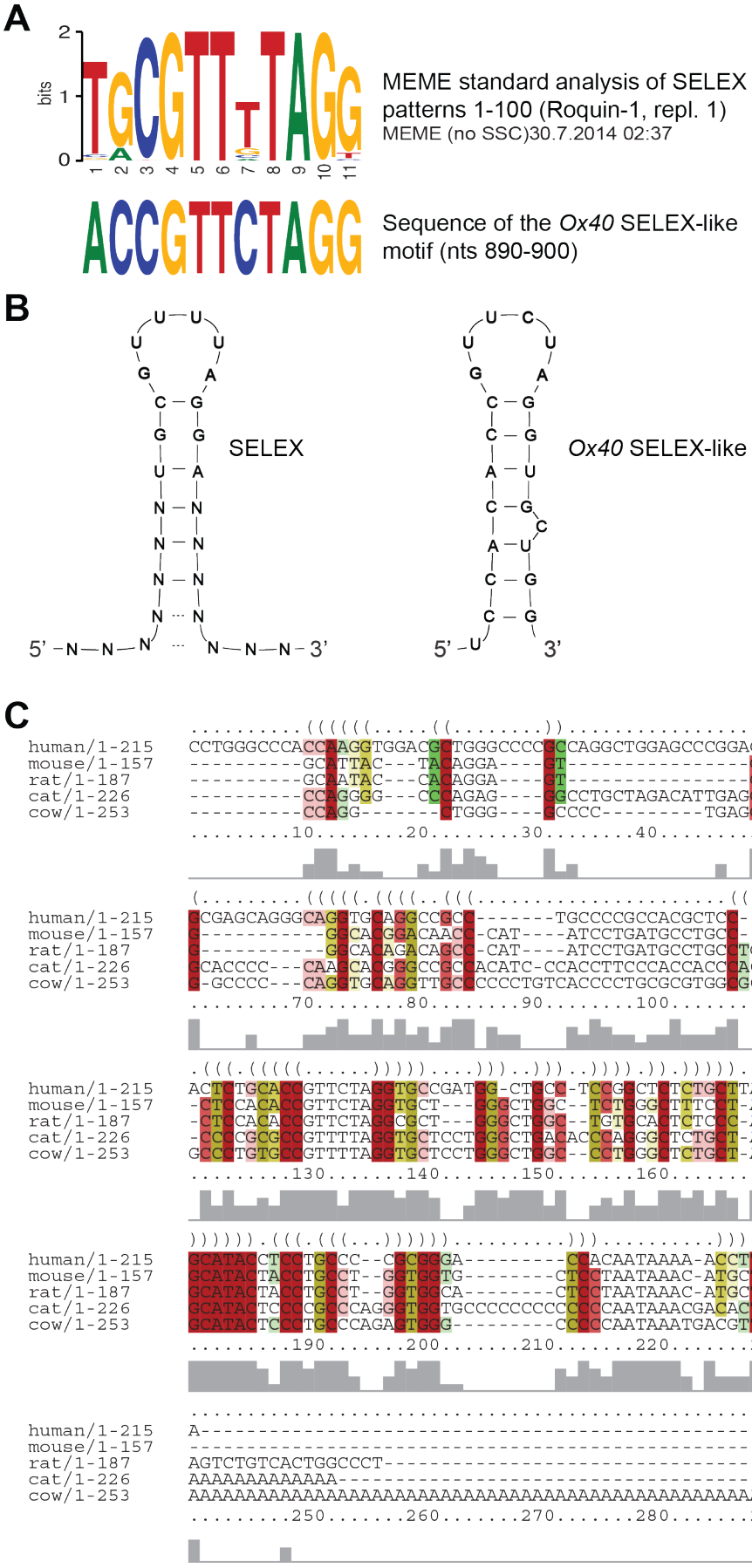

Figure 43: Motif and conservation analysis of the *Ox40* 3'UTR. A A SELEX-like sequence in the *Ox40* 3'UTR closely resembles the MEME motif found in SELEX-enriched RNA sequences.

B Schematic representation of the predicted SELEX stem-loop and the *Ox40* SELEX-like stem-loop as used for binding analyses. **C** Multiple alignment of *Ox40* 3'UTR sequences from different species demonstrates sequence conservation (grey boxes) and structural conservation (obtained from Clustalw2 and subsequent RNAalifold analysis). The darker the color of the nucleotide position the more likely it forms the indicated (top row, brackets and dots) structure. Here, the SELEX-like stem-loop is located at position 128-137 and the CDE-like stem-loop is located at position 171-185.

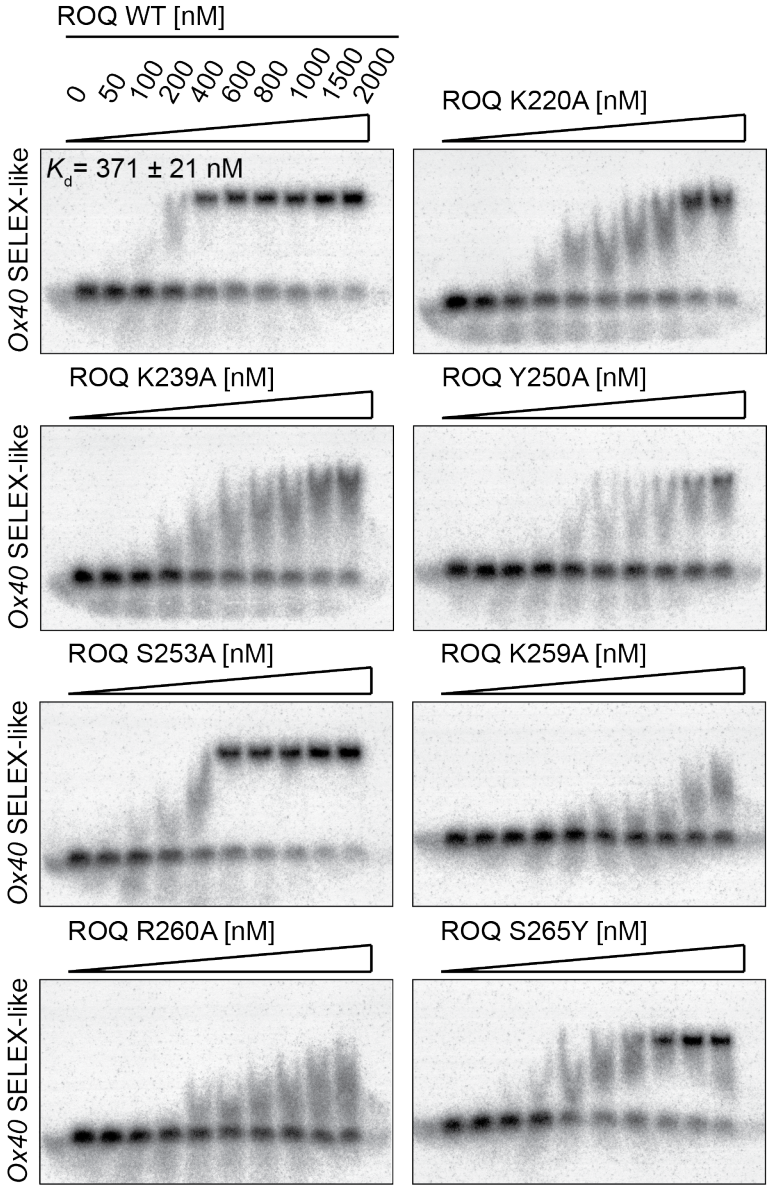

Figure 44: *Ox40* SELEX-like RNA binding analysis with ROQ domain mutants. Autoradiographies visualizing the binding of ROQ WT and of different ROQ mutants to the *Ox40* SELEX-like RNA stem-loop. K_d±s.e. for ROQ WT binding was calculated by curve fitting to the relative bound fraction per lane.

In the last part of this study, the contribution of the two *Ox40* stem-loops to the protein-RNA interaction and the Roquin-mediated post-transcriptional regulation was examined. Different *Ox40* constructs were designed to investigate the necessity of the SELEX-like and the CDE-like stem-loop within their sequence context (**Figure 45**). Truncation of the *Ox40* 3'UTR in a retroviral expression vector abolished both stem-loops (*Ox40* 3'UTR 1-40 and 1-80) or destroyed the CDE-like stem-loop alone (*Ox40* 3'UTR 1-120). In addition to that, parts of the sequence were mutated to prevent stem formation of the SELEX-like or the CDE-like element or both at the same time (**Figure 45 and Appendix V**).

Figure 45: *Ox40* 3'UTR constructs as tested in binding and functional analyses. Green boxes: SELEX-like stem-loop, red boxes: CDE-like stem-loop, grey boxes: truncations and mutations that prevent stem- loop formation.

EMSA experiments using the complete *Ox40* 3'UTR and recombinant Roquin-1 N-terminus (aa 2-440) for binding revealed two high-affinity binding modes as seen from the two band shifts (75nM) (**Figure 46**). Only one high-affinity band shift was observed for the SELEX-like and the CDE-like single mutants, indicating that the second band depended on the presence of a second binding element. In line with this, high-affinity binding of Roquin-1 (aa 2-440) to the *Ox40* 3'UTR was completely abolished when both stem-loops were mutated. In all four EMSAs a supershift was observed for protein concentrations of 400 nM and higher, which seemed to be independent from the presence of specific *cis*-elements.

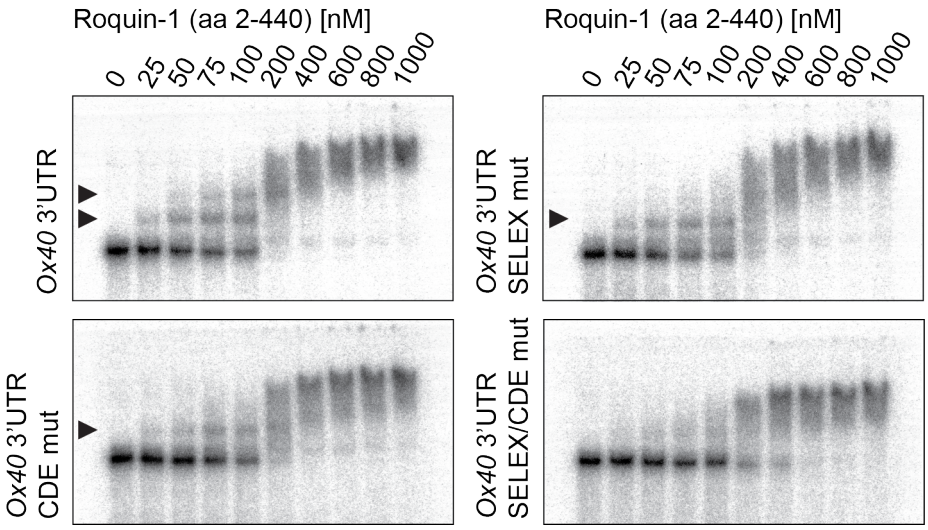

Figure 46: Binding analysis of the *Ox40* 3'UTR in band shift assays. EMSA experiment with the complete *Ox40* 3'UTR and the indicated mutated versions binding to Roquin-1 (aa 2-440). Arrowheads indicate specific high-affinity band shifts.

The *Ox40* constructs with shortened 3'UTRs or the mutant variants (**Figure 45**) were probed in a functional assay using the previously described Roquin-1-inducible *Rc3h1-2*$^{-/-}$ MEFs (see section 4.1.2). After expression of Ox40 via retrovirus transduction, half of the cells were treated with doxycyclin to induce Roquin-1 and mCherry overexpression. Roquin-1 overexpression in turn reduced Ox40 surface expression depending on the provided 3'UTR (**Figure 47A**). Calculation of the relative MFI and normalization to the *Ox40* CDS revealed a clear correlation between the presence of specific *cis*-elements and the ability of Roquin-1 to regulate Ox40 expression (**Figure 47B**). The two truncated 3'UTRs 1-40 and 1-80 do not contain an intact SELEX-like or CDE-like stem-loop and were not substantially regulated by Roquin-1 overexpression. The SELEX-like stem-loop, present in 3'UTR 1-120, allows intermediate repression as compared to the *Ox40* full-length construct. Specific mutations of the SELEX-like or the CDE-like motif in the context of the full-length construct also resulted in an intermediate regulation upon Roquin-1 induction. Finally, a construct with mutations destroying both stem-loops was no longer a target of Roquin-1-mediated regulation. Instead, this constructs exhibited a relative Ox40 protein expression, which was comparable to the *Ox40* CDS. These functional experiments clearly indicate that Roquin-1 post-transcriptionally regulates the *Ox40* mRNA via recognition and binding of two distinct stem-loop structures within its 3'UTR.

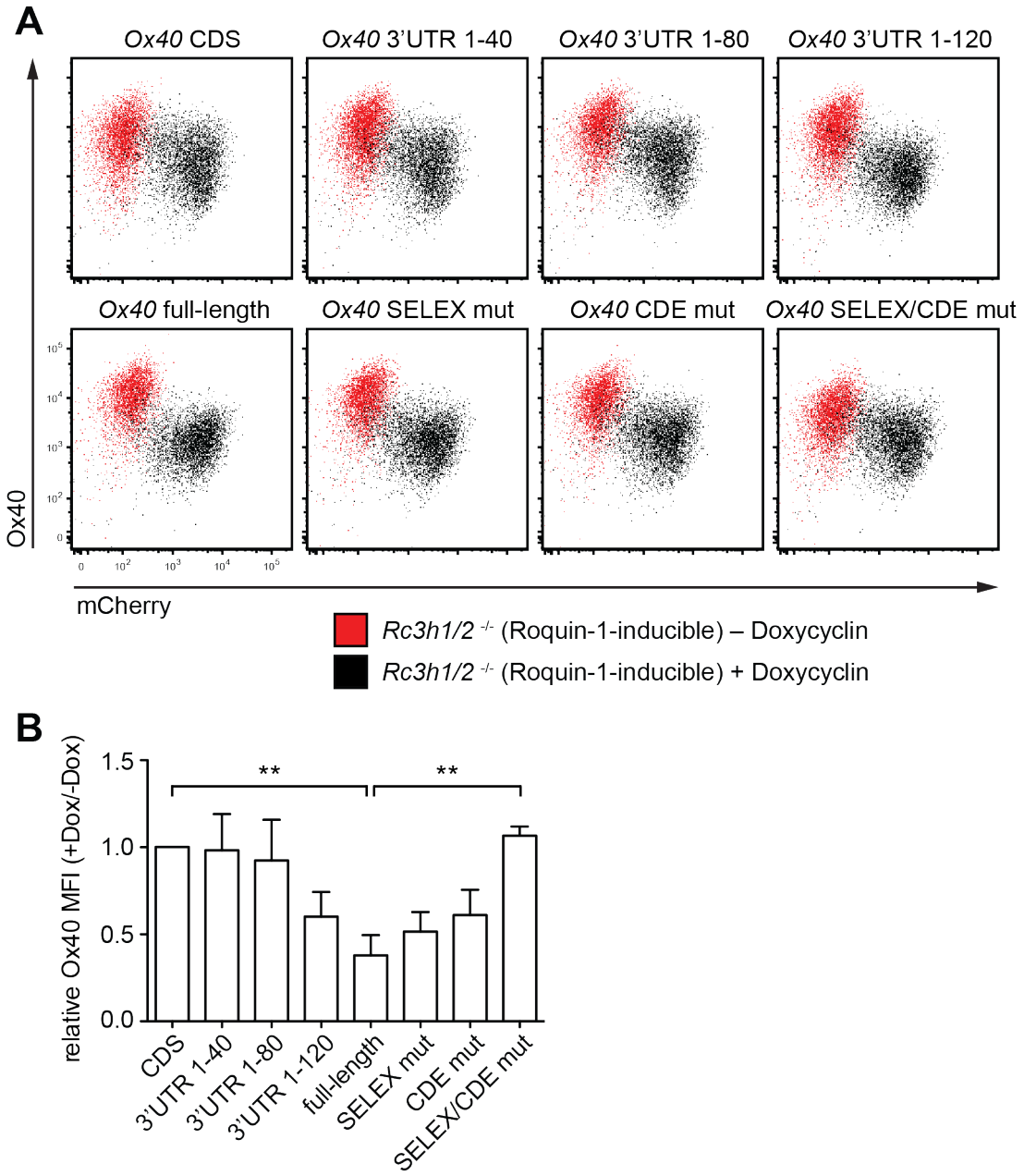

Figure 47: Functional analysis of truncated and mutated *Ox40* 3'UTRs. A Representative dot plots showing expression levels of Ox40 depending on the expression construct (indicated above each plot) and on Dox-induced expression of Roquin-1-p2A-mCherry in *Rc3h1-2*$^{-/-}$ MEFs. **B** Relative Ox40 MFI normalized to expression levels from the *Ox40* CDS construct. Error bars show SD of 7 (CDS, 1-40, 1-80, 1-120, full-length), 6 (SELEX mut, CDE mut) or 3 (SELEX/CDE mut) independent experiments. Statistical significance was calculated by one-way ANOVA Kruskal-Wallis test followed by Dunn's multiple comparison test (**p<0.01).

5 Discussion

5.1 Roquin target identification

5.1.1 Microarray analyses of Th1 cells upon acute deletion of Roquin

5.1.1.1 Microarrays as tools for Roquin target identification

Microarrays are an established tool to detect mRNAs that are differentially regulated in two groups of samples. Our well-controlled Th1 cell culture system of retrovirus-mediated Roquin-1 and Roquin-2 deletion and simultaneous upregulation of CAR on the cell surface allowed the identification of Roquin-regulated mRNAs. Since deletion of *Rc3h1-2* is only induced *in vitro* in Th1 cell cultures that contain similarly activated T cells, we circumvented the massive T cell activation difference observed in *Rc3h1-2$^{fl/fl}$; CD4 Cre* mice compared to controls (Vogel et al. 2013).

In a time course experiment, progressive Roquin deletion and upregulation of its target Icos was monitored to find the best time point for microarray analyses. No differences in Roquin-1 and Roquin-2 protein levels were observed comparing wild-type and *Rc3h1-2$^{fl/fl}$* samples until 72 hours after T cell activation (**Figure 10B**). However, after 72 hours the Roquin degradation bands were less prominent than after 48 hours, indicating that cleavage of Roquin specifically happens shortly after T cell activation. This is in line with recent findings of our group (Jeltsch et al. 2014). 96 and 120 hours after activation, Roquin protein levels were reduced in the *Rc3h1-2$^{fl/fl}$* samples. The remaining Roquin protein was presumably derived from the 40% of cells that did not experience efficient virus infection and thus Cre-recombinase activity resulting in an upregulation of CAR (**Figure 10A**). Therefore, we enriched Thy1.1$^+$ CAR$^+$ cells by cell sorting to prepare RNA for the microarray analysis. To avoid secondary effects of Roquin deletion, I wanted to harvest the cells as early as possible after T cell activation. Since *Icos* mRNA levels only increased massively 120 hours after T cell activation, this time point was chosen for the analysis.

Using the *Icos$^{-/-}$* background in a repeat experiment allowed excluding targets that were only regulated in response to high Icos levels and thus strengthened the obtained data. Yet, no such targets were present among the top 20 candidates. Nevertheless, the method detects both primary, directly bound mRNA targets and mRNAs that are regulated as a secondary effect, for example in response to changes in T helper cell activation or differentiation. Only some of those false positive candidates can be excluded via the *Icos$^{-/-}$* control arrays.

As microarrays only detect mRNAs included in the analysis they do not represent a completely unbiased and global approach. RNA sequencing is a method offering global investigation of the transcriptome with a very high sensitivity. The technique even enables the discovery of unknown or non-coding transcripts and splice variants. However, this was not required, since the study aimed at identifying known mRNAs that are targeted by Roquin. Moreover, RNA sequencing would also detect indirect Roquin targets and is considerably more cost-intensive.

Another drawback of microarray analyses and other methods investigating the transcriptome of target cells is their dependency on altered mRNA expression levels. Hence, mRNA targets bound by Roquin and only regulated on the translational level will not be identified in these assays. A connection of translational regulation and Roquin was found in the time course experiment to evaluate the retrovirally induced deletion of Roquin-1 and Roquin-2 in Th1 cells (**Figure 10**). Expression of the known target *Icos* in response to Roquin deletion was measured both on the protein and on the mRNA level (**Figure 10C and D**). Whereas *Icos* mRNA amounts only changed drastically after 120 hours of Th1 cell culture (80 hours post retroviral infection), the amount of Icos protein on the cell surface was already strongly increased 96 hours after T cell activation as determined by flow cytometry. This suggests that Roquin regulation involves translational inhibition as well as mRNA destabilization and decay.

Nevertheless, the microarray analyses provided a comprehensive list of target candidates. As expected, most of the differentially regulated mRNAs were upregulated in the samples lacking Roquin-1 and Roquin-2, and only a few genes showed decreased expression (**Figure 13**). The high reproducibility of upregulated but not downregulated genes further underlined the reliability of the data. Differential expression of selected target candidates was confirmed by qPCR measurements, which offer a broad dynamic range for mRNA quantification (Provenzano & Mocellin 2007; Wang et al. 2006). Hence, the qPCR data revealed that fold changes obtained from the array data analysis rather underrated the extent of differential regulation. Consequently, the list (**Table 20**) of mRNAs contains promising candidates with strongly increased expression levels in response to *Rc3h1-2* deletion in Th1 cells.

5.1.1.2 Roquin target candidates

The target candidate with the highest fold change was Ccl22 (**Table 20**), a secreted chemokine, which is mainly expressed in macrophages and monocyte-derived DCs (Vulcano et al. 2001). As a chemoattractant, it seems to play a role in trafficking activated/effector T cells to sites of inflammation (Chantry et al. 1999; Chang et al. 1997). However, there is no evidence that T cells themselves are a major source of Ccl22.

Another strongly regulated factor was Ebi3, which associates as heterodimer with p28 to form IL-27 and with IL-12p35 to form IL-35. IL-27 has been shown to induce proliferation of naïve $CD4^+$ T cells and to promote the production of the Th1 cytokine IFN-γ in cell culture (Pflanz et al. 2002). IL-35 has been involved in immunosuppression by direct action on effector T cells or by promoting Treg cell proliferation (Olson et al. 2013). Yet, there is poor evidence that Th1 cells themselves produce IL-27 or IL-35.

The serine-threonine protein kinase Pim2 is a target candidate mainly expressed in spleen, thymus and brain of mice (Allen et al. 1997). According to the ImmGen database Pim2 is highly expressed in most lymphocytes, including T cells. Pim2 is described as a proto-oncogene, since overexpression through proviral insertion or transgenic alleles increases the incidence of lymphoid tumors (Breuer et al. 1989; Allen et al. 1997). On a molecular level, Pim2 stabilizes c-myc, reduces apoptosis via Bad and increases survival and proliferation of cells by phosphorylation of different target proteins (Yan et al. 2003; Zhang et al. 2008; Hammerman et al. 2005). Thus, high Pim2 levels in T cells lacking Roquin-1 and Roquin-2 might promote increased T cell survival and proliferation. In addition, T cell proliferation is supported by the IL-2 cytokine, which is also a target candidate in our array analyses.

Costimulatory receptors of T cells form a group of genes that appears to be affected by Roquin deletion. This is particularly interesting, since Icos functions as an inducible co-stimulator on T cells and thus promotes prolonged T cell activation and supports Tfh cell differentiation (Hutloff et al. 1999; Choi et al. 2011). Similarly, the expression of the costimulatory molecules Ox40 (Tnfrsf4), CD30 (Tnfrsf8) and Ctla4, which are among the top 20 Roquin target candidates, is only induced by T cell activation (Croft 2010; Carreno & Collins 2002; Watts 2005). Ctla4 is expressed in the late phase of T cell activation and is an inhibitor of T cell immune responses, since it antagonizes CD28 costimulation (Rudd & Schneider 2003). This is not in line with the hypothesis that targets of Roquin promote T cell activation and autoimmunity. CD30 is a costimulator mainly described in the context of lymphocyte malignancies. It is expressed on activated T cells, and it was shown to promote Th2 and Th17 differentiation (Romagnani et al. 1995; Sun et al. 2010). Interestingly, we also observed increased Th17 differentiation of *Rc3h1-2*$^{-/-}$ T cells *in vivo* and in cell culture (Jeltsch et al. 2014). Recently, is has been shown that CD30 is increased on $CD8^+$ T cell from SLE patients (Cabrera et al. 2013), indicating that CD30 might be involved in the development of autoimmunity. Moreover, the deletion of both CD30 and Ox40 in FoxP3-deficient mice prevented tissue infiltrations and autoimmunity in these animals (Gaspal et al. 2011). Increased Ox40 signaling has been involved in autoimmunity by different other studies (Bansal-Pakala et al. 2001; Murata et al. 2002). Since the target candidate Ox40 was investigated in more detail throughout this thesis work, it is discussed separately in 5.3.

Surprisingly, a number of target candidates are only expressed in lymphocytes other than T cell as for example CD19, a prominent B lymphocyte antigen. Other candidates are CD86, a ligand of the T cell costimulator CD28 also known as B7, as well as CD180, CD24a and CD79a/b. According to the ImmGen database (Kim & Lanier 2013) these genes are exclusively expressed on B cells, DCs, macrophages or monocytes, which raises the question how they can be differentially expressed in Th1 cells. One possible explanation is the purity of $CD4^+$ cells isolated from spleen and lymph nodes. Surface staining and flow cytometry show that >94% of the cells are $CD4^+$ after five days of Th1 cell culture (data not shown). Subsets of DCs express CD4 and could contaminate the T cells culture. However, DCs are short-lived cells and do not survive five days in cell culture. Also, it is not clear whether contaminating cells are retrovirally infected. Only upon efficient infection and Cre-recombinase activity, the cells express CAR on their surface, which was a prerequisite for our cell sorting protocol. Non-T-cell-specific target mRNAs could also be explained by an upregulation of those genes in response to Roquin deletion causing a loss of tissue identity. In this scenario, Roquin proteins would be required to control the integrity of T cells by suppressing the expression of B cell- and DC-specific genes. Yet, Roquin proteins are also expressed in these lymphocytes, raising the question how cell-type-specific regulation of target mRNAs is achieved. In addition to differential expression upon acute Roquin deletion in the Th1 cell culture, one also has to consider the expression levels of the respective mRNAs. To test this, qPCR measurements of *Syk*, one predominantly B-cell-expressed gene (Chan et al. 1994) among the target candidates, was performed (data not shown). Upregulated mRNA levels in *Rc3h1-2*$^{-/-}$ cells were confirmed, but *Syk* exhibited low overall expression levels. Thus, *Syk* is an unlikely target candidate of Roquin.

Other functional groups of Roquin target candidates are negative regulators of the mitochondrial apoptotic pathway, like Bcl2a1a/b/d and Bcl2l1 (Bcl-XL), and factors involved in the NF-κB signaling pathway, like Ox40, CD30, Nfkbid, Bcl-3, Il-2 and Icos. Interestingly, Bcl2a1 and Bcl2l1 are induced upon NF-κB signaling to promote cell survival (Zong et al. 1999; Chen et al. 2000). Therefore, upregulation of Bcl2a1 and Bcl2l1 might be a downstream effect of non-canonical NF-κB signaling, which is strongly activated in T cells lacking Roquin-1 and Roquin-2 (Vogel et al. 2013).

5.1.1.3 Potential Roquin targets in the context of Roquin-related mouse phenotypes

Roquin deficiency and the M199R mutation of Roquin-1 have been found to promote different immune diseases. *Sanroque* mice that are homozygous for the M199R mutation of Roquin-1 have increased numbers of Tfh cells and GC B cells and produce high-affinity ANAs, resembling the human disease SLE (Vinuesa et al. 2005;

Linterman, Rigby, R. K. Wong, et al. 2009). Furthermore, plasmacytoid infiltrations in liver, lung and kidneys were found in those mice (Vinuesa et al. 2005). In different models for autoimmune diseases, such as autoimmune diabetes and antibody-induced arthritis, *sanroque* mice exhibited enhanced disease parameters (Silva et al. 2011; Pratama et al. 2013). In this context, co-stimulatory receptors like Icos, Ox40 and CD30 are promising target candidates. Also, factors that promote T cell activation and survival, such as Bcl2l1, Bcl2a1, Il-2, Nfkbid and Bcl-3, are likely to be involved in excessive immune responses and autoimmunity. Interestingly, heterozygosity for the *Rc3h1*^{san} allele strongly increased the frequency of angioimmunoblastic T cell lymphomas in mice (Ellyard et al. 2012). Pim2, a proto-oncogene, induced T cell lymphomas when overexpressed from a lymphoid-cell-specific transgene (Allen et al. 1997) suggesting that dysregulation of this gene due to a lack of Roquin could promote tumorigenesis.

Taken together, the array data show that the lack of both Roquin-1 and Roquin-2 leads to the upregulation of numerous genes involved in T cell activation and survival. On the one hand, those targets are likely to reduce the threshold for T cell activation resulting in autoimmunity as in *sanroque* mice and in the accumulation of activated T cells as observed in *Rc3h1-2*$^{fl/fl}$*; CD4 Cre* mice. On the other hand, increased proliferation and survival of T cells might be the underlying cause for the development of T cell lymphomas in heterozygous *Roquin*^{san} mice.

5.1.2 Roquin CLIP and PAR-CLIP assays in primary Th1 cells

As a second approach of target identification, CLIP and PAR-CLIP assays were performed for Roquin. In contrast to microarrays, this method is designed to identify RBP-bound RNAs by UV cross-linking of protein-RNA contacts within the cell and subsequent IP (Ule et al. 2005; Hafner et al. 2010). Therefore, CLIP assays with Roquin-specific antibodies are a possibility to isolate Roquin-bound RNAs independent of the regulatory effect of Roquin on the respective mRNA or protein amount. In addition, sites of protein-RNA interaction can be investigated, because UV cross-linking results in mutagenesis during reverse transcription of the purified RNAs. Treatment with 4SU and irradiation with 365 nm UV light specifically induces T to C conversions at positions where the protein had close contact to a 4SU molecule (Meisenheimer & Koch 1997; Hafner et al. 2010).

Unfortunately, the performed assays did not yield very conclusive results due to various reasons. One important factor is that my experiments were performed with primary Th1 cells and therefore lower cell numbers than suggested for cell lines. Also, Roquin proteins, which are not highly expressed in cells, were not overexpressed as most

publications suggest. My decision for endogenous protein levels was based on the observation that cells only tolerate Roquin overexpression for about 24 hours without obvious signs of cellular stress. Thus, the starting conditions were not optimal, which was reflected by weak protein and RNA bands throughout the procedure (**Figure 23**). In addition, the sequencing data revealed a high frequency of multimeric adapter sequences, suggesting a failure to fully remove the adapter RNAs used during cDNA library preparation. This reduced the number of unique reads to 5.5 million per sample or less (**Table 22**), which is still comparable to published PAR-CLIP data ranging from 1 to 10 million reads per sample (Hafner et al. 2010). Optimizing the adapter ligation and using for example the Roquin-1-inducible *Rc3h1-2*$^{-/-}$ MEFs to obtain higher Roquin-1 protein levels could help to increase the number and quality of specifically clipped sequences. However, MEF lysates will not provide any information about T-cell-specific targets.

For the performed assays, reads mapping to mRNAs were analyzed with respect to T to C conversions and to their flanking sequence preferences. To our surprise, clipped sequences did not show any nucleotide bias upstream and downstream of cross-linked U sites (**Figure 25**). An explanation could be that Roquin proteins recognize and bind mRNA mainly in a non-sequence-specific manner. This hypothesis is supported by our own data (Schlundt et al. 2014) and by a publication showing that the CDE stem-loop structure within the *Tnf* 3'UTR is specifically bound by Roquin (Leppek et al. 2013). Based on that, Dr. Andreas Gruber plotted the number of reads mapping to the vicinity of putative CDE stem-loops. The data exposed spots of high read frequency close to CDE sequences, yet with various patterns, which does not indicate a clear preference for upstream or downstream sequences (**Figure 26**). Therefore, the observed clusters possibly reflect the accessibility of a CDE-neighboring sequence for cross-linking rather than a pattern of Roquin-RNA interaction.

By now, our own investigations of the crystal structure of the ROQ domain and the ROQ-*Tnf* CDE complex show that indeed recognition and binding of CDE stem-loops is mainly not sequence- but shape-specific (see 4.2.2). Most interactions target the phosphate backbone of the double-stranded RNA stem. Another publication confirms our ROQ domain interaction with the CDE stem-loop and additionally describes a second RNA-binding site for Roquin, which binds double-stranded RNA without sequence specificity (Tan et al. 2014). The dispensability of base-specific interactions in RNA binding could explain the missing sequence bias nearby sites of T to C conversion. Moreover, these structural analyses give a possible explanation for the poor outcome of the CLIP and PAR-CLIP assays, since double-stranded RNA is less efficiently cross-linked to protein by UV irradiation (Liu et al. 1996). In addition, the data evaluation would have to be changed for PAR-CLIP assays on proteins like Roquin. Instead of starting with a search for enriched nucleotide sequences within the

clipped RNAs, a more structure-based approach would be required. Although protein binding-site identification recently also implemented structural features of RNA (Hu et al. 2014; Lambert et al. 2014), it is still not a standardized procedure. This is due to increasing complexity when sequence restrictions are absent or when structural requirements are unknown.

Nevertheless, clipped sequences for known targets or target candidates can be extracted from the CLIP and PAR-CLIP data sets. Thus, an analysis of certain read clusters is possible, which supports the discovery of unknown Roquin *cis*-elements as shown for the newly identified target *Ox40* (**Figure 27**). The largest sequence cluster was found at the 3' end of the *Ox40* CDS, which raised the question whether Roquin could also mediate post-transcriptional regulation via *cis*-elements in the CDS of an mRNA. Other CLIP data sets indicate that RBPs do not exclusively bind to 3'UTRs (Hafner et al. 2010), but the functional impact of these interactions has not been investigated. Yet, miRNA binding in the CDS of mRNAs inducing post-transcriptional regulation is well-accepted by now (Brümmer & Hausser 2014; Hausser et al. 2013). Thus, it is possible that mediators of post-transcriptional regulation, such as Roquin, recognize their target elements within the CDS of an mRNA. However, there were also two sequence clusters within the *Ox40* 3'UTR among the clipped sequences. Comparing the positions of these two clusters with a prediction of the *Ox40* 3'UTR folding revealed that the clusters are in close proximity of two putative stem-loop structures (**Figure 27**). One of these stem-loops is a triloop and resembles a CDE-like structure, which suggests that the sequence clusters indeed are indicative of specific Roquin-RNA interactions. Similarly, several clipped sequence clusters could be identified within the *Icos* 3'UTR, one also covering the area of the proposed CDE stem-loop (data not shown) (Leppek et al. 2013). Even though a global analysis of the obtained CLIP and PAR-CLIP data sets was not possible, they contain valid information about sites of Roquin-mRNA interaction in Th1 cells.

5.1.3 Conclusions on Roquin target identification

For the identification of Roquin-regulated mRNAs, different methods with certain advantages and disadvantages are available (**see Table 23**). They detect either the protein-RNA interaction directly or the downstream effects of this interaction, such as altered mRNA levels. CLIP and PAR-CLIP experiments offer a global view on the Roquin-RNA interaction, but the quality of the data is strongly dependent on the binding mode and thus the efficiency of UV cross-linking. The microarray analyses provided a more reliable list of target candidates, however, with a certain false positive rate due to secondary effects and poorly expressed non-T-cell targets. Therefore, the microarray data requires follow-up evaluation on the mRNA and on the protein level.

To account for the finding that Roquin also involves translational regulation, another method can be applied, which is known as ribosome profiling (Ingolia et al. 2009; Ingolia et al. 2012). Ribosomes are fixed in their position on mRNAs by cycloheximide treatment, and partial RNase digest removes RNA that is not protected by ribosome binding. The protected RNA fragments can be analyzed by high-throughput sequencing to obtain a picture of the ribosome occupancy of individual mRNAs. A change of this pattern upon deletion of Roquin would indicate translational regulation of the respective mRNA by Roquin. Since the Icos protein amount increased faster to acute Roquin deletion than mRNA levels (**Figure 10**), ribosome profiling would be the method of choice to identify targets earlier after T cell activation. Yet, it is unclear whether translational inhibition and mRNA destabilization are promoted by Roquin on the same target mRNAs to the same extent, or whether one or the other mechanism is preferred in certain situations. Therefore, performing different target identification assays at different time points after T cell activation could yield an extended set of mRNA candidates.

My analyses clearly show that Roquin not only targets a few mRNAs but rather a large set of mRNAs. These mRNAs belong to different gene families indicating that Roquin-mediated post-transcriptional regulation alters T helper cell homeostasis simultaneously on the level of activation, proliferation and apoptosis. Since Roquin proteins are expressed in various organs and cell types (Vogel et al. 2013), they might also regulate cell type-specific sets of target mRNAs. Thus, Roquin proteins might be able to fulfill a wide range of tasks in different cells. To get a comprehensive picture of Roquin-mediated post-transcriptional regulation in Th1 cells or other cell types, different approaches for target identification ideally have to be combined and performed at different stages of cell activation and differentiation.

Table 23: Comparison of methods for Roquin target identification and summary of the subsequent target validation procedure

Scheme	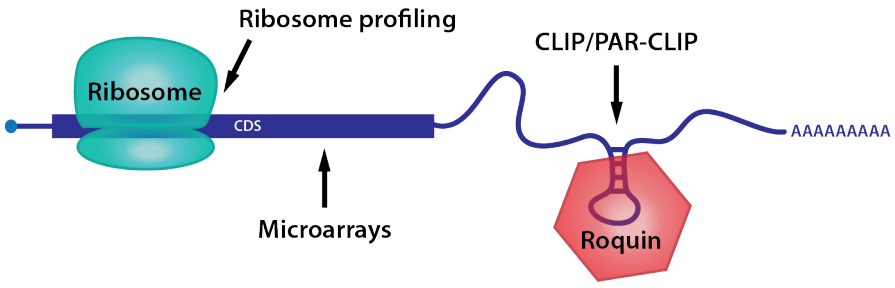		
Method	**Microarrays**	**CLIP/PAR-CLIP**	**Ribosome profiling*** *not done in this study
Technology	mRNA expression arrays (Affymetrix)	Deep sequencing (Illumina Solexa)	Deep sequencing (Illumina Solexa)
Targeted Roquin function	mRNA destabilization → Differential mRNA expression depending on Roquin levels	mRNA binding → Roquin-bound mRNA fragments	Translation regulation → Differential ribosome occupancy depending on Roquin levels
Maximum output	Target mRNAs	Target mRNAs and site of Roquin binding	Target mRNAs and mechanistic insight
False positives	Secondary effects and expression levels	Background signals	Secondary effects and background signals
Sensitivity	+ + +	+ Loss of material due to multistep experimental procedure	+ Loss of material due to multistep experimental procedure
Costs	+ +	+ + +	+ + +
Validation	✓ Differential expression of targets on the protein level in response to Roquin overexpression or deletion (Immunoblotting or flow cytometry) ✓ Requirement of the 3'UTR for Roquin-mediated regulation of the target mRNA (Reporter assay upon Roquin induction or deletion) ✓ Direct and specific binding of Roquin (ROQ domain) to the target mRNA via the 3'UTR *in vitro* (EMSA or FBA)		

Having found target candidates by high-throughput methods, further validation is the important next step in Roquin target identification (**see Table 23**). Since the described methods investigate the mRNA level, it is necessary to prove that Roquin also alters the protein expression of a putative target gene. By immunoblotting or flow cytometry, an increase of the target protein as a result of Roquin deletion in primary $CD4^+$ T cells or MEFs can be detected. Subsequently, Roquin-mediated regulation of the putative target mRNA needs to be attributed to the presence of cis-regulatory RNA elements, which are likely to be located in the 3'UTR. To this end, reporter assays in Roquin-inducible cells can be performed either comparing the full-length target mRNA to the respective CDS or fusing the target 3'UTR to a reporter gene. The 3'UTR of a direct Roquin target will confer post-transcriptional regulation of the reporter gene, whereas the 3'UTR of an indirect target most likely has no effect in response to Roquin induction. Similarly, reporter assays can be performed in MEFs upon acute deletion of Roquin (**Figure 42**). In addition to cell based analyses, the direct interaction of the putative target mRNA with Roquin has to be shown using *in vitro* binding assays. The specificity of the Roquin-RNA contact can be determined by addition of specific competitor RNAs or by using an RNA-binding-deficient Roquin mutant (**Figure 15C, D and Figure 37**).

The combination of functional assays and *in vitro* binding analyses is required and sufficient to clearly identify mRNAs that are directly targeted and regulated by Roquin. Unfortunately, not all suggested Roquin targets were validated with this accuracy, as for example IFN-γ, for which deregulation in *sanroque* mice but no direct binding of Roquin proteins to the mRNA was shown (Chang et al. 2012). Since Roquin interferes with many cellular processes, validation is essential to distinguish primary, direct target from genes that are indirectly regulated due to aberrant Roquin function.

5.2 Molecular requirements for the Roquin-RNA interaction

5.2.1 Identification of high-affinity Roquin binding sites by SELEX

5.2.1.1 Selection of RNAs bound by Roquin from a random RNA library

To identify RNAs bound by Roquin in an unbiased approach, I performed SELEX experiments with recombinant Roquin-1 N-terminal protein (aa 2-440). A similar experimental approach has been successfully used to identify RNA binding sites, for example using the STAR protein QKI (Galarneau & Richard 2005) or Fox-1 and Fox-2 splicing factors (Jin et al. 2003; Ponthier et al. 2006). For our selection, a single-stranded RNA library with a 47 nts random sequence was used to potentially provide the protein with high-affinity binding sites. After three rounds of selection, enriched

sequences were identified, clustered into groups of sequence patterns and experimentally validated in FBAs. Indeed, most of the tested patterns were confirmed, since they bound to Roquin-1 N-term stronger than the starting pool of RNAs (**Figure 30**). Pattern 9 and 12, which were among the strongest binders in the FBA validation, were further analyzed to determine the dissociation constant. In radioactive EMSAs, both patterns showed a distinguished band shift upon addition of the minimal ROQ domain (aa 147-326) with a K_d value of about 80 nM (**Figure 31, upper panel**). This is the same order of magnitude as for ROQ binding to the *Tnf* CDE (K_d~120 nM) (**Figure 34C**) and underlines that SELEX succeeded in identifying RNAs that are bound by Roquin with high affinity. In a second set of EMSAs using a ROQ mutant that was impaired in binding the *Tnf* CDE (K239A R260A), I confirmed the SELEX patterns to target the same protein interface like the *Tnf* CDE (**Figure 31, lower panel**).

5.2.1.2 Sequence motif and structural preference in SELEX patterns

Using a bioinformatics approach, the enriched patterns were further analyzed to identify shared sequence motifs. Hexamer enrichment analysis revealed that SELEX patterns share certain hexamer sequences, which were also enriched in a repeat experiment using Roquin-1 N-terminus and Roquin-1 M199R N-terminus for selection (**Figure 32**). Thus, during the *in vitro* selection process from random RNA sequences, Roquin-1 does exhibit a preference for a sequence motif. This is in contrast to the finding that Roquin-1 predominantly binds RNA in a sequence-independent manner in our CLIP and crystal structure analyses. One explanation for this paradox is the fact that the selection was performed *in vitro* and from a pool of artificial RNA sequences. Here, artificial RNA elements could bind to Roquin-1 with higher than natural affinities and could bring out a sequence-specificity that is not used in natural targets. In fact, this might not be favorable in cells, because very tight macromolecular interactions would interfere with the dynamics of regulatory processes. The drawbacks of artificial RNA elements can be overcome by designing an RNA library based on naturally occurring mRNAs as in Reid et al., 2009, yet with the disadvantage of creating a selection bias.

Interestingly, the enriched sequence motif was predominantly located at the 3' end of the random RNA sequence (**Appendix I**). This prompted us to check whether the RNA context flanking the sequence motif shows a particular structural preference that was selected by Roquin-1. Indeed, Dr. Andreas Gruber found that the sequence motif is embedded in a stem-loop structure (**Figure 33**). Therefore, the SELEX experiments discovered a potential Roquin *cis*-element, which combines sequence-specific binding with structural preferences.

The clear preference for the 3' end of the random RNA sequence indicates that the adjacent primer sequence can influence the selection process. Selection can be

performed in a different RNA library to exclude a bias due to fixed primer sequences. In addition, the importance of the combined sequence-structure motif has to be addressed in further binding studies. Removing the flanking RNA context and mutational analyses are required to determine the specificity of the motif recognition. A first experiment using the Roquin-1 M199R N-terminus exhibited comparable hexamer enrichment, indicating an unchanged RNA binding preference of the *sanroque* protein. This is in line with the finding that the amino acid M199 does not form close contacts to the *Tnf* CDE in our crystal structures (**Figure 36**) and thus might not be directly involved in RNA binding. Yet, further binding experiments are necessary to draw final conclusions. Moreover, the importance of the SELEX stem-loop for natural Roquin-RNA interactions in cells needs to be determined. To address this, the mouse genome was screened for SELEX stem-loop elements and the resulting list of genes was compared to the list of Roquin target candidates from the microarray analysis. However, among the target candidates with a high fold change (**Table 20**), only the early B cell factor 1 mRNA (*Ebf1*) harbors a sequence able to form a SELEX stem-loop (data not shown). Further experimental validation is required to clearly define the conformation of the SELEX stem-loop motif for Roquin binding. Nevertheless, I identified a SELEX-like hexaloop within the *Ox40* 3'UTR by *in situ* RNA folding analysis. The functional impact of this SELEX-like stem-loop in the context of *Ox40* regulation is discussed in 5.3.3.

5.2.2 Structural analysis of the Roquin-RNA interaction

5.2.2.1 Crystal structures of the ROQ domain and the ROQ *Tnf* CDE complex

In collaboration with Dr. Robert Janowski, Prof. Dr. Dierk Niessing's group, and Dr. Andreas Schlundt, Prof. Dr. Michael Sattler's group, we were able to obtain the crystal structures of the minimal ROQ domain (aa 147-326) and of the ROQ-*Tnf* CDE complex. These structures were published together with a mutational screening of the RNA-binding interface of ROQ and mutational analyses of the CDE RNA stem-loop in Schlundt et al., 2014. In the same issue of the journal, a second structural investigation of Roquin-1-RNA interactions was published by Tan et al., 2014. A comparison of the two studies is given in **Table 24** and will be discussed in the following passages.

The crystal structure of the ROQ domain adopted an extended winged-helix (WH) fold. This domain type is predominantly involved in DNA binding, with the Fox family of transcription factors being prominent representatives (Gajiwala & Burley 2000; Benayoun et al. 2011). However, there are also examples of WH domains recognizing RNA either in a single-stranded or stem-loop conformation (Teplova et al. 2006; Yoshizawa et al. 2005; Soler et al. 2007; Harami et al. 2013). The WH fold of the ROQ

domain was not altered upon binding of the *Tnf* CDE stem-loop RNA except for a more compact conformation of the W1 fold. Tan et al. solved the crystal structure of a larger human ROQUIN-1 construct (aa 90-400) with additional sequences flanking the ROQ domain, and they identified three subdomains within this structure. Domain II and III together resemble our ROQ domain, whereas domain I is the additional part (**see Table 24**). In addition to the WH fold in domain III, Tan et al. described in more detail a second helix-turn-helix (HTH) motif in domain II, which is similar to the WH fold except for the missing β-sheets to form the wing. Domain I consists of three N-terminal and three C-terminal α-helices packed together.

Tan et al. identified two RNA interaction sites in crystal structures of Roquin-1 with different RNAs. The A site recognized a canonical CDE RNA stem-loop (*Hmg$_{19}$*) from the 3'UTR of *HMGXB3* (HMG box domain containing 3), whereas the B site bound to an artificial *Tnf* CDE RNA duplex. Comparing the A site binding of the *Hmg$_{19}$* stem-loop to binding of the *Tnf* CDE stem-loop in our study shows identical protein-RNA interactions. The main contacts were non-sequence-specific interactions with the phosphate backbone of the 5' stem (**Figure 36**). Moreover, sequence-specific contacts were observed for the flipped-out Us in the loop (U11 and U13 or U8 and U10 respectively), the G in the center of the loop (G12 or G9) and for a U (U4 or U1) that is sticking out from the stem and interacts with W184. The remarkable identity of two different Roquin-1-RNA complex structures underlines the specific recognition of CDE RNA stem-loop folds by Roquin-1. Surprisingly, the *Tnf* CDE adopted a double-stranded duplex conformation in crystal structures by Tan et al. and was bound to the B site, the groove between domain I and domain II. Protein-RNA interactions appeared to be weak and rather non-sequence-specific. In our hands, the *Tnf* CDE formed a stem-loop structure in solution, as proven in NMR measurements, and it also seemed to adopt this conformation in binding assays performed by Tan et al.. Therefore, the double-stranded *Tnf* CDE duplex observed in the complex structure is most likely a crystallization artifact. Nevertheless, it indicated that Roquin-1 is able to bind double-stranded RNA and raised several questions. Does the B site RNA binding occur under physiological conditions, such as in solution or in cells? Can B site and A site binding take place simultaneously on one Roquin molecule? Are the RNA stem-loop for the A site and the double-stranded RNA for the B site present within the same mRNA in cells? What is the functional impact of RNA binding by the B site? Some of these questions are addressed in the manuscript of Tan et al.. Presence of a ternary complex consisting of Roquin-1 (aa 90-400), *Hmg$_{19}$* CDE and a double-stranded *Tnf* RNA was shown in a binding assay, suggesting that *in vitro* both RNA binding sites can be used at the same time. However, it remains elusive whether this also happens within cells and if so whether both binding sites are provided by one mRNA.

Taken together, both studies confirmed specific recognition of CDE stem-loop structures by the ROQ domain of Roquin-1 as suggested by Leppek et al. (Leppek et al. 2013). Since we showed that full-length Roquin-1 and our minimal ROQ domain bound the *Tnf* CDE with similar affinities (**Figure 34C and D**), the quantitative involvement of other domains of Roquin in CDE stem-loop binding can be neglected. Nevertheless, they might support RNA recognition or binding through different mechanisms on composite *cis*-elements.

Roquin-1 has a RING finger domain as found in E3 ubiquitin ligases. Whereas E3 ligase activity was observed for Roquin-2 (Maruyama et al. 2014), it is not known whether the Roquin-1 RING finger is functional, even though RING-less Roquin mutants seemed to be impaired in immune regulation (Pratama et al. 2013). A whole group of RNA-binding E3 ubiquitin ligases has been described by now, but the connection of ubiquitination and RNA binding remains unclear (Cano et al. 2010). MEX-3C, one such protein, has been studied in more detail showing that its E3 ubiquitin ligase function is required for degradation of target mRNAs but not for translational inhibition (Cano et al. 2012). The Roquin-1 N-terminus also contains a CCCH-type zinc finger C-terminal to the ROQ domain. This type of protein domain is known to bind to AU-rich RNA elements (AREs), best described for the RNA-binding protein TTP (Hall 2005). Although CCCH zinc fingers mostly occur in tandem or even higher numbers of modules, specific interaction with AREs was also observed with a single CCCH zinc finger (Michel et al. 2003). Thus, the Roquin-1 CCCH zinc finger might bind to AREs as an independent form of Roquin-1-RNA interaction in addition to the ROQ-mediated CDE stem-loop binding. The C-terminus of Roquin-1 contains a proline-rich sequence (PRS) and a putative coiled-coil domain (Vinuesa et al. 2005). PRSs are important sites for protein-protein interactions and can be found in a large number of proteins (Williamson 1994). Different domain types are known to interact preferentially with PRSs, such as WW domains and Src homology (SH) domains (Kay et al. 2000). Coiled-coils are abundant structural elements found in proteins with diverse functions, such as transcription factors or structural proteins, and they serve as oligomerization domains, spacers or building blocks in the cytoskeleton (Mason & Arndt 2004; Burkhard et al. 2001). Thus, the functional elements in the C-terminus of Roquin-1 are most likely involved in protein-protein interactions.

Table 24 Comparison of Roquin structure investigations from Schlundt et al. and Tan et al.

Feature	Schlundt et al.	Tan et al.
Species	Mouse and human Roquin-1 are identical in this region	Human Roquin-1
Model	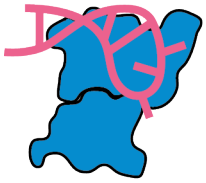	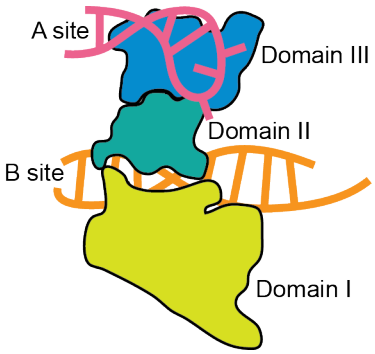
Domains	ROQ domain: aa 174-325	Domain III+II+I: aa 89-398 Domain III+II: aa 175- 324 Domain III: aa 195-271
Motifs	WH: aa 195-271	WH: aa 195-271, HTH: aa 274-324
RNA-binding interfaces	One: stem-loop binding	**A site:** stem-loop binding **B site:** dsRNA binding
RNA structure	*Tnf* CDE as triloop	**A site:** Hmg_{19} as triloop **B site:** *Tnf* CDE as duplex
RNA binding	5' stem, phosphate backbone	**A site:** 5' stem, phosphate backbone **B site:** weak 5' and 3' interactions
RNA loop contacts	U11 and U13: flipped out G12: stacking and R219, Q247	U8 and U10: flipped out G9: stacking and R219
RNA stem contacts	U4 flipped out, contact to W184 and F194	U1 flipped out, contact to W184
Protein mutants	K220A, K239A, R260A, K239A/R260A, R188A, R219A, R229A, R233A, S238A, Y250A, R251A, S253A, K259A, S264A, S265Y, E293A, K314A	**A site:** K239A/T240A, Q247A/Y250A/R251A **B site:** Q318A/S319A, R135E/K136E/R164E, R135E/K136E/D322A/K323A
RNA mutants	Extension mutant, loop mutants 1-3, stem mutants 1-3 CDE-like RNA stem-loops	none
Functional assays	Protein expression levels measured by flow cytometry	mRNA half-life measured by qPCR

5.2.2.2 Mutational analysis of the ROQ RNA-binding interface

The contribution of single amino acids within the RNA-binding interface of the ROQ domain was determined by mutational analyses in shift assays. K220, K239 and R260 were identified as major players in the ROQ-RNA interaction (**Figure 37**), and therefore the respective mutants were investigated in cell-based functional assays. Importantly, combining two mutations (K239A and R260A) further reduced binding to the *Tnf* CDE. This indicated that changes in the amino acid composition of the RNA-binding interface of ROQ reduced the RNA affinity and two changes at once had a stronger effect. In fact, Tan et al. only tested Roquin variants with two or more mutations in binding assays. Amongst others, they target the amino acids K239, Y250 and R251, which were also included in our mutational screening. Since titration experiments are not shown, it is unclear whether there were gradual differences between a double mutant (K239A T240A) and a triple mutant (Q247A Y250A R251A) in RNA binding. To test functionality of the Roquin-1 mutants, Tan et al. knocked down endogenous Roquin by si-RNAs and re-expressed wild-type or mutant Roquin-1. Roquin-1 function was determined by qPCR measurements of RNA stability upon actinomycin D treatment. Interestingly, A site as well as B site mutations completely abolished Roquin-1-mediated reduction of the *HMGXB3* mRNA half-life. In contrast, our cell-culture-based functional assay used surface expression of Roquin target proteins (ICOS or Ox40) as read-out for Roquin function in cells. This is advantageous because the result of Roquin-1-mediated regulation on the protein-level is monitored and thereby effects on mRNA stability and translational efficiency are integrated.

As reporter constructs, I used the two natural Roquin targets *ICOS* fl, *Ox40* fl and a chimeric *ICOS* CDE_{260}, which has a shortened *Tnf* 3'UTR (260 nts) containing the CDE stem-loop sequence. Instead of knocking down Roquin-1 and Roquin-2 with siRNAs, I used *Rc3h1-2*$^{-/-}$ MEFs and introduced the reporter constructs and the different Roquin-1 variants by retroviral transduction. The two natural Roquin targets *ICOS* fl and *Ox40* fl showed comparable regulation patterns with the strongest reduction upon overexpression of wild-type Roquin-1. The single mutants K220A, K239A and R260A exhibited substantial residual activity, and the double mutant K239A R260A did no longer reduce ICOS and Ox40 expression compared to uninfected cells (**Figure 39**). This again highlights how single mutations reduce RNA affinity of the protein and how this adds up to a loss of function in the double mutant. Interestingly, the *ICOS* CDE_{260} construct exhibited the strongest regulation in response to Roquin-1 WT. Accordingly, the single mutants caused a considerable reduction of ICOS on the cell surface, and even expression of the double mutant resulted in a downregulation of ICOS by 40%. Hence, reporter genes with different 3'UTRs (*ICOS* fl and *ICOS* CDE_{260}) exhibited different responsiveness to Roquin-1 overexpression. As a consequence, mutations reducing the affinity of the protein-RNA interaction also affect the Roquin-1 mediated

post-transcriptional regulation to different degrees. This shows that Roquin proteins are able to confer different modes of post-transcriptional regulation. High-affinity target sequences like the CDE_{260} 3'UTR experience an on-off regulation, if graded Roquin-1 expression levels are compared, whereas targets like the *Ox40* mRNA are rather subject to a modulation of expression. Thus, my findings provide different Roquin-1 mutants for functional assays and thereby enable an investigation and comparison of complex *cis*-regulatory RNA elements concerning their affinities and modes of regulation.

5.2.2.3 CDE-like stem-loops as Roquin-1 *cis*-elements

Having found that ROQ-*Tnf* CDE binding is mainly non-sequence-specific prompted us to perform a mutational analysis of this RNA stem-loop (**Figure 40**). Loop mutants with only one nucleotide exchange did not show strongly reduced ROQ binding affinity (**Figure 40B**). However, a Pu-Py-Pu sequence instead of Py-Pu-Py in the loop was no longer bound by the ROQ domain. This indicated that despite the tolerance for single nucleotide changes a certain sequence composition within the loop is required for Roquin binding. Different mutations of the stem (SM1-3 and EXT) reduced the ROQ binding affinity but did not abolish the protein-RNA interaction (**Figure 40C and D**). Thus, Roquin-1 seems to accept a much greater variety of RNA stem-loops than anticipated from the consensus CDE published by Leppek et al., 2013. Based on this hypothesis, I identified two CDE-like stem-loops, one in the *ICOS* 3'UTR and one in the *Ox40* 3'UTR, with considerable deviation from the CDE consensus sequence. As expected, both CDE-like stem-loops were bound by the ROQ domain even though with strongly reduced affinities (**Figure 41**).

Moreover, these CDE-like stem-loops also functioned as *cis*-elements in Roquin-mediated post-transcriptional regulation. This was shown in cellular assays monitoring the expression of different *ICOS* and *Ox40* reporter constructs in response to acute deletion of Roquin-1 and Roquin-2 (**Figure 42**). In contrast to the functional assay using overexpression of Roquin-1 in *Rc3h1-2*$^{-/-}$ MEFs, the acute deletion system enabled us to study the effects of endogenous Roquin amounts. Roquin deletion increased the expression of ICOS and Ox40 from full-length mRNA constructs, whereas expression from CDS constructs was not altered. Shortening of the 3'UTRs selectively removed stem-loop sequences and revealed the contribution of CDE-like stem-loops to Roquin-mediated regulation.

Binding analyses using CDE mutants together with the information from the ROQ-*Tnf* CDE complex structure suggested a broad range of CDE-like RNA stem-loops to be accepted by Roquin-1. Even more, the conformation of the protein-RNA contact indicated that stem-loop structures with larger loops might be bound as well. In SELEX experiments, a hexaloop structure was identified as potential Roquin *cis*-element

(**Figure 33**) and I found an analog RNA sequence in the *Ox40* 3'UTR (**Figure 43**). The crystal structure of the ROQ-*Ox40* SELEX-like complex revealed that the ROQ domain is indeed capable of binding an RNA hexaloop through an enlarged protein-loop interface compared to the *Tnf* CDE binding (data not shown). Furthermore, in shift assays I observed binding of two SELEX patterns and of the *Ox40* SELEX-like stem loop, which was abolished using the double-mutant K239A/R260A ROQ domain (**Figure 31 and 44**).

Taken together, the crystal structures provided an insight into Roquin-RNA interaction that revealed binding to be achieved mainly via non-sequence-specific contacts recognizing the stem-loop fold throughout the protein-RNA interface. Mutational analyses of protein and RNA as well as functional assays further underlined that Roquin-RNA recognition accepts a broad range of affinities resulting in gradual post-transcriptional regulation of target mRNAs.

5.3 The inducible costimulator Ox40 is a target of Roquin

5.3.1 *Ox40* is specifically bound and regulated by Roquin

Ox40 was 2-fold upregulated in the microarray analyses of Th1 cells after acute deletion of *Rc3h1-2* and showed a similar regulation on the $Icos^{-/-}$ background. As a member of the Tnf receptor super family (Tnfrsf), Ox40 is induced on the cell surface in response to T cell activation and serves as a costimulator to promote cytokine expression as well as T cell proliferation and memory formation (Croft 2010). Moreover, excessive Ox40 signaling was associated with different autoimmune diseases and impaired peripheral tolerance (Bansal-Pakala et al. 2001; Murata et al. 2002). Thus, Ox40 shares a lot of characteristics with the costimulatory receptor Icos, which was the first Roquin target being described (Yu et al. 2007; Athanasopoulos et al. 2010; Glasmacher et al. 2010). To prove that Roquin directly and specifically binds the *Ox40* mRNA and that binding results in changes of Ox40 protein expression, different experiments were applied.

Ox40 levels on $CD4^+$ T cells from *Rc3h1-2*$^{fl/fl}$*; CD4 Cre* and wild-type mice were investigated by flow cytometry (**Figure 15A**). Indeed, $CD4^+$ T cells lacking Roquin-1 and Roquin-2 had higher Ox40 levels in the naïve (**Figure 15A, left**) and more prominently in the effector-like (**Figure 15A, right**) compartment. Ox40 expression on naïve cells was particularly striking, since it is only induced upon activation in wild-type T cells (Mallett et al. 1990; al-Shamkhani et al. 1996). In MEFs, Ox40 regulation was directly connected to Roquin-1 activity. Upon induced expression of Roquin-1, Ox40 expression from a full-length construct was strongly downregulated (**Figure 15B, right**), whereas the *Ox40* CDS construct lacking the 3'UTR only showed a minimal

response (**Figure 15B, left**). Thus, Roquin-1 regulates Ox40 protein expression levels in the presence of the *Ox40* 3'UTR, suggesting that it targets this part of the Ox40 mRNA.

In vitro binding assays were performed to prove the direct interaction of Roquin with the *Ox40* mRNA. FBAs with specific and unspecific competitor RNAs thereby demonstrated the specificity of Roquin binding to the *Ox40* 3'UTR. In view of the fact that Roquin-1 overexpression also slightly reduced Ox40 expression from a *Ox40* CDS construct (**Figure 15B, left**), Roquin might also functionally target the *Ox40* CDS to a certain extend. This was supported by finding a cluster of clipped sequences mapping to the *Ox40* CDS in our CLIP and PAR-CLIP assays (4.1.4.2). Nevertheless, Roquin binding via the *Ox40* 3'UTR resulted in a more prominent regulation of Ox40 protein levels (**Figure 15B, right**). Taken together, my experiments showed that the *Ox40* mRNA is a direct target of Roquin-mediated post-transcriptional regulation, which was published in Vogel et al., 2013. Roquin clearly binds to the *Ox40* 3'UTR, while the CDS might provide further target elements for Roquin-mediated regulation.

5.3.2 Ox40 contribution to the Roquin knockout phenotype in T cells

Having identified Ox40 as a direct target of Roquin-mediated post-transcriptional gene regulation, I aimed at determining its contribution to the phenotype of mice with a T-cell-specific Roquin-1 and Roquin-2 knockout. To this end, splenocytes of *Rc3h1-2$^{fl/fl}$; CD4 Cre* mice (termed double knockout mice) and *Ox40$^{-/-}$; Rc3h1-2$^{fl/fl}$; CD4 Cre* mice (termed triple knockout mice) were isolated and analyzed. In addition, *Ox40$^{-/-}$; Rc3h1-2$^{fl/fl}$* mice were analyzed and *CD4 Cre* or *Rc3h1-2$^{fl/fl}$* mice served as controls.

Macroscopic analyses of the spleens indicated that the lack of Ox40 indeed ameliorates the phenotype of the double knockout mice. The number of splenocytes in the triple knockout mice showed no increase compared to the control animals, and the spleen weight was just slightly higher in triple knockout than in control mice (**Figure 16**). The increased weight in combination with unchanged numbers of splenocytes can possibly be explained by an increased number of erythrocytes, since the organs of triple knockout mice exhibited a darker red color compared to the other animals (Maekawa et al. 2013).

Flow cytometric investigation of the $CD4^+$ and the $CD8^+$ T cell compartment (**Figure 17 and 18**) did not show considerable differences between the double and the triple knockout mice, and the same result was obtained from the analysis of Tfh cells and GC B cells (**Figure 19**), SLECs, NK cells and NKT cells (**Figure 20C and D**). The only significant difference was observed for the frequency of peripheral Tregs, which increased to 25% in the triple knockout mice. In contrast, in double knockout mice and in control mice only about 10% of the $CD4^+$ T cells expressed FoxP3. It was described

that Ox40 is important for Treg cell expansion and responsiveness to IL-2, whereas development of *Ox40*$^{-/-}$ Tregs is normal (Xiao et al. 2012). In line with this *Ox40*$^{-/-}$*; Rc3h1-2*$^{fl/fl}$ mice had normal levels of peripheral Tregs. However, in the triple knockout mice the lack of Ox40 in addition to Roquin-1 and Roquin-2 seemed to increase the numbers of peripheral Treg cells either due to increased expansion or survival. It would be interesting to determine the suppressive capacity of those peripheral Tregs.

Moreover, the expression of Roquin targets was determined in the different knockout mice. As expected, Icos expression was high in effector-like CD4$^+$ and CD8$^+$ T cells lacking Roquin-1 and Roquin-2 (**Figure 21A**). An additional lack of Ox40 did not influence Icos levels. Ctla4 is a further costimulatory receptor identified as potential Roquin target in the described microarray analyses (**Table 20**). Comparable to Icos but less prominent, Ctla4 expression is increased in cells that lack Roquin proteins and similarly high in triple knockout cells (**Figure 21B**).

In summary, abolishing high Ox40 levels in mice with a T-cell-specific deletion of Roquin by introduction of *Ox40*$^{-/-}$ alleles did not rescue any of the prominent phenotypes. T cells were equally activated and showed strong Icos expression, and the numbers of Tfh cells and GC B cells were increased. This is in line with the microarray data showing that Roquin targets various mRNAs. Since many factors that drive T cell activation and expansion are highly expressed, the lack of one Roquin target gene is likely to only have a minor impact. However, the study can be extended to assays on T cell function. Ox40 is an activation-induced costimulator, and it will be interesting to see how triple knockout T helper cells respond to T cell activation signals. In vitro differentiation experiments (Th1, Th2, Th17 and Tregs) will reveal whether triple knockout cells have the same intrinsic preferences as double knockout cells, which showed increased Th17 differentiation (Jeltsch et al. 2014). The effect of Ox40 on memory formation in the context of the double knockout mice can be investigated by *in vivo* immunization experiments. Recently, it was described that an Ox40 agonistic antibody promotes massive infiltration of mononuclear cells into the lung (Xiao et al. 2012). Moreover, it was shown that Ox40L-transgenic mice develop autoimmune-like disease due to constitutive Ox40 ligation. In the lungs from double knockout mice, we also observed lymphocyte infiltrates (Jeltsch et al. 2014), suggesting that high levels of Ox40 could cause T cell infiltration in these animals. To prove this, the lungs of triple knockout mice should be analyzed with respect to lymphocyte infiltrations.

Taken together, double knockout mice with an additional deletion of Ox40 maintained their prominent phenotypic features, suggesting that Ox40 is just one target within a whole network of mRNAs regulated by Roquin. Nevertheless, further investigations of T cell function and differentiation are likely to identify characteristics of double knockout T cells caused by high Ox40 levels.

5.3.3 Roquin recognizes two distinct *cis*-elements in the *Ox40* 3'UTR

The data collected in structural analyses, the different binding studies and functional assays increased our knowledge on Roquin-mRNA interactions but also pointed out the complexity of this regulatory process. The ROQ domain recognized a variety of RNA stem-loop structures from CDE triloops to SELEX hexaloops and it remains elusive whether and how different *cis*-elements cooperate in Roquin-mediated regulation. The newly identified Roquin target *Ox40* has a rather short 3'UTR (~ 150 nts) with two putative stem-loop structures. In addition to the CDE-like stem-loop described in 4.2.4.2, I found a hexaloop, which closely resembles the SELEX hexaloop regarding shape and nucleotide sequence (**Figure 43B**). A conservation analysis of the *Ox40* 3'UTR combining RNA sequence and structure revealed that both stem-loops are highly conserved (**Figure 43C**). Interestingly, the nucleotide sequence within the loop was slightly less conserved, indicating that the integrity of the RNA folding was of greater importance than the sequence motif. Moreover, conservation of the two stem-loops implies an involvement of both structures as functional elements.

Specific recognition of the *Ox40* SELEX-like stem-loop by the ROQ domain was shown in binding experiments with RNA-binding-deficient ROQ mutants. Amino acid exchanges that reduced binding to the *Tnf* CDE also affected binding to the *Ox40* SELEX-like element (**Figure 44**). Together with the crystal structure of the ROQ-*Ox40* SELEX-like complex this underlined that CDE stem-loops and SELEX stem-loops use the same interface for binding to Roquin-1. However, compared to the SELEX patterns 9 and 12, the *Ox40* SELEX-like RNA stem-loop has an almost 5-fold higher K_d value for Roquin-1 binding. This might be due to the larger sequence context or a potentially more stable secondary structure of the SELEX patterns. It might indicate that binding sites with lower affinity are favorable in natural 3'UTRs due to a larger flexibility in regulatory processes.

The influence of both RNA structures in the *Ox40* 3'UTR in Roquin-mediated *Ox40* regulation was tested using mutants, in which one stem-loop or both were abrogated by an exchange of the stem forming nucleotides. In EMSA experiments with the complete *Ox40* 3'UTR and recombinant Roquin-1 N-terminus (aa 2-440), two high-affinity band shifts were dependent on the presence of two RNA stem-loops (**Figure 46**). A supershift induced by higher protein concentrations was independent from the integrity of CDE-like and SELEX-like stem-loop structures. This experiment indicated that the presence of two *cis*-elements provides two high-affinity binding sites for Roquin proteins, whereas disruption of either stem-loop resulted in the binding of just one Roquin protein. The observed supershift could be caused by an unspecific RNA affinity of the Roquin-1 N-terminus at higher concentrations, which has already been observed in EMSAs using the complete *ICOS* CDS (Glasmacher et al. 2010). Also, the *Ox40*

3'UTR could obtain a fold *in vitro* that allows binding of high concentrations of Roquin-1 N-terminal protein. The presence of the CDS and other RBPs involved in translation and stabilization of the mRNA might prevent such a folding in cells.

The responsiveness of *Ox40* constructs with different 3'UTR lengths and mutations was tested in functional assays using the Roquin-1-inducible *Rc3h1-2*$^{-/-}$ MEFs (**Figure 47**). The experiment nicely showed that Roquin-mediated Ox40 regulation via the 3'UTR is dependent on the presence of the SELEX-like as well as the CDE-like RNA stem-loop. Mutations and truncations leaving one stem-loop intact resulted in a partial Roquin-response. Furthermore, an *Ox40* full-length construct without intact *cis*-elements exhibited the same responsiveness to Roquin-1 overexpression as the *Ox40* CDS. Therefore, Roquin-mediated post-transcriptional regulation of Ox40 can be attributed to two distinct RNA stem-loop structures within the *Ox40* 3'UTR that act as Roquin-1 *cis*-elements. Unfortunately, the experiments did not clarify whether both *cis*-elements have the same impact on Roquin-mediated regulation. Binding affinities within the context of the complete mRNA, accessibility of the 3'UTR and responsiveness to changing amounts of Roquin proteins simultaneously influence the regulatory process. This complexity has to be considered in continuative studies.

5.4 Conclusions and perspectives for Roquin-mediated post-transcriptional gene regulation

Using the *Ox40* mRNA and mutated variants thereof in binding analyses and functional assays, I was able to show that Roquin-1 binds two independent and entirely different RNA stem-loops as functional *cis*-elements within one 3'UTR. This was possible due to the low complexity of the short *Ox40* 3'UTR, comprising only 150 nts. Investigating Roquin-mediated regulation via large 3'UTRs such as the *ICOS* 3'UTR (2 kb), which might harbor several Roquin-responsive elements, will be even more challenging. Every artificial alteration of the 3'UTR sequence by truncations or nucleotide exchanges could bring about changes in the folding and stability of RNA structures. This could in turn change binding of *trans*-acting factors and post-transcriptional regulation, even though the nucleotides forming the *cis*-element are still present. For many target mRNAs, these circumstances complicate the analysis of single regulatory elements within their natural context, which is required to obtain a clear picture of Roquin-mediated regulation. Therefore, experiments screening 3'UTRs for Roquin *cis*-elements and subsequently testing their functional impact have to be designed with great accuracy. Using different approaches that complement each other, like 3'UTR truncation, scanning and mutational analyses, will help to obtain reliable results.

In line with this, the extent of physiologic regulation by Roquin also depends on the accessibility of target 3'UTRs in terms of protein occupation and RNA structure. If an RNA stem-loop cannot fold due to steric hindrance, it will not serve as Roquin *cis*-element. Moreover, 3'UTR shortening, as it broadly occurs upon cell activation (Sandberg et al. 2008), could abolish Roquin-responsive RNA elements and thus reduce Roquin-mediated repression of target mRNAs. Also, the interplay of different *cis*-elements recruiting *trans*-acting factors within one 3'UTR has to be considered. Post-transcriptional regulation of *Tnf* has mainly been attributed to the presence of an ARE in its 3'UTR (Anderson 2000). Yet, ARE-independent regulation also takes place via the CDE, forming a stem-loop structure that is targeted by Roquin-1 (Stoecklin et al. 2003; Leppek et al. 2013). Currently, it is unclear how these two mechanisms interfere with each other or whether they regulate *Tnf* expression at different stages of cell activation or differentiation. Similarly, all kinds of *trans*-acting factors such as RBPs, miRNAs and other non-coding RNAs act together on 3'UTRs to control protein expression. This also provides a basis for differential regulation of various Roquin targets within one cell at the same time. Unraveling these regulatory networks is essential to understand the impact of Roquin for post-transcriptional gene regulation.

Furthermore, 3'UTRs with more than one Roquin *cis*-element could serve as platforms for Roquin binding and thereby be sensors for varying Roquin amounts. On the one hand, Roquin expression is regulated on the transcriptional level. A recent publication shows that Roquin levels increase upon IL-10 treatment in murine EL4 T cells (Schaefer et al. 2014). This is due to an IL-10-mediated induction of the transcription factors STAT1, STAT3, GATA2 and c-Rel, which bind to the Roquin-1 promoter region and drive Roquin-1 transcription. Interestingly, our own observations show that c-Rel levels are increased in Th1 cells upon acute deletion of Roquin and that the *c-Rel* 3'UTR is targeted by Roquin-1 (Jeltsch et al. 2014). This indicates that Roquin-1 directly targets *c-Rel* and thereby reduces its own expression via a negative feedback loop. On the other hand, Roquin levels are regulated by degradation of Roquin proteins upon T cell activation (**Figure 10B**). Recently, our group identified the Roquin fragments to be derived from site-specific cleavage by the paracaspase Malt1 (Jeltsch et al. 2014). T cell receptor stimulation in combination with costimulatory signals promotes Malt1-mediated cleavage of Roquin proteins, which results in the deregulation of Roquin targets. The most prominent Malt1 cleavage product of Roquin-1 comprises aa 1-510 and contains the RNA-binding ROQ domain (Jeltsch et al. 2014; Schlundt et al. 2014). However, it is not clear whether binding to target mRNAs takes place in T cells. Lacking the C-terminus, the protein fragment does not confer post-transcriptional regulation (Glasmacher et al. 2010; Jeltsch et al. 2014) and thus enables expression of Roquin targets. In this context, target mRNAs with less or lower-affinity *cis*-elements

would respond faster to reduced Roquin levels, whereas mRNAs with more or higher-affinity *cis*-elements could still be repressed by low Roquin amounts (**see Figure 48**).

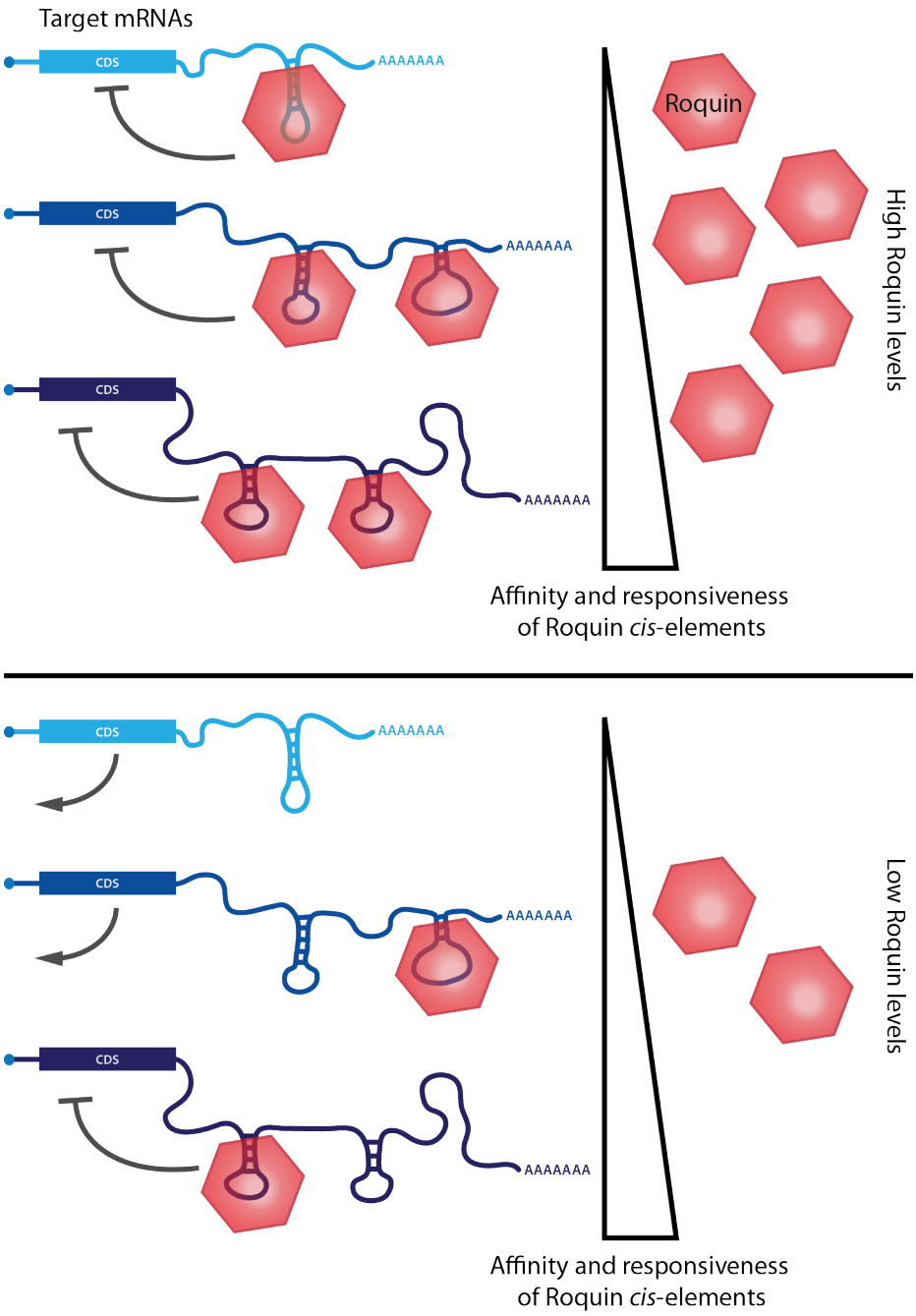

Figure 48: Model of Roquin-mediated post-transcriptional regulation targeting different 3'UTRs. Upper half: High Roquin levels lead to comparable repression of targets with high- and low-affinity *cis*-elements. Lower half: Reduced Roquin levels release targets with low-affinity *cis*-elements or little responsiveness from repression, whereas expression of targets with high-affinity binding sites and strong responsiveness remains suppressed.

Further validating the stability and function of Roquin cleavage products is necessary to fully understand the impact of Malt1 cleavage. Also, investigating transcriptional regulation of Roquin should be continued to get a more comprehensive picture of tissue- and differentiation-stage-specific processes. Furthermore, it remains elusive how Roquin is regulated on the post-transcriptional level. There is evidence that Roquin binds to its own 3'UTR via a CDE stem-loop (Leppek et al. 2013), but experimental confirmation is lacking. Currently, tightly regulated transcription, translation and cleavage in combination with negative feedback loops seem to coordinate a balanced expression of Roquin proteins in T cells (**see Figure 49**). This would be beneficial to prevent inappropriate T cell activation and autoimmunity and at the same time to allow fast and effective T cell responses upon pathogen encounter.

On the molecular level, my data suggest mRNA binding by Roquin to be less stringent than expected. Thus, the question arises how specificity is achieved in Roquin-mediated post-transcriptional regulation. An obvious assumption is that Roquin-1 interacts with other proteins to confer regulation of translation or mRNA decay. The availability of different co-factors would add to the selectivity of Roquin-mediated regulation concerning target mRNAs as well as cell types or differentiation stages. The regulatory RNase Regnase-1, encoded by *Zc3h12a*, post-transcriptionally regulates a similar set of mRNAs like Roquin (Uehata et al. 2013; Jeltsch et al. 2014). Moreover, the phenotype of *Zc3h12a*$^{-/-}$ mice closely resembles that observed in *Rc3h1-2*$^{fl/fl}$*; CD4 Cre* mice (Matsushita et al. 2009; Uehata et al. 2013). Together with our recently published data on cooperation of Roquin-1 and Regnase-1 in post-transcriptional regulation (Jeltsch et al. 2014), these observations suggest that Regnase-1 is a co-factor of Roquin proteins. In addition, the *Zc3h12a* mRNA is also a target candidate in the microarray analyses (**Table 20**), suggesting another negative feedback loop of Roquin.

Integrating the different mechanisms regulating Roquin levels, the interplay with co-factors and other *trans*-acting factors and the abundance of Roquin-targeted mRNAs with complex 3'UTRs will be the big challenge in continuative studies. Single aspects need to be addressed separately to collect the basic pieces of information, as shown in this study for the identification of mRNAs targeted by Roquin. However, only linking the various regulatory levels and pathways influencing each other will deepen the understanding of post-transcriptional gene regulation in general. Thereby, the study of Roquin offers a great chance to refine the picture of post-transcriptional mechanisms in T cells necessary to maintain self-tolerance and fast responsiveness.

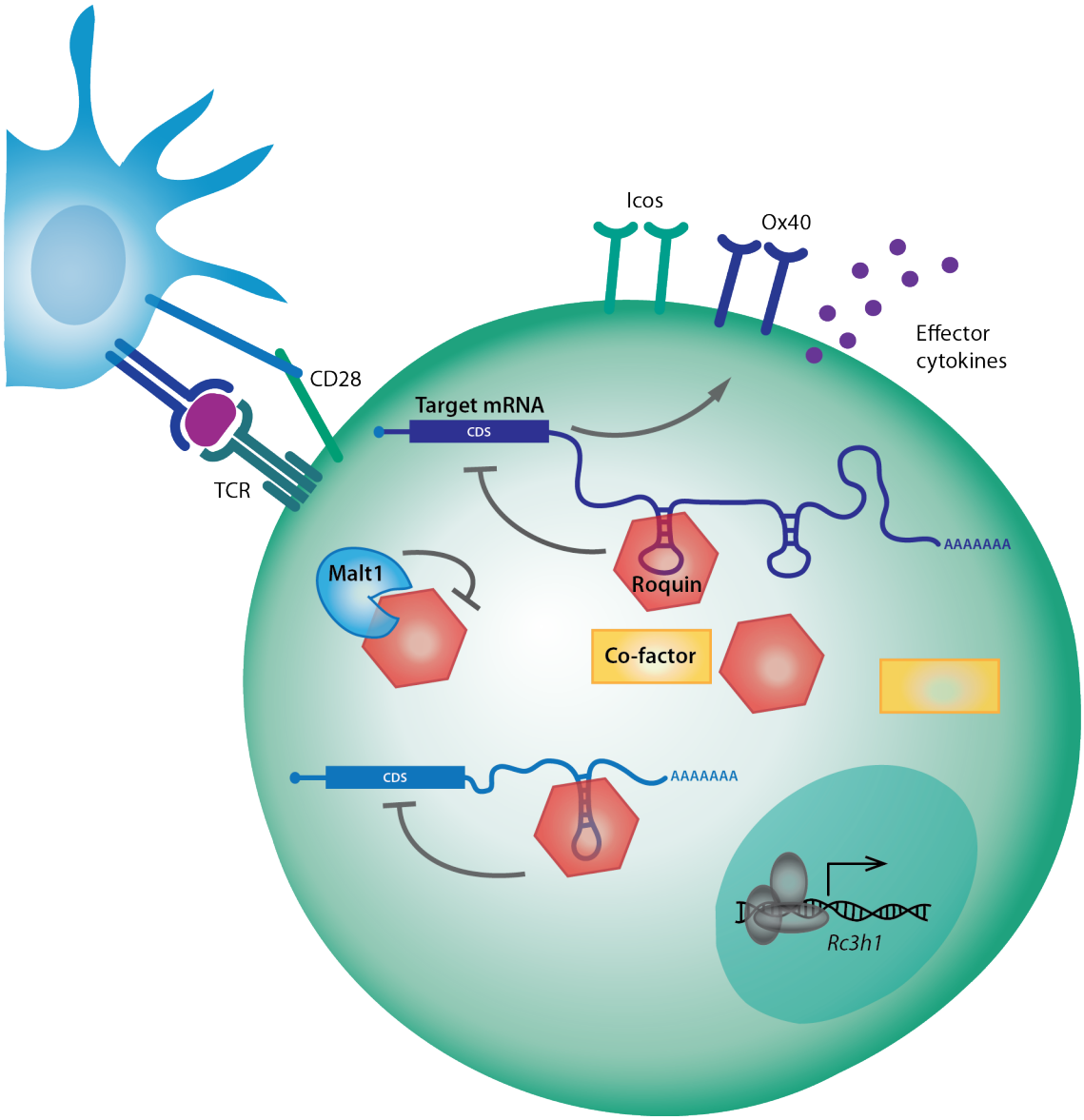

Figure 49: Model of Roquin function in T cells. Roquin binds to stem-loop structures within the 3'UTR of its target mRNAs and thereby reduces protein expression levels. This interaction and subsequent regulation depend on the accessibility of *cis*-elements and the availability of co-factors. Roquin itself is regulated on the transcriptional level as indicated in the nucleus of the T cell (green). Furthermore, upon T cell activation by antigen presenting cells (blue) the paracaspase Malt1 is activated and specifically cleaves Roquin, which releases target mRNAs like *Icos* and *Ox40* from Roquin-mediated post-transcriptional repression.

References

Akiba, H. et al., 2005. The Role of ICOS in the CXCR5+ Follicular B Helper T Cell Maintenance In Vivo. *The Journal of Immunology*, 175(4), pp.2340–2348.

al-Shamkhani, A. et al., 1996. OX40 is differentially expressed on activated rat and mouse T cells and is the sole receptor for the OX40 ligand. *European journal of immunology*, 26, pp.1695–1699.

Allen, J.D. et al., 1997. Pim-2 transgene induces lymphoid tumors, exhibiting potent synergy with c-myc. *Oncogene*, 15, pp.1133–1141.

Anderson, P., 2000. Post-transcriptional regulation of tumour necrosis factor α production. *Annals of the rheumatic diseases*, 59(suppl I), pp.5–8.

Ansel, K.M. et al., 2008. Mouse Eri1 interacts with the ribosome and catalyzes 5.8S rRNA processing. *Nature structural & molecular biology& molecular biology*, 15(5), pp.523–530.

Athanasopoulos, V. et al., 2010. The ROQUIN family of proteins localizes to stress granules via the ROQ domain and binds target mRNAs. *The FEBS journal*, 277(9), pp.2109–2127.

Ausubel, F.M., 2005. Are innate immune signaling pathways in plants and animals conserved? *Nature immunology*, 6, pp.973–979.

Aviv, T. et al., 2003. The RNA-binding SAM domain of Smaug defines a new family of post-transcriptional regulators. *Nature structural biology*, 10, pp.614–621.

Bansal-Pakala, P., Jember, A.G. & Croft, M., 2001. Signaling through OX40 (CD134) breaks peripheral T-cell tolerance. *Nature medicine*, 7, pp.907–912.

Battle, D.J. & Doudna, J.A., 2001. The stem-loop binding protein forms a highly stable and specific complex with the 3' stem-loop of histone mRNAs. *RNA (New York, N.Y.)*, 7, pp.123–132.

Benayoun, B.A., Caburet, S. & Veitia, R.A., 2011. Forkhead transcription factors: key players in health and disease. *Trends in genetics : TIG*, 27(6), pp.224–232.

Bennett, C.L. et al., 2001. The immune dysregulation, polyendocrinopathy, enteropathy, X-linked syndrome (IPEX) is caused by mutations of FOXP3. *Nature genetics*, 27, pp.20–21.

Bertossi, A. et al., 2011. Loss of Roquin induces early death and immune deregulation but not autoimmunity. *The Journal of experimental medicine*, 208(9), pp.1749–1756.

Bhattacharyya, S.N. et al., 2006. Relief of microRNA-Mediated Translational Repression in Human Cells Subjected to Stress. *Cell*, 125, pp.1111–1124.

Brengues, M., Teixeira, D. & Parker, R., 2005. Movement of eukaryotic mRNAs between polysomes and cytoplasmic processing bodies. *Science (New York, N.Y.)*, 310, pp.486–489.

Breuer, M.L., Cuypers, H.T. & Berns, A., 1989. Evidence for the involvement of pim-2, a new common proviral insertion site, in progression of lymphomas. *The EMBO journal*, 8, pp.743–748.

Brocker, T. et al., 1999. CD4 T cell traffic control: in vivo evidence that ligation of OX40 on CD4 T cells by OX40-ligand expressed on dendritic cells leads to the accumulation of CD4 T cells in B follicles. *European journal of immunology*, 29(5), pp.1610–1616.

Brümmer, A. & Hausser, J., 2014. MicroRNA binding sites in the coding region of mRNAs: Extending the repertoire of post-transcriptional gene regulation. *BioEssays*, 36, pp.617–626.

Brunkow, M.E. et al., 2001. Disruption of a new forkhead/winged-helix protein, scurfin, results in the fatal lymphoproliferative disorder of the scurfy mouse. *Nature genetics*, 27(1), pp.68–73.

Bull, M.J. et al., 2008. The Death Receptor 3-TNF-like protein 1A pathway drives adverse bone pathology in inflammatory arthritis. *The Journal of experimental medicine*, 205, pp.2457–2464.

Burkhard, P., Stetefeld, J. & Strelkov, S. V, 2001. Coiled coils: a highly versatile protein folding motif. *Trends in cell biology*, 11(2), pp.82–88.

Cabrera, C.M. et al., 2013. Differential expression of CD30 on CD3 T lymphocytes in patients with systemic lupus erythematosus. *Scandinavian journal of immunology*, 78(3), pp.306–312.

Camerini, D. et al., 1989. Leu-8/TQ1 is the human equivalent of the Mel-14 lymph node homing receptor. *Nature*, 342, pp.78–82.

Cano, F. et al., 2012. The RNA-binding E3 ubiquitin ligase MEX-3C links ubiquitination with MHC-I mRNA degradation. *The EMBO journal*, 31(17), pp.3596–3606.

Cano, F., Miranda-Saavedra, D. & Lehner, P.J., 2010. RNA-binding E3 ubiquitin ligases: novel players in nucleic acid regulation. *Biochemical Society transactions*, 38(6), pp.1621–1626.

Carreno, B.M. & Collins, M., 2002. The B7 family of ligands and its receptors: new pathways for costimulation and inhibition of immune responses. *Annual review of immunology*, 20, pp.29–53.

Castello, A. et al., 2012. Insights into RNA Biology from an Atlas of Mammalian mRNA-Binding Proteins. *Cell*, 149(6), pp.1393–1406.

Chan, A.C. et al., 1994. Differential expression of ZAP-70 and Syk protein tyrosine kinases, and the role of this family of protein tyrosine kinases in TCR signaling. *Journal of immunology (Baltimore, Md : 1950)*, 152(10), pp.4758–4766.

Chang, C., 2014. Autoimmunity: From black water fever to regulatory function. *Journal of Autoimmunity*, 48-49, pp.1–9.

Chang, M. s et al., 1997. Molecular cloning and functional characterization of a novel CC chemokine, stimulated T cell chemotactic protein (STCP-1) that specifically acts on activated T lymphocytes. *The Journal of biological chemistry*, 272(40), pp.25229–25237.

Chang, P.-P. et al., 2012. Breakdown in repression of IFN-γ mRNA leads to accumulation of self-reactive effector CD8+ T cells. *Journal of immunology (Baltimore, Md : 1950)*, 189(2), pp.701–710.

Chang, T.-W. et al., 2010. In vitro selection of RNA aptamers that inhibit the activity of type A botulinum neurotoxin. *Biochemical and biophysical research communications*, 396(4), pp.854–860.

Chantry, D. et al., 1999. Macrophage-derived chemokine is localized to thymic medullary epithelial cells and is a chemoattractant for CD3(+), CD4(+), CD8(low) thymocytes. *Blood*, 94(6), pp.1890–1898.

Cheadle, C. et al., 2005. Control of gene expression during T cell activation: alternate regulation of mRNA transcription and mRNA stability. *BMC genomics*, 6, p.75.

Chen, C., Edelstein, L.C. & Gélinas, C., 2000. The Rel/NF-kappaB family directly activates expression of the apoptosis inhibitor Bcl-x(L). *Molecular and cellular biology*, 20(8), pp.2687–2695.

Chen, C.Y. & Shyu, A.B., 1995. AU-rich elements: characterization and importance in mRNA degradation. *Trends in biochemical sciences*, 20, pp.465–470.

Chen, L. & Flies, D.B., 2013. Molecular mechanisms of T cell co-stimulation and co-inhibition. *Nature reviews. Immunology*, 13, pp.227–42.

Choi, Y.S. et al., 2011. ICOS Receptor Instructs T Follicular Helper Cell versus Effector Cell Differentiation via Induction of the Transcriptional Repressor Bcl6. *Immunity*, 34, pp.932–946.

Clement, S.L. et al., 2011. Phosphorylation of tristetraprolin by MK2 impairs AU-rich element mRNA decay by preventing deadenylase recruitment. *Molecular and cellular biology*, 31, pp.256–266.

Constant, S. et al., 1995. Extent of T cell receptor ligation can determine the functional differentiation of naive CD4+ T cells. *Journal of Experimental Medicine*, 182, pp.1591–1596.

Croft, M., 2010. Control of immunity by the TNFR-related molecule OX40 (CD134). *Annual review of immunology*, 28, pp.57–78.

Crotty, S., 2011. Follicular helper CD4 T cells (TFH). *Annual review of immunology*, 29, pp.621–663.

Crucs, S., Chatterjee, S. & Gavis, E.R., 2000. Overlapping but Distinct RNA Elements Control Repression and Activation of nanos Translation. *Molecular Cell*, 5(3), pp.457–467.

Dahanukar, A., Walker, J.A. & Wharton, R.P., 1999. Smaug, a novel RNA-binding protein that operates a translational switch in Drosophila. *Molecular Cell*, 4, pp.209–218.

Dahanukar, A. & Wharton, R.P., 1996. The Nanos gradient in Drosophila embryos is generated by translational regulation. *Genes and Development*, 10, pp.2610–2620.

DeGrendele, H.C., Kosfiszer, M., et al., 1997. CD44 activation and associated primary adhesion is inducible via T cell receptor stimulation. *J Immunol*, 159, pp.2549–2553.

DeGrendele, H.C., Estess, P. & Siegelman, M.H., 1997. Requirement for CD44 in activated T cell extravasation into an inflammatory site. *Science (New York, N.Y.)*, 278, pp.672–675.

Dember, L.M. et al., 1996. Individual RNA recognition motifs of TIA-1 and TIAR have different RNA binding specificities. *Journal of Biological Chemistry*, 271, pp.2783–2788.

Dominski, Z. et al., 2003. A 3′ Exonuclease that Specifically Interacts with the 3′ End of Histone mRNA. *Molecular Cell*, 12(2), pp.295–305.

Dong, C. et al., 2001. ICOS co-stimulatory receptor is essential for T-cell activation and function. *Nature*, 409, pp.97–101.

Ellyard, J.I. et al., 2012. Heterozygosity for Roquin san leads to angioimmunoblastic T-cell lymphoma-like tumors in mice. *Blood*, 120, pp.812–821.

Estep, P. et al., 2013. High throughput solution-based measurement of antibody-antigen affinity and epitope binning. *mAbs*, 5, pp.270–278.

Eulalio, A., Behm-Ansmant, I. & Izaurralde, E., 2007. P bodies: at the crossroads of post-transcriptional pathways. *Nature reviews. Molecular cell biology*, 8, pp.9–22.

Gajiwala, K.S. & Burley, S.K., 2000. Winged helix proteins. *Current opinion in structural biology*, 10(1), pp.110–116.

Galarneau, A. & Richard, S., 2005. Target RNA motif and target mRNAs of the Quaking STAR protein. *Nature structural & molecular biology*, 12(8), pp.691–698.

Garneau, N.L., Wilusz, J. & Wilusz, C.J., 2007. The highways and byways of mRNA decay. *Nature reviews. Molecular cell biology*, 8(2), pp.113–126.

Gaspal, F. et al., 2011. Abrogation of CD30 and OX40 signals prevents autoimmune disease in FoxP3-deficient mice. *The Journal of experimental medicine*, 208, pp.1579–1584.

Glasmacher, E. et al., 2010. Roquin binds inducible costimulator mRNA and effectors of mRNA decay to induce microRNA-independent post-transcriptional repression. *Nature immunology*, 11(8), pp.725–733.

Gottschalk, R.A., Corse, E. & Allison, J.P., 2010. TCR ligand density and affinity determine peripheral induction of Foxp3 in vivo. *The Journal of experimental medicine*, 207, pp.1701–1711.

Gramaglia, I. et al., 1998. Ox-40 ligand: a potent costimulatory molecule for sustaining primary CD4 T cell responses. *Journal of immunology (Baltimore, Md. : 1950)*, 161, pp.6510–6517.

Gramaglia, I. et al., 2000. The OX40 costimulatory receptor determines the development of CD4 memory by regulating primary clonal expansion. *Journal of immunology (Baltimore, Md : 1950)*, 165(6), pp.3043–3050.

Grawunder, U., West, R.B. & Lieber, M.R., 1998. Antigen receptor gene rearrangement. *Current opinion in immunology*, 10, pp.172–180.

Hafner, M. et al., 2010. Transcriptome-wide identification of RNA-binding protein and microRNA target sites by PAR-CLIP. *Cell*, 141(1), pp.129–141.

Halees, A.S., El-badrawi, R. & Khabar, K.S.A., 2008. ARED Organism: Expansion of ARED reveals AU-rich element cluster variations between human and mouse. *Nucleic Acids Research*, 36.

Hall, T.M.T., 2005. Multiple modes of RNA recognition by zinc finger proteins. *Current opinion in structural biology*, 15(3), pp.367–373.

Hameyer, D. et al., 2007. Toxicity of ligand-dependent Cre recombinases and generation of a conditional Cre deleter mouse allowing mosaic recombination in peripheral tissues. *Physiological genomics*, 31(1), pp.32–41.

Hammerman, P.S. et al., 2005. Pim and Akt oncogenes are independent regulators of hematopoietic cell growth and survival. *Blood*, 105, pp.4477–4483.

Harami, G.M., Gyimesi, M. & Kovács, M., 2013. From keys to bulldozers: expanding roles for winged helix domains in nucleic-acid-binding proteins. *Trends in biochemical sciences*, 38(7), pp.364–371.

Hausser, J. et al., 2013. Analysis of CDS-located miRNA target sites suggests that they can effectively inhibit translation. *Genome research*, 23, pp.604–15.

He, F. et al., 2003. Genome-Wide Analysis of mRNAs Regulated by the Nonsense-Mediated and 5’ to 3' mRNA Decay Pathways in Yeast. *Molecular Cell*, 12, pp.1439–1452.

Hegazy, A.N. et al., 2010. Interferons Direct Th2 Cell Reprogramming to Generate a Stable GATA-3+T-bet+ Cell Subset with Combined Th2 and Th1 Cell Functions. *Immunity*, 32, pp.116–128.

Higgins, L.M. et al., 1999. Regulation of T cell activation in vitro and in vivo by targeting the OX40-OX40 ligand interaction: amelioration of ongoing inflammatory bowel disease with an OX40-IgG fusion protein, but not with an OX40 ligand-IgG fusion protein. *Journal of immunology (Baltimore, Md. : 1950)*, 162(1), pp.486–93.

Hoefig, K.P. et al., 2013. Eri1 degrades the stem-loop of oligouridylated histone mRNAs to induce replication-dependent decay. *Nature structural & molecular biology*, 20(1), pp.73–81.

Hoinka, J. et al., 2012. Identification of sequence-structure RNA binding motifs for SELEX-derived aptamers. *Bioinformatics (Oxford, England)*, 28(12), pp.i215–23.

Hosken, N.A. et al., 1995. The effect of antigen dose on CD4+ T helper cell phenotype development in a T cell receptor-alpha beta-transgenic model. *The Journal of experimental medicine*, 182, pp.1579–1584.

Houalla, R. et al., 2006. Microarray detection of novel nuclear RNA substrates for the exosome. *Yeast*, 23, pp.439–454.

Hu, X. et al., 2014. Computational identification of protein binding sites on RNAs using high-throughput RNA structure-probing data. *Bioinformatics (Oxford, England)*.

Hutloff, A. et al., 1999. ICOS is an inducible T-cell co-stimulator structurally and functionally related to CD28. *Nature*, 397(6716), pp.263–266.

Ingolia, N.T. et al., 2009. Genome-wide analysis in vivo of translation with nucleotide resolution using ribosome profiling. *Science (New York, NY)*, 324(5924), pp.218–223.

Ingolia, N.T. et al., 2012. The ribosome profiling strategy for monitoring translation in vivo by deep sequencing of ribosome-protected mRNA fragments. *Nature protocols*, 7(8), pp.1534–1550.

Ivanov, P. & Anderson, P., 2013. Post-transcriptional regulatory networks in immunity. *Immunological reviews*, 253(1), pp.253–272.

Iwasaki, H. et al., 2011. The IκB kinase complex regulates the stability of cytokine-encoding mRNA induced by TLR-IL-1R by controlling degradation of regnase-1. *Nature immunology*, 12(12), pp.1167–1175.

Janeway, C.A. & Medzhitov, R., 2002. Innate immune recognition. *Annual review of immunology*, 20, pp.197–216.

Jeltsch, K.M. et al., 2014. Cleavage of roquin and regnase-1 by the paracaspase MALT1 releases their cooperatively repressed targets to promote TH17 differentiation. *Nature immunology*, 15(11), pp.1079–1089.

Jin, Y. et al., 2003. A vertebrate RNA-binding protein Fox-1 regulates tissue-specific splicing via the pentanucleotide GCAUG. *The EMBO journal*, 22(4), pp.905–912.

Johnston, R.J. et al., 2009. Bcl6 and Blimp-1 are reciprocal and antagonistic regulators of T follicular helper cell differentiation. *Science (New York, N.Y.)*, 325, pp.1006–1010.

Josefowicz, S.Z., Lu, L.-F. & Rudensky, A.Y., 2012. Regulatory T Cells: Mechanisms of Differentiation and Function. *Annual Review of Immunology*, 30, pp.531–564.

Katsanou, V. et al., 2005. HuR as a negative posttranscriptional modulator in inflammation. *Molecular Cell*, 19, pp.777–789.

Kay, B.K., Williamson, M.P. & Sudol, M., 2000. The importance of being proline: the interaction of proline-rich motifs in signaling proteins with their cognate domains. *FASEB journal : official publication of the Federation of American Societies for Experimental Biology*, 14(2), pp.231–241.

Kedersha, N. et al., 2000. Dynamic shuttling of TIA-1 accompanies the recruitment of mRNA to mammalian stress granules. *The Journal of cell biology*, 151(6), pp.1257–68.

Kedersha, N., Gupta, M. & Li, W., 1999. RNA-binding proteins TIA-1 and TIAR link the phosphorylation of eIF-2α to the assembly of mammalian stress granules. *The Journal of cell biology*, 147(7), pp.1431–1441.

Khorshid, M., Rodak, C. & Zavolan, M., 2011. CLIPZ: a database and analysis environment for experimentally determined binding sites of RNA-binding proteins. *Nucleic acids research*, 39, pp.D245–52.

Kim, C.C. & Lanier, L.L., 2013. Beyond the transcriptome: completion of act one of the Immunological Genome Project. *Current opinion in immunology*, 25(5), pp.593–597.

Kim, H.J. et al., 2012. The role of Roquin overexpression in the modulation of signaling during in vitro and ex vivo T-cell activation. *Biochemical and biophysical research communications*, 417(1), pp.280–286.

Koch, M.A. et al., 2009. The transcription factor T-bet controls regulatory T cell homeostasis and function during type 1 inflammation. *Nature immunology*, 10, pp.595–602.

Kontoyiannis, D. et al., 1999. Impaired on/off regulation of TNF biosynthesis in mice lacking TNF AU-rich elements: implications for joint and gut-associated immunopathologies. *Immunity*, 10(3), pp.387–98.

Kopf, M. et al., 1999. OX40-deficient mice are defective in Th cell proliferation but are competent in generating B cell and CTL Responses after virus infection. *Immunity*, 11(6), pp.699–708.

Lafferty, K.J. & Cunningham, A.J., 1975. A new analysis of allogeneic interactions. *The Australian journal of experimental biology and medical science*, 53, pp.27–42.

Lai, W.S. et al., 1999. Evidence that tristetraprolin binds to AU-rich elements and promotes the deadenylation and destabilization of tumor necrosis factor alpha mRNA. *Molecular and cellular biology*, 19, pp.4311–4323.

Lai, W.S. et al., 2000. Interactions of CCCH zinc finger proteins with mRNA. Binding of tristetraprolin-related zinc finger proteins to AU-rich elements and destabilization of mRNA. *Journal of Biological Chemistry*, 275, pp.17827–17837.

Lambert, N. et al., 2014. RNA Bind-n-Seq: quantitative assessment of the sequence and structural binding specificity of RNA binding proteins. *Molecular cell*, 54(5), pp.887–900.

Lapadula, G. et al., 2014. Adalimumab in the treatment of immune-mediated diseases. *International journal of immunopathology and pharmacology*, 27, pp.33–48.

Lee, P.P. et al., 2001. A critical role for Dnmt1 and DNA methylation in T cell development, function, and survival. *Immunity*, 15(5), pp.763–774.

Lee, S.K. et al., 2012. Interferon-gamma Excess Leads to Pathogenic Accumulation of Follicular Helper T Cells and Germinal Centers. *Immunity*, 37, pp.880–892.

Lee, Y.K. et al., 2009. Late Developmental Plasticity in the T Helper 17 Lineage. *Immunity*, 30, pp.92–107.

Leppek, K. et al., 2013. Roquin promotes constitutive mRNA decay via a conserved class of stem-loop recognition motifs. *Cell*, 153(4), pp.869–881.

Li, M. et al., 2012. MCPIP1 down-regulates IL-2 expression through an ARE-independent pathway. *PloS one*, 7(11), p.e49841.

Liao, B., Hu, Y. & Brewer, G., 2007. Competitive binding of AUF1 and TIAR to MYC mRNA controls its translation. *Nature structural & molecular biology*, 14, pp.511–518.

Licatalosi, D.D. et al., 2008. HITS-CLIP yields genome-wide insights into brain alternative RNA processing. *Nature*, 456(7221), pp.464–469.

Lin, W.-J. et al., 2011. Posttranscriptional control of type I interferon genes by KSRP in the innate immune response against viral infection. *Molecular and cellular biology*, 31, pp.3196–3207.

Ling, V. et al., 2001. Assembly and annotation of human chromosome 2q33 sequence containing the CD28, CTLA4, and ICOS gene cluster: analysis by computational, comparative, and microarray approaches. *Genomics*, 78, pp.155–168.

Linterman, M.A., Rigby, R.J., Wong, R.K., et al., 2009. Follicular helper T cells are required for systemic autoimmunity. *The Journal of experimental medicine*, 206(3), pp.561–576.

Linterman, M.A., Rigby, R.J., Wong, R., et al., 2009. Roquin differentiates the specialized functions of duplicated T cell costimulatory receptor genes CD28 and ICOS. *Immunity*, 30(2), pp.228–241.

Lippert, E., Müller, M. & Ott, C., 2014. Golimumab in unresponsive ulcerative colitis. *Biologics: Targets and Therapy*, 8, pp.207–210.

Liu, Z.R. et al., 1996. Detection of double-stranded RNA-protein interactions by methylene blue-mediated photo-crosslinking. *RNA*, 2(6), pp.611–621.

Loflin, P., Chen, C.Y.A. & Shyu, A. Bin, 1999. Unraveling a cytoplasmic role for hnRNP d in the in vivo mRNA destabilization directed by the AU-rich element. *Genes and Development*, 13, pp.1884–1897.

Lu, J.Y., Sadri, N. & Schneider, R.J., 2006. Endotoxic shock in AUF1 knockout mice mediated by failure to degrade proinflammatory cytokine mRNAs. *Genes and Development*, 20, pp.3174–3184.

Lunde, B.M., Moore, C. & Varani, G., 2007. RNA-binding proteins: modular design for efficient function. *Nature reviews. Molecular cell biology*, 8(6), pp.479–490.

Maekawa, S., Iemura, H. & Kato, T., 2013. Enhanced erythropoiesis in mice exposed to low environmental temperature. *The Journal of experimental biology*, 216, pp.901–8.

Mallett, S., Fossum, S. & Barclay, A.N., 1990. Characterization of the MRC OX40 antigen of activated CD4 positive T lymphocytes--a molecule related to nerve growth factor receptor. *The EMBO journal*, 9, pp.1063–1068.

Marchese, F.P. et al., 2010. MAPKAP kinase 2 blocks tristetraprolin-directed mRNA decay by inhibiting CAF1 deadenylase recruitment. *Journal of Biological Chemistry*, 285, pp.27590–27600.

Martin-Orozco, N. et al., 2003. Paradoxical dampening of anti-islet self-reactivity but promotion of diabetes by OX40 ligand. *Journal of immunology (Baltimore, Md. : 1950)*, 171, pp.6954–6960.

Maruyama, T. et al., 2014. Roquin-2 promotes ubiquitin-mediated degradation of ASK1 to regulate stress responses. *Science signaling*, 7(309), p.ra8.

Mason, J.M. & Arndt, K.M., 2004. Coiled coil domains: stability, specificity, and biological implications. *Chembiochem : a European journal of chemical biology*, 5(2), pp.170–176.

Matoulkova, E. et al., 2012. The role of the 3' untranslated region in post-transcriptional regulation of protein expression in mammalian cells. *RNA biology*, 9(5), pp.563–576.

Matsushita, K. et al., 2009. Zc3h12a is an RNase essential for controlling immune responses by regulating mRNA decay. *Nature*, 458(7242), pp.1185–1190.

McAdam, A.J. et al., 2001. ICOS is critical for CD40-mediated antibody class switching. *Nature*, 409(6816), pp.102–105.

Meisenheimer, K.M. & Koch, T.H., 1997. Photocross-linking of nucleic acids to associated proteins. *Critical reviews in biochemistry and molecular biology*, 32(2), pp.101–140.

Meylan, F. et al., 2008. The TNF-Family Receptor DR3 is Essential for Diverse T Cell-Mediated Inflammatory Diseases. *Immunity*, 29, pp.79–89.

Miao, R., Huang, S. & Zhou, Z., 2013. Targeted disruption of MCPIP1/Zc3h12a results in fatal inflammatory disease. *Immunology and cell biology*, 91(5), pp.368–376.

Michel, S.L.J., Guerrerio, A.L. & Berg, J.M., 2003. Selective RNA binding by a single CCCH zinc-binding domain from Nup475 (Tristetraprolin). *Biochemistry*, 42(16), pp.4626–4630.

Murata, K. et al., 2002. Constitutive OX40/OX40 ligand interaction induces autoimmune-like diseases. *Journal of immunology (Baltimore, Md : 1950)*, 169(8), pp.4628–4636.

Murphy, K., Travers, P. & Walport, M., 2008. *Janeway's Immunobiology*,

Nakayamada, S. et al., 2012. Helper T cell diversity and plasticity. *Current opinion in immunology*, 24(3), pp.297–302.

Ndhlovu, L.C. et al., 2001. Critical involvement of OX40 ligand signals in the T cell priming events during experimental autoimmune encephalomyelitis. *Journal of immunology (Baltimore, Md. : 1950)*, 167, pp.2991–2999.

Nohara, C. et al., 2001. Amelioration of experimental autoimmune encephalomyelitis with anti-OX40 ligand monoclonal antibody: a critical role for OX40 ligand in migration, but not development, of pathogenic T cells. *Journal of immunology (Baltimore, Md. : 1950)*, 166, pp.2108–2115.

Nurieva, R.I. et al., 2009. Bcl6 mediates the development of T follicular helper cells. *Science (New York, N.Y.)*, 325, pp.1001–1005.

Olasz, K. et al., 2012. T cell receptor (TCR) signal strength controls arthritis severity in proteoglycan-specific TCR transgenic mice. *Clinical and Experimental Immunology*, 167, pp.346–355.

Olson, B.M., Sullivan, J.A. & Burlingham, W.J., 2013. Interleukin 35: a key mediator of suppression and the propagation of infectious tolerance. *Frontiers in immunology*, 4, p.315.

Pagano, J.M. et al., 2009. RNA recognition by the embryonic cell fate determinant and germline totipotency factor MEX-3. *Proceedings of the National Academy of Sciences of the United States of America*, 106(48), pp.20252–20257.

Van Panhuys, N., Klauschen, F. & Germain, R.N., 2014. T-Cell-Receptor-Dependent Signal Intensity Dominantly Controls CD4(+) T Cell Polarization In Vivo. *Immunity*, 41, pp.63–74.

Park, H. et al., 2005. A distinct lineage of CD4 T cells regulates tissue inflammation by producing interleukin 17. *Nature immunology*, 6, pp.1133–1141.

Paschoud, S. et al., 2006. Destabilization of interleukin-6 mRNA requires a putative RNA stem-loop structure, an AU-rich element, and the RNA-binding protein AUF1. *Molecular and cellular biology*, 26(22), pp.8228–8241.

Patel, A.M. & Moreland, L.W., 2010. Certolizumab pegol: a new biologic targeting rheumatoid arthritis. *Expert review of clinical immunology*, 6, pp.855–866.

Pflanz, S. et al., 2002. IL-27, a heterodimeric cytokine composed of EBI3 and p28 protein, induces proliferation of naive CD4+ T cells. *Immunity*, 16(6), pp.779–790.

Piecyk, M. et al., 2000. TIA-1 is a translational silencer that selectively regulates the expression of TNF-alpha. *The EMBO journal*, 19, pp.4154–4163.

Ponthier, J.L. et al., 2006. Fox-2 splicing factor binds to a conserved intron motif to promote inclusion of protein 4.1R alternative exon 16. *The Journal of biological chemistry*, 281(18), pp.12468–12474.

Pratama, A. et al., 2013. Roquin-2 Shares Functions with Its Paralog Roquin-1 in the Repression of mRNAs Controlling T Follicular Helper Cells and Systemic Inflammation. *Immunity*, 38(4), pp.669–680.

Provenzano, M. & Mocellin, S., 2007. Complementary techniques: Validation of gene expression data by quantitative real time PCR. *Advances in Experimental Medicine and Biology*, 593, pp.66–73.

Qureshi, O.S. et al., 2011. Trans-endocytosis of CD80 and CD86: a molecular basis for the cell-extrinsic function of CTLA-4. *Science (New York, NY)*, 332(6029), pp.600–603.

Reid, D.C. et al., 2009. Next-generation SELEX identifies sequence and structural determinants of splicing factor binding in human pre-mRNA sequence. *RNA*, 15(12), pp.2385–2397.

Romagnani, S. et al., 1995. CD30 and type 2 T helper (Th2) responses. *Journal of leukocyte biology*, 57(5), pp.726–730.

Rudd, C.E. & Schneider, H., 2003. Unifying concepts in CD28, ICOS and CTLA4 co-receptor signalling. *Nature reviews. Immunology*, 3(7), pp.544–556.

Sandberg, R. et al., 2008. Proliferating cells express mRNAs with shortened 3' untranslated regions and fewer microRNA target sites. *Science (New York, NY)*, 320(5883), pp.1643–1647.

Schaefer, J.S. et al., 2011. Selective Upregulation of microRNA Expression in Peripheral Blood Leukocytes in IL-10-/- Mice Precedes Expression in the Colon. *Journal of immunology (Baltimore, Md : 1950)*.

Schaefer, J.S., Montufar-Solis, D. & Klein, J.R., 2014. A role for IL-10 in the transcriptional regulation of Roquin-1. *Gene*.

Schlundt, A. et al., 2014. Structural basis for RNA recognition in roquin-mediated post-transcriptional gene regulation. *Nature structural & molecular biology*, 21(8), pp.671–678.

Shortman, K. et al., 1990. The generation and fate of thymocytes. *Seminars in immunology*, 2, pp.3–12.

Siess, D.C. et al., 2000. A human gene coding for a membrane-associated nucleic acid-binding protein. *The Journal of biological chemistry*, 275(43), pp.33655–62.

Silva, D.G. et al., 2011. Anti-islet autoantibodies trigger autoimmune diabetes in the presence of an increased frequency of islet-reactive CD4 T cells. *Diabetes*, 60(8), pp.2102–2111.

Smibert, C.A. et al., 1996. smaug protein represses translation of unlocalized nanos mRNA in the Drosophila embryo. *Genes and Development*, 10, pp.2600–2609.

Smibert, C.A. et al., 1999. Smaug, a novel and conserved protein, contributes to repression of nanos mRNA translation in vitro. *RNA (New York, N.Y.)*, 5, pp.1535–1547.

Smyth, G.K. & Speed, T., 2003. Normalization of cDNA microarray data. *Methods (San Diego, Calif)*, 31(4), pp.265–273.

Soler, N., Fourmy, D. & Yoshizawa, S., 2007. Structural insight into a molecular switch in tandem winged-helix motifs from elongation factor SelB. *Journal of molecular biology*, 370(4), pp.728–741.

Spolski, R. & Leonard, W.J., 2010. IL-21 and T follicular helper cells. *International immunology*, 22(1), pp.7–12.

Srinivasan, M. & Frauwirth, K.A., 2009. Peripheral tolerance in CD8+ T cells. *Cytokine*, 46, pp.147–159.

Stoecklin, G. et al., 2003. A constitutive decay element promotes tumor necrosis factor alpha mRNA degradation via an AU-rich element-independent pathway. *Molecular and cellular biology*, 23(10), pp.3506–3515.

Stoecklin, G. et al., 2008. Genome-wide analysis identifies interleukin-10 mRNA as target of tristetraprolin. *Journal of Biological Chemistry*, 283, pp.11689–11699.

Storey, J.D. & Tibshirani, R., 2003. Statistical significance for genomewide studies. *Proceedings of the National Academy of Sciences of the United States of America*, 100(16), pp.9440–9445.

Sun, X. et al., 2010. CD30 ligand/CD30 plays a critical role in Th17 differentiation in mice. *Journal of immunology (Baltimore, Md. : 1950)*, 185, pp.2222–2230.

Tafuri, A. et al., 2001. ICOS is essential for effective T-helper-cell responses. *Nature*, 409(6816), pp.105–109.

Takedatsu, H. et al., 2008. TL1A (TNFSF15) Regulates the Development of Chronic Colitis by Modulating Both T-Helper 1 and T-Helper 17 Activation. *Gastroenterology*, 135.

Tan, D. et al., 2013. Structure of histone mRNA stem-loop, human stem-loop binding protein, and 3'hExo ternary complex. *Science (New York, NY)*, 339(6117), pp.318–321.

Tan, D. et al., 2014. The ROQ domain of Roquin recognizes mRNA constitutive-decay element and double-stranded RNA. *Nature structural & molecular biology*, 21(8), pp.679–685.

Taylor, G.A. et al., 1996. A pathogenetic role for TNFα in the syndrome of cachexia, arthritis, and autoimmunity resulting from tristetraprolin (TTP) deficiency. *Immunity*, 4, pp.445–454.

Temme, C. et al., 2004. A complex containing the CCR4 and CAF1 proteins is involved in mRNA deadenylation in Drosophila. *The EMBO journal*, 23, pp.2862–2871.

Teplova, M. et al., 2006. Structural basis for recognition and sequestration of UUU(OH) 3' temini of nascent RNA polymerase III transcripts by La, a rheumatic disease autoantigen. *Molecular cell*, 21(1), pp.75–85.

Tharun, S. et al., 2000. Yeast Sm-like proteins function in mRNA decapping and decay. *Nature*, 404, pp.515–518.

Totsuka, T. et al., 2003. Therapeutic effect of anti-OX40L and anti-TNF-alpha MAbs in a murine model of chronic colitis. *American journal of physiology. Gastrointestinal and liver physiology*, 284(4), pp.G595–603.

Uehata, T. et al., 2013. Malt1-Induced Cleavage of Regnase-1 in CD4(+) Helper T Cells Regulates Immune Activation. *Cell*, 153(5), pp.1036–1049.

Ule, J. et al., 2003. CLIP identifies Nova-regulated RNA networks in the brain. *Science (New York, NY)*, 302(5648), pp.1212–1215.

Ule, J. et al., 2005. CLIP: a method for identifying protein-RNA interaction sites in living cells. *Methods (San Diego, Calif)*, 37(4), pp.376–386.

Villarino, A. V. et al., 2011. Posttranscriptional Silencing of Effector Cytokine mRNA Underlies the Anergic Phenotype of Self-Reactive T Cells. *Immunity*, 34, pp.50–60.

Vinuesa, C.G. et al., 2005. A RING-type ubiquitin ligase family member required to repress follicular helper T cells and autoimmunity. *Nature*, 435(7041), pp.452–458.

Vogel, K.U. et al., 2013. Roquin Paralogs 1 and 2 Redundantly Repress the Icos and Ox40 Costimulator mRNAs and Control Follicular Helper T Cell Differentiation. *Immunity*, 38(4), pp.655–668.

Vulcano, M. et al., 2001. Dendritic cells as a major source of macrophage-derived chemokine/CCL22 in vitro and in vivo. *European journal of immunology*, 31(3), pp.812–822.

Wang, Y. et al., 2006. Large scale real-time PCR validation on gene expression measurements from two commercial long-oligonucleotide microarrays. *BMC genomics*, 7, p.59.

Watts, T.H., 2005. TNF/TNFR family members in costimulation of T cell responses. *Annual review of immunology*, 23, pp.23–68.

Weinberg, A.D. et al., 1999. Blocking OX-40/OX-40 ligand interaction in vitro and in vivo leads to decreased T cell function and amelioration of experimental allergic encephalomyelitis. *Journal of immunology (Baltimore, Md. : 1950)*, 162, pp.1818–1826.

White, E.K., Moore-Jarrett, T. & Ruley, H.E., 2001. PUM2, a novel murine puf protein, and its consensus RNA-binding site. *RNA (New York, N.Y.)*, 7, pp.1855–1866.

Williams, a S. & Marzluff, W.F., 1995. The sequence of the stem and flanking sequences at the 3' end of histone mRNA are critical determinants for the binding of the stem-loop binding protein. *Nucleic acids research*, 23(4), pp.654–62.

Williamson, M.P., 1994. The structure and function of proline-rich regions in proteins. *The Biochemical journal*, 297(Pt 2), pp.249–260.

Wohlfert, E.A. et al., 2011. GATA3 controls Foxp3$^+$ regulatory T cell fate during inflammation in mice. *The Journal of clinical investigation*, 121, pp.4503–15.

Xiao, X. et al., 2012. New insights on OX40 in the control of T cell immunity and immune tolerance in vivo. *Journal of immunology (Baltimore, Md : 1950)*, 188(2), pp.892–901.

Yamane, H. & Paul, W.E., 2013. Early signaling events that underlie fate decisions of naive CD4(+) T cells toward distinct T-helper cell subsets. *Immunological reviews*, 252(1), pp.12–23.

Yan, B. et al., 2003. The PIM-2 kinase phosphorylates BAD on serine 112 and reverses BAD-induced cell death. *The Journal of biological chemistry*, 278, pp.45358–45367.

Yoshioka, T. et al., 2000. Contribution of OX40/OX40 ligand interaction to the pathogenesis of rheumatoid arthritis. *European Journal of Immunology*, 30, pp.2815–2823.

Yoshizawa, S. et al., 2005. Structural basis for mRNA recognition by elongation factor SelB. *Nature structural & molecular biology*, 12(2), pp.198–203.

Yu, D. et al., 2007. Roquin represses autoimmunity by limiting inducible T-cell co-stimulator messenger RNA. *Nature*, 450(7167), pp.299–303.

Yu, D. et al., 2009. The Transcriptional Repressor Bcl-6 Directs T Follicular Helper Cell Lineage Commitment. *Immunity*, 31, pp.457–468.

Zaessinger, S., Busseau, I. & Simonelig, M., 2006. Oskar allows nanos mRNA translation in Drosophila embryos by preventing its deadenylation by Smaug/CCR4. *Development (Cambridge, England)*, 133, pp.4573–4583.

Zhang, Y. et al., 2008. Pim kinase-dependent inhibition of c-Myc degradation. *Oncogene*, 27(35), pp.4809–4819.

Zong, W.X. et al., 1999. The prosurvival Bcl-2 homolog Bfl-1/A1 is a direct transcriptional target of NF-kappaB that blocks TNFalpha-induced apoptosis. *Genes & development*, 13(4), pp.382–387.

Appendices

Appendix I: Position of Roquin-1 SELEX-enriched hexamers within the random RNA sequence.

Enriched 6-mer: CGTTTT

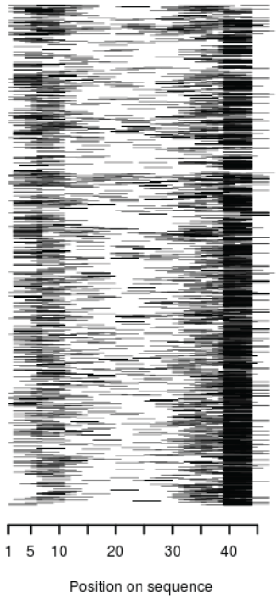

Enriched 6-mer: GTTTTA

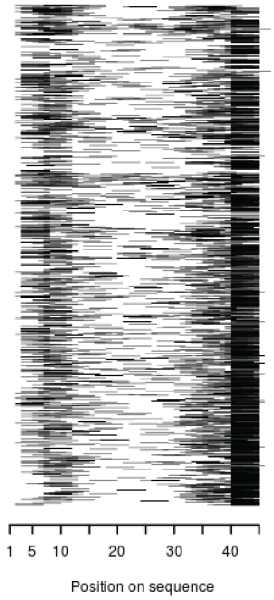

Enriched 6-mer: TGCGTT

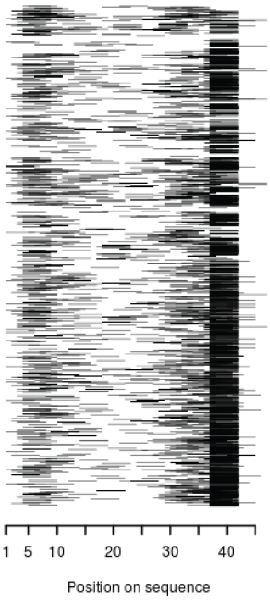

Enriched 6-mer: TTTTAG

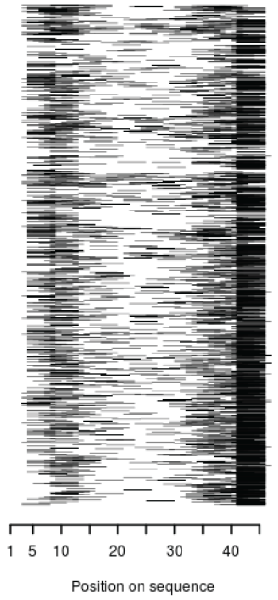

Enriched 6-mer: CTGCGT

Enriched 6-mer: GCGTTT

Appendix II: Shift assays using different concentrations of mutant versions of the ROQ domain (aa 147-326) binding to the ^{32}P-labeled *Tnf* CDE stem-loop RNA.

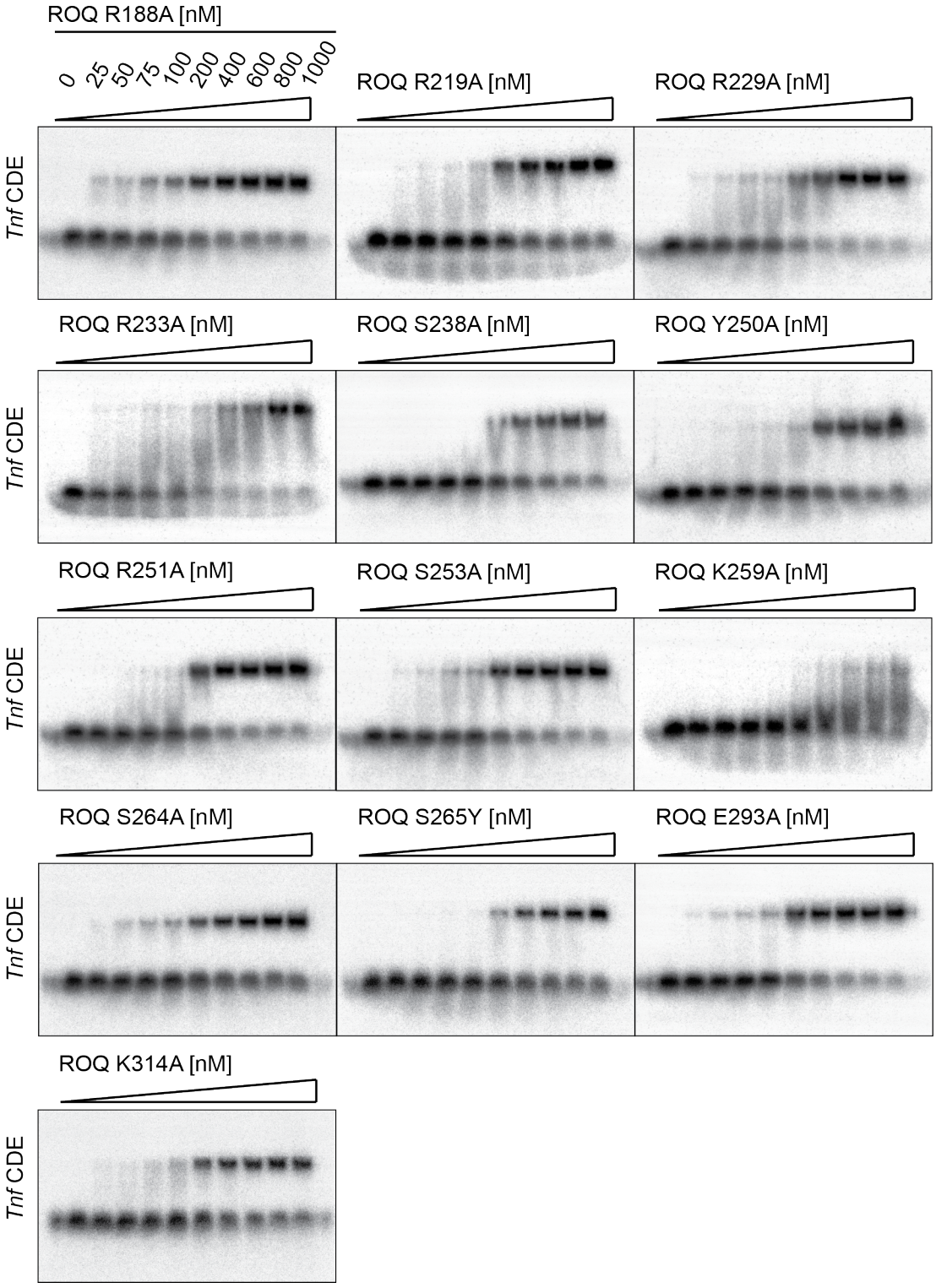

Appendix III: Overview table of all ROQ mutants tested in binding assays with the *Tnf* CDE. Information about the RNA contacts of the respective amino acid residue is derived from the crystal structure of the ROQ-*Tnf* CDE complex. Dissociation constants (K_d values) were calculated by curve fitting and are given ± standard error.

Mutants	RNA contacts	RNA binding K_d [nM]	Functional activity tested
R188A	phosphate contact?	143 ± 5	
R219A	loop purin stack	220 ± 15	
K220A	phosphate contact	n/a	x
R229A		174 ± 4	
R233A		288 ± 11	
S238A	phosphate contact?	373 ± 14	
K239A	phosphate contact	n/a	x
Y250A	phosphate contact	325 ± 9	
R251A	phosphate & E293 contact	174 ± 5	
S253A	loop py contact	159 ± 6	
K259A	loop Py/phos contact	n/a	
R260A	loop indirect	n/a	x
S264A	phosphate contact	290 ± 28	
S265Y		405 ± 17	
E293A	contact R190, R251	174 ± 9	
K314A		197 ± 12	
R239A/R260A		n/a	x

Appendix IV: Titration of amphotropic retrovirus supernatants to achieve comparable infection levels (proportion of Thy1.1$^+$ cells) and thus comparable expression of Roquin-1 proteins. Different volumes of virus supernatants (right side) were complemented with medium to use identical infection volumes during spin infection. For final experiments a volume was used that resulted in about 50% infection in the titration experiment.

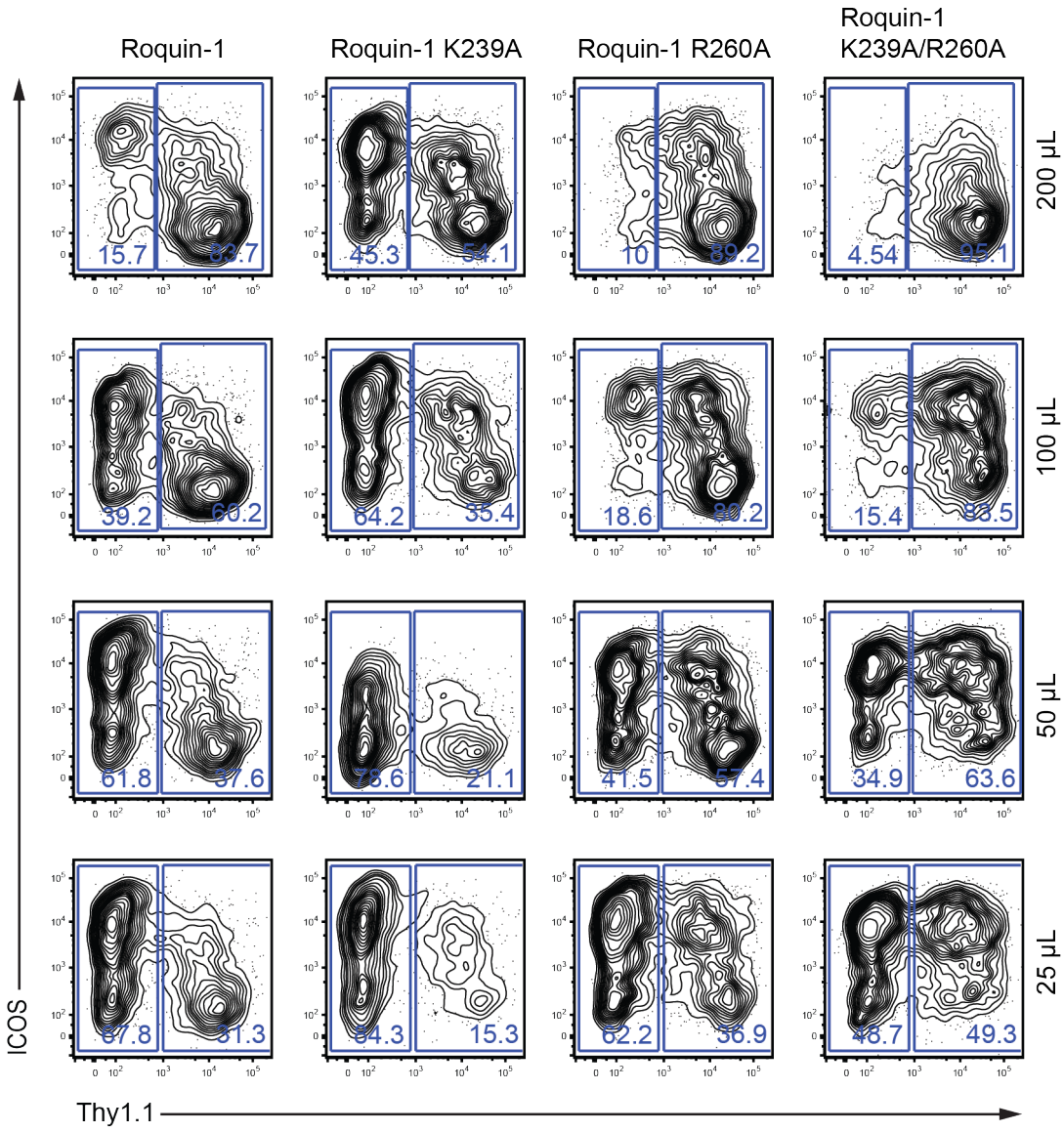

Appendix V: *Ox40* 3'UTR, truncations and mutations abrogating putative stem-loop structures (SELEX-like stem-loop: green, CDE-like stem-loop: red).

Ox40 3'UTR

SELEX-like stem loop **CDE-like stem loop**

5′gcattactacaggagtggatttatggggcacggacaacccatatcctgatgcctgccagtaccctccacaccgttctaggtgctgggctggctctgggcttttcctatgtatgctatgcatactacctgcctggtggtgctcctaataaacatgcta 3′

5′gcattactacaggagtggatttatggggcacggacaacccatatcctgatgcctgccagtaccctccacaccgttctaggtgctgggctggctctgggcttttcctatgtatgctatgca 1-120

5′gcattactacaggagtggatttatggggcacggacaacccatatcctgatgcctgccagtaccctccacaccgttctag 1-80

5′gcattactacaggagtggatttatggggcacggacaac 1-40

5′gcattactacaggagtggatttatggggcacggacaacccatatcctgatgcctgccagtaccctccacaccgttctaCCAgctgggctggctctgggcttttcctatgtatgctatgcatactacctgcctggtggtgctcctaataaacatgcta 3′

5′gcattactacaggagtggatttatggggcacggacaacccatatcctgatgcctgccagtaccctccacaccgttctaggtgctgggctggctctgggcttttcctatgtatgctatCGTtactacctgcctggtggtgctcctaataaacatgcta 3′

5′gcattactacaggagtggatttatggggcacggacaacccatatcctgatgcctgccagtaccctccacaccgttctaCCAgctgggctggctctgggcttttcctatgtatgctatCGTtactacctgcctggtggtgctcctaataaacatgcta 3′

Publications

Articles connected to this thesis

Jeltsch KM*, Hu D*, Brenner S*, Zöller J, **Heinz GA**, Nagel D, Vogel KU, Rehage N, Warth SC, Edelmann SL, Gloury R, Martin N, Lohs C, Lech M, Stehklein JE, Geerlof A, Kremmer E, Weber A, Anders HJ, Schmitz I, Schmidt-Supprian M, Fu M, Holtmann H, Krappmann D, Ruland J, Kallies A, Heikenwalder M, Heissmeyer V. **Cleavage of roquin and regnase-1 by the paracaspase MALT1 releases their cooperatively repressed targets to promote TH17 differentiation.** *Nat Immunol*. 2014 Nov; 15(11), pp. 1079-1089 * Equal contribution

Schlundt A*, **Heinz GA***, Janowski R*, Geerlof A, Stehle R, Heissmeyer V, Niessing D, Sattler M.2014. **Structural basis for RNA recognition in roquin-mediated post-transcriptional gene regulation.** *Nature structural & molecular biology*. 2014 Aug; 21(8), pp. 671–678 * Equal contribution

Vogel KU*, Edelmann SL*, Jeltsch KM, Bertossi A, Heger K, **Heinz GA**, Zöller J, Warth SC, Hoefig KP, Lohs C, Neff F, Kremmer E, Schick J, Repsilber D, Geerlof A, Blum H, Wurst W, Heikenwälder M, Schmidt-Supprian M, Heissmeyer V. **Roquin paralogs 1 and 2 redundantly repress the Icos and Ox40 costimulator mRNAs and control follicular helper T cell differentiation.** *Immunity*. 2013 Apr 18; 38(4), pp. 655-668 * Equal contribution

Additional articles

Bronevetsky Y, Villarino AV, Eisley CJ, Barbeau R, Barczak AJ, **Heinz GA**, Kremmer E, Heissmeyer V, McManus MT, Erle DJ, Rao A, Ansel KM. **T cell activation induces proteasomal degradation of Argonaute and rapid remodeling of the microRNA repertoire.** *J Exp Med*. 2013 Feb 11; 210(2), pp. 417-432

Hoefig KP, Rath N*, **Heinz GA***, Wolf C, Dameris J, Schepers A, Kremmer E, Ansel KM, Heissmeyer V. **Eri1 degrades the stem-loop of oligouridylated histone mRNAs to induce replication-dependent decay.** *Nat Struct Mol Biol*. 2013 Jan; 20(1), pp. 73-81 * Equal contribution

Poster presentations connected to this thesis

Molecular requirements for Roquin-mediated RNA recognition and post-transcriptional gene regulation. RNA 2014, Annual Meeting of the RNA Society, Quebec City, Canada

Roquin and Regnase-1 control TH_{17} differentiation by post-transcriptional regulation of shared target mRNAs. SFB 1054 „Control and plasticity of cell-fate decisions in the immune system“ Annual Meeting 2013, Venice, Italy

Molecular function of Roquin-1 and Roquin-2 proteins in the prevention of autoimmunity. Eukaryotic RNA Turnover: From Structural insights to Diseases, EMBO Conference, 2013, Strasbourg, France

Curriculum vitae

Education

09/10 – 03/15	PhD in molecular Biology Helmholtz Zentrum Muenchen, Germany Institute of molecular Immunology, Prof. Dr. Vigo Heissmeyer
10/07 – 12/09	Master's program "Molecular Medicine" Charité University Medicine Berlin, Germany
10/04 – 07/07	Bachelor's program "Molecular Medicine" University of Ulm, Germany
08/95 – 06/04	Richard-Wagner-Gymnasium, Baden-Baden, Germany Abitur (German university entrance qualifications)

Scholarships

05/11 - 04/13	PhD Fellowship of the Boehringer Ingelheim Fonds
2005 - 2009	Scholarship of the German National Academic Foundation

Research experience

01/10 - 07/10	Karolinska Institutet, Stockholm, Sweden Department of Medicine, Clinical Immunology and Allergy Unit Research fellow with Prof. PhD Gunnar Nilsson on the topic "Mast cell activation in response to cell damage"

Acknowledgements

This thesis work would not have been possible without the help and support of many people, that did a great job maintaining facilities I was able to use, that created an enjoyable working atmosphere, that were interested in my project and were willing to spend time thinking about it and to collaborate, and finally people that are passionate about science and thereby remind me of why I started my PhD.

I want to thank Prof. Dr. Vigo Heissmeyer for providing me with this interesting and challenging project and for his eagerness and support in following its twists and turns.

I am thankful to Prof. Dr. Daniel Krappmann for being my first reviewer and a member of my thesis committee and for spending extra time on discussing the written thesis.

I also want to express my gratitude to Prof. Dr. Elisabeth Weiß, who did not hesitate in agreeing to be the second reviewer of this thesis.

I feel honored to have received the PhD fellowship of the Boehringer Ingelheim Fonds and deeply appreciate the seminars and encounters with other fellows as well as the financial support not only of my trip to the RNA meeting in Canada.

Over the past years I had the pleasure of working together with many people, who shared their methods and expertise with me:

The microarray hybridization was performed by Andrea Klanner from Dr. Helmut Blum's group at the Gene Center Munich. Dr. Dirk Repsilber (University of Örebro) provided the bioinformatics data analysis and created the heatmap.

For CLIP and PAR-CLIP assays, I worked together with Prof. Dr. Mihaela Zavolan's group. Georges Martin was an invaluable help for planning and performing the experiments and he and the other group members made my stay in Basel very pleasant. Dr. Andreas Gruber kindly performed bioinformatics analyses of the sequencing data and also fulfilled my special requests concerning the SELEX data analysis.

The SELEX experiments were designed and conducted together with Dr. Raymund Buhmann's group. Dr. Marion Bräu and Kerstin Görke introduced me to the experimental side of the method and I learned a lot about the bioinformatics side from Dr. Michael Blank and Dr. Carsten Gröber (both AptaIT). I really appreciated the welcoming attitude and the interest in my project.

I enjoyed the collaboration with Prof. Dr. Michael Sattler and PD Dr. Dierk Niessing, who was also a member of my thesis committee, Dr. Arie Geerlof, who purified the Roquin-1 full-length protein, Dr. Robert Janowski, who solved the crystal structures, and Dr. Andreas Schlundt, who significantly contributed to the project and provided NMR data. It was great to experience how different approaches and skills can complement each other and shortly result in a high-ranking publication. I am particularly thankful to Dr. Andreas Schlundt for his outstanding commitment to my project and his continuous support of my thesis writing by proof reading and many helpful discussions.

I would also like to mention Michael Hagemann and his team from the animal facility at the Hämatologikum, who took great care of the mice and were always helpful and friendly.

The production of new monoclonal antibodies was only possible in collaboration with Dr. Elisabeth Kremmer and her team, who were also very helpful by providing me with antibodies for all kinds of methods.

Furthermore, I want to thank former and current members of the group, especially Dr. Katharina Vogel for introducing me to agarose EMSAs, Christine Wolf for teaching me about proteins and immunoprecipitations, Dr. Kai Höfig for help with the qPCR measurements, Dr. Stephanie Edelmann for proof reading of the thesis and providing the *ICOS* CDE-like stem-loop data and Claudia Lohs for managing the mouse breedings, being a great lab organizer and a reliable colleague.

In the institute, there are many more people who supported me with quick solutions to problems, flexibly sharing machines, with answers to questions or just with a coffee break at the right time. I really enjoyed being a part of this.

Finally, I want to express my gratitude to my friends and family that accompanied me during the last years and helped me keep the balance.